THE SIX International Exhibition and Scientific Congress "GEO-Siberia-2010" 27-29 April 2010, Novosibirsk, Russian Federation

INSTITUTE FOR MICRO PROCESS ENGINEERING (IMVT), KARLSRUHE
INSTITUTE OF TECHNOLOGY, GERMANY
KUTATELADZE INSTITUTE OF THERMOPHYSICS SB RAS, RUSSIAN
FEDERATION
SIBERIAN STATE ACADEMY OF GEODESY (SSGA), RUSSIAN FEDERATION

### **International Workshop on**

# "MICRO PROCESS ENGINEERING AND NANOTECHNOLOGY APPLICATIONS T"

28-29 April 2010 Novosibirsk, Russian Federation

## **Proceedings**

Novosibirsk, Russian Federation SSGA 2010

### **ABOUT ORGANIZERS**



Institute for Micro Process Engineering (IMVT), Karlsruhe Institute of Technology

Legally founded on October 01, 2009, the Karlsruhe Institute of Technology (KIT) is a merger of Forschungszentrum Karlsruhe and Universität Karlsruhe. KIT bundles the missions of both precursory institutions: A university of the state of Baden-Wuerttemberg with teaching and research tasks and a large-scale research institution of the Helmholtz Association conducting program-oriented provident research on behalf of the Federal Republic of Germany.

With roundabout 8000 employees and 20000 students and an annual budget of about EUR 700 million, KIT is one of the largest research and teaching institutions worldwide. The main areas of research include energy, health, nano- and microsystems, scientific computing, atmosphere and climate, as well as elementary particle physics and astroparticle physics. In addition, material sciences, communication and information technology, optics and photonics, and mobility systems complete the KIT profile.

The Institute for Micro Process Engineering (IMVT) was founded in July 2001 at the former Forschungszentrum Karlsruhe and is currently embedded in the Helmholtz research programs on "Nano- and Microsystems" and "Sustainability and Technology Regarding education, it is associated with the chemical and process engineering department. IMVT performs R&D on microstructured components and systems with channel dimensions typically between some dozen  $\mu m$  and 1 mm for application in chemical reactions and other process engineering operations.

Micro process engineering mainly relies on fast heat transfer and rapid mixing through reduction of transport resistances by microstructuring of the flow geometry. These features allow for an improved control of the process conditions enabling higher selectivity, space-time-yield and energy efficiency in many applications. Microstructured units can be very compact, which is a peculiar advantage when space is limited. Hydrocarbon fuel processing for portable, mobile, or small-scale stationary fuel cell systems fall into this category. Transportable, modular plants e.g. for exploitation of small natural gas reservoirs would be a second example. Improved plant safety by minimization of the reactive inventory and quenching of radical reactions through wall effects can be another benefit of microstructured units. On-site production of hazardous chemicals avoiding risks associated with the transport and storage of such chemicals further adds to the potential of micro process technology for safe industrial production. And micro process technology is one enabling technology for the paradigm shift from batch to continuous processing in the finechemicals and pharmaceuticals industry targeting faster process development and increased product quality due to improved process control.

With about 65 employees and an annual budget of roughly EUR 5.5 million, IMVT is active in the following fields:

- Design, construction, and fabrication of microstructured devices for chemical and thermal process engineering. Examples include cross-flow and counterflow micro heat exchangers, electrically heated micro heat exchangers, micromixers, and microreactors. Metals dominate as construction materials but technologies have been developed for polymers and ceramics as well. The design of multifunctional microstructured units is a new focus, for example by integration of membranes for selective product removal or supply of reactants.
- Extensive characterization of microstructured devices (manufacturing tolerances, reproducibility of manufacture, etc.) and of the processes performed in these devices (flow behavior, mixing behavior, heat transfer rates, etc.) including the development of measurement techniques for in situ investigations in microstructures.
- Optimization of existing techniques and development of new methods for structuring and assembling for the manufacture of microstructured devices.
- Development of functional layers for application in microstructured devices.
   Examples include anti-corrosion, anti-fouling, catalytically active coatings, and membrane layers.
- Demonstration of selected examples of chemical and thermal process engineering in microstructured devices. Applications are diverse ranging from liquid phase reactions to heterogeneous gas phase catalysis and multiphase catalysis. Particular emphasis is on energy-related reactions such as hydrogen generation from methane, propane, methanol, gasoline and diesel, and conversion of natural gas, biogas, or synthesis gas to liquids. Another field of activity is the energy-efficient production of emulsions. In many of these applications IMVT is working closely together with companies from the chemical, pharmaceutical, food, automotive and energy industry.

### **Contact information:**

Prof. Dr.-Ing. Roland Dittmeyer
DirectorInstitute for Micro Process Engineering (IMVT)
Forschungszentrum Karlsruhe GmbH
Hermann-von-Helmholtz-Platz 1
76344 Eggenstein-Leopoldshafen Germany
Tale +40.7247.82, 2114

Tel: +49 7247 82-3114 Fax: +49 7247 82-3186

E-Mail: roland.dittmeyer@imvt.fzk.de

http://www.fzk.de/

### Kutateladze institute of thermophysics sb ras



The **Institute of Thermophysics** of Siberian Branch Russian Academy of Sciences was established in 1957 in Novosibirsk Scientific Center (Akademgorodok). In 1994 the Institute of Thermophysics was named after academician S. Kutateladze. Now the **Institute of Thermophysics SB RAS**, being one of the leading centers of the heat transfer theory and physical hydrodynamics, is dealing with fundamental research in the following areas:

- Heat and mass transfer in single-phase systems (turbulent boundary layer, radiation and combined heat transfer, free-convection heat transfer, gas screen);
- Heat and mass transfer in systems with phase transformations (boiling, condensation, absorption) including those at cryogenic temperatures;
- Heat and mass transfer in dispersed systems (porous and grainy media, fluidized bed, swirl dispersed flows, and micro-dispersed systems);
- Hydrodynamic stability and turbulence (jets and wakes, coherent structures, turbulence models, near-wall turbulence, turbulent boundary layer, polymer additives);
- Vortex flows (swirl flow, vortex structures, Ranque's effect, vortices in superfluid helium);
- Multiphase flows (gas-liquid flow, film flow, gas-saturated boundary layer, spray flow);
- Wave dynamics (acoustics of two-phase media, nonlinear waves in dispersive media, waves in films, intrinsic waves, detonation);
- Dynamics of rarefied gases (non-equilibrium processes, clusters and fullerenes, laser ablation, discharge);
- Thermophysical properties of substances (fluorocarbons; solutions of salts, semiconductors, metals, and oxides; pure substances);
- Thermophysical foundations for the production of new materials (Chokhralski's method, jet plasma chemical method, high-temperature superconductive films);
- Modeling of thermophysical processes in heat power engineering (aerodynamics in chambers with complex geometry, combustion in a boundary layer, heat and mass transfer and combustion in a sonic field, combustion of a water-coal suspense, fluidized bed, circulating fluidized bed);
- Low-temperature plasma (ignition by plasma in pulverized-coal boiler, plasma incineration of complex waste, methods for production of gaseous media).

Several unique experimental techniques have been developed at the Institute: the electro-diffusion method for the measurement of shear stress and local velocities in a flow, stroboscopic visualization of particles, LDA systems (including those with fiber optics), electron-beam diagnostics of rarefied gases, and the method of colored

Hilbert- visualization. The Institute possesses a unique shadow device with extremely high aperture.

We have a number of unique computerized experimental setups: wind tunnels, a large hydrodynamic and freon loops, large-scale vacuum chambers "Vika" and "Viking", a fire bench with plasma ignition, and a setup for study of thermodynamic properties of melts.

The successful activity of the Institute is insured to great extent to our high-qualified specialists inclusive 3 academicians of the Russian Academy of Sciences, 3 corresponding members of RAS, 53 Professors, and 94 Ph.D.s. The number of research personnel at the Institute amounts to 185, and the total number of employees is 490.

The Institute has close scientific relations with foreign research centers and companies in the USA, UK, Germany, France, Italy, Belgium, Norway, Japan, Poland, The Czech Republic, China, and South Korea. We are have research contracts with several world-wide companies such as "Air Products and Chemicals", "Hewlett Packard", "General Motors", etc., "More Energy" (Israel).

### **Contact information:**

Prof. Dr. Sergei V. Alekseenko, Corresponding Member of the RAS

Director

Kutateladze Institute of Thermophysics SB RAS

1, Prosp. Akademika Lavrentieva

Novosibirsk, 630090 Russian Federation

Phone: 7 (383) 330-70-50, Fax: 7 (383) 330-84-80

E-mail: aleks@itp.nsc.ru Internet: http://www.itp.nsc.ru/

### SIBERIAN STATE ACADEMY OF GEODESY (SSGA)



The **Siberian State Academy of Geodesy (SSGA)**, the oldest in Siberia, was founded in 1933. Today it is the recognized leader in training specialists for geodesy, cartography, cadastre, environmental management, exploration of natural recourses, metrology and opto-electronics. There are four institutes in SSGA: Institute of Geodesy and Management, Institute of Cadastre and Geographic Information Systems, Institute of Remote Sensing and Natural Resources Management, Institute of Optics and Optical Technologies. The graduates of **SSGA** receive Bachelor's (**B.Sc**) and Master's Degrees (**M.Sc.**, 2 years after B.Sc.) or qualification of Engineer's/Specialist's Diploma. The SSGA offers educational programs, focused on geoinformation management for sustainable development, each with specialization: digital photogrammetry, urban planning and land administration and GIS.

The Academy carries out a large volume of researches and the major fields of them are: surveying, geodetic maintenance for construction and operation of engineering structures, cartography, GIS technologies, digital and thematic map compilation, cadastre, photogrammetry and remote sensing, satellite geodesy, optics and spectrometry, uses of GPS for the purposes of applied geodesy and land cadastre, and environmental monitoring. The main tendency of research activity is to implement the advanced digital technologies, terrestrial 3D laser scanning, 3D modelling, GIS and GPS technologies. Besides, the academy took an active part in implementing GLONASS/GPS project including 19 reference stations established on the territory of Novosibirsk Region.

SSGA together with ITE Siberian Fair are the organizers of the international exhibition and scientific congress "GEO-Siberia", the first exhibition experience beyond the Urals representing also innovative developments oriented to Siberia subsurface use. Various companies exhibit their highly specialized equipment and there is nothing like it on the Siberian market. "GEO-Siberia" demonstrated the growing interest to this event not only in Russia but abroad too. It has gained a merited recognition among professionals of geo-industry and become an example of collaboration of professionals and scientists from the whole world.

### **Contact information:**

Prof. Dr. Alexander P. Karpik

Rector

Siberian State Academy of Geodesy, SSGA

10, Plakhotnogo Ul.

Novosibirsk, 630108, Russian Federation

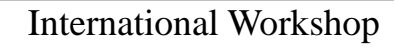
Tel: +7 (383) 343-39-37, Fax: +7 (383) 344-30-60

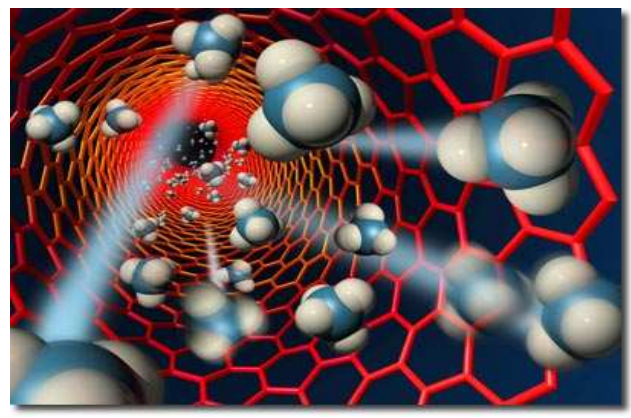
E-mail: rektorat@ssga.ru

Web: www.ssga.ru

**ISBN:** 978-5-87693-374-4

Printed in Novosibirsk, April 2010







April 27-28, 2010 Novosibirsk Russian Federation

ITE Siberian Fair, Novosibirsk, Krasny Prospekt 220







### **ORGANIZERS:**

- Institute for Micro Process Engineering (IMVT), Karlsruhe Institute of Technology, Germany
  - Kutateladze Institute of Thermophysics SB RAS, Russian Federation
  - Siberian State Academy of Geodesy (SSGA), Russian Federation

### ORGANIZING COMMITTEE

### - Chairmen:

Prof. Dr. Vladimir Kuznetsov Head of the Department of Thermophysics of Multiphase

System, Kutateladze Institute of Thermophysics SB RAS,

Russian Federation

Prof. Dr.-Ing. Roland Dittmeyer Director of the Institute for Micro Process Engineering

(IMVT), Karlsruhe Institute of Technology, Germany

– Co-Chairmen:

Dr.-Ing. Juergen J. Brandner Group Leader for Thermal Micro Process Engineering,

Institute for Micro Process Engineering (IMVT), Karlsruhe Institute of Technology, Germany

Prof. Oleg K. Ushakov Director of the Institute of Optics and Optical

Technologies, Siberian State Academy of Geodesy,

Russian Federation

Secretaries

Dr.-Ing. Eugen Anurjew Institute for Micro Process Engineering (IMVT),

Karlsruhe Institute of Technology, Germany

Dr. Alisher S. Shamirzaev Kutateladze Institute of Thermophysics SB RAS,

Russian Federation

Pavel V. Petrov, PhD Siberian State Academy of Geodesy, Russian

Federation

### **GENERAL THEMES AND TOPICS**

### Micro Process Engineering

- Design and Operation of Microstructured Devices
- Heat and Mass Transfer in Microstructured Systems
- Synthesis using Microstructured Systems
- Energy Conversion, Storage and Distribution
- Applications of Microstructured Systems in Industrial Production

### Nano Technology

- Multiscale Systems (Nano Micro Systems)
- Synthesis of Nanoparticles using Microstructured Systems
- Nanostructures and Nanoparticles
- Applications in Industry

Round-table discussion

# International Workshop on "Micro Process Engineering and Nanotechnology Applications" 27-28 April 2010

Novosibirsk, Russian Federation

### TECHNICAL PROGRAMME

TEOTIMO (ET INCOTO MINISTE								
Tuesday, 27	7 April 2010							
Tuesday	Session I							
27 April 2010 10:30-13:00 Siberian Fair Hall 3	Chairs:	Prof. Dr. Vladimir Kuznetsov, Head of the Department of Thermophysics of Multiphase System, Kutateladze Institute of Thermophysics SB RAS, Russian Federation Prof. DrIng. Roland Dittmeyer, Director of the Institute for Micro Process Engineering (IMVT), Karlsruhe Institute of Technology, Germany						
	Secretaries:	DrIng. Eugen Anurjew, Institute for Micro Process Engineering (IMVT), Karlsruhe Institute of Technology, Germany Dr. Alisher S. Shamirzaev, Kutateladze Institute of Thermophysics SB RAS, Russian Federation Pavel V. Petrov, PhD, Siberian State Academy of Geodesy, Russian Federation						
	Rapporteur:  Eugen Anurjew, Edgar Hansjosten, Stefan Maikowske, Ulrich Schygu Juergen J. Brandner (Institute of Technology (KIT), Institute of Mi Process Engineering (IMVT), Germany):  Microstructure Devices for Water Evaporation							
	Prof. DrIng. <b>Stephan Scholl</b> (Institute for Chemical and Thermal Process Engineering Technische Universität Carolo-Wilhelmina zu Braunschweig, Institute of Technology, Germany):  From Macro Batch to Micro Conti: Eco-friendly Processes and New Products Through Micro Process Engineering Technology							
	P. Pfeifer, O. Görke, P. Piermartini, S. Tauro, J. Thormann, R. Dittmeyer (Karlsruhe Institute of Technology (KIT), Institute of Micro Process Engineering (IMVT), Germany):  Recent Advances in Heterogeneously Catalysed Processes for Energy Related Applications							
	Manfred Kraut, Andreas Hensel, Roland Dittmeyer (Institute Technology (KIT), Institute of Micro Process Engineering (IMV Germany):  Contacting of Immiscible Liquids Using Microstructured Devices							
	of Micro Process	Juergen Brandner (Institute of Technology (KIT), Institute s Engineering (IMVT), Germany):  erization of Microstructured Evaporators						

Tuesday	
27 April	2010
14:00-17:	00
Siberian F	air
Hall 3	

### **Session 2**

Rapporteur:

**Vladimir V. Kuznetsov, Oleg V. Vitovsky, Olga A. Gasenko** (Kutateladze Institute of Thermophysics SB RAS, Russian Federation):

Control of the Reactions of Hydrogen Production at Steam Reforming in Micro and Nanoscale

**Stanislav Kozlov, Vladimir Kuznetsov** (Kutateladze Institute of Thermophysics SB RAS, Russian Federation):

The Modeling of Chemical Transformations at Methane Steam Reforming and Water Gas Shift Reaction in a Microchannel

Anatoly A. Vostrikov, Andrey V. Shishkin, Oxana N. Fedyaeva, Mikhail Ya. Sokol (Kutateladze Institute of Thermophysics SB RAS, Russian Federation):

Synthesis of ZnO, ZrO<sub>2</sub> and WO<sub>3</sub> Nanoparticles at Interaction of Bulk Metal Samples with Sub- and Supercritical Water

**Alisher Shamirzaev, Vladimir Kuznetsov, Stanislav Kozlov** (Kutateladze Institute of Thermophysics SB RAS, Russian Federation):

Flow Boiling Heat Transfer of Refrigerant in Mini and Micro Channels

**Igor A. Kozulin, Vladimir V. Kuznetsov** (Kutateladze Institute of Thermophysics SB RAS, Russian Federation):

Structure of Two-phase Flow in Mini- and Micro Channel

Wednesday					
28 April 2010					
10:00-13:00					
Siberian Fair					
Hall 3					

### **Session 3**

Wednesday, 28 April 2010

Chairs:	Prof. Dr. Vladimir Kuznetsov, Head of the Department of					
	Thermophysics of Multiphase System, Kutateladze					
	Institute of Thermophysics SB RAS, Russian Federation					
	Prof. DrIng. <b>Roland Dittmeyer</b> , Director of the Institute					
	for Micro Process Engineering (IMVT), Karlsruhe Institute					
	of Technology, Germany					
	DrIng. <b>Juergen J. Brandner</b> , Group Leader for Thermal Micro Process Engineering, Institute for Micro Process					
	Engineering (IMVT), Karlsruhe Institute of Technology,					
	Germany					
	Prof. Oleg K. Ushakov, Director of the Institute of Opt					
	and Optical Technologies, SSGA, Novosibirsk					
Secretaries:	DrIng. Eugen Anurjew, Institute for Micro Process					
	Engineering (IMVT), Karlsruhe Institute of Technology,					
	Germany					
	Dr. Alisher S. Shamirzaev, Kutateladze Institute of					
	Thermophysics SB RAS, Russian Federation					
	Pavel V. Petrov, PhD, Siberian State Academy of					
	Geodesy, Russian Federation					
Donnortour						

Rapporteur:

Thomas Gietzelt, Lutz Eichhorn, Markus Guttmann (Institute of Technology (KIT), Institute of Micro Process Engineering (IMVT),

Germany):

Manufacturing of a Sputter Mask for Selective Coating of Large-Area Resist Structures by Microdrilling

Valerik S. Ayrapetyan, Oleg K. Ushakov (SSGA, Novosibirsk, Russian Federation):

IR Lidar Sounding of Atmospheric Gases

Vladimir V. Chesnokov, Dmitry V. Chesnokov, Valery A. Raihert (SSGA, Novosibirsk, Russian Federation):

Termomechanical Process in Multi-Layer Nanostructures Initiated by Laser Irradiation

**N.R. Rahimov, O.K. Ushakov. B.N. Rahimov** (SSGA, Novosibirsk, Russian Federation):

Investigation of Photoelectric Properties of Anomalous Photovoltaic CdTe Films and Development of Optoelectronic Devices on Their Basis

**Daria S. Mikhaylova, Vladimir V. Chesnokov, Dmitry V. Chesnokov** (SSGA, Novosibirsk, Russian Federation): Principle and Arrangement of Absorption Spectrum Measurement of the Layers Adsorbed on Transparent Substrates

**Dmitry M. Nikulin, Vladimir V. Chesnokov, Dmitry V. Chesnokov** (SSGA, Novosibirsk, Russian Federation): *Multiplex Colour Filter in Micromechanical Performance* 

**Round-table discussion** 

### **TABLE OF CONTENTS**

About Organizers
Organizing Committee
General Themes and Topics
Technical Programme9
Anurjew Eugen, Hansjosten Edgar, Maikowske Stefan, Schygulla Ulrich,
Brandner Juergen J. Microstructure Devices for Water Evaporation 13
Scholl Ing. Stephan From Macro Batch to Micro Conti: Eco-Friendly Processes
and New Products Through Micro Process Engineering Technology 28
Pfeifer P., Görke O., Piermartini P., Tauro S., Thormann J., Dittmeyer R. Recent Advances in Heterogeneously Catalysed Processes for Energy Related
Applications30
Kraut Manfred, Hensel Andreas, Dittmeyer Roland. Contacting of Immiscible
Liquids Using Microstructured Devices
Vittoriosi Alice, Brandner Juergen. Optical Characterization of Microstructured
Evaporators53
Kuznetsov Vladimir V., Vitovsky Oleg V., Gasenko Olga A. Control of the
Reactions of Hydrogen Production at Steam Reforming in Micro and
Nanoscale64
Kozlov Stanislav, Kuznetsov Vladimir. The Modeling of Chemical
Transformations at Methane Steam Reforming and Water Gas Shift
Reaction in a Microchannel
Vostrikov Anatoly A., Shishkin Andrey V., Fedyaeva Oxana N., Sokol Mikhail
Ya. Synthesis of ZnO, ZrO2 and WO3 Nanoparticles at Interaction of Bulk
Metal Samples with Sub- and Supercritical Water
Shamirzaev Alisher, Kuznetsov Vladimir, Kozlov Stanislav. Flow Boiling Heat
Transfer of Refrigerant in Mini and Micro Channels
Kozulin Igor A., Kuznetsov Vladimir V. Structure of Two-Phase Flow in Mini-
and Micro Channel 104
Gietzelt Thomas, Eichhorn Lutz, Guttmann Markus. Manufacturing of a Sputter
Mask for Selective Coating of Large-Area Resist Structures by
Microdrilling
Ayrapetyan Valerik S., Ushakov Oleg K. Ir Lidar Sounding of Atmospheric
Gases
Chesnokov Vladimir V., Chesnokov Dmitry V., Rayhert Valery A.
Termomechanical Process in Multi-Layer Nanostructures Initiated by Laser
Irradiation
Investigation of Photoelectric Properties of Anomalous Photovoltaic CdTe films and Development of Optoelectronic Devices on their Basis
Mikhaylova Daria S., Chesnokov Vladimir V., Chesnokov Dmitry V. Principle
and Arrangement of Absorption Spectrum Measurement of the Layers
Adsorbed on Transparent Substrates143
Nikulin Dmitry M., Chesnokov Vladimir V., Chesnokov Dmitry V. Multiplex
Colour Filter in Micromechanical Performance

### MICROSTRUCTURE DEVICES FOR WATER EVAPORATION

# Eugen ANURJEW <sup>1</sup>, Edgar HANSJOSTEN <sup>1</sup>, Stefan MAIKOWSKE <sup>1</sup>, Ulrich SCHYGULLA <sup>1</sup> and Juergen J. BRANDNER <sup>1,\*</sup>

\* Corresponding author: Tel.: ++49 (0)7247 82 3963; Fax: ++49 (0)7247 82 3186; Email: juergen.brandner@kit.edu

**Key words:** Evaporation, Microstructures, Visualization, Superheating

### **Summary**

Evaporation of liquids is of major interest for many topics in process engineering. One of these is chemical process engineering, where evaporation of liquids and generation of superheated steam is mandatory for numerous processes. Generally, this is performed by use of classical pool boiling and evaporation process equipment, providing rather limited performance. Due to the advantages of microstructure devices especially in chemical process engineering the interest in microstructure evaporators and steam generators has been increased through the last decade.

In this publication different microstructure devices used for evaporation and generation of steam will be described. Starting with simple liquid-heated devices, electrically powered devices containing micro channels as well as non-channel microstructures are shown.

Micro channel heat exchangers have been designed, manufactured and tested at the Institute for Micro Process Engineering of the Karlsruhe Institute of Technology for more than 15 years. Starting with the famous Karlsruhe Cube (see Fig. A), not only conventional heat transfer between liquids or gases has been theoretically and experimentally examined but also phase transition from liquids to gases (evaporation).



Fig. A: Stainless steel crossflow micro channel heat exchangers of different sizes.

Front middle: The Karlsruhe Cube

<sup>&</sup>lt;sup>1</sup>: Institute for Micro Proces Engineering (IMVT), Karlsruhe Institute of Technology, North Campus, Hermann-von-Helmholtz-Platz 1, DE-76344 Eggenstein-Leopoldshafen, Germany

To obtain more information on the evaporation process itself, an electrically powered device for optical inspection of the microstructures and the processes inside has been designed and manufactured. Exchangeable metallic micro channel array foils as well as an optical inspection of the evaporation process by high-speed videography have been integrated into this test system. Fundamental research into the influences of the geometry and dimensions of the integrated micro channels, the inlet flow distribution system geometry as well as the surface quality of the micro channels have been performed.

While evaporation of liquids in crossflow and counter-current flow or co-current flow micro channel devices is possible, it is, in many cases, not possible to obtain superheated steam due to certain boundary conditions. Thus, a new design was proposed to obtain complete evaporation and steam superheating. This microstructure evaporator consists of a concentric arrangement of semi-circular walls or semi-elliptic walls providing at least two nozzles to release the generated steam. The complete arrangement forms a row of circular blanks. An example of such a geometry is shown in Fig. B.

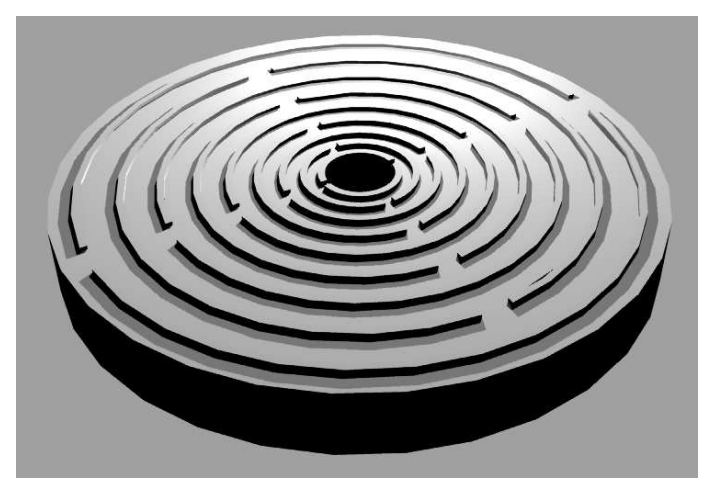


Fig. B: Design of an arrangement of circular blanks for evaporation

A maximum power density of  $1400~kW\cdot m^{-2}$  has been transferred using similar systems, while liquid could be completely evaporated and the generated steam superheated. It could also be shown that the arrangement in circular blanks acts as a kind of micro mixer for the remaining liquid and generated steam and, therefore, enhances the evaporation.

### 1. INTRODUCTION

Microstructured devices have become increasingly important in thermal and chemical process engineering within the last years. These devices are often made out of micro structured metal foils, which are connected by diffusion bonding. The hydraulic diameters of the micro channels, generated by precision machining or wet chemical etching, are in the range of a few hundred micrometres.

Metallic microstructured devices provide high pressure resistance and small residual volumes. Due to the size of the microstructures they act as flame arresters or explosion barriers; thus they are well suited to handle dangerous or explosive fluids.

The small dimensions of micro channels enable very high surface-to-volume ratios up to 30 000 m<sup>2</sup>·m<sup>-3</sup>, which are about one or two orders of magnitude higher than those of conventional process engineering devices. This high surface-to-volume ratio leads to increased heat transfer, the micro dimensions of the channels to short diffusion lengths. Therefore, microstructured devices are well suited for operations dealing with high heat fluxes and rapid mass transfer like evaporation.

Phase transition and multiphase flow in macro channels have been intensively investigated and are well known and understood. In micro channels, phase transition, related phenomena and multiphase flow have been partially investigated. Most results presented so far have been obtained with single micro channels, sometimes multimicro channel arrays have been investigated for their behaviour in evaporation. However, results about the phenomena occurring in multi micro channel arrays are often not consistent, depending on the experimental setup, the fluid looked at and the measurement methods.

### 2. METALLIC MULTI-MICROCHANNEL DEVICES

First attempts to evaporate water have been done using micro channel heat exchangers in crossflow design. Manufacturing of these devices was described before in details [1, 2, 3]. Fig. 1 shows different examples for microstructure foils integrated into crossflow heat exchangers made of stainless steel, shown in Fig. 2 (left). A stainless steel counter-current flow heat exchanger is shown in Fig. 2 (right).

Several experiments with crossflow devices showed that evaporation of water is possible, using hot thermo oil in the heating passage of the device. However, wet steam was generated containing very high percentage of droplets, and no superheating could be obtained. This was, at least partly, due to short residence time of the fluid and limited temperature of the heating side. Thus, electrically powered micro heat exchangers have been developed, manufactured and tested to provide higher temperatures with good controllability of the power supplied [7, 8]. Fig. 3 shows three different sizes of electrically powered micro heat exchangers.

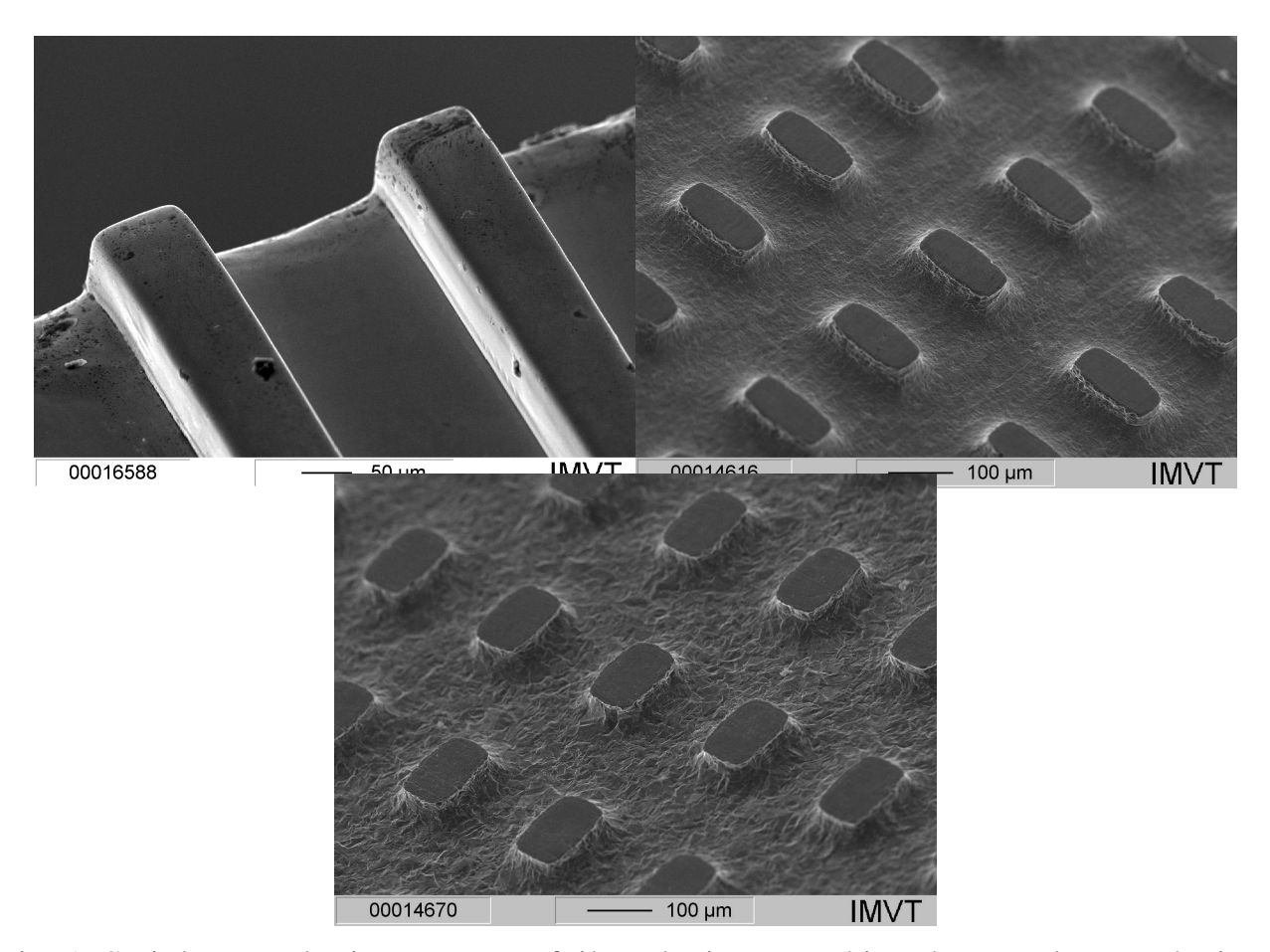


Fig. 1. Stainless steel microstructure foils to be integrated into heat exchanger devices



Fig. 2. Left: Stainless steel crossflow micro heat exchangers of different size. Right: Stainless steel counter-current / co-current flow microstructure heat exchanger. For technical details see [1, 3, 5]

With these devices, not only straight rectangular micro channels but also semielliptic micro channels in convoluted or sinusoidal arrangements have been tested for evaporation. It could be shown that, depending on the applied mass flow, either a single microstructure device or a two-stage-arrangement, which means two devices in a row, can be used for complete evaporation and superheating of water and other liquids [9]. Substantial data on the droplet content contained in the vapour flow could be obtained by a simple photometer setup. A photo current was measured, obtained by scattered laser light in full reflection from the vapour outlet of different arrangements of electrically powered devices. The amplitude of photo current could directly be correlated to the droplet content of the vapour as well as to the vapour temperature [1, 10].

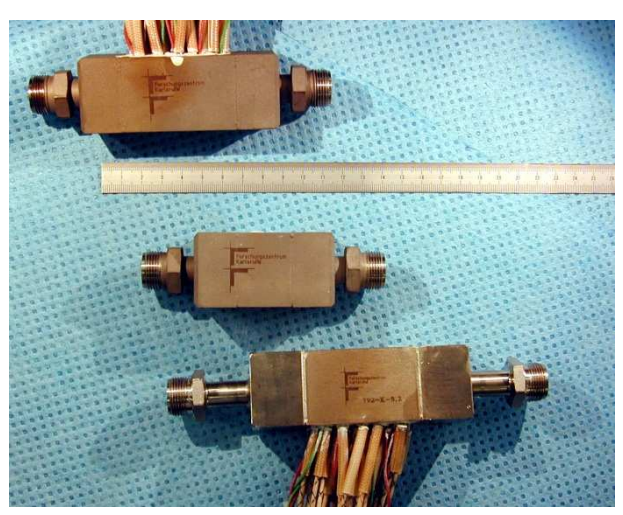


Fig. 3. Electrically powered microstructure heat exchangers of different size. Technical details can be obtained from [1, 7, 8]

# 3. MULTI-MICROCHANNEL DEVICE FOR VISUALISATION OF EVAPORATION

Although evaporation of liquids can be performed successfully using devices like those described in section 2, it was still not quite clear which parameters strongly influence the evaporation process inside a multi-micro channel system. Numerous research activities have been done to clarify the evaporation processes taking place in single micro channels (see e.g. [11–15]), but not so many research activities have been dedicated to multi-micro channel array evaporators.

An electrically powered stainless steel frame was manufactured to allow the exchange of micro channel structures as well as the optical inspection of the processes inside the micro channels using high speed videography. More details of the design as well as of an improved device can be found in [1]. Fig. 4 shows a photo of the device.

The apparatus design provides the possibility to vary different parameters like temperature, applied electrical power, volume flow rate or pressure drop. Additionally, microstructured metal foils – including multi-micro channel arrays – are exchangeable. Thus, phase transition and multiphase flow in several kinds of different micro channel geometries and arrangements could be investigated.



Fig. 4. Electrically powered microstructure device, providing exchangeable micro channel foils and a glass lid for high speed videography

The method of visualization by high speed videography has been applied to perform initial investigations on phase transition as well as on the dynamics of gasliquid flows in narrow channels [11, 16]. The experimental setup used here contains a microscope in combination with a digital high-speed camera. The microscope is arranged above the horizontal multi-micro channel layer.

The digital high-speed camera records pictures at frequencies of up to 200 000 frames per second with very low motion blur. Special computational algorithms can be used to analyse these recorded high-speed picture sequences to extract information about different phases.

### 3.1.Phase transition phenomena

Phase transition in micro channels is accompanied by several phenomena like vapour plugging or vapour slugging, which occur only to a minor extent or are not available in macro channels. Two different types of vapour plugging were observed – vapour plugging at channel inlets and vapour plugging inside of micro channels. All these observations of evaporation were performed with liquid water and related steam in micro channels with rectangular cross-sections in the range of about 200  $\mu$ m (width) and 100  $\mu$ m (depth).

Vapour plugging at channel inlets occurs when existing vapour bubbles, which have been generated by boiling inside the inlet void, agglomerate at channel entrances. These bubbles are temporarily fixed and expand by capturing small bubbles. The fixed bubbles can partially be discharged by micro channels when a specific bubble size is reached. Consequently, channel entrances are temporarily plugged by bubbles. Fig. 5 shows a picture sequence of plugged channel entrances. Gas fractions inside of these channel inlets (indicated in the right picture of Fig. 5.) indicate bubble drainages by micro channels.

Another type of vapour plugging is the plugging inside micro channels. Rapidly growing bubbles are accompanied by accelerated bubble-endings and decelerated bubble-beginnings. If the motion of a bubble beginning stops due to the bubble-growing, the corresponding micro channel is temporarily plugged by vapour. Another effect of this channel-plugging is the reversal of flow direction of bubble beginnings caused by explosively growing bubbles. Fig. 6 shows a section of a multi-micro channel array at different time steps. Fluid flow direction is from left to right. The movement of bubble beginnings in both channels decreases continuously until it

stops. At this point ( $t = 221 \cdot 10^{-3}$  s) both channels are temporarily plugged by stagnant bubble beginnings. Eventually, the bubble beginnings start moving in the opposite direction to the fluid flow and thereby transport liquid fluid backwards. Vapour slugging is also caused by rapidly growing bubbles. Liquid fractions, trapped between two bubbles, are slugged out of the micro channel by accelerated bubble-endings. The contact time between these liquid fractions and the heated micro channel wall is too low for a complete evaporation.

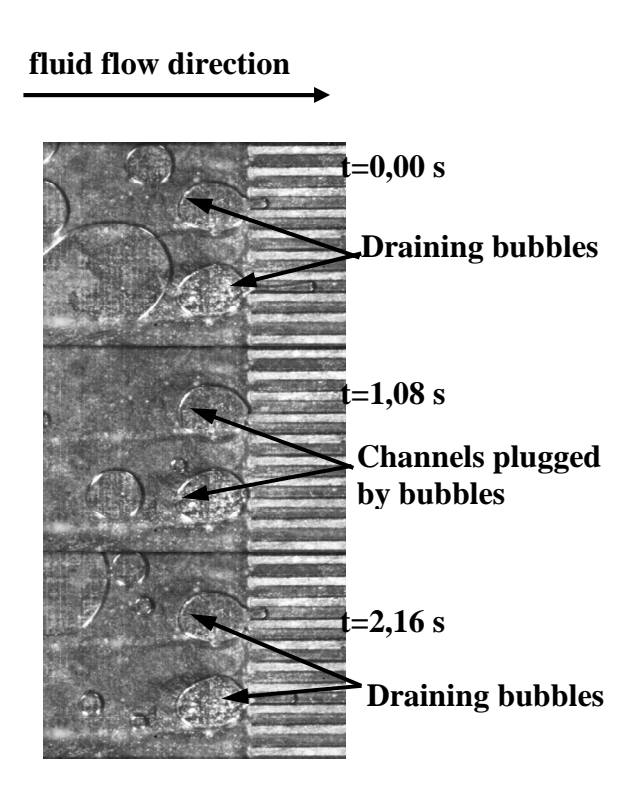


Fig. 5. Vapour plugging at channel inlets, 100°C, the multi-micro channel array is located on the right side

The above mentioned phase transition phenomena lead to non-uniform fluid flow distribution in multi-micro channel arrays and result in non-uniform vapour quality at evaporator outlets. Controlling or reducing these phenomena results in a nearly constant phase transition inside of multi-micro channel arrays and in a related constant vapour quality at the evaporator outlet. Fig. 8 shows an example of such a nearly constant phase transition inside of a multi-micro channel array. The parabolic shape is probably caused by non-uniform fluid flow distribution at the channel entrances.

The parabolic shape is due to a non-uniform distribution of the flow velocity by the inlet structure. CFD calculations performed at the Technical University of Graz showed that it might be avoided by use of a tree-like distribution system at the entrance of the multi-micro channel array to provide equal distribution of flow velocity to all micro channels and, therefore, an equal distribution of the residence time in the evaporation area. Fig. 8 shows the CFD simulation results for the triangular inlet void (left) and a tree-like shaped void (right) [17]. Fig. 9 shows a

microstructure foil with conventional distribution system on the left side and a tree-like distribution system on the right side. Flow direction can easily be changed with this foil.

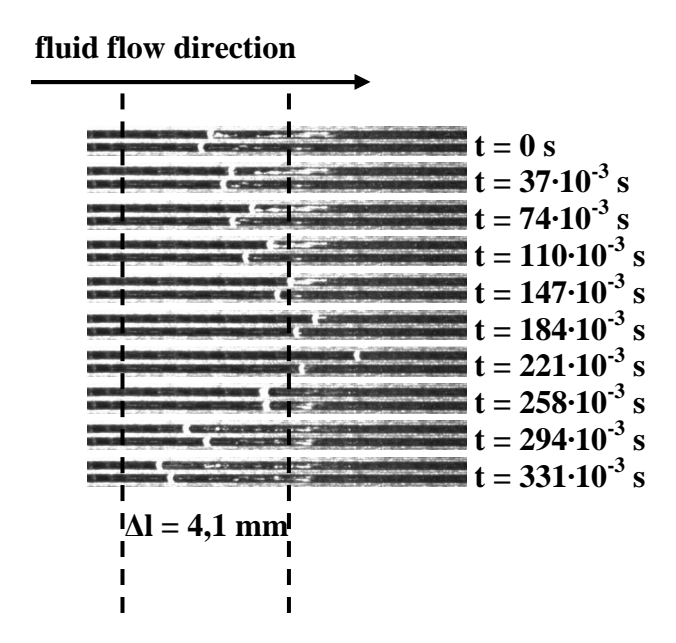


Fig. 6. Vapour plugging inside of micro channels, reversal of flow direction by rapidly growing bubbles, 150 °C

# liquid vapour phase transition region

Fig. 7. Nearly constant phase transition inside of a multi-micro channel array at 130 °C

The tree-like system was tested, and, as expected, the parabolic shape of the phase transition front could be drastically changed to a phase transition front more or less perpendicular to the streamline and the micro channel direction.

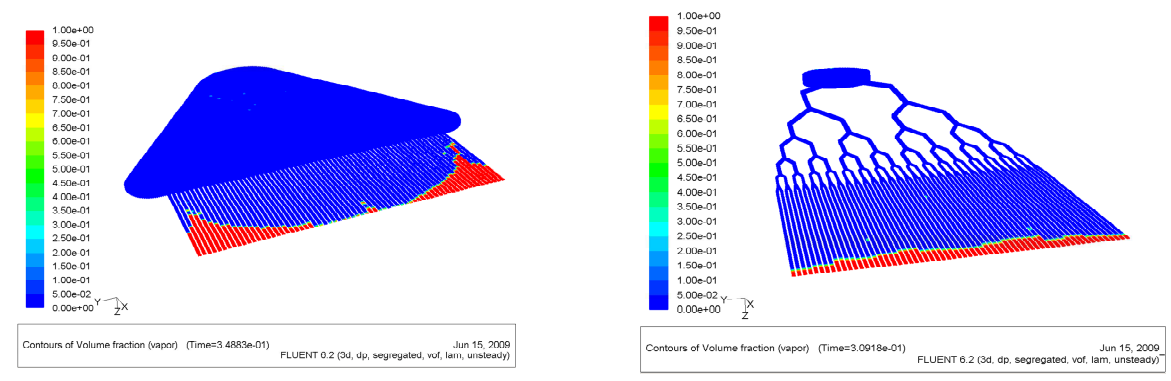


Fig. 8. CFD simulation of the flow distribution for different inlet design. Left: triangular inlet. Right: tree-like inlet structure

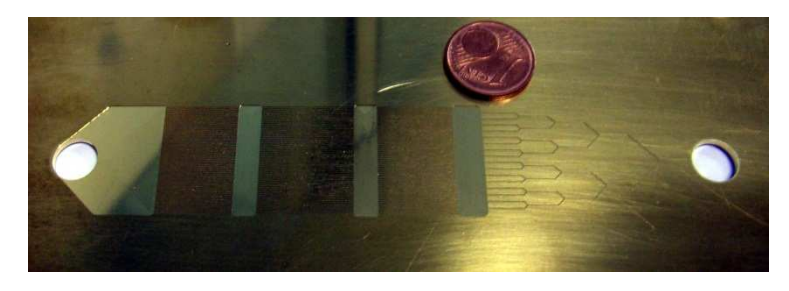


Fig. 9. Multi-micro channel foil providing a standard flow distribution void (left) and a tree-like distribution system (right). Evaporation takes place in a three-staged multi-micro channel array (center)

The tree-like structure is designed for branching of the flow into sub-flows providing the same hydrodynamic properties at any position in the distribution system, acting as a bionic distributor. Aside of this, the micro-channel arrays are separated into three stages with connecting voids in between to allow evaporation and superheating.

### 4. EVAPORATOR DESIGN WITH CIRCULAR BLANKS

Due to the strong increase in volume while the phase transition takes place evaporation in long straight micro channels is limited. This is based on thermodynamic considerations. It is, in many cases, possible to evaporate a liquid volume flow completely, but superheating is difficult. A flow velocity limit, depending on the temperature and the pressure inside the evaporation system, can be obtained [18]. This flow velocity limit provides information on the maximum volume flow which can be evaporated and superheated using straight micro channels.

It is, thus, useful to think about micro evaporator designs which are not limited by flow velocity. One possibility is the use of concentric circular blanks. This new design consists of circular or elliptically shaped ring walls which are arranged concentrically around a feed hole. Each of the ring walls show two overflow openings, which act as expansion nozzles. The position of those overflow openings is changed by 180° from one ring to the next. Fig. 10 shows two examples of such microstructures, each generated on a round plate with 1.7 cm diameter. The first

devices have been manufactured from a polymer by micro-stereolithography [1, 2, 19], later devices have been manufactured by precision micromachining from copper to obtain higher steam temperatures.

The experiments have been performed using a metallic adapter system to house the circular blank arrangements. Water inlet and steam outlet as well as electric heaters and sensors have been integrated into the adapter system, which is shown in Fig. 11. Water mass flow was varied between 0.3 kg · h<sup>-1</sup> and 1.0 kg · h<sup>-1</sup>, and evaporation was performed with ambient outlet pressure. The electrical heating power applied was varied according to this mass flow range to obtain full evaporation and superheating. A heating surface temperature limit of 170 °C was randomly set, resulting in an applied electrical power of about 820W and an evaporation power of 600W for the maximum mass flow.

A brief summary of experimental parameters is given in table 1. The differences between applied electrical power and evaporation power are heat losses as well as the power consumed for superheating. It was, at least in the existing experimental setup, not possible to determine the heat losses exactly. However, the power applied for superheating can be neglected in comparison to what is needed for evaporation, thus most of the difference is most likely heat losses.

Numerous designs have been tested experimentally. The main focus was set to three points: how many semi-circular walls (semi-elliptic walls) are really necessary for evaporation and superheating, what is the influence of the position of these walls, and is there a connection between the steam temperature and the number and arrangements of walls?

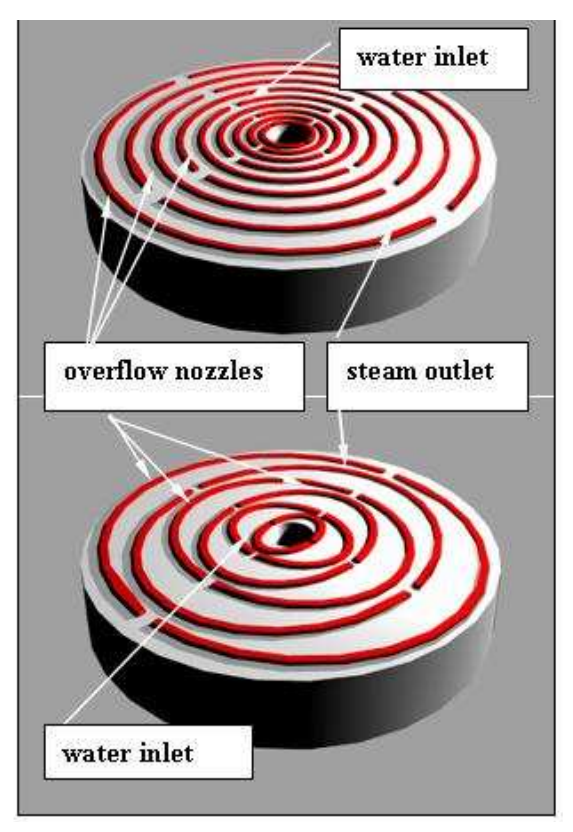


Fig. 10. Examples for circular blank arrangements used for water evaporation

Table 1. Experimental parameters used for evaporation and superheating with different geometries

Water mass flow [kg · h-1]	0.3	0.5	0.7	1.0
Heating surface temperature [°C]	130	140	155	170
Applied electrical power [W]	254	407	560	820
Evaporation power [W]	190	306	430	600

It was experimentally shown that it is possible to generate superheated steam with a single sidewall around a circular or elliptic blank, if this is arranged at the outermost circumference of the microstructure inlay. A single circular blank with sidewalls arranged directly around the water inlet will lead to complete evaporation, but almost no superheating is possible with this arrangement. Results of further experiments are given in Fig. 12 and Fig. 13. Here, the outlet steam temperature is plotted against time for complete evaporation. This plot style was chosen to show the transient behaviour of superheating. In all experiments the flow velocity of the steam was increased drastically due to an increase in volume by the evaporation inside the circular blanks. Maximum flow velocity and maximum superheating temperature are coincident, which is shown in both figures Fig. 12 and Fig. 13 by reaching the saturation.

Fig. 12 shows the outlet steam temperature obtained with the same water mass flow of  $0.7 \text{ kg} \cdot \text{h}^{-1}$  and the same electrical power. It is obvious that evaporation and superheating can be obtained with the sidewalls arranged at the outer limit of the circular blank, but not with those arranged at the inner limit.

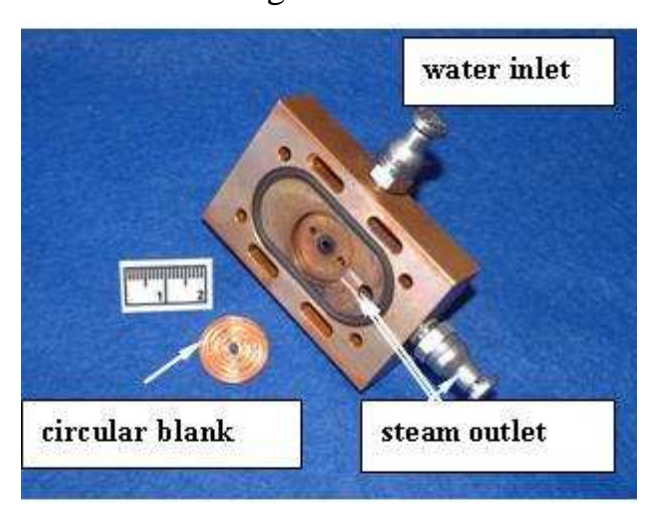


Fig. 11. Test adapter system to house copper circular blanks

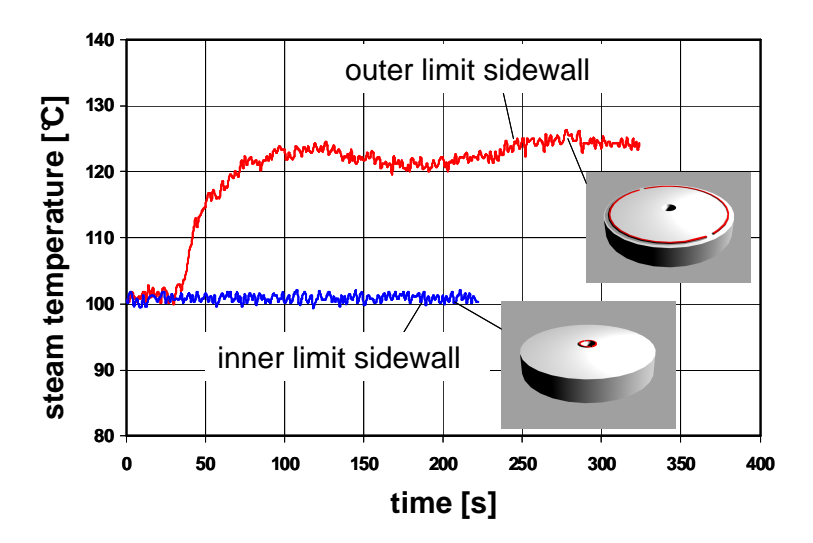


Fig. 12. Results obtained with two different sidewall arrangements, obtained with the same electrical power and water mass flow. Only the arrangement of sidewalls at the outer limits of the circular blank leads to steam superheating

More experiments showed that the number of sidewalls or structures inside the outer limits of the circular blanks influences the exit temperature of the steam. At the same water mass flow of  $1.0~{\rm kg}\cdot{\rm h}^{-1}$  and the same electrical power applied three different arrangements have been tested for their capability to generate superheated steam. It was shown that a slight superheating was possible with a single sidewall arrangement at the outer limits. Higher temperatures have been obtained when several inner sidewalls or structures have been used. The same results have been obtained with circular sidewalls, as it is shown in Fig. 13. Similar results have been obtained with elliptic sidewalls.

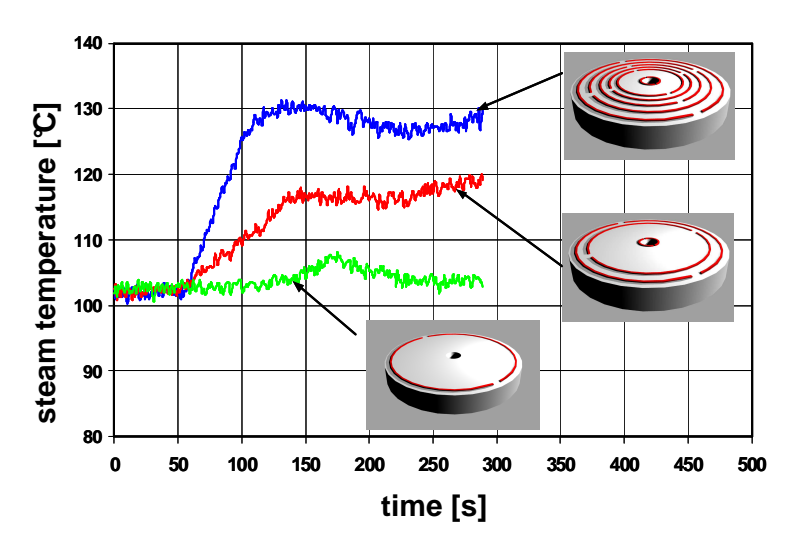


Fig. 13. Steam outlet temperature obtained with different numbers of sidewalls

The plots in Fig. 13 show that the steam temperature is decreasing with decreasing number of sidewalls, and that steam superheating is very limited with a single sidewall arrangement at the outer blank limit. No higher temperature is

possible, no matter what electrical power is applied. This can partly be explained by an increase of the evaporation pressure for larger numbers of circular blanks, but the pressure difference between the two structures used for the red and the blue plot are within measurement uncertainty. Thus, more experiments have to be performed to clarify the influence of pressure inside the circular blanks. However, the temperature shown in Fig. 13 was measured at ambient pressure.

The plots shown in Fig. 12 have been obtained with a lower water mass flow of  $0.7 \text{ kg} \cdot \text{h}^{-1}$ . Thus, a mass flow limit for the use of a single sidewall arrangement for superheating seems to be somewhere in between  $0.7 \text{ kg} \cdot \text{h}^{-1}$  and  $1.0 \text{ kg} \cdot \text{h}^{-1}$ . According to this finding, an optimum design in terms of evaporation, superheating temperature and pressure drop can probably be defined for every mass flow range. However, more work has to be done in future to find this optimum and to define perhaps a theoretical model description which allows a pre-calculation of the design.

### 5. CONCLUSION

Several metallic microstructure devices with multi-micro channel array arrangements for evaporation of liquids, especially water, have been designed, manufactured and tested. Fluid driven devices in crossflow and counter-current or cocurrent design are quite limited in temperature, while electrically powered devices are much more flexible to use. A special device was generated to allow optical inspection of the evaporation process through a glass lid by high speed videography. Several evaporation effects like micro channel plugging have been visualized, and different designs of the inlet for flow distribution into the micro channel array have been tested. It was found that long straight micro channels are not optimal for evaporation. Thus, a new design based on circular blanks including numerous circular or elliptic sidewalls at different positions have been tested. It was shown that full evaporation and some superheating could be obtained with a single side wall at the outer limit. This arrangement is only suitable for a certain mass flow range, as it was shown. Further investigations will be done to optimize the performance and to allow a precalculation of the design to the desired mass flow as well as to the superheating temperature.

### **REFERENCES**

- [1] Brandner, J.J., Micro Process Engineering: Aspects of Miniaturization for a New Technology, Habilitation Thesis, Technical University of Dresden, 2008.
- [2] Brandner, J.J., T. Gietzelt, T. Henning, M. Kraut, H. Moritz and W. Pfleging, Micro Process Engineering Sec. 10: Microfabrication in Metals and Polymers. Advanced Micro & Nanosystems (O. Brand, G.K. Fedder, C. Hierold, J.G. Korvik, O. Tabata, (Eds.) and N. Kockmann (Volume Ed.)), Wiley-VCH, Weinheim, Germany, 2006, 267–319.
- [3] Schubert, K., J.J. Brandner, M. Fichtner, G. Lindner, U. Schygulla and A. Wenka, Microstructure Devices for Applications in Thermal and Chemical Process Engineering. Microscale Thermophysical Engineering, Vol. 5 No. 1, 2001, 17–39.

- [4] Goedde, M., Liebner, C., Hieronymus, H., Sicherheit in der Mikroreaktionstechnik, Chemie Ingenieur Technik, 1–2, 2009, 73–78.
- [5] Brandner, J.J., E. Anurjew, L. Bohn, E. Hansjosten, T. Henning, U. Schygulla, A. Wenka and K. Schubert, Concepts and Realization of Microstructure Heat Exchangers for Enhanced Heat Transfer. Experimental Thermal and Fluid Science, Vol. 30, 2006, 801-809.
- [6] Thome, J.R., State-of-the-Art of Boiling and Two-Phase Flows in Microchannels, Heat Transfer Engineering, 27(9), 2006, 4–19.
- [7] Henning, T., Brandner, J.J., Schubert, K., Characterisation of electrically powered micro heat exchangers, Chemical Engineering Journal 101/1-3, 2004, 339–345.
- [8] Henning, T., Brandner, J.J., Schubert, K., Lorenzini, M. and Morini, G.L., Low-Frequency Instabilities in the Operation of Metallic Multi-Microchannel Evaporators. Heat Transfer Engineering, Vol. 28, No. 10, 2007, 834–841.
- [9] Knauss, R., Marr, R., Brandstätter, R., Dynamic Optimization of an Evaporator by a Nonlinear Model Predictive Controller for Operation at modular Micro Rectification, Proc. Int. Symposium on Micro Chemical Process and Synthesis MIPS2009, Sep 11-13, 2009, Kyoto, Japan, 108–111.
- [10] Vittoriosi, A., Characterization of Microstructure Evaporators using Optical Measurements, Diploma Thesis, Forschungszentrum Karlsruhe, IMVT, Universita di Bologna, 2009.
- [11] Bauer, T., Experimental and theoretical investigations of monolithic reactors for three-phase catalytic reactions, PhD thesis. Faculty of Mechanical Engineering, Dresden University of Technology, 2007.
- [12] Cortina Diaz, M., Flow boiling heat transfer in narrow channels, PhD thesis, University of Magdeburg, Faculty of Process and System Technology, 2008.
- [13] Chen, W.L., Twu M.C., Pan, C., Gas-liquid two-phase flow in microchannels. International Journal of Multiphase Flow, Vol. 28, 2002, 1235–1247.
- [14] Coleman, J.W., Garimella, S., Characterization of two-phase flow patterns in small diameter round and rectangular tubes. International Journal of Heat and Mass Transfer, Vol. 42, 1999, 2869–2881.
- [15] Cubaud, T., Ho, C.-M., Transport of Bubbles in Square Microchannels. Physics of Fluids, Vol. 16, 2004, 4575-4585.
- [16] Henning, T., Brandner, J.J., Schubert, K., High-Speed Imaging of Flow in Microchannel Array Evaporators. Microfluidics and Nanofluidics, Vol. 1, 2007, 128–136.
- [17] Wiesegger, L., Entwicklung und Untersuchung eines neuartigen Mikrostrukturapparates zur Durchführung einer Absorption und Destillation, PhD thesis, Graz Technical University, Graz, Austria, 2009
- [18] Bosnjakovic, F., Technische Thermodynamik Teil 1, 8. corr. ed., Steinkopf Darmstadt, Germany, 1998
- [19] Brandner, J.J., Anurjew, E., Hansjosten, E., Pfleging, W., Schubert, K., Microstructure Device Generation by Selective Laser melting, Proc. SPIE Photonics West, San Jose, CA, USA, Jan 25–27, 2007.

### **CONTACTS**

### Dr.-Ing. habil. J.J. Brandner

Karlsruhe Institute of Technology North Campus Institute for Micro Process Engineering Hermann-von-Helmholtz-Platz 1 D-76344 Eggenstein-Leopoldshafen GERMANY

Tel. +49 7247 82 3963 Fax + 49 7247 82 3186

Email: *juergen.brandner@kit.edu*Web site: www.fzk.de/imvt-en

© E. Anurjew, E. Hansjosten, S. Maikowske, 2010

# FROM MACRO BATCH TO MICRO CONTI: ECO-FRIENDLY PROCESSES AND NEW PRODUCTS THROUGH MICRO PROCESS ENGINEERING TECHNOLOGY

### Prof. Dr.-Ing. Stephan SCHOLL, Germany

### **SUMMARY**

In recent years micro process engineering equipment and production methods have gained significant attention and increasing application in the process industries. Typical characteristic dimensions range from 10 µm to 1000 µm. Processes operated in geometries of this size exhibit a number of advantages compared to macroscopic structures: Mixing and reaction may be accelerated significantly, heat and mass transfer intensity may be increased allowing a much tighter process control. The limited equipment holdup of micro manufacturing plants reduces the hazardous potential for safety-relevant and toxic substances. Critical components may be produced in-situ and converted immediately after that. Also from the perspective of production concepts micro conti manufacturing offers special opportunities compared to macro batch production.

Continuous micro production plants may also result in significant reductions of the environmental impact connected to the production. Demand for chemical cleaning agents, amount of waste water and rinse water as well as other aspects relate to the holdup of the production facility. Reducing this may lead to significant reductions in the environmental impact as well as operating costs connected to that.

The advantages and possibilities due to the use of micro process engineering is demonstrated for two examples: the continuous manufacturing of writing ink and the crystallization of solid lipid nanoparticles (SLN) as novel drug carrier systems. For writing ink a macro batch production process was transferred to micro conti manufacturing. The specific waste water production may be reduced by > 98 % compared to the standard macro batch process. Additionally the manufacturing scheme proves to be very flexible with minimized product losses. For SLN systems the cooling rate in the crystallization step proves to be crucial for optimizing the product properties: a high capacity, morphological stability as well as targeting and release properties have to be met at the same time. Both processes – SLN and writing ink – are solid-containing liquid phase processes which in the past has been one of the major obstacles against the use of micro process technology. With today's micro processing components and equipment capacities ranging from 10 kg/a to 1000 t/a (in special cases even higher) may be realized without major problems.

Micro process engineering potentially opens the way to better products and superior processes for their manufacture. There is still a strong demand for more research and development in various areas, on the equipment side as well as on the process side. Development and commercialization of micro-sensors with minimized dead-volume and capable of being integrated into micro systems is crucial, pulsation-free pumping in the range of 1 L/h to 100 L/h still calls for improvement. This presents market chances as equipment manufacturers especially for small and

medium size enterprises. On the process side a transfer from macro batch to micro conti in many cases requires recipe modifications to meet micro processing constraints. Additionally new process control strategies need to be tested and implemented to allow optimum leverage of conti manufacturing advantages.

### **CONTACTS**

### Prof. Dr.-Ing. Stephan Scholl

Institute for Chemical and Thermal Process Engineering Technische Universität Carolo-Wilhelmina zu Braunschweig, Institute of Technology Langer Kamp 7, D – 38106 Braunschweig Germany E-Mail s.scholl@tu-braunschweig.de

© S. Scholl, 2010

# RECENT ADVANCES IN HETEROGENEOUSLY CATALYSED PROCESSES FOR ENERGY RELATED APPLICATIONS

# P. PFEIFER, O. GÖRKE, P. PIERMARTINI, S. TAURO, J. THORMANN, R. DITTMEYER

Karlsruhe Institute of Technology (KIT), Institute of Micro Process Engineering (IMVT)

Herrmann-von-Helmholtz-Platz 1, 76344 Eggenstein-Leopoldshafen, Germany www.kit.edu / www.fzk.de/imvt-en

### **SUMMARY**

Microreactors have gained attention over the last two decades with respect to process intensification due to their enhanced mass and heat transfer characteristics and as well due to their low inventory of reactants when reaction rates are increased. IMVT has identified this potential for energy related applications as early as in 1997 and started projects on hydrogen and syngas production. Several methods for catalyst application to microchannel walls have been developed for enabling the conduction of heterogeneously catalysed processes in microreactors.

Within this contribution, an outline of different processes and recent advances will be given in the field of catalyst preparation, hydrogen from hydrocarbon fuels as well as for fuel synthesis from syngas. Additionally, recent results will be shown about of conducting heterogeneously catalysed gas-liquid reactions, e.g. hydrogenations, and exothermic equilibrium reactions such as water-gas shift and oxidation of  $SO_2$ .

### Introduction

Fuel cells allow the direct conversion of chemicals into electrical energy. Efficiencies above the Carnot efficiency of combustion engines can be reached. However, for low-temperature fuel cells hydrogen is required. The problem so far is the storage of H<sub>2</sub>. Even with optimized metal hydride materials or new types of high pressure or cryogenic liquid tanks, the weight and volume of the entire hydrogen storage system is higher than for conventional fuels [1]. Thus, the use of hydrogen leads to in a lower range of vehicles in comparison to an internal combustion engine.

 $H_2$  production from hydrocarbons in a chemical process on site is also problematic. Since  $H_2$  demand can vary significantly over time, the system components like reformer and heat exchangers have to be able to cope with highly dynamic operation, and a high efficiency is required. This kind of operation is not possible with conventional chemical reactors, as they are optimized for steady state operation.

The Institute for Micro Process Engineering (IMVT) develops microstructured devices, which consist of several thousands of micro-channels in metals since 1989. With the help of nanostructured catalyst layers on the channel walls these devices can be used as reactors. Due to the small distance between the micro-channels, the

temperature of the hydrogen production system can be established within seconds. Extremely high amounts of heat and mass can be transferred in a short time. Thus, the equipment size, weight and energy losses can be reduced to a level that the overall efficiency of the system for generating of  $H_2$  can almost reach the theoretical efficiency [2, 3].

Direct coupling of an exothermic reaction to the endothermic hydrogen production is favourable for the design of the  $H_2$  production system. Heating of reformers via externally generated hot flue gas by homogeneous combustion is not feasible, since the hot gas temperature must be lowered by additional air dilution to a level below  $1000\,^{\circ}$  C to avoid damaging of the metallic microstructure. An important aspect is the formation of coke at specific reaction temperatures. However, for the production of clean hydrogen in microreactors a targeted "plugging" of microsystems with coke seems feasible.

The second energy related application, which is of great importance for the future, is the conversion of syngas into liquid fuels. With around 25 % of world's proven natural gas reserves located in remote areas offshore, conversion so called "stranded gas" into transportable fuels and chemicals calls for new technologies. The Fischer-Tropsch synthesis is now a commercial pathway for the conversion of natural gas to transportation fuels. However, for offshore production, the conversion technology should be compact, modular and have low weight. Microstructured reactors enable for example isothermal operation of the highly exothermic Fischer-Tropsch reactions (165 kJ/mol). Hence, microstructured reactors could be especially suitable for highly active Fischer-Tropsch catalysts.

A highly efficient generation of fuels and platform chemicals from biomass with respect to energy balance and resources is necessary to avoid competition of fuel and food. Second generation biofuels and biochemicals, i.e. the conversion of gasified biomass to fuels and chemicals, would in principle enable a much higher biomass utilisation compared to processes like fermentation of corn. However, product shaping in the synthesis is difficult due to mass transfer limitations and hot spots occurring in conventional reactors. Therefore new developments at IMVT comprise also systems for methanol synthesis, direct di-methyl ether synthesis and high temperature / high pressure shift reactions.

A specific point which is addressed by IMVT for the latter type of reactions is that most studies in literature refer to just keeping the reactor temperature constant and thus enabling isothermal operation conditions. For exothermic equilibrium reactions, such as the water-gas shift or methanol synthesis, this is, however, not the optimum temperature profile. The initial rate is mainly influenced by the Arrhenius dependence and thus high reaction temperatures are favourable. With increasing conversions, the approach to equilibrium, however, will reduce the rate considerably and a lower reaction temperature should be employed. The maximum rate r as a

function of the conversion X can be found by letting  $\frac{dr(X)}{dT} = 0$ .

By using counter-current cooling in microreactors, the optimum falling temperature profile may be approximated in an effective way. Laboratory

microreactors are usually small in size, i.e. channel length is below 10 cm, so heat conduction in the microstructure may significantly contribute to the heat flux along the reaction zone. If this axial heat flux is within the range of the heat to be transferred, the desired temperature gradients may be significantly reduced. On the contrary, the conductive heat flux in the microstructure can be used on purpose to establish a certain temperature profile, but due to the fact that the heat production rate is usually decreasing with increasing conversion, heat removal by effective cooling may be higher than desired at the reactor outlet.

### Coupling Exothermic and Endothermic Reactions for H<sub>2</sub>-Generation

Figure 1 shows the dependence of the pressure loss and the stack height equivalent to the size of the reactor - depending on the number of microstructured metal sheets for a gasoline reformer with a flue gas heating (homogeneous combustion of gasoline). The calculation takes into account full conversion for reforming. The two different flue gas fluxes (38.5 and 12.5 kg / h) for the pressure drop calculation are equivalent to different inlet temperatures (850 °C and 1 100 °C) and temperature differences between inlet and outlet of the flue gas, respectively. With a low mass flow of flue gas, equivalent to a very high inlet temperature of the flue gas and a possible damage of the microstructure, a pressure drop of 30 mbar can be achieved with a number of 70 metal sheets. On the other hand, with a higher flux the boundary conditions for the maximum size of the reformer can not be obtained.

Due to the problem of optimization of the pressure loss in combination with the flue gas temperature, we consider that a direct coupling of an exothermic reaction with the endothermic steps in hydrogen production in microreactors is absolutely necessary. A total oxidation could be carried out at nearly-stoichiometric condition without a temperature maximum as occurring with homogeneous combustion.

A schematic of the overall process for the production of  $H_2$  for fuel cells from liquid hydrocarbon mixtures such as Diesel under the provision of a combined endoand exothermic process for steam reforming is shown in Figure 2. The fuel is mixed with evaporated water and converted in the reformer into a hydrogen rich gas. The reformate is cooled, and is cleaned, for example, by shift reaction and selective oxidation to remove carbon monoxide (CO). The cleaned gas is used for the production of electrical energy in a PEM fuel cell. The residual  $H_2$  in the fuel cell offgas can be burnt and used for heating and evaporation of the reactant flows or to meet the energy demand of the steam reforming.

Taking into account the efficiency of the individual steps yields an overall efficiency, including that of the fuel cell, of 22 %. This is significantly higher than for a system of diesel engine and generator [4] with 4.5 %.

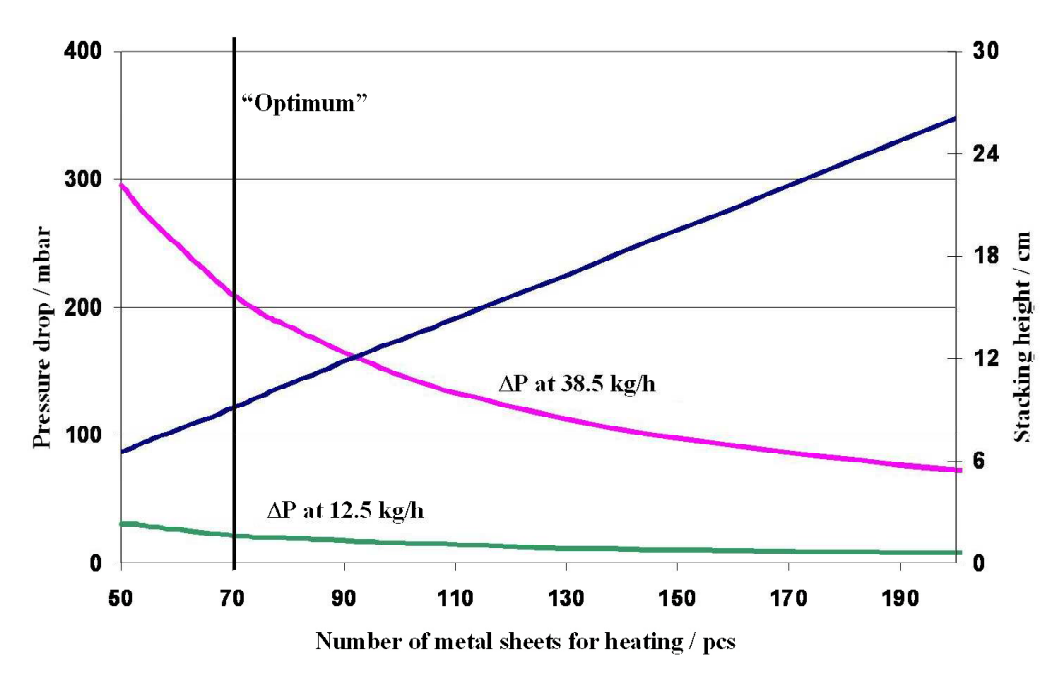


Figure 1. Pressure drop calculation for a steam reformer at different mass flows of hot flue gas and component height as a function of number structured metal plates

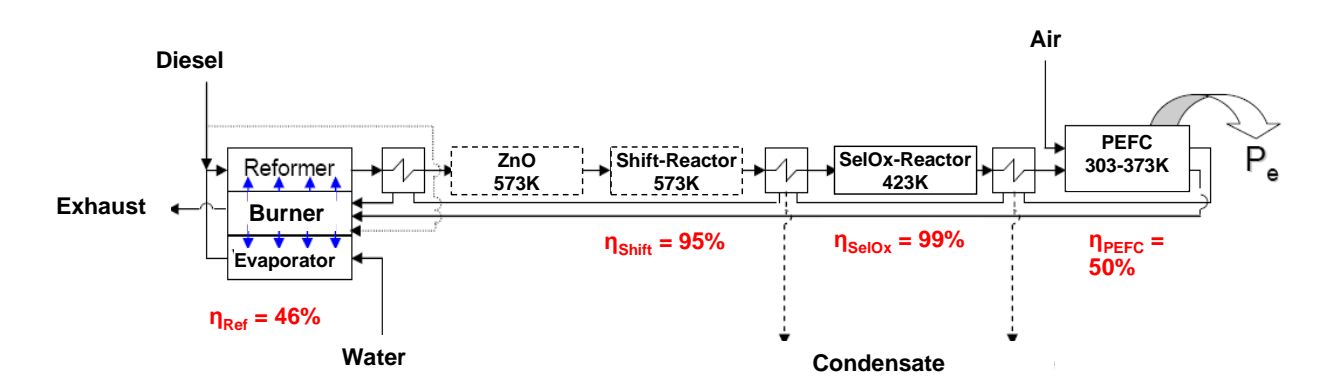


Figure 2. Flowchart of the overall system for generating electrical energy with direct thermal coupling of combustion and evaporation and condensation on the example of diesel steam reforming

However, in order to perform such a coupling of endothermic and exothermic reactions, the system must be optimized for operation with the evaporator and the reformer. Because of the different reaction rates of combustion of hydrogen (the anode exhaust of the fuel cell included) and reforming, this is not trivial. To start a system from ambient temperature requires a very active noble metal catalyst. With such a catalyst the hydrogen conversion can be very fast at final operating temperature of the reformer, i.e. in a few millimeters of microchannel length full conversion can be reached at a residence of only 3 ms. Steam reforming, which requires according to our experience 50 to 300 ms residence time [5, 6], possesses a fundamentally different heat demand. To balance heat supply and demand, hydrogen can be mixed with air in sections. To be able to balance heat generation and

consumption by this procedure, kinetic models are needed. Power law models or elementary step models are produced in collaboration with other research groups. Isothermally designed experiments in test reactors where the catalyst layers are produced on exchangeable microstructured sheets serve for the verification of the models [7, 8].

In addition to maximizing the volume fraction of catalyst, an important aspect is the optimization of the catalyst productivity. The mass ratio of catalyst and reactor volume or weight of microstructure reactors is rather low [9]. We have already achieved values for the catalyst productivity of up to 40  $g_{hydrocarbon}$  / ( $g_{cat}h$ ). The productivity and the volume fraction ultimately decide on a minimization of system weight, the ratio  $m_{steel}$  /  $F_{in}$ , i.e. the mass of steel from the reactor in relation to a given hydrocarbon flux. This ratio should be in the range of about 5  $g_{steel}h$  /  $g_{hydrocarbon}$ .

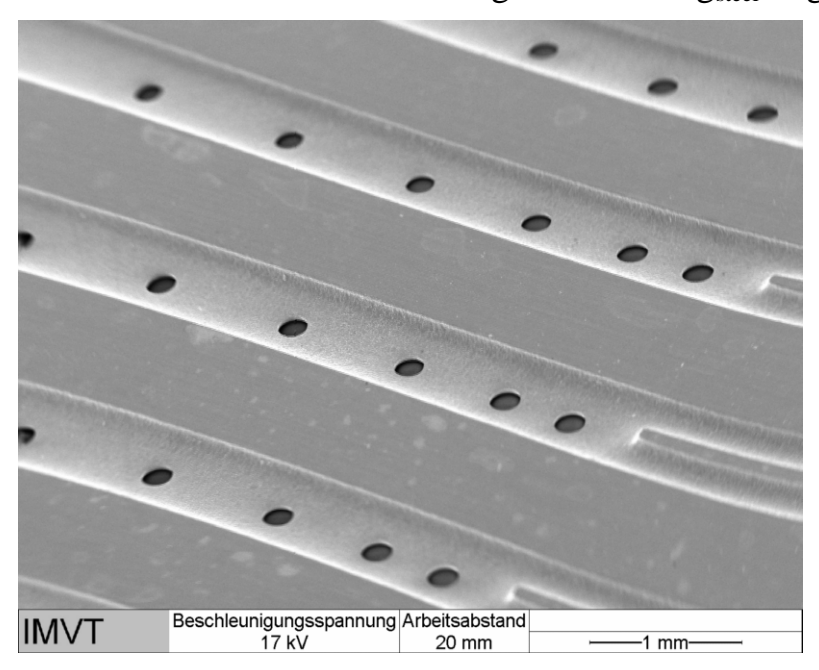


Figure 3. Hydrogen distribution holes with increasing spacing to approximate the heat demand of methanol steam reforming

Figure 3 shows, based on modeling, the distribution of interconnecting holes for hydrogen transfer into the channel for the conduction of the exothermic reaction. In this design the consideration of the pressure loss in the hydrogen distribution channels below the transfer holes and the pressure loss in the combustion channel in relation to the pressure loss in each transfer hole is important. The intended flow per transfer hole should be equal. An alternative to the design shown by etching is the use of even smaller holes made by laser structuring. Examples of such reactor designs can be found in our publications [10]. Since the lab –scale systems either combine reforming or evaporation and heat supply, the heat losses may, depending on the temperature level of the process, be between negligible [10] and dominant [11].

### **Example: pure hydrogen from cracking propane**

The opinion prevails that coking or hydracarbon cracking reactions are not compatible - in the sense of avoiding solids and associated plugging - with microsystems. However, we only observed coke formation in substantial amounts in steam reforming of diesel and ethanol, although this has not led to blockage of the channels. This is even valid for situations when the vapor dosage failed during the experiments. It appeared that in this context, the stability of the catalyst and the choice of the reactor material is more important. For example, systems comprising alumina were irreversible damaged in absence of steam, whereas cerium oxide layers showed no reduction in catalyst activity. We attribute this to the reported cerium oxide oxygen storage effect [7, 8]. A complete regeneration of the cerium-based catalyst systems was possible by short-term oxygen treatment at reforming temperature. Nicrofer 3220H or the American Alloy 800 H show little catalytic function to form coke and low adherence of coke, while stainless steel well promotes coke formation.

Based on this experience, a system was built to be used specifically for the cracking reactions of propane for hydrogen production. An advantage of this technology was that the reaction product almost exclusively consisted of hydrogen gas. The catalyst system was a vanadium oxide coated stainless steel net integrated in a Nicrofer reactor. The stainless steel catalyzes an initial coke formation and coke itself becomes the active catalyst. For a permanent production of hydrogen, regeneration of the catalyst is required, i.e. at least two separate reaction zones for cracking and regeneration are needed. These zones have to be alternatively switched. For additional warming-up and maintaining the operating temperature, combustion of the fuel cell anode exhaust gas or of the regeneration exhaust gas is necessary. The exhaust gas from regeneration is mainly containing carbon monoxide. In principle, the following two reaction equations are valid for cracking and regeneration.

$$C_3H_8 = 4 H_2 + 3 C$$
  $\Delta H_R = + 104 \text{ kJ/mol } C_3H_8$  (1)

$$3 C + 1.5 O_2 = 3 CO$$
  $\Delta H_R = 3 * (-110.5 kJ/mol C)$  (2)

Figure 4 shows the basic structure of the developed apparatus and a photograph of the system which was designed for a flow rate of 3  $l_{\rm N}$  / min. The reactor contains alternating stacks of four pieces of steel net and two microstructured plates for the dosing of combustion air into the combustion channels. The orientation of the steel net changes after each combustion zone by 90° so that two passages, one for regeneration and one for cracking are formed.

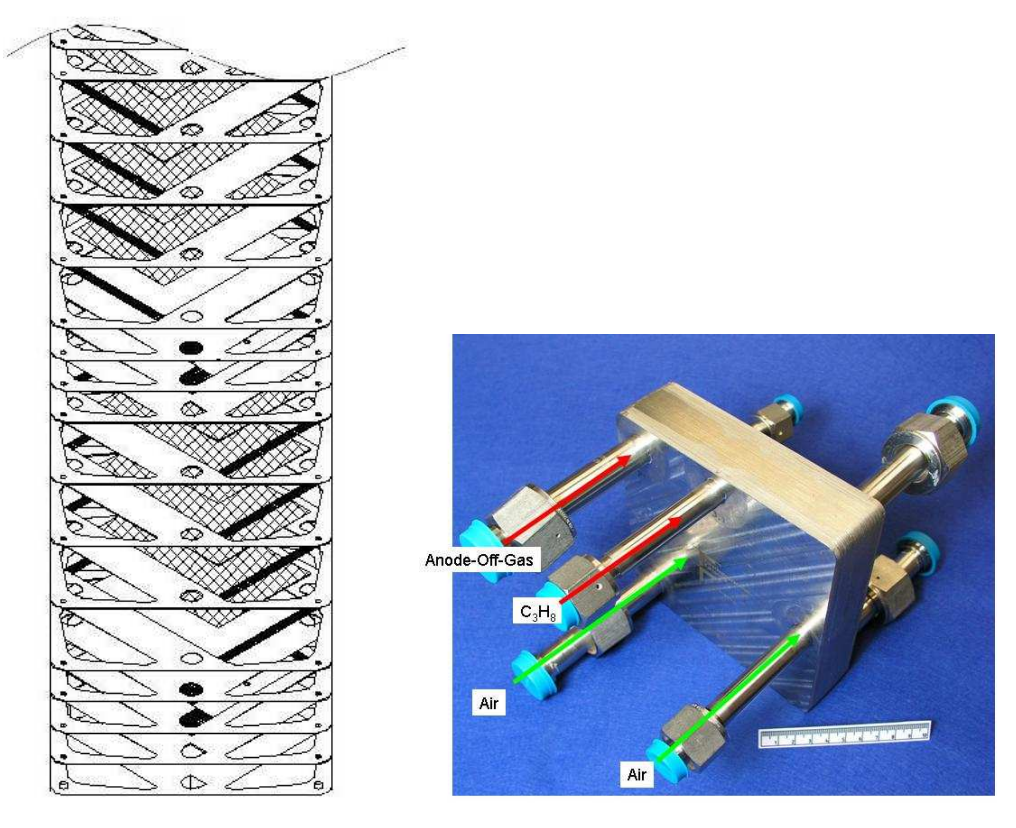


Figure 4. Stacking sequence of cracking reactor (left) and photograph of the cracking reactor (right)

Currently, the time requirements for regeneration and for cracking are different. The regeneration phase is about five times longer than the cracking. In addition, the required length of the steel net is significantly shorter, i.e. carbon deposits are found only at the entrance. Thus the total number of required passages and switching actions are higher. It is necessary in the current design to burn considerable amounts of anode off-gas to maintain the temperature of the system due to the different time scales of regeneration and cracking (for details see [12]). The design for such reactors has to be modified in the future.

### **Examples from XtL Technology**

For the production of liquid synfuels from biomass feedstocks and low-hydrogen fossil raw materials (XtL), a *water gas shift reaction* step carried out at high pressure and temperature may be advantageous for minimizing energy losses. If gasification yields an insufficient H<sub>2</sub>/CO ratio for fuel synthesis and high pressure can be applied, subsequent gas cleaning and water gas shift should be carried out at elevated pressure and above the temperature level of the synthesis.

For the laboratory tests a new microstructured reactor design was built, which allows testing of catalysts powder in a micro fixed bed or as sheets with channel wall catalyst coating at elevated pressure and temperature (up to 50 bars, 600 °C). The catalysts investigated so far have been applied as wall coating. The catalyst systems Pt/CeO<sub>2</sub>, Pt/CeO<sub>2</sub>/Al<sub>2</sub>O<sub>3</sub> (Fig. 5) and Ru/ZrO<sub>2</sub> have been produced by incipient wetness impregnation and sol-gel technology.

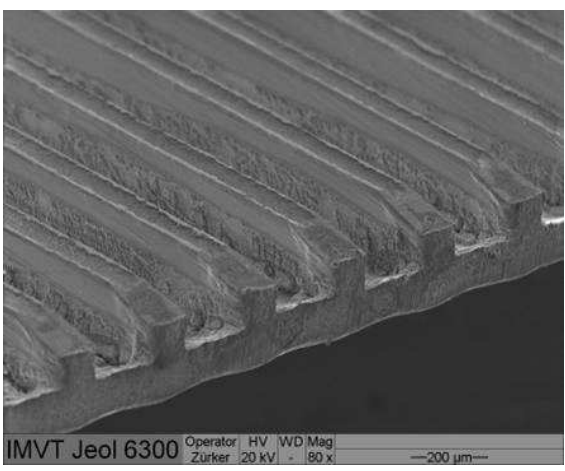


Figure 5. Scanning Electron Microscopy image of the applied  $Pt/CeO_2/Al_2O_3$  coating on 200 x 200  $\mu m$  microchannels

The platinum catalyst systems were shown to be highly active under operating conditions above 400 °C, and equilibrium yields of CO<sub>2</sub> can be reached at 500 to 600 °C. At elevated pressure, the reaction rate increases due to increased partial pressure of the reactants (Fig.6). We found negligible hydrocarbon product concentrations such as methane which would be thermodynamically attractive under the process conditions. Also coke formation happened in the microreactor inlet which has been found to be formed in the gas phase during heating up the gas mixture. The Ruthenium catalyst system enables high reaction rates below 400 °C (see also [13]).

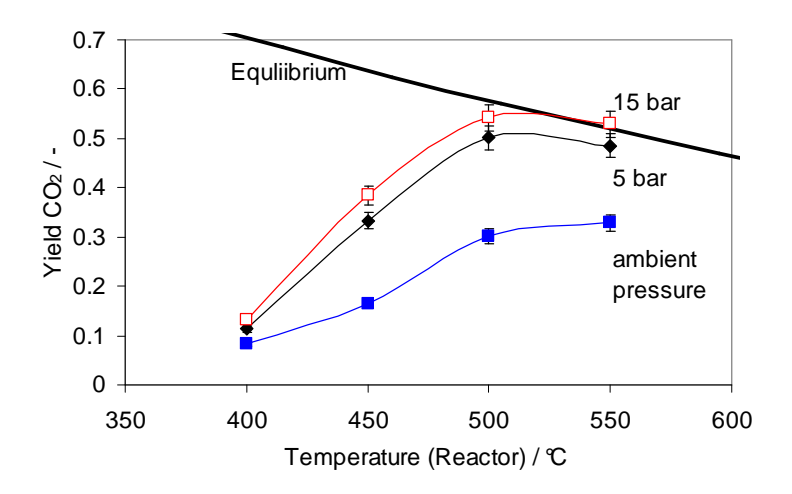


Figure 6. Measured yields of  $CO_2$  compared to equilibrium values for the  $Pt/CeO_2/Al_2O_3$  coating at different pressures, modified residence time of 4e-4  $g*min/cm^3$ , and a feed composition of 32 % CO, 10 %  $CO_2$ , 18 %  $H_2$ , 10 %  $N_2$ , 30 %  $H_2O$ 

In the conversion of syngas to methanol, the applied pressure is usually around 50–100 bar, since the thermodynamic equilibrium is unfavourable at lower pressure. In terms of the chemical equilibrium shift, an option to methanol separation arises, by simultaneous conversion of methanol to di-methyl ether (DME). This *one-step* 

process for DME synthesis is thermodynamically favorable, and a higher CO conversion rate can be achieved over hybrid catalysts, even operating at lower pressures and higher temperatures than a two step process. However, there is a clear increase in the potential for thermal runaway of the catalyst bed due to the lower methanol partial pressure and the associated CO conversion rate increase. The application of micro-structure reactors would reduce this risk considerably, and thus process intensification with optimized process conditions seems possible. The advantages may be useful for compact GTL (gas-to-liquid) or remote BTL (biomass-to-liquid) applications.

Various methods have been investigated for the deposition of a mixture of the methanol synthesis catalyst and the dehydration catalyst. For the preparation of the methanol synthesis catalyst  $\text{Cu/ZnO/Al}_2\text{O}_3$  we followed a method of stepwise coprecipitation of the metal nitrates at elevated temperature of 65°C [14]. For the dehydration catalyst we performed direct  $\text{Al}_2\text{O}_3$  deposition by a sol-gel synthesis developed in our institute [15], and alternatively H-ZSM5 catalysts were produced by hydrothermal synthesis.

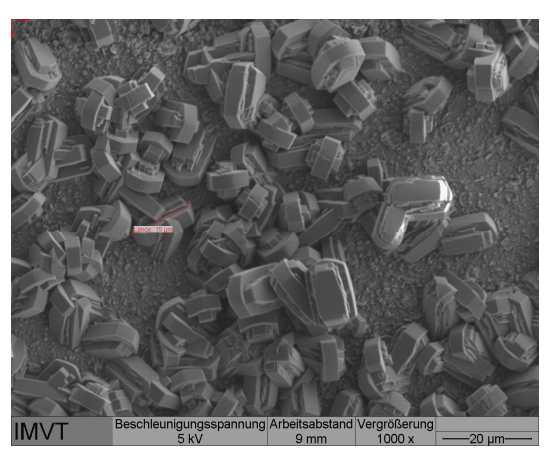


Fig. 7. Applied H-ZSM5 crystals on pre-coated stainless steel sheets with sol-gel generated alumina and silicalite seeds

From XRD we have found that the alumina prepared by sol gel and calcined at different temperatures showed no transition from the amorphous state into gamma alumina up to 700 °C, but was converted into the delta and alpha phase at 800 and 1 000 °C respectively. This is in agreement with ammonia desorption experiments where we found also negligible acidic function. The HZSM-5 instead, created by growth on silicalite seeds, exhibited good crystallinity and reasonable acidity but its growth on stainless steel plates was much more difficult. Almost homogenous growth of the zeolites has been reached by initial sol-gel coating, followed by silicalite seeding and hydrothermal synthesis of the H-ZSM5 (Fig. 7). For the copper catalyst system we obtained compositions of 65/25/10 wt% of CuO/ZnO/Al<sub>2</sub>O<sub>3</sub> with BET surface areas of approximately 125 m<sup>2</sup>/g.

# Shaping reaction rates for exothermic equilibrium reactions

As stated in the introduction, microreactors can offer more than just enabling isothermal conditions. For exothermic equilibrium reactions a decreasing temperature profile would be advantageous for following the optimum trajectory of the reaction rate in the conversion-temperature plot. For SO<sub>2</sub> oxidation we used a model developed in cooperation with Fila et al. [16] to initially judge the heat flux to be transferred from the reaction zone to the cooling channels. It was clearly demonstrated in that publication that too effective cooling in countercurrent mode could lead to quenching of the reaction – starting from the reactor outlet.

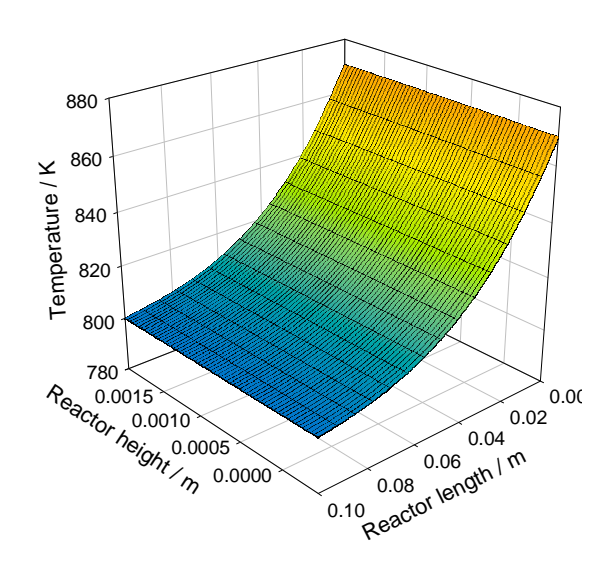


Figure 8. Calculated temperature profile in  $SO_2$  oxidation inside a stack of 200 x 200  $\mu$ m channels in 300  $\mu$ m thick foils for reaction and only one for cooling; temperature as a function of the reactor length and, rectangular, in the direction of heat transfer (reactor height)

To avoid such quenching, a more detailed investigation of the importance of the axial heat flux along the reactor is needed. Investigating a stack of multiple microstructured foils for the reaction and only one cooling foil, the result was that the effect of quenching can be avoided. The semi-porous body model gave us an indication that an increase of the foil ratio (reaction vs. cooling) increases the axial temperature gradients, while the temperature of the stack of reaction foils in such an arrangement remains almost constant at any axial position in the direction of the heat transfer (see Fig. 8).

In the water gas shift reaction, so far, we used a kinetic rate expression for a copper catalyst system [17] with the pre-exponential factor adjusted to obtain conversions close to our experimental results. The model suggests that the expected conversion for a linear decrease of temperature is above the conversion for isothermal operation both for low and high operating temperature (Fig. 9).

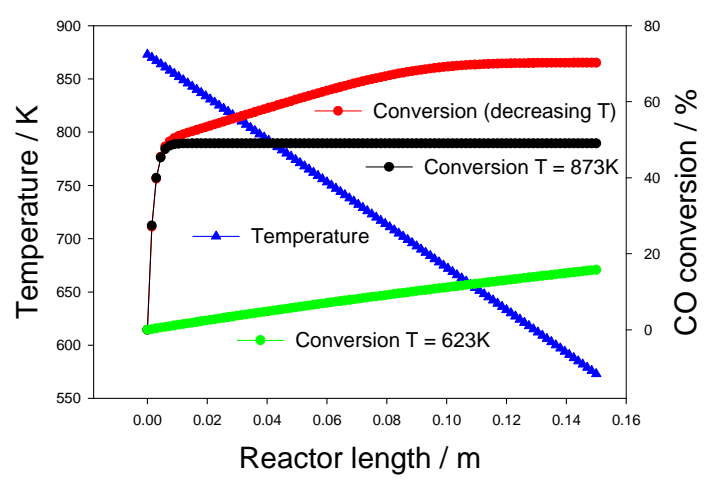


Figure 9. Calculated conversion for isothermal operation at low and high temperature and for a linear falling temperature profile for the water gas shift reaction

## **Conclusions**

The current contribution shows that microreactor technology has great potential for energy related processes. Two major applications are in the focus at IMVT: hydrogen production for fuel cell applications and fuel synthesis (XtL). The demand for compact systems in both applications, however, may only be fulfilled by advanced catalyst design enabling high reaction rates and by optimized temperature profiles in the reactor. The latter is of great importance for exothermic equilibrium reactions. Finally, we see potential collaboration possibilities in terms of catalyst preparation and kinetic studies with Russian researchers.

## References

- [1] S. Satyapal, J. Petrovic, C. Read, G. Thomas, G. Ordaz, Catalysis Today 2007, 120, 246–256.
- [2] P. Pfeifer, K. Haas-Santo, O. Görke, Micro Process Engineering, Volume 2, Wiley-VCH, Weinheim, 2009, 445–463.
  - [3] G. Kolb, Micro Process Engineering, Volume 2, 2009, 421–439.
- [4] J. Thormann, Diesel-Dampfreformierung in Mikrostrukturreaktoren, Dissertation TU Clausthal, 2008.
- [5] P. Pfeifer, K. Schubert, M.A. Liauw, G. Emig, Chem. Eng. Res. Des., 2003, 81, 711.
- [6] P. Pfeifer, K. Schubert, M.A. Liauw, G. Emig, Appl. Cat. A: Gen. 2004, 270, 165–175.
- [7] J. Thormann, P. Pfeifer, U. Kunz, K. Schubert, Reforming of Diesel Fuel in a Micro Reactor, Int. J. Chem. React. Eng. 2008, 6, Presentation 1.
- [8] J. Thormann, L. Maier, P. Pfeifer, U. Kunz, K. Schubert, O. Deutschmann, Steam Reforming of Hexadecane over a Rh/CeO2 Catalyst in Microchannels: Experimental and Numerical Investigation, J. Hydrogen Energy, 34 (2009) 5108–5120.

- [9] E. Klemm, H. Döring, A. Geißelmann, S. Schirrmeister, Chemie Ingenieur Technik 2007, 79, No. 6, 697.
- [10] O. Görke, P. Pfeifer, K. Schubert, Chem. Eng. Technol. 2007, 30, No. 3, 363–369.
- [11] J. Thormann, P. Pfeifer, U. Kunz, K. Schubert, Hexadecane Reforming in a Microreactor Heated by Catalytic Combustion, Proceedings of MIPS 2008: Int. Symposium on Micro Chemical Process and Synthesis, Sept. 11. 13.2008, Kyoto, Japan.
- [12] O. Görke, P. Pfeifer, K. Schubert, Kombination von katalysiertem Cracken von Propan in einem Mikroreaktor mit Beheizung durch katalytische Verbrennung Jahrestreffen Reaktionstechnik 2009, Würzburg, 8.6. 10.6.2009.
- [13] O. Goerke, P. Pfeifer, K. Schubert, Applied Catalysis A: General 263 (2004), 11–18.
- [14] D. Cornthwaite: Methanol synthesis catalyst, United States Patent Nr. 3923694 (1975).
- [15] K. Haas-Santo, M. Fichtner, K. Schubert, Appl. Catal. A, 220, 79-92 (2001).
- [16] K. Haas-Santo, K; Kraut, M; Pfeifer, P.; Schubert, K; Bernauer, M.; Fila, V.; Sulfur dioxide oxidation reactor with internal heat profile for a one-step synthesis of sulfur trioxide, 18th CHISA, Praha, CZ, August 24–28, 2008.
  - [17] Van den Bussche, K. M.; Froment, G.F.; J. Catal., 1996, 161, 1.
  - © P. Pfeifer, O. Görke, P. Piermartini, S. Tauro, J. Thormann, R. Dittmeye, 2010

# CONTACTING OF IMMISCIBLE LIQUIDS USING MICROSTRUCTURED DEVICES

# Manfred KRAUT, Andreas HENSEL, Roland DITTMEYER, Germany

Key words: microstructured device, emulsion, micro mixing

## **Summary**

Contacting immiscible liquids is an important task in food processing and cosmetics, as well as in chemical and pharmaceutical industry. Interfacial area is created by hydrodynamic effects, which can result in the formation of droplets. Either these are stabilized, for example by emulsifiers on the surface of the droplets or, in the case of phase transfer catalysis, the stabilization of the surface is not intended.

Microstructured devices have been applied to generate emulsions in all of the above mentioned areas. In the contribution examples of these applications are presented.

In food processing a specially designed device for mixing and homogenization has been successfully applied for milk homogenization. Savings in terms of specific energy consumption per unit of processed milk has been achieved. Besides that the process can be simplified by eliminating now obsolete process steps resulting in lower capital and operating cost.

Microstructured mixers have also been successfully applied in the manufacturing of cosmetics. Major improvements in homogeneity as compared to the conventional process have been achieved. Conventional manufacturing in cosmetics industry is batch processing resulting in quality variation per batch, while the new process on the basis of microstructured devices is a continuous process which results in stable and reproducible product quality.

Solid wax globules have been produced using microstructured devices. In this case the stabilization of the particles has been achieved without addition of an emulsifying agent. With the microstructured devices it is possible to dilute and cool in the exact location of droplets formation thereby stabilizing the droplets and inhibiting coalescence.

#### Introduction

Emulsions are ubiquitous in our life. They are found in food, in drugs, in personal care products. When they are well defined, people won't even suspect that they are no homogeneous liquids. However it is by far not trivial to make high quality emulsions. This is partly due to the devices in which they are made. If emulsification is done in big stirred tanks, the shearing, which is the responsible effect to enlarge surface area, is different for each differential volume of said tank. To ensure good quality the residence time (=stirring time) has to be chosen so that all droplets have been through the area with the highest shear stress. It is therefore straightforward to think of devices which ensure similar forces acting on each liquid volume within a

very short time. The result would be saving of energy and guaranteeing of good product quality.

At the Institute of micro process engineering we worked with several partners in a number of projects to achieve emulsions with superior product quality by using micro channel devices.

#### **Devices**

## a) V-type micro mixer

These mixers are made by stacking foils which are microstructured with channels. The fluids are distributed into the channels and the ensuing streaks exit the structure in a pitch of 45 degrees. The contacting is achieved by the stacking. Since the streaks exit under an angle secondary flow effects increase the surface area. An added advantage of this design is the ability of providing the same environment for a vast variation of flows by the simple means of using more or fewer foils per device. A standard flange adapter has been designed to allow the variation between 1 and 34 foils per stack.

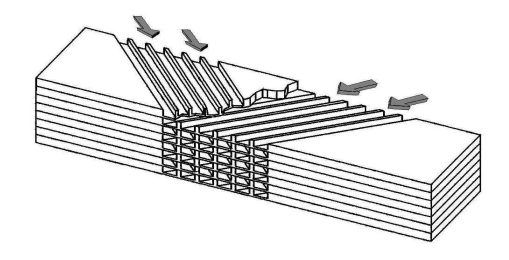


Figure 1. Schematic drawing of a typical micro-mixer, used for emulsification: V-Type Micro Mixer

#### b) SHM valve

This type of device has been developed in close cooperation with the Institute of Food process engineering of the University of Karlsruhe, KIT. The device incorporates a nozzle, which is in fact a micro channel, and channels perpendicular to the entrance nozzle to enable direct mixing after the nozzle's exit. Here primarily the elongational flow at the nozzle is responsible for the deformation and breakup of droplets, while the mixing step is preventing coalescence by dilution with providing emulsifiers simultaneously and furthermore by shear stress in turbulent flow, which results in stabilizing the emulsion.

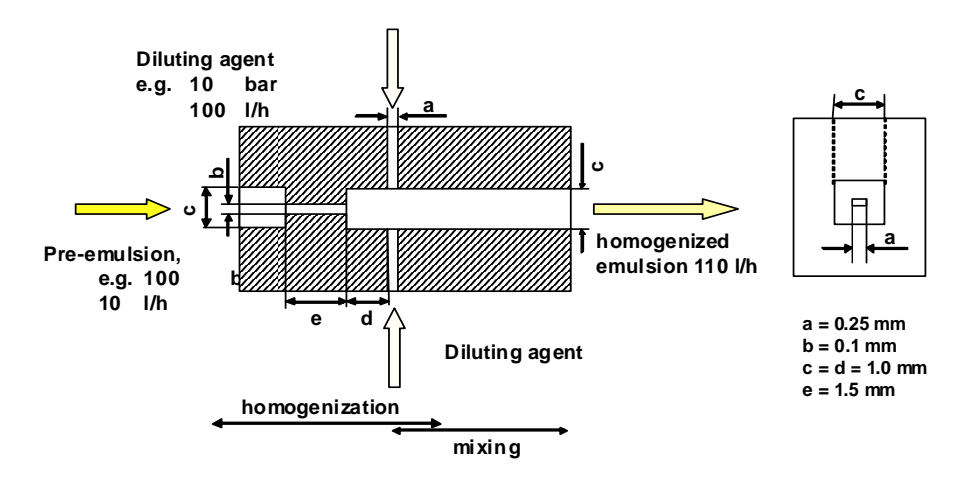


Figure 2. Principle design of the simultaneous homogenization and mixing valve (SHM valve) [14]

# **Experimental**

In the course of this contribution a few examples of the application of the micro structured devices are shown. In Fig. 3 the basic experimental setup is demonstrated, which consists of membrane piston pumps for the fatty and the aqueous phase respectively as well as thermostats for temperature control and the equipment to provide flow, pressure and temperature information.

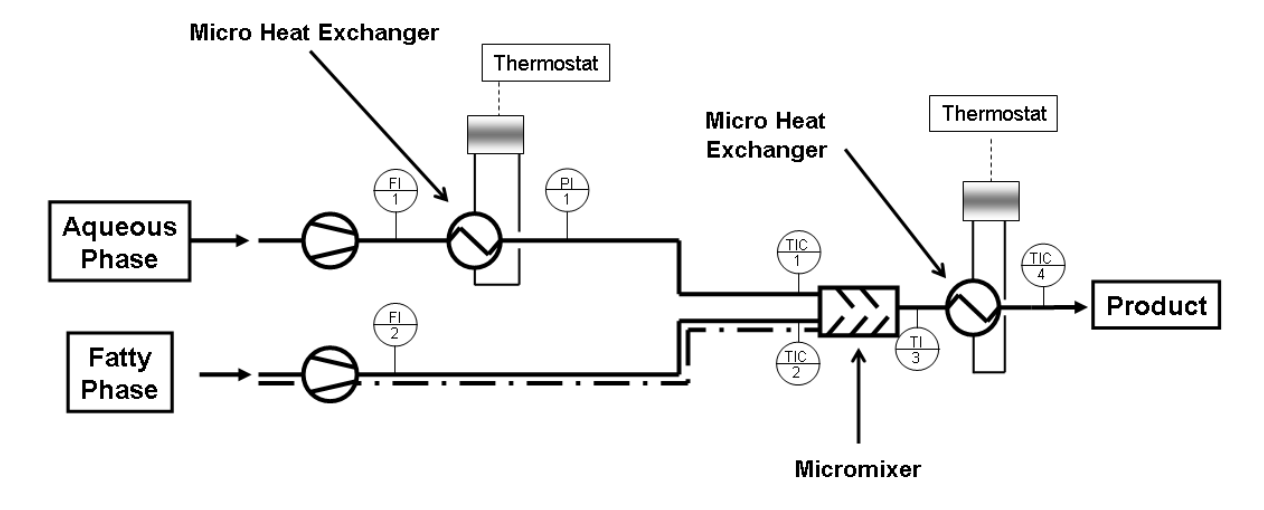


Figure 3. Basic experimental setup for producing emulsions

The emulsions produced are characterized by measuring the droplet and accordingly particle size using a Laser diffraction spectrometer (Beckman Coulter, LS 230). To characterize the droplet collective the volume size distributions were used. As a measure for the physical stability (creaming) the maximum droplet diameter of the volume size distribution  $x_{90,3}$  is depicted, which means the higher the maximum droplet diameter, the lower the creaming stability.

Furthermore, in case of cosmetic emulsions the dynamic viscosity is measured by a Haake Rheometer (Rheo Stress 1) with a cone-plate system for characterization.

# **Application example: cosmetic formulation**

Two cosmetic formulations are chosen to be described below. In conventional production these formulations are produced by using a rotor-stator system in a batch. Recurrent problems occur by this procedure, which can be observed in inhomogeneous products by oversized droplets or products containing air bubbles. In addition, a selective adjustment of the viscosity can not be achieved, also because of the previous problems.

Using a symmetrical V-type micro mixer at different flow velocities resulted in a very homogenous distribution of small fatty droplets in the aqueous matrix. The resulting product was applied by test persons to compare it with the conventional product. The result of the evaluation of the micro mixed formulation by test persons obtained an equal quality compared to the conventional produced formulation, which addressed successfully the issues of our project partner. To interpret the results one has to consider the spatial and temporal distribution of shear stress. In the rotor-stator system the shear stress varies both with respect to location and time. The permanent alteration of stress can be beneficial and is intended, but it can also lead to inhomogeneous distributions depending on the system (aqueous phase, fatty phase and emulsifier) and the conditions applied. As opposed to that the shear stress in using a micro mixer is constant in both respects. Optimization of the emulsion can be done by altering the shear stress by varying the flow velocity. This will result also in a variation of pressure drop, the source of energy to increase surface area.

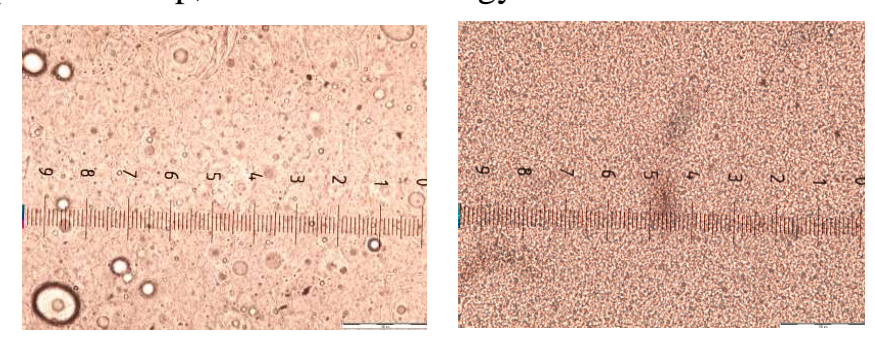
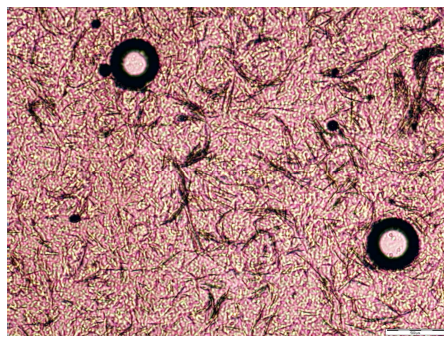


Figure 4. Microscopic photos of a fat/water-emulsion: Left-hand side: Produced by a rotor-stator-system, right-hand side: produced by V-type micro-mixer

Another investigated cosmetic formulation was an emulsion containing solid crystals. Like in the former example using the rotor-stator-system was not yielding homogenous product. Using a V-type mixer a very nice distribution could be achieved (Fig. 5). The emulsion created using the micro structured device show also a better long-term stability, another important property of the product. This is due to the absences of bigger droplets which tend to impact the viscosity in a negative way, since the product is not in a thermodynamic equilibrium, but in a metastable state, due to kinetic hindrance. The shelf live of the product is an important economic metric for cosmetics manufacturers, and is evaluated by determining the viscosity.



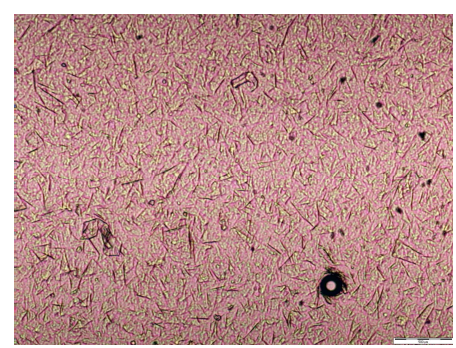


Figure 5. Microscopic photos of a fat/water emulsion containing solid crystals: Left-hand side: Produced by a rotor-stator-system, right-hand side: produced by V-type micro-mixer

Comparing the methods of production, rotor-stator system batch-wise vs. micro mixing continuously, it can be observed a major difference in containing air bubbles in the product. Producing cosmetic formulations by rotor-stator systems it is difficult to prevent inserting air into the product. In case of production by micro mixing devices no air bubbles can be observed in the ready product (see Fig. 4 and Fig. 5).

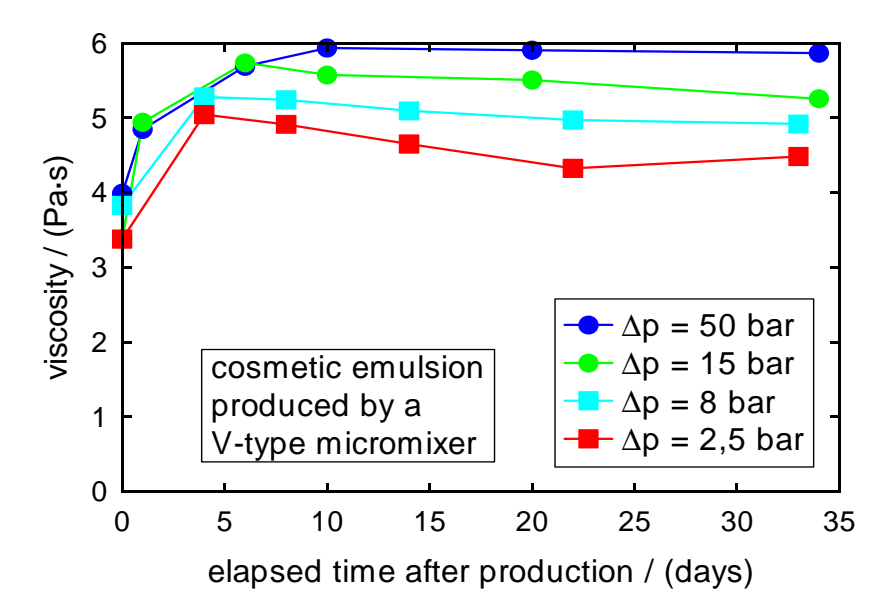


Figure 6. Progress of viscosity over time depending on the pressure loss at time of production for four samples of a cosmetic formulation made by a micro structured mixing device (V-type micro mixer)

Viscosity is often a major measure for quality of cosmetic products. Both influence the formulation and the manufacturing method, the viscosity and thus the quality of the product. While it is used in batchwise operation, despite strict manufacturing processes, different viscosities of the product are obtained. In continuous operation using micromixers under certain operating conditions consistent viscosities can be achieved. Looking at the operating parameters of pressure drop (see Fig. 6), one realizes that we obtain with increasing pressure drop over the micro-

mixer an increased viscosity in the product. The reasons can be found in better homogeneity and smaller particle size (see Fig. 4 and Fig. 5).

## **Application example: Milk homogenization**

In case of milk homogenization high pressure homogenizers are broadly used. Milk is homogenized in order to reduce droplet size and thus to prevent the formation of a cream layer during storage time. The mean diameter of the fat droplets in pasteurized milk has to be well below 1  $\mu$ m. The volume based averaged fat droplet diameter  $x_{3,2}$  in raw milk being in the range of 4  $\mu$ m is usually reduced to 0.6 ... 0.7  $\mu$ m [1]. Conventional processing comprises homogenization in one or two stages at pressure levels between 100 and 200 bar and temperatures between 50 and 70 °C [2].

In order to adjust the fat content to the required value for specific product qualities, raw milk is separated prior to homogenization into a low-fat (0,03...0.3 vol.-% fat, 'skim milk') and a fat-enriched phase (30...42 vol-% fat, 'cream') using a separator. Cream must then diluted with skim milk to a fat content of 12...17 vol.-% and homogenized [3]. The target fat concentration of, for example, 3.5 vol.-% in full cream milk is achieved by a second mixing step in which the homogenized fat-enriched phase is diluted again with the low-fat skim milk phase. This step-wise process is called partial homogenization (see Fig. 7, left-hand side).

This two-step re-mixing process interrupted by high pressure homogenization is required as to date cream of fat contents higher than 17 vol.-% cannot be homogenized with satisfying results. After break-up, fat globules tend to coalesce as new interfaces are generated, but not sufficiently stabilized. Coalescence of fat droplets is found until adsorbing dairy proteins stabilize the droplets. Stabilization kinetics, however, is slow [4]. Coalescence thus can only be prevented at low fat content. [5]. In stabilization of fat globules in cream, a secondary droplet membrane is built up by adsorbing casein micelles and sub-micelles as well as lacto albumins and lacto globulins [6, 7]. As adsorbed casein micelles strongly interact and form bridges, aggregates of fat droplets are formed.

For stabilisation of the droplets against coalescence and aggregation, droplet stabilizing molecules have to be injected directly into the zone of disruption. By injecting skim milk which is rich in whey proteins the new fat globule interfaces are helping to stabilize them in the moment of their creation. Further the droplet collision rate has to be reduced significantly at that time of disruption and stabilization. In this case the high volume of skim milk dilutes the product and thus increases the distance between fat globules and reduces their collision rate. Thus both coalescence and aggregate build-up rates can be reduced. Both require a high mixing quality.

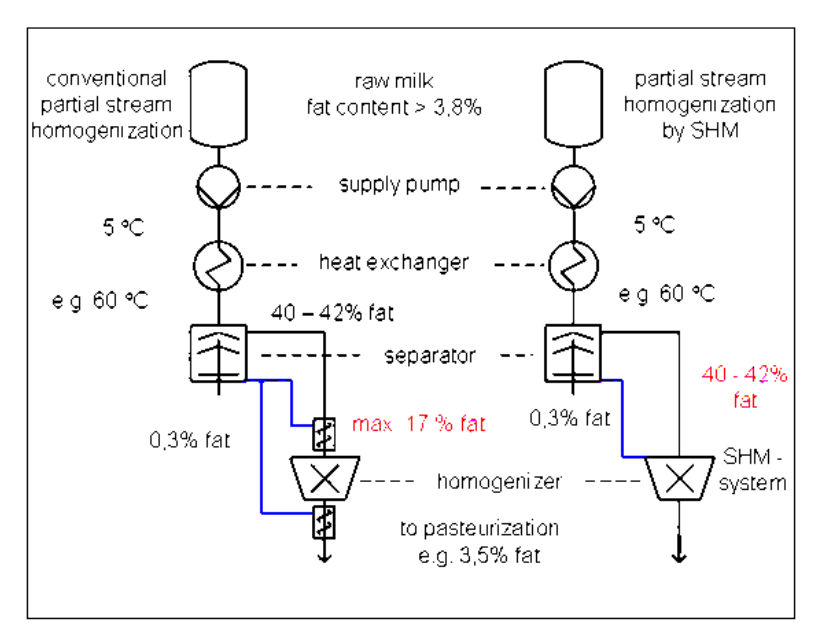


Figure 7. Flow chart of the conventional partial (left-hand side) and the novel partial homogenization process (right-hand side)

In experiments, commercial non homogenized, pasteurized cream with a fat content of 32 to 42 vol.-% and pasteurized skim milk with a fat content of maximum 0.3 vol.-% were used. In comparison, non-homogenized milk of a fat content of 3.5 % was homogenized in one stream passing the homogenization orifice without any side-stream mixing. This full cream milk was produced by mixing the cream with the skim milk to the required fat content by using a paddle mixer. The standard homogenization temperature was set to 65 °C. Heating and cooling of the cream and the full cream milk (fat content 3.5 %) prior to and after the homogenization were realized by micro heat exchangers enabling rapid temperature changes ( $\Delta T/\Delta t \sim 850$ K/s). The residence time within the heat exchangers was about 0.02 seconds. The fatenriched phase (cream) is pumped through the homogenization valve (central channel) at pressures of up to 300 bar, corresponding to a volume flow rate of up to 14 l/h. Skim milk is injected through the lateral inductors of the SHM-valve. A maximal feeding pressure of 30 bar and a max. Volume flow rate of approx. 112 l/h is realized in the test rig. Using a pressure ratio of 10 to 1 between the homogenization pressure of the fat-enriched phase (cream) and the feeding pressure of the skim milk, a mixing volume ratio of 1 to 8 was achieved.

In general, droplet sizes (here  $x_{90,3}$ ) decrease with increasing homogenization pressure as long as droplets are stabilized against coalescence and aggregation after break-up.

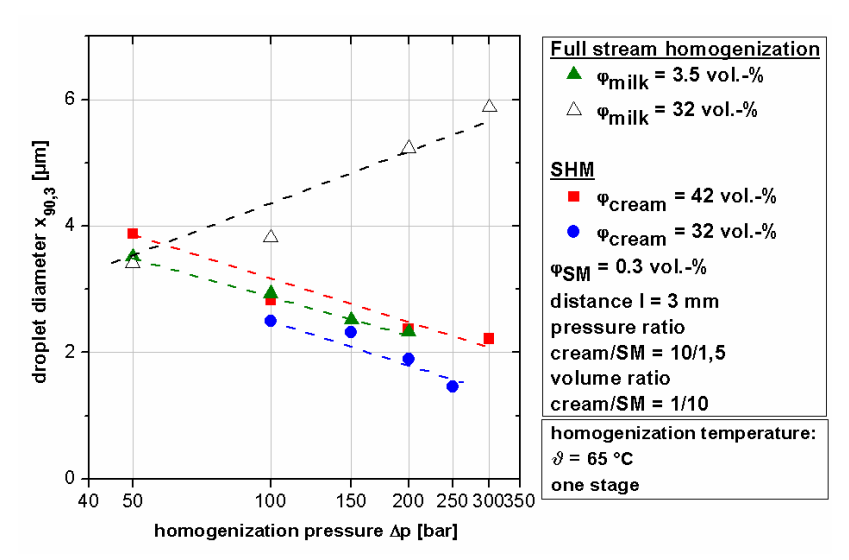


Figure 8. Influence of the fat content of the homogenized cream and the homogenization pressure on the droplet diameter  $x_{90,3}$  for partial homogenization of cream (32 and 42 vol.-% fat) with skim milk ( $\varphi = 0.3 \text{ vol.-}\%$ ) in the novel SHM-valve compared to conventional full stream homogenization of milk (volume fat content  $\varphi = 3.5 \text{ vol.-}\%$ ) and cream ( $\varphi = 32 \text{ vol.-}\%$ )

This is also true for the homogenization of milk (3.5 vol.-% fat, full stream homogenization) with conventional flat valves, as commonly used in the dairy industry, or simple orifice valves (Fig. 8, triangle symbols  $\triangle$ ). However, increasing the fat content to 32 vol.-% fat results in droplet sizes increasing with increasing homogenization pressure, as an increased disruption effect results in a higher number of smaller droplets and thus, in an increased coalescence and aggregation rate (Fig. 8, triangle symbols  $\triangle$ ). When using the novel SHM-valve droplet sizes decrease with increasing pressure, even for 32 vol.-% (Figure 8, round symbols  $\bullet$ ), as it does for full stream homogenization of low fat content milk (3,5 vol.-%). The course of both curves matches accordingly, emphasizing that aggregation in cream could be effectively prevented by dilution at the moment of the droplet break-up.

When comparing SHM partial homogenization technology to conventional full stream homogenization of full cream milk (Fig. 8, triangle symbols  $\triangle$ ), homogenizing cream of 32 vol.-% results in milk of slightly improved quality while using cream of 42 vol.-% fat as main stream, respectively, results in milk of slightly inferior quality (see Figure 8). In all, product quality can be maintained by partial homogenization using the SHM valve technology for typical technical fat contents of 32-42 vol.-%.

Emulsifying efficiency usually is increased at elevated temperatures as droplet viscosity decreases and droplet disruption is facilitated. However, in homogenizing milk, dairy proteins required for stabilization are heat sensitive and denature at elevated temperatures. Therefore, optimal results are found at T = 60 - 70 °C in conventional milk homogenization [2]. The SHM valve technology allows adjusting the temperatures of both streams separately. Thus, skim milk, containing most of the heat-sensitive dairy proteins, can be applied at moderate temperatures, while cream,

containing only a minor amount of the proteins [8, 9], can be homogenized at elevated temperatures.

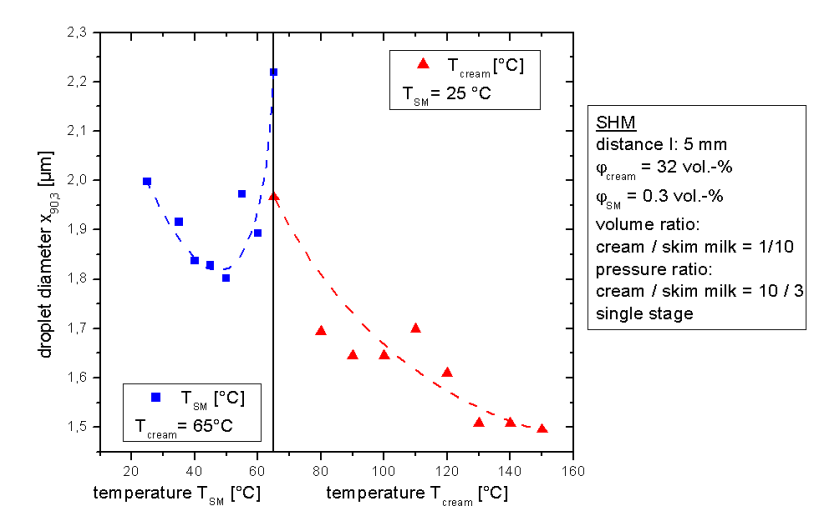


Figure 9. Homogenization results (maximum droplet diameter  $x_{90,3}$  of the volume distribution) for SHM partial stream homogenization of cream (32 vol.-% fat) with skim milk (0.3 vol. - %) for different temperatures of the skim milk and the cream

Fig. 9 gives the maximum droplet diameters  $x_{90,3}$  as a function of the homogenization temperature of the skim milk, and the cream, respectively. For of a constant temperature  $T_{SM}$  of the mixing stream (skim milk) of 25 °C, higher homogenization temperatures of the cream  $T_{cream}$  result in improved homogenization results ( $\triangle$ ). This can be explained by the fact of decreased droplet viscosity with increased homogenization temperatures resulting in an improved droplet deformation and break-up. Decreased droplet sizes can be used for altering product characteristics (product design) or for reducing the homogenizing pressure (energy saving).

When varying the skim milk temperature  $T_{SM}$  at a constant cream temperature  $(T_{cream})$  of 65°C we observed that the maximum droplet diameter  $x_{90,3}$  decreases until a skim milk temperature  $T_{SM}$  of around 45°C is reached and increases at higher temperatures. The decreasing of the  $x_{90,3}$  may be explained by the lower viscosity of the fat globules or faster stabilization kinetics of dairy proteins. However, by exceeding the melting point of milk fat (around 45 °C), droplets stabilization effect is apparently reduced, and resulting droplet sizes increase. Further investigations into this effect will enable us to predict the optimal temperature ratio between both homogenizing streams.

As the SHM valve system allows stabilizing fat droplets mainly against aggregation even at fat contents up to 42 vol.-%, it is possible to decrease droplet sizes with increasing pressure or increasing temperature of the homogenizing stream up to 150 °C. Skim milk temperature has to be adapted for a proper cooling rate of the fat droplets.

For milk homogenization, the new SHM-valve reduces the product volume to be homogenized at high pressure and reduces the number of processing units in dairy homogenization processes. In comparison with a one-stage conventional homogenization, the new system for combining homogenization and micro-mixing

requires only 20 % of energy input compared to full stream, and only 60 % of energy input compared to conventional partial homogenization of milk. This results in considerable energy and cost savings in milk processing without any loss in product quality. In addition two mixing units can be eliminated from the process line resulting in less investment, cleaning and maintenance costs.

# Application example: production of micro particles by emulsification

The SHM-valve was also applied in the manufacturing of micro globules. The reasoning behind the experiment is analogous to the previous example of milk homogenization. Fat droplets are made by pressing the molten fat phase through the micro structured nozzle, and stabilizing them by cooling them below melting temperature using cold water. After the stabilization of the outermost layer of fat, the globules can't coalesce anymore yielding highly homogenous fat particles. An example of fat particles can be seen in Fig. 10.

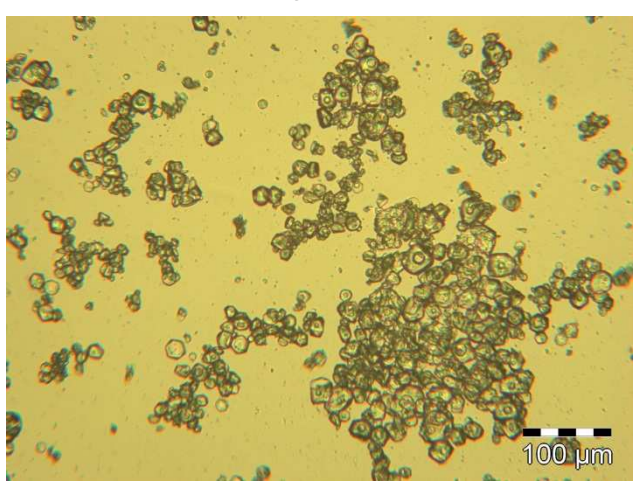


Figure 10. Particles of solidified fat particles produced by using SHM valve

#### **Conclusions**

Micro structured devices are applicable for the contacting of immiscible fluids to yield homogenous emulsions or micro spheres. The advantage of the V-type mixer is the high homogeneity in flow profile respectively shear stress, and the ease of adapting the device, keeping the hydrodynamic effects constant.

The SHM valve has been shown to suppress coalescence very effectively. The design has been shown to be a useful tool for the homogenization of milk and the production of micro spheres from wax, respectively.

#### References

- [1] Walstra, P. et. al.: Dairy technology: Principles of milk properties and processes, Marcel Dekker Inc., New York, 1999.
- [2] Kessler, H. G.: Food and Bio Process Engineering Diary Technology, Verlag A. Kessler, München, 2002.
- [3] Goulden, J. D. S., Phipps, L. W.: Factors Affecting Fat Globule Sizes During Homogenization of Milk + Cream, Journal of Dairy Research, 31 (2) 195-&, 1964.

- [4] Danner, T., Schubert, H.: Investigations on Droplet Coalescence Process in Emulsions, Product Engineering & Chemical Engineering Now, 13 (64) 335–342, 1999.
- [5] Darling, D. F., Brikett, R. J.: Food colloids in practice, Spec.Pulb.-R.Soc.Chem., 58 1-29, 1978.
- [6] Walstra, P., Oortwijn, H.: The Membranes of Recombined Fat Globules .3. Mode of Formation, Netherlands Milk and Dairy Journal, 36 (2) 103–113, 1982.
- [7] Dalgleish, D. G., Tosh, S. M., West, S.: Beyond homogenization: The formation of very small emulsion droplets during the processing of milk by a Microfluidizer, Netherlands Milk and Dairy Journal, 50 (2) 135–148, 1996.
- [8] Souci, S. W. et. al.: Die Zusammensetzung der Lebensmittel, Nährwert-Tabellen; Food Composition and Nutrition Tables; La composition des alime, CRC Press, 2000.
- [9] Karasch, S., Kulozik, U.: Hochdruckhomogenisierung von Milch mit modifizierten Lochblenden im Vergleich zu konventionellen Flachventilen, Chemie Ingenieur Technik, 80 (8) 1117–1124, 2008.

© M. Kraut, A. Hensel, R. Dittmeyer, 2010

# OPTICAL CHARACTERIZATION OF MICROSTRUCTURED EVAPORATORS

# Alice VITTORIOSI, Juergen BRANDNER, Germany

**Key words**: microstructured evaporators, vapor quality, laser photometry

## **Summary**

A new optical measurement technique for the qualitative characterization of microstructured evaporators is presented. The set-up, mainly consisting of a laser source and a photometer transducer, will be described in its working principle. Three types of microstructured evaporators, manufactured at IMVT in the Karlsruhe Institute of Technology, have been characterized with changing operating conditions and different working configurations.

The experimental set-up allows an evaluation of vapor quality and an easy comparison of the performances of different kinds of microstructure evaporators.

The results obtained from the tests will be presented and discussed. Also, the influence of the inlet parameters and of the boundary conditions on the outlet vapor quality will be pointed out. Finally, comparisons with two reference methods for the production of vapor will be presented and commented.

#### 1. INTRODUCTION

Phase transition is an important procedure in chemical and thermal process engineering and in many other applications. With conventional techniques evaporation is accomplished by heating a fluid tank into a more or less void volume. Systems acting by this principle are characterized by long thermal time constants and relatively low heat transfer coefficients.

To emphasize the heat transfer efficiency when phase transition occurs, evaporation in microchannels is realized. The main advantage of microstructured devices is the very high surface to volume ratio (typical values can go up to several  $10,000~\text{m}^2\cdot\text{m}^{-3}$ ), which is one or two orders of magnitude higher than that of conventional systems. Moreover, as the overall heat transfer coefficient is inversely proportional to the hydraulic diameter and the channel wall thickness, the smaller the characteristic lengths of the system are, the more the heat transfer is enhanced.

The increasing number of applications of microstructures in process engineering problems is widely documented (see Schubert et al. (2001) and Brandner et al. (2007)). This has required efforts for the identification of the driving mechanisms taking place in such structures and for the further improvement of their performances.

The importance of bubble growth and of two-phase flow patterns in microchannels has been pointed out by i.e. Kandlikar (Kandlikar (2002)) and others. Pressure fluctuations might influence bubble expansion and thus affect the vapor quality and stability at the exit of the channels.

The relative difficulty of obtaining very high vapor qualities in a wide range of exit conditions is one of the limits of microstructured evaporators. This is mainly due to instabilities arising in flow evaporation processes (Henning et al. (2007)) and the

problems to control them. However, the phenomena occurring inside the micro channels during phase transition are not well identified yet, and a correct manipulation of the devices for the achievement of the desired exit conditions is still rather complicated.

The direct visualization of evaporation in microchannels with high speed imaging techniques can be a useful tool for the understanding of the phase transition mechanisms (see Maikowske (2009)).

#### 2. EXPERIMENTAL SET-UP

In most applications where vapor is required, a fluid flow with defined throughput and temperature and homogeneous characteristics is demanded. Here, the term homogeneous refers both to stability of the exhaust characteristics in time and to uniformity of the jet in the entire area where vapor is released. In other terms, for industrial vapor production, the presence of non-uniformly distributed and non-uniformly sized liquid droplets among the vapor phase has to be avoided.

From a practical point of view, a quick procedure to identify the different features of the evaporators in terms of vapor characteristics at the exit is needed. This kind of approach can suggest the properties that affect the homogeneity of the exiting stream more and the possible instabilities which lead to a non optimal phase transition. Moreover, the understanding of the inlet parameters influence on the outlet characteristics of the vapor is important to obtain highly performing devices in a wide range of operating conditions. Guide lines stating how the device should be managed and set depending on the required specifications (outlet temperature, average liquid phase content, vapor density, etc.) can be identified.

The above mentioned considerations have led to the conception of a new experimental procedure for the qualitative characterization of vapor produced with microstructured devices. The measuring technique uses the principle of laser photometry and consists mainly of a laser light source and a light detection sensor (photodiode). In Fig.1 a scheme of the optical investigation system is shown.

The laser passes through the vapor release area, where scattering phenomena occur if light photons collide with molecules of vapor or liquid water. The scattered light is diffused in all directions with a highest probability of being diverted backward in the direction of the laser source (backscattering).

The amount of diverted light depends on the kind of scattering medium colliding with the photons and its physical state. The parameter accounting for this is the refraction index which is higher for liquids than for the gaseous phase. A distinction between scattering events originating from liquid molecules (higher intensity of scattered light) and those coming from gaseous molecules (lower intensity of scattered light) is therefore possible.

The backscattered light is focused with a lens and collected with a light intensity sensor (photodiode).

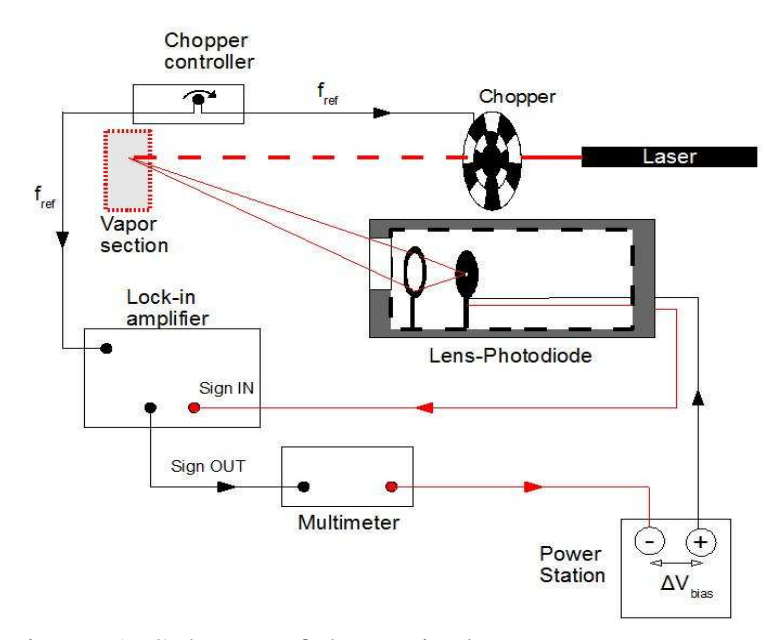


Figure 1. Scheme of the optical measurement set-up

The sensor, opportunely screened from the noise of surrounding light sources, produces a current signal which is proportional to the intensity of the incident light. This last one is related to the amount and the distribution of the liquid phase in the exiting jet as well as to the extent of focusing of the stream (density of scattering molecules). Information about the characteristics of vapor can be drawn from an analysis of the current signal, which is first filtered (for noise reduction purposes) and then amplified (for a better reading).

Although the thermodynamic density and quality of vapor can not be measured with the described system, a set of data for the performance evaluation of different devices can be created. This can be very useful when specific vapor characteristics are required for a given process, and the best technology needs to be identified along with the required optimal settings.

The variation of the results in answer to changes of the inlet parameters can be investigated, and comparisons with the characteristics of vapor produced by conventional systems can be done as well.

The described measuring technique is easily adaptable for the testing of a variety of systems in different configurations. In the following paragraph, some results obtained with the experimental set-up are presented.

### 3. RESULTS AND DISCUSSION

Three different microstructured evaporators have been tested, having a multi layer, a rod and a ring surface geometry, respectively (see Fig.2).

The multi layer evaporator presents 612 microchannels each with a rectangular cross section of  $200x200 \mu m^2$  arranged in 6 different stainless steel foils.

Heat is delivered by three rows of electrically powered heating elements, which can be controlled either in the surface temperature or in the electrical input power.

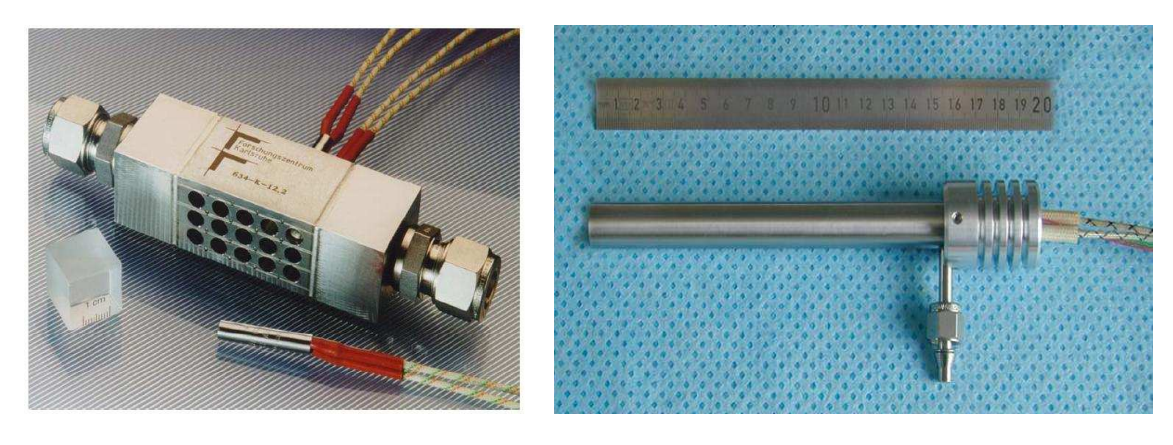


Figure 2. Picture of two of the tested devices with multi layer (left) and rod (right) geometry

The first tests have been performed with saturated conditions at the exit, keeping the outlet temperature constant at a value of  $100\,^{\circ}\text{C}$  and recording the current signal. Successively, the temperature profile has been increased up to the beginning of superheating, and then further until complete highly superheated vapor was produced (Tout ~  $250\,^{\circ}\text{C}$ ). In Fig.3, Fig.4 and Fig.5 the resulting signals with non-superheated and superheated vapor are shown.

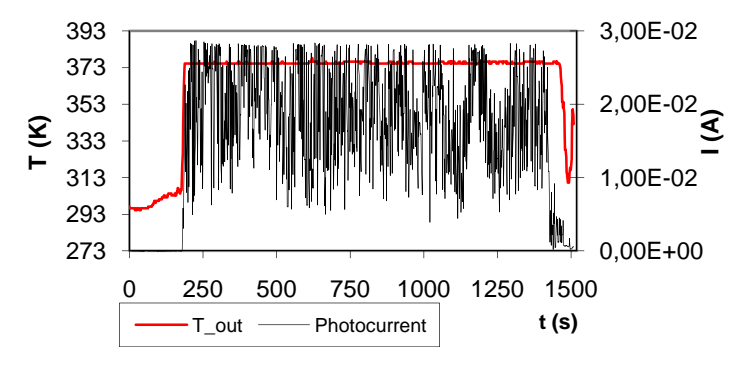


Figure 3. Signal recorded with the multi layer evaporator under saturated exit conditions. The peaks of the current signal correspond to reflection phenomena of big liquid droplets contained in the vapor stream

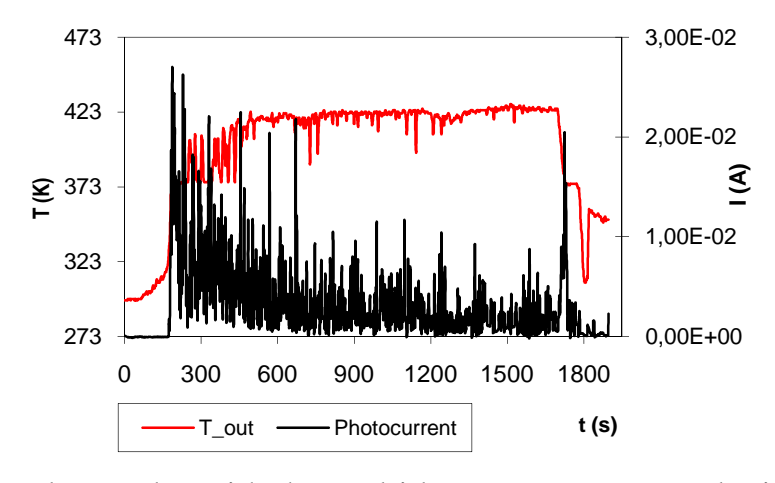


Figure 4. Signal recorder with the multi layer evaporator and with an average superheating level for the exiting vapor

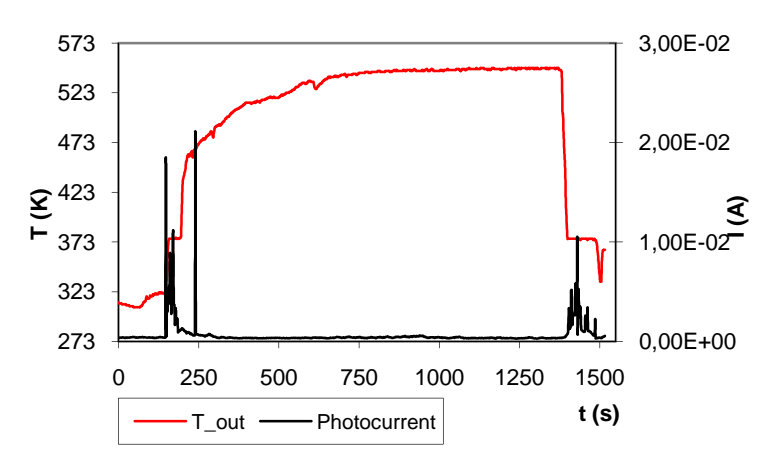


Figure 5. Signal recorded with the multi layer evaporator under complete superheating conditions

In the first case the current shows high amplitude and high frequency oscillations. The average signal level reveals the high presence of liquid which is distributed in differently sized droplets (uneven peaks of the signal). The non-homogeneity oscillations disappear only with high levels of superheating, although the average current progressively decreases with increasing input power (i.e. the amount of liquid fraction is reduced, but it is always non-homogeneously distributed).

The high non-homogeneity is most likely caused by instabilities occurring between the inlet and the outlet of the channels. Pressure fluctuations or non uniform temperature distribution might be at the basis of these instabilities, giving rise to phenomena such as channel inlet chocking. A proper verification of these theories can be obtained by including the multi layer evaporator in a two-stage configuration (i.e. adding another device at the exit of the first). This would allow the creation of a smoother temperature profile and, at the same time, increase the residence time of the fluid flow inside the heated microchannels. The influence of channel choking and pressure fluctuation should be eliminated or at least mitigated.

The rod evaporator presents a compact geometry consisting of a single microchannel wrapped around a cylindrical tube. The channel is covered by an outer cylinder, coaxial with the first one and welded at the top with it. A small passage is left open for the vapor release. The inside of the inner cylinder is left empty for the housing of a heating cartridge, which realizes the heat supply.

The signal recorded with this device shows a reduced presence of oscillations and a lower current level with respect to the multi layer evaporator (increased outlet vapor quality). However, if the same throughput used in the multi layer configuration is imposed (about 1 kg/h), the presence of re-condensation and bottom dropping phenomena has been detected. This is mainly due to the low thermal inertia of the device, and thus to the higher influence of the external heat losses on the fluid dynamics.

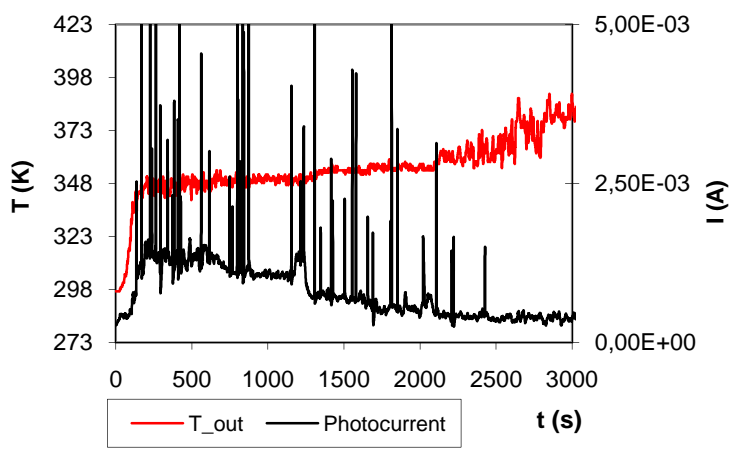


Figure 6. Signal recorded with the rod evaporator and a mass flow rate of 1 kg/h. The input power during the tests has been increased in steps until superheating has been achieved.

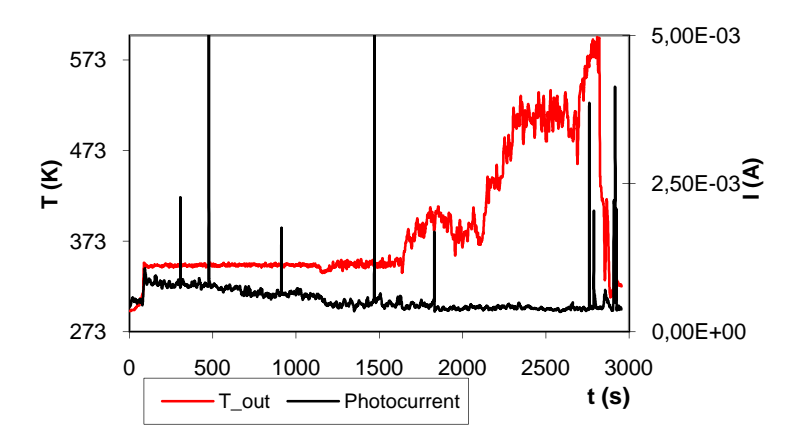


Figure 7. Signal recorded with the rod evaporator and a mass flow rate of 0.5 kg/h

A further reduction of the oscillations and the elimination of re-condensation phenomena can be observed if the flow rate is reduced and the input power is kept constant. Fig. 6 and Fig.7 compare the signals recorded with a mass flow rate of 1 kg/h and 0.5 kg/h respectively.

In general, the rod configuration, with an accurate cross-tuning between mass flow rate and input power, allows the production of homogeneous vapor over a larger range of operating conditions with respect to the multilayer device. Nevertheless, heat losses must be controlled as they can cause re-condensation of vapor at the exit of the device.

The ring evaporator (Fig.8) is a copper disk where water enters at the centre, is heated and expanded through circular blanks and exits at the periphery of the disk. In this case evaporation is realized not only by electrical heating but also by a flash expansion through the orifices connecting the concentric blanks. This phenomenon enhances the performance of the device which produces high quality vapor.

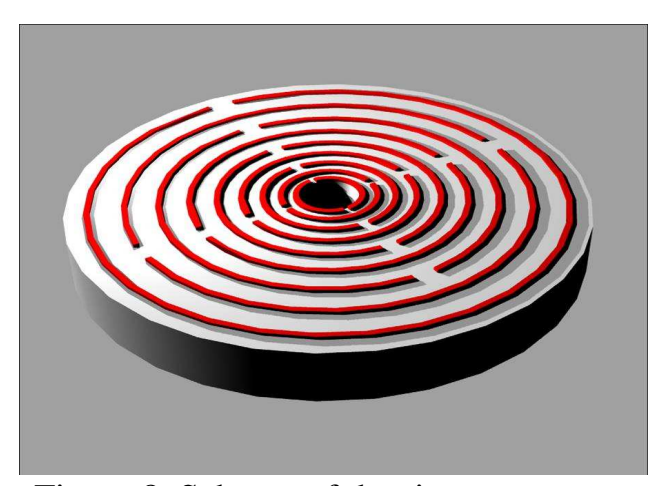


Figure 8. Scheme of the ring evaporator

The signal characterizing this kind of evaporator (Fig.9) presents a reduced average current (nearly zero). Oscillations are very low and localized at the beginning of the evaporation.

The most interesting feature of the ring evaporator is the possibility of producing dry-vapor in saturated conditions (i.e. Tout~100 °C with absence of any liquid fraction). This result can be achieved by adjusting the input power in dependence of the water flow rate entering the device, until all the current oscillations are eliminated.

In this particular kind of geometry phase transition takes place homogeneously, and thus, the characteristics of the exiting vapor are more controllable and less dependent on flow instabilities or on the thermal processes parameters.

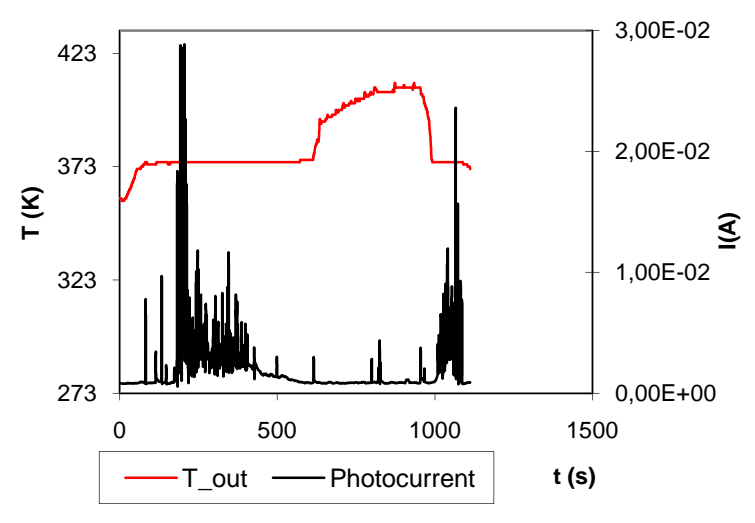


Figure 9. Signal recorded with the ring surface evaporator with a mass flow rate of 0.7 kg/h

#### 4. COMPARISONS WITH REFERENCE SIGNALS

The developed analysis technique for vapor quality evaluation can be adapted for the characterization of conventional and well known vapor production methods. These signals can then be used as references for comparison with those registered with microstructured evaporators.

In this way the characteristics of vapor achievable with every single structure can be identified in terms of density, focusing and velocity of the jet, but also content and distribution of liquid fraction.

Two reference signals have been considered for comparison with the multi layer evaporator.

For the first reference signal vapor is produced by heating up a bowl containing water ("free evaporation"). The release to the atmosphere is driven only by buoyancy effects and vapor is not focused. The second system is a commercial steam cleaner, where the vapor jet is focused and has a high homogeneous content of liquid fraction.

Both saturated and superheated conditions have been compared with the references.

In Fig.10 the comparison between the "free evaporation" reference and the non-superheated vapor signal is shown.

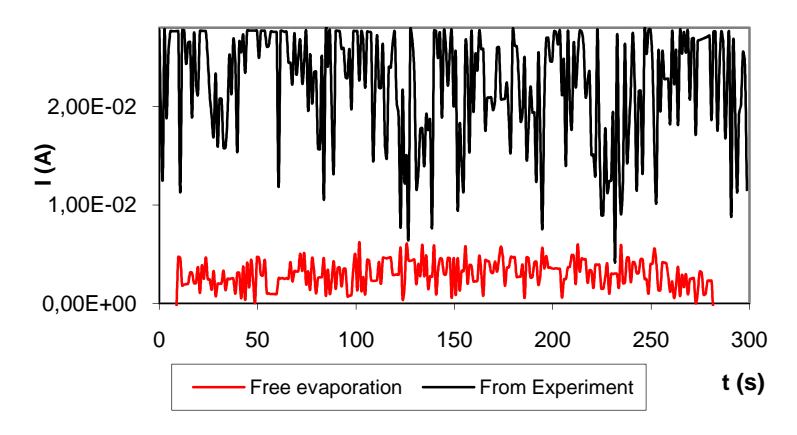


Figure 10. Comparison between "free evaporation" reference and non-superheated vapor signal recorded from the multi layer device

Vapor produced in the two cases has very different characteristics, resulting in two distinct current levels. With the multi layer evaporator a highly dense jet exits from a small pipe with a velocity determined by the imposed mass flow rate. On the other hand, vapor from the bowl is released at the free interface between water and air and rises only under buoyancy forces. The higher density of vapor produced with the microstructured device results in a sharp and intense reflection dot. In the reference, light is diffused along the bowl opening, creating a non-defined reflected line across the diameter.

The oscillations of the reference signal originate from the non-uniform density of vapor rising from the open surface. On the contrary, with the evaporator, oscillations are mainly due to light reflection of water droplets inside the stream.

In Fig.11 the "free evaporation" reference is compared with the signal coming from superheated vapor produced with the multi layer device. In this case, the absence of any liquid fraction results in a drastic reduction of the refraction index, and thus of the average current level (lower than the reference). Also the oscillations due to the presence of droplets have almost disappeared.

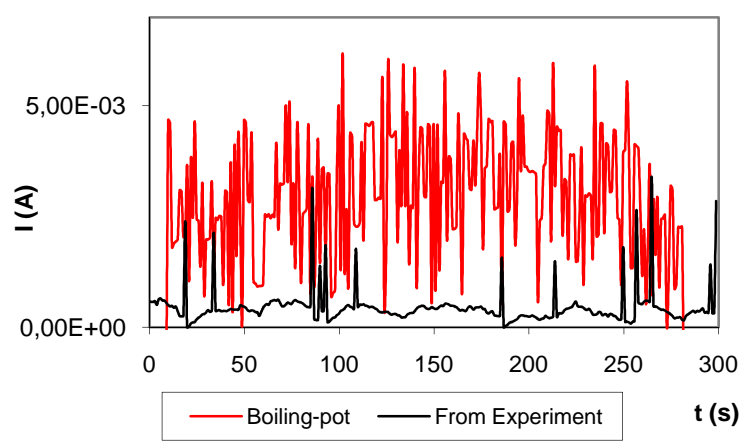


Figure 11. Comparison between "free evaporation" reference and superheated vapor signal recorded from the multi layer device

The same signals for non-superheated and superheated conditions have been compared with the second reference. The high density and velocity of the steam-cleaner jet results in a sharp and non-dispersed reflection dot, while the high content of water fraction increases the refraction index. As a result, the reference signal in this case has a very high and constant level.

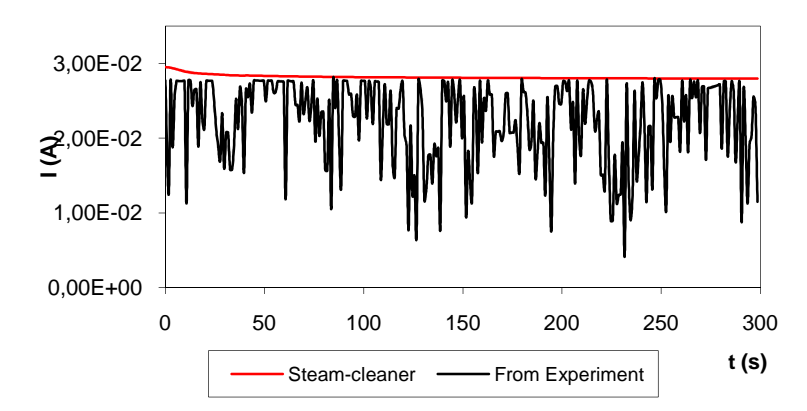


Figure 12. Comparison between "Steam cleaner" reference and non-superheated vapor signal recorded from the multi layer device

The comparisons (Fig.12 and Fig.13) show that in this case the differences between the two signals are more evident. Vapor from the steam-cleaner has very high, constant and uniform water content, while in the case of the multi layer device, a stream of almost dry-vapor with dispersed irregular liquid droplets is produced. However the volumetric flow rate of the steam-cleaner is much higher than that set for the microstructured device. A higher amount of vapor means necessarily more reflection events and consequently a higher average current through the photodiode.

When comparisons are made with the superheated vapor signal, the differences between the two average current levels are more evident.

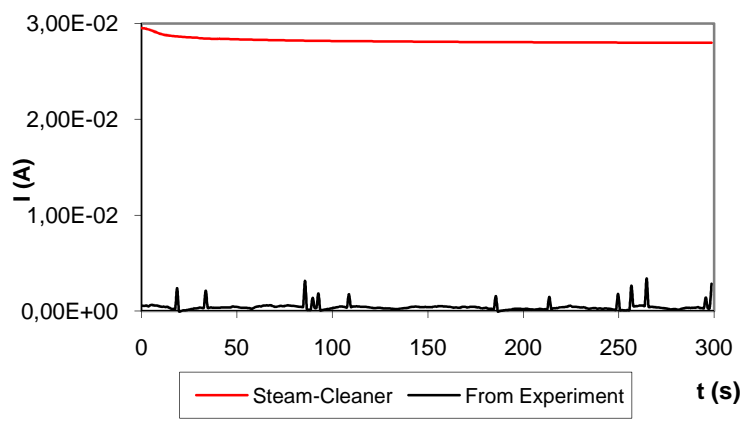


Figure 13. Comparison between "Steam cleaner" reference and superheated vapor signal recorded from the multi layer device

### 5. CONCLUSIONS

An experimental system for a quick qualitative optical characterization of microstructured evaporators has been realized. It allows non-invasive investigations for the analysis of the performances of different devices in terms of characteristics of the produced vapor.

The influence of the inlet conditions on the resulting outlet properties can be investigated and it is possible to make comparisons with reference situations.

The performed tests suggest that the fluid dynamics of the phase transition plays a major role in determining the characteristics of the vapor. Clogging phenomena, incomplete evaporation or re-condensation before the exit section have been observed, each giving rise to different behavior of the exiting jet.

The present experimental apparatus has been found to be a good tool to investigate which configurations and test conditions are the best when particular characteristics at the exit are requested.

Guidelines for the improvement of the evaporator performance can also be deduced from the presented results.

Future works should be concentrated on the achievement of smooth phase transition and on the production of homogeneous vapor in a wide range of exiting conditions, both with the multi layer and the rod evaporators. This could be done by modifying the configuration of the devices and thus reducing the influence of external or internal instabilities on the evaporation mechanisms.

#### 6. ACKNOWLEDGMENTS

Part of the research leading to these results has received funding from the European Community's Seventh Framework Program (FP7/2007-2013) under grant agreement n° 215504.

#### 7. REFERENCES

Schubert, K., Brandner, J.J., Fichtner, M., Linder, G., Schygulla, U., Wenka, A., Microstructure devices for applications in thermal and chemical process engineering, Microscale Thermo-Physical Engineering, Vol.5(1), pp. 17–39 (2001).

Brandner, J.J., Bohn, L., Henning, T., Schygulla, U., Schubert, K., Microstructure heat exchanger applications in laboratory and industry, Heat Transfer Engineering, Vol.28(8-9), pp. 761–771 (2007).

Kandlikar, S.G., Fundamental issues related to flow boiling in minichannels and microchannels, Experimental Thermal and Fluid Science, Vol.26(2), pp. 389–407 (2002).

Henning, T., Brandner, J. J., Schubert, K., Lorenzini, M. and Morini, G. L., Low-frequency instabilities in the operation of metallic multi-microchannel evaporators, Heat Transfer Engineering, Vol.28(10), pp.834–841 (2007).

Maikowske, S., Brandner, J.J., Lange, R., Schubert, K., Optical Investigations of Evaporation in Multi-Microchannel Arrays, Proc. 8th World Congress of Chemical Engineering, August 23–27, 2009, Montréal, Quebec, Canada.

#### **CONTACTS**

# Dipl. Ing. Alice Vittoriosi

Karlsruhe Institute of Technology, Campus North, Institute for Micro Process Engineering

Hermann-von-Helmholtz-Platz 1 Eggenstein-Leopoldshafen, D-76344 GERMANY Tel. +49 7247 82-8136

Fax +49 7247 82-3186

Email: alice.vittoriosi@kit.edu

Web site: www.kit.edu

© A. Vittoriosi, J. Brandner, 2010

# CONTROL OF THE REACTIONS OF HYDROGEN PRODUCTION AT STEAM REFORMING IN MICRO AND NANOSCALE

# Vladimir V. KUZNETSOV, Oleg V. VITOVSKY, Olga A. GASENKO, Russian federation

**Key words**: microchannel reactor, hydrogen, nanocatalyst, steam reforming, ethanol, carbon monoxide

#### **SUMMARY**

Experimentally were obtained patterns of steam reforming ethanol and carbon monoxide in a microchannel reactor upon activation of chemical reactions at the nanoscopic catalyst. Consistent implementation of these processes can increase the hydrogen yield and reduce the concentration of carbon monoxide. Steam reforming of ethanol was studied on Rh/Al2O3 nanocatalyst deposited on the inner wall of the annular microchannel, with supply of heat through the gap channel from the outer wall. Steam conversion of carbon monoxide was studied at Pt/CeO2/Al2O3 nanocatalyst deposited on the walls of the microchannel plate. Obtained the data on the composition of the products of conversion in the temperature range of reactors from 760 oC to 320 oC. Determine the temperature regimes in which the proportion of hydrogen in the reaction products reaches 68% and carbon monoxide content is reduced to 1 %.

### **АННОТАЦИЯ**

Экспериментально получены закономерности паровой конверсии этанола и в микроканальном реакторе при активировании углерода химических превращений на наноструктурном катализаторе. Последовательное проведение этих процессов позволяет увеличить выход водорода и снизить концентрацию монооксида углерода. Паровая конверсия этанола исследована на Rh/Al<sub>2</sub>O<sub>3</sub> нанокатализаторе, нанесенном на внутреннюю стенку кольцевого микроканала, при подводе тепла через зазор канала от внешней стенки. Паровая монооксида исследована Pt/CeO<sub>2</sub>/Al<sub>2</sub>O<sub>3</sub> конверсия углерода на нанокатализаторе, нанесенном на стенки микроканальной пластины. Получены данные по составу продуктов конверсии в диапазоне температур реакторов от 760  $^{\circ}$ С до 320  $^{\circ}$ С. Определены температурные режимы, при которых доля водорода в продуктах реакции достигает 68 %, а содержание монооксида углерода снижено до 1 %.

#### 1. INTRODUCTION

Recently, the use of hydrogen is considered as an environmentally safe way to generate energy. Storage, transportation and distribution of hydrogen is still no reliable technical solutions and therefore the production of hydrogen from the liquid organic material with its subsequent use in fuel cells for power generation is particularly relevant.

The catalytic steam conversion of ethanol is one of the most effective ways to produce hydrogen from renewable sources. To reduce the concentration of carbon monoxide in the reaction products is used consistently steam conversion of carbon monoxide, which allows reducing its share to 1 %, and the subsequent fine cleaning processes. When using polymeric membranes based on polibenzimidazol, we can use hydrogen fuel containing carbon monoxide to 3 % without the use of fine purification.

Great interest is the realization of the processes based on microchannel technology. Compared with previously developed systems microconvectors have smaller effective length of the transfer, which largely eliminates the diffusion limitations, speeds up the reaction rate and allows you to create compact hydrogen generation device. Most full advantage of microchannel reactors occur in endothermic and exothermic reactions, including the steam reforming of ethanol (Wanat E.C., et al. 2004) and carbon monoxide (Tonkovich A.Y., et al. 2007). For high-speed chemical reactions and reduce the temperature conversion catalyst is used. It must be stable under extreme conditions, as well as high ethanol conversion is achieved at temperatures close to 800° C and at a high probability of deposition of carbon. Among the most active catalysts are catalysts based on noble metals (Tonkovich A.Y., et al. 2007, Liguras D.K., et al., 2003, Diagne C., et al., 2002).

The dominant reactions in the steam reforming of ethanol are two reversible reactions: highly endothermic reaction of steam reforming of ethanol and moderate the exothermic reaction of steam conversion of carbon monoxide (Liguras D.K., et al., 2003, Diagne C., et al., 2002). The mechanism and kinetics of multistage chemical conversion of ethanol and carbon monoxide with an excess of water vapor being actively discussed in the literature (Wanat E.C., et al. 2004, Tonkovich A.Y., et al. 2007, Liguras D.K., et al., 2003, Diagne C., et al., 2002), at the same time, very little experimental works to study the relationship of heat, mass transfer and physical-chemical processes for steam reforming in microchannels with highly active nanocatalyst on the walls.

In this paper we experimentally studied the chemical conversion during the steam reforming of ethanol in the annular microchannel with the catalyst nanostructure with an external heat supply through the gap of the channel and follow the steam conversion of carbon monoxide in the assembly of the microchannels. Synthesized Rh/Al<sub>2</sub>O<sub>3</sub> nanocatalyst for steam reforming of ethanol and Pt/CeO<sub>2</sub>/Al<sub>2</sub>O<sub>3</sub> catalyst for steam reforming of carbon monoxide, worked out methods for their attachment to the walls of the microchannel. We consider the contribution of conductive, convective and radiative heat transfer in these conditions.

# 2. METHODS OF INVESTIGATION

## 2.1.Experimental equipment

Experimental study of chemical conversion of ethanol in the medium of water vapor carried in an annular microchannel reactor with a annular gap of 1 000 microns, as shown in Fig. 1 (a). As a catalyst used in nanocomposite material deposited on the surface of a replaceable cartridge inner-cylinder with an outer diameter of 6 mm and 40 mm long, made of heat-resistant alloy. He pressed into the

outer cylindrical tube made of stainless steel with wall thickness of 2 mm, which ensured the supply of heat to the cylinder from the outer wall of the heated reactor. For the heating and temperature stabilization reactor was placed in a heated electric shock quartz tube coated with a layer of insulating material to prevent heat loss. The temperature of the outer wall of the reactor was monitored using a chromel-alumel thermocouple. The thickness of the channel was sufficient for the efficient supply of heat to the reaction zone and the reaction took place in a weak non-isothermal along the length of reactor.

Experimental study of steam conversion of carbon monoxide is conducted in microchannel reactor containing 11 microchannels, the wall which caused aerosol method nanocomposite catalyst – Fig. 1 (b). Microchannel plate 4 mm thick made of heat-resistant stainless steel and contained a microchannel with a gap of 600 microns and a length of 40 mm. After the deposition of the catalyst microchannel plate cover plate thickness of 2 mm and scald argon welding. Made way microchannel reactor located between the heater plates with mounted electric cartridges. The temperature of the external walls of the microchannel plate was controlled by chromel-alumel thermocouple. The thickness of the reactor and crimp plates was sufficient for the efficient distribution of heat in the reaction zone, and the reaction took place in the weak non-isothermal conditions along the reactor length.

As the reaction mixture with steam reforming of ethanol used a mixture of ethyl alcohol and water with molar ratio H2O/C2H5OH = 4. Experiments were conducted with the input volume flow of the mixture per gram of catalyst GHSV = 262 Nl/gcat/hr. Reynolds number, determined by the velocity of the mixture at the entrance to the channel and the gap was equal to 63. As the reaction mixture with steam conversion of carbon monoxide used a mixture of carbon monoxide, hydrogen and water with molar ratio H2O/CO = 2.7-4. Experiments were conducted with the input volume flow of the mixture per gram of catalyst GHSV = 7.5–25 Nl/gcat/hr and a pressure of 1.4 bar. The experiments were conducted in the temperature range 550-750 K. The Reynolds number, determined by the velocity of the mixture at the entrance to the channel and the hydraulic diameter, ranged from 5 to 23. The temperature of the reaction mixture of gases at the reactor inlet and outlet are measured by a chromel-alumel thermocouple. For the evaporation of liquid, preheating and mixing of the reaction mixture of gases to the reactors, the evaporator / heater, heated electric shock. Filing fluid made with the help of mass flow controllers firm Bronkhorst HI-TECH.

Output gas mixture passed through the cooler / condenser, where the pair were condensed and water separator. Dry mixture of gases is released for analysis in the gas chromatograph (Perkin Elmer model 1016 with its heat conductivity detector). Volumetric flow rate of the dried mixture of gases at the outlet of the reactor was measured by flow meter OMEGA. Volume fraction of vapor liquid phases was measured by the flow of condensate. To determine the component and measuring their concentrations in the condensate used chromatomasspectrometer Agilent 6850 with mass selective detector. The error in measuring the concentration does not exceed 2%.

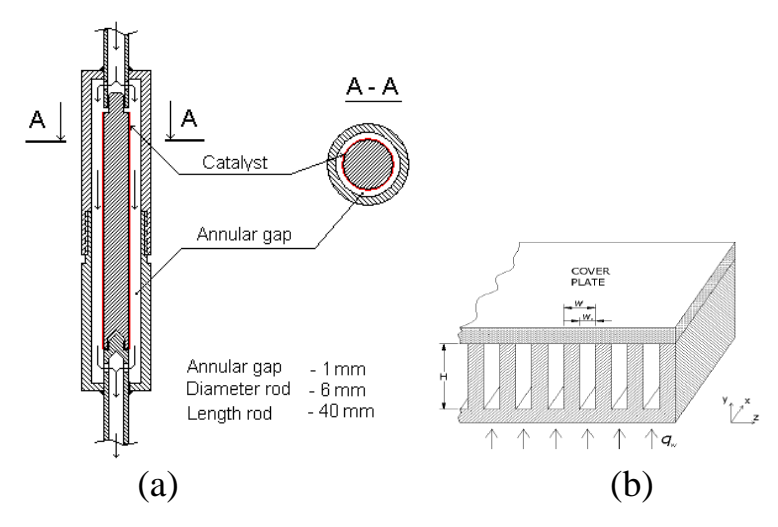


Fig.1. Scheme of the microchannel reactors

# 2.2. Catalyst preparation

Based on the synthesis of multi-coordination compounds with subsequent thermal decomposition to highly dispersed nanosized oxides synthesized composite nanocatalyst for steam reforming of ethanol and carbon monoxide with high homogeneity of the phase composition. For the reaction of ethanol steam reforming catalyst synthesized on the basis of rhodium and made methods to improve the adhesion properties of the coating and its resistance to fracture. Catalysts are made on the basis of  $\gamma$ -Al<sub>2</sub>O<sub>3</sub> with a specific surface area of 150–170 m<sup>2</sup>/g, calcined at high temperatures and impregnated of the aqueous solution of rhodium nitrate (Rh content up to 5 % by mass). After heat treatment of the catalyst slurry was applied to the prepared surface of the cartridge-cylinder. Measured the size of nanoparticles of rhodium does not exceed 2 nm.

Catalyst for steam conversion of carbon monoxide produced by  $\gamma$ -Al<sub>2</sub>O<sub>3</sub> and CeO<sub>2</sub> with a specific surface  $\gamma$ -Al<sub>2</sub>O<sub>3</sub> 150–170 m<sup>2</sup>/g, calcined at high temperatures and impregnated of the aqueous solution chloroplatinic acid (Pt content up to 5 % by mass). After heat treatment of the catalyst slurry was applied to the prepared surface of the microchannels.

#### 3. EXPERIMENTAL RESULTS

# 3.1. Experimental study of steam reforming of ethanol

Thermal regime of the catalyst in the annular microchannel in Fig. 1 with the heated outer wall was considered in (Kuznetsov V.V, et al., 2009). It was found that the chemical conversion with the absorption of heat on the outer surface of the inner cylinder may be three ways of heat supply to the reaction zone: conductive heat input via the attachment of the inner cylinder, convective heat transfer in the gap of the reacting mixture and radiation heat transfer through the gap channel. Fig. 2 shows the composition of products of steam reforming of ethanol at the outlet microchannel reactor, depending on the temperature of the catalyst at GHSV = 262 Nl/gcat/hr. Experiments were conducted at a pressure in the reactor of 1.4 bar. The temperature of the catalyst is determined by the temperature of the outer wall of the reactor based

on the calculation (Kuznetsov V.V, et al., 2009). The resulting temperature difference varies from 2 to 25 degrees with increasing conversion.

Chemical conversion of ethanol starting at more than  $550^{\circ}$  C catalyst and the concentration of ethanol and water in the products of conversion decreases with increasing temperature. Significant conversion of ethanol is observed at a temperature of more than  $620^{\circ}$  C, when increasing the proportion of hydrogen. Lines in Fig. 2 show the calculated dependence of the equilibrium molar composition of the products of conversion. It is seen that the experimental data fall on the equilibrium values at temperatures of catalyst above  $670^{\circ}$  C. In Fig. 3 shows the dependence of the conversion of ethanol on the temperature of the outer wall of the reactor at GHSV = 262 Nl/gcat/hr. The data in Fig. 2 and 3 show that the process of chemical conversion of ethanol is activated when the temperature of the reactor is more than  $600^{\circ}$ C.

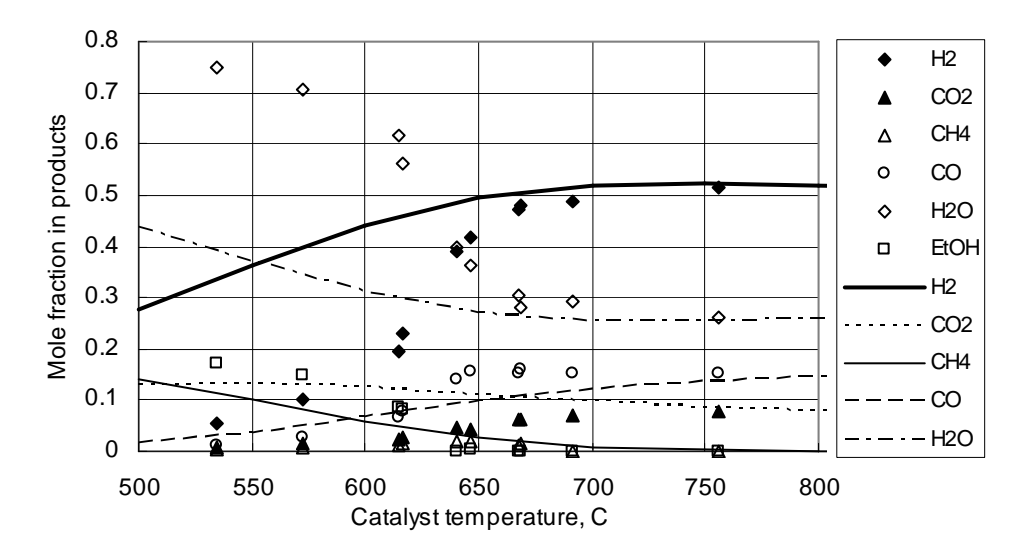


Fig. 2. The dependence of the molar fraction of products of steam reforming of ethanol on the temperature of the catalyst. Residence time in the reactor a mixture of  $190 \text{ msec. H}_2\text{O/EtOH} = 4.03$ 

Rhodium is one of the most active catalysts for the adsorption, surface reaction and desorption of ethanol and its decomposition products in the environment of water vapor. The high content of hydrogen in the output of the mixture shows that in this temperature range is the main reaction is steam reforming of ethanol. Increased carbon dioxide in the output of the mixture shows that simultaneously with the reaction of steam reforming of ethanol and the formation of carbon monoxide takes place the reaction of steam conversion of carbon monoxide to form carbon dioxide, although its rate of occurrence is low.

Conversion of ethanol proceeds with significant heat absorption. The calculation of the average temperature of the catalyst (Kuznetsov V.V, et al., 2009) showed that at the outer wall more than  $700^{\circ}$  C, radiative heat transfer in circular microchannel with an external heating plays a significant role, and allows the heat supply to the catalyst needed to ensure high conversion with temperature heads up to  $30^{\circ}$ C.

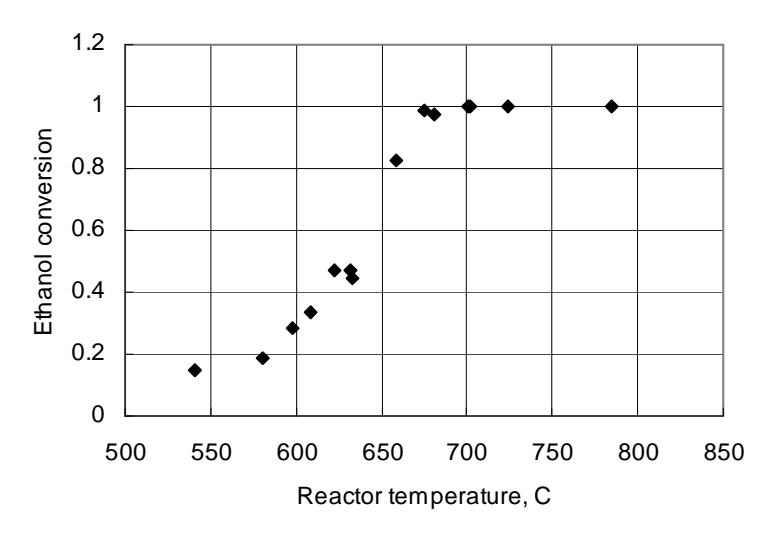


Fig. 3. Conversion of ethanol depending on the temperature of the outer wall of reactor

## 3.2. Experimental study of steam conversion of carbon monoxide

Fig. 4 shows the dependence of the conversion of carbon monoxide on the temperature of the outer wall of the reactor at its chemical conversion in the microchannel reactor with an excess of water vapor in the initial mixture of gases. The experiments used a mixture of carbon monoxide, hydrogen and water vapor in the range of molar ratios  $CO/H_2/H_2O = (0.06-0.12) / (0.6-0.53) / (0.32-0.35)$ , which simulates the composition of the products discussed earlier steam reforming of ethanol. Experiments were conducted at a pressure of 1.4 bar for residence times of the initial mixture in microchemical reactor 40, 80 and 140 msec. The time is defined as the ratio of reactor volume to volumetric flow rate of the initial mixture under normal conditions. Line in Fig. 4 shows the equilibrium conversion of carbon monoxide for a given composition of the initial mixture and the pressure in a reactor. It is seen that with increasing temperature of the reactor when the residence time of 140 and 80 msec conversion of carbon monoxide increases and approaches the equilibrium value at the temperature of the reactor 430 °C. By reducing the residence time to 40 msec conversion of carbon monoxide considerably decreases and reaches its equilibrium value even at 470 °C.

For the reaction rate constant and activation energy on the basis of experimental data used approach (Kuznetsov V.V, et al., 2009). It is assumed that the molar flow of the reacting mixture on the surface of the channel unit is determined Arrhenius dependence for the reaction of the first order. In the one-dimensional model of the reacting mixture in the channel, taking into account the external diffusion resistance, defined by the coefficient of mass transfer in (Kuznetsov V.V, et al., 2009) derived an equation for the change of the molar concentration of reactive component along the channel.

Mass transfer coefficient was determined based on the analogy of heat and mass transfer, using the value of Nusselt number for a rectangular channel. This solution was used to obtain the reaction rate constant and activation energy on the basis of experimental data. In processing the data has been simplified Arrhenius kinetics of

steam conversion of carbon monoxide leakage in the light of both forward and reverse reactions with a linear dependence on the pressure in the reactor  $P_0$ .

Fig. 5 shows the dependence of the logarithm of the reaction rate constant on the inverse temperature of the walls of the microchannel reactor. The dots show the experimental data, line - calculation with the activation energy of 47 kJ/mol. This value of activation energy for the synthesized catalyst is slightly lower activation energy of 67.1 kJ/mol obtained in (Tonkovich A.Y., 2007). The data show that the reaction of steam conversion of carbon monoxide is a reaction of first order and the accompanying reaction products of steam conversion of carbon monoxide in a microchannel are mild.

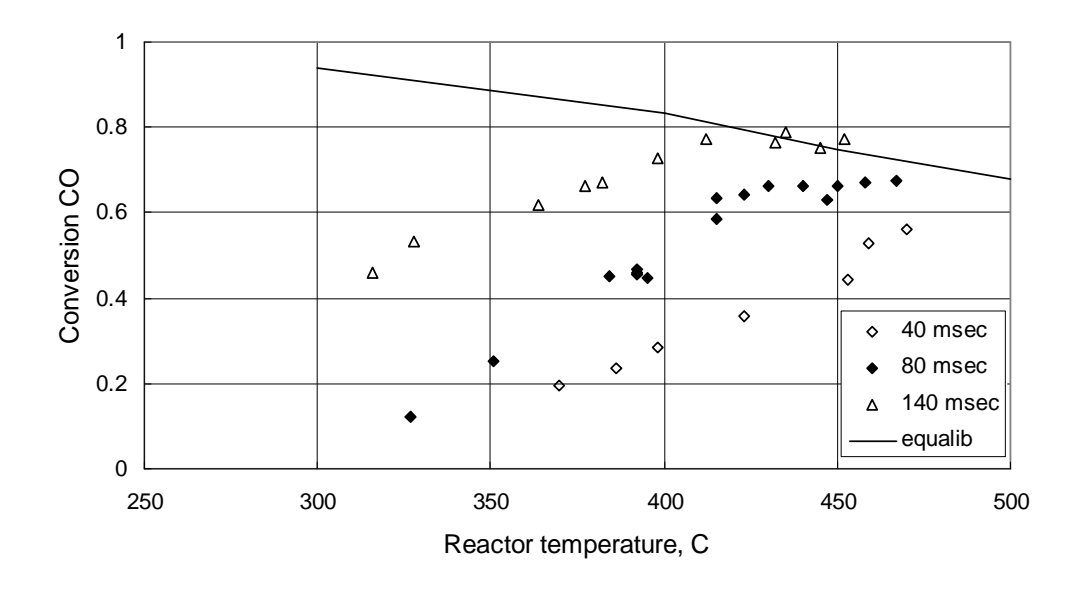


Fig. 4. Conversion of carbon monoxide vs the reactor temperature for a residence time in microchemical reactor 40, 80 and 140 msec

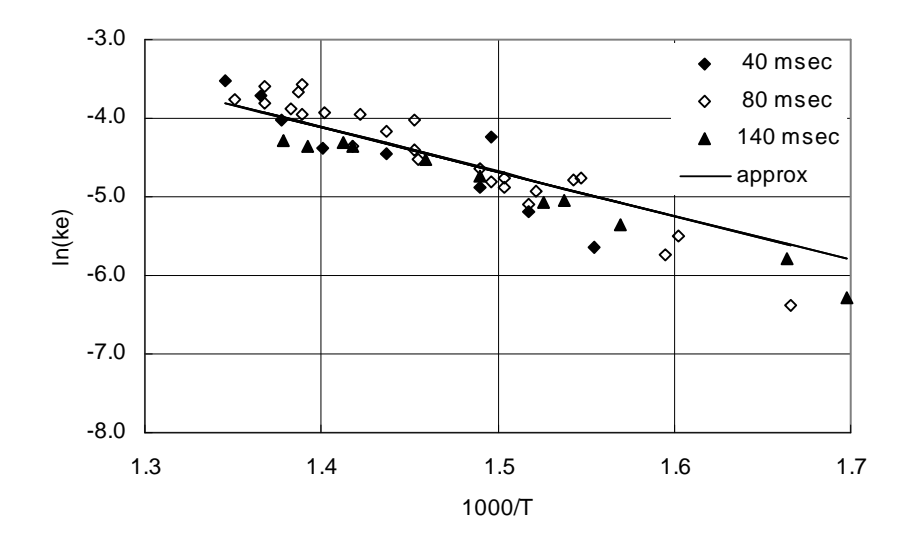


Fig. 5. The logarithm of the rate constants for reaction of steam conversion of carbon monoxide, depending on the inverse temperature of the reactor wall. Points – experiment, line – approximation

## 4. CONCLUSION

Experimental study of chemical reactions at the steam reforming of ethanol in the annular microchannel and steam conversion of carbon monoxide in the assembly of microchannels were carried out to determine the composition of the products of these reactions, depending on the volume flow of the mixture and the temperature of the catalyst. It is important to build a kinetic scheme of reactions and heat transfer model for chemical conversion in microchannel. Synthesized Rh/Al<sub>2</sub>O<sub>3</sub> and Pt/Al<sub>2</sub>O<sub>3</sub>/CeO nanocatalyst composite yielded the higher conversion as ethanol at temperatures of more than 600° C and carbon monoxide at temperatures above 400° C, when reached thermodynamic equilibrium conversion. It was found that complete conversion of ethanol is observed at temperatures above 640° C catalyst, while the proportion of hydrogen and carbon dioxide output of the mixture significantly increased, indicating a concomitant increase in the rate of reaction of steam conversion of carbon monoxide that occurs simultaneously with the reaction of steam reforming of ethanol. The calculation of the average temperature of the catalyst showed that at the outer wall more than 700 °C, radiative heat transfer in circular microchannel with an external heating plays a significant role, and allows the heat supply to the catalyst needed to ensure high conversion, with the temperature heads up to 30 °C. Obtained the effect of flow mixture on the conversion of carbon monoxide, which reduces to the residence time is less than 80 milliseconds. Determine the activation energy of the steam conversion of carbon monoxide. We achieved reduction in the concentration monoxide in the products of conversion of up to 1%, which allows the use of microchannel reactors consecutive steam reforming of ethanol and carbon monoxide to produce hydrogen with the necessary degree of purity for feeding solid oxide fuel cells.

This work was supported in part by: Rosnauka FTP Program state contract  $N_2$  02.740.11.0054 and grant RFFI 07-08-12212-ofi.

#### REFERENCES

- 1. Diagne C., Idriss H., Kiennemann A., 2002, Hydrogen production by ethanol reforming over  $Rh/CeO_2 ZrO_2$  catalysts // Catalysis Communications, Vol. 3, pp. 565–571.
- 2. Kuznetsov V.V., Vitovsky O.V., Gasenko O.A., 2009, Methane steam reforming in an annular microchannel with Rh/Al<sub>2</sub>O<sub>3</sub> catalyst // Journal of Engineering Thermophysics, Vol. 18, No. 3, pp. 187–196.
- 3. Liguras D.K., Kondarides D.I., Verykios X.E., 2003, Production of hydrogen for fuel cells by steam reforming of ethanol over supported noble metal catalysts // Applied Catalysis B: Environmental, Vol. 43, pp. 345–354.
- 4. Tonkovich A.Y., Yang B., Perry S.T., Fitzgerald S.P., Wang Y., 2007, From seconds to milliseconds through tailored microchannel reactor design of a steam methane reformer // Catalysis Today, Vol. 120, pp. 21–29.
- 5. Wanat E.C., Venkataraman K., Schmidt L.D., 2004, Steam reforming and water-gas shift of ethanol on Rh and Rh-Ce catalysts in a catalytic wall reactor // Applied Catalysis A: General, Vol. 276, pp. 155–162.

### **BIOGRAPHICAL NOTES**

Vladimir V. Kuznetsov: Ph.D., professor of Novosibirsk State University, Head of the Department of Thermophysics of Multiphase Systems of the Kutateladze Institute of Thermophysics, Siberian Branch of the Russian Academy of Sciences. Research interests: heat and mass transfer with phase change, chemical conversion in the presence of a catalyst in microchannel reactors, catalytic nanotechnology, hydrogen production, wave processes in multiphase media, explosive boiling and the phase decomposition of metastable liquids, multiphase flow in porous media. He published more than 200 papers in variety of topics. V. Kuznetsov is Deputy Editor of the international journal "Journal of Engineering Thermophysics", member of *National committee on Heat and Mass Transfer of Russian Academy of Sciences*.

## **CONTACTS**

### Prof. Dr. Vladimir V. Kuznetsov

Kutateladze Institute of Thermophysics SB RAS 1, pr. Akademika Lavrentjeva Novosibirsk, 630090 Russian Federation

Tel: +7 (383) 330-71-21 Fax: +7 (383) 330-84-80 Email: vladkuz@itp.nsc.ru

© V.V. Kuznetsov, O.V. Vitovsky, O.A. Gasenko, 2010

# THE MODELING OF CHEMICAL TRANSFORMATIONS AT METHANE STEAM REFORMING AND WATER GAS SHIFT REACTION IN A MICROCHANNEL

### Stanislav KOZLOV, Vladimir KUZNETSOV, Russian Federation

**Key words**: methane steam reforming, water gas shift reaction, microchannel, catalytic reactions.

### **Summary**

The numerical investigation of the flow structure, thermal conditions and physicochemical processes at catalytic methane steam reforming and water gas shift reaction in the microchannel was performed. The detailed information about the structure of the temperature and the mixture components concentration fields and rates of chemical transformations in the microchannel has been obtained. The temperature regimes of high conversion of the initial products were defined.

The influence of the external heat flux supplied to the gas mixture and its distribution along the channel length on the properties of the methane steam reforming have been investigated. It has been shown that not only the amount of heat supplied to the reaction zone is essential, but also the distribution of heat supply along the channel length is important. The peculiarities of the catalytic water gas shift reaction with non uniform temperature distribution have been investigated. Non uniform temperature distribution along the reactor makes it possible to combine the advantages of high-temperature and low-temperature conversions.

### **Summary**

В работе проводится численное моделирование структуры течения, физико-химических теплового режима И процессов в микроканале высокоактивным нанокатализатором на стенках при высокотемпературных химических превращениях метана и монооксида углерода с образованием водорода. Получена детальная информация о структуре полей температур и концентраций компонент в микроканале и скоростях химических превращений в зоне реакции, определены температурные режимы высокой конверсии исходных продуктов. Исследовано влияние неравномерных по длине канала температуры и подвода тепла на степень химических превращений. Показано что на степень конверсии метана при его паровом риформинге существенным оказывается не только количество подведенного тепла к зоне реакции, а так же распределение подводимого тепла вдоль химического реактора. Так же в работе исследованы особенности паровой конверсии монооксида углерода при неравномерной температуре реактора. Не равномерный по длине профиль температуры на стенке реактора позволяет объединить преимущества как высокотемпературной и так и низкотемпературной конверсии монооксида углерода.

### 1. INTODUCTION

The catalytic methane steam reforming and water gas shift reaction are widely spread technological processes for the hydrogen producing. Recently there is considerable interest in these processes as a result of possibilities to use them in the compact fuel-oil processors to obtain the feed mixture for the fuel cells. The methane steam reforming is the one of the most effective ways to produce hydrogen. The water gas shift reaction is used a method for further enhancing the yield of hydrogen from industrial processes such as the steam reforming of natural gas or the gasification of heavy carbonaceous materials. Syngas mixtures containing mostly hydrogen and carbon monoxide are typically generated at elevated temperatures via the combustion of natural gas, coal, biomass, petroleum and organic wastes (Wender 1996). If syngas are planned to use for the fuel cells feeding, it is essential to refine syngas from the carbon monoxide, since the latter is a poison for fuel cells. Usually it is carried out in two steps in separate reactors: the high-temperature and then the low-temperature water gas shift reaction. It allows reducing the monoxide concentration up to 1 %.

The phosphoric acid-doped polybenzimidazole membrane based fuel cells seem so far the most successful system in the field. The high temperature PEMFC has been successfully demonstrated at temperatures of up to 200 C under ambient pressure. No gas humidification is mandatory, which enables the elimination of the complicated humidification system, compared with Nafion cells. Other operating features of the PBI cell include easy control of air flow rate, cell temperature and cooling. The PBI cell operating at above 150 C can tolerate up to 1 % CO and 10 ppm SO2 in the fuel stream, allowing for simplification of the fuel processing system and possible integration of the fuel cell stack with fuel processing units.

The application of microchannel devices to the considering processes is the state of the art technology. Microchannel reactors have less effective transport lengths than previously developed systems. It eliminates diffusion limitations and intensifies the reaction rates. The numerical simulations of methane steam reforming and water gas shift reaction in the microchannels are considered in the several works (Tonkovich et al. 2007; Spatenka et al. 2005). There are a lot of works where the simplified flow models such as plug flow model are used. In these models the effective coefficients of heat and mass transfer between the wall and the flow are applied. The numerical simulation of the methane steam reforming in the frame of the full Navier-Stokes equations without taking into account the multicomponent diffusion of the mixture components were performed in (Kuznetsov, Kozlov 2008).

This work is aimed at numerical investigation of correlations between heat, mass transfer and physical-chemical processes at the reactions of methane steam reforming and water gas shift reaction in two-dimensional microchannel with highly active nanokatalizatorom the walls. The multicomponent diffusion of the mixture components are taken into account. The methane steam reforming is considered in the case of the external heat supply distributed along the microchannel. The water gas shift reaction is simulated with non-uniform microchannel wall temperature. It can combine the advantages of high-temperature conversion with advantages of low-temperature conversion.

### 2. NUMERICAL SIMULATION METHOD

The 2D gas flow and transfer processes in a 2D slot microchannel at chemical transformations activated on channel walls were simulated numerically in the framework of Navier-Stokes equations of a laminar flow of multicomponent compressible gas. The system of Navier-Stokes equations was written in the stream function-vorticity formulation, and it was solved by the finite-difference method according to implicit three-layer difference scheme.

$$\frac{\partial}{\partial x} \left( \frac{1}{\rho} \frac{\partial \psi}{\partial x} \right) + \frac{\partial}{\partial y} \left( \frac{1}{\rho} \frac{\partial \psi}{\partial y} \right) + \omega = 0 \tag{1}$$

$$\frac{\partial}{\partial x} \left( \frac{\partial \psi}{\partial y} \omega \right) - \frac{\partial}{\partial y} \left( \frac{\partial \psi}{\partial x} \omega \right) - \frac{1}{2} \left( \frac{\partial \rho}{\partial y} \frac{\partial (U^2 + V^2)}{\partial x} - \frac{\partial \rho}{\partial x} \frac{\partial (U^2 + V^2)}{\partial y} \right) = \frac{\partial^2}{\partial x^2} (\mu \omega) + \frac{\partial^2}{\partial y^2} (\mu \omega) - 2 \left( \frac{\partial}{\partial x} \left( \frac{\partial \mu}{\partial y} \frac{\partial U}{\partial x} - \frac{\partial \mu}{\partial x} \frac{\partial U}{\partial y} \right) + \frac{\partial}{\partial y} \left( \frac{\partial \mu}{\partial y} \frac{\partial V}{\partial x} - \frac{\partial \mu}{\partial x} \frac{\partial V}{\partial y} \right) \right) \tag{2}$$

$$\frac{\partial(\rho Uh)}{\partial x} + \frac{\partial(\rho Vh)}{\partial y} = \frac{\partial}{\partial x} \left( \lambda \frac{\partial T}{\partial x} \right) + \frac{\partial}{\partial y} \left( \lambda \frac{\partial T}{\partial y} \right) + \frac{\partial}{\partial x} \left( \sum h_i \rho D_{im} \frac{\partial Y_i}{\partial x} \right) + \frac{\partial}{\partial y} \left( \sum h_i \rho D_{im} \frac{\partial Y_i}{\partial y} \right) + U \frac{\partial^2}{\partial x} \left( \sum h_i \rho D_{im} \frac{\partial Y_i}{\partial x} \right) + \frac{\partial}{\partial y} \left( \sum h_i \rho D_{im} \frac{\partial Y_i}{\partial y} \right) + \frac{\partial}{\partial y} \left( \sum h_i \rho D_{im} \frac{\partial Y_i}{\partial y} \right) + U \frac{\partial^2}{\partial y} \left( \sum h_i \rho D_{im} \frac{\partial Y_i}{\partial y} \right) + \frac{\partial}{\partial y} \left( \sum h_i \rho D_{im} \frac{\partial Y_i}{\partial y} \right) + \frac{\partial}{\partial y} \left( \sum h_i \rho D_{im} \frac{\partial Y_i}{\partial y} \right) + \frac{\partial}{\partial y} \left( \sum h_i \rho D_{im} \frac{\partial Y_i}{\partial y} \right) + \frac{\partial}{\partial y} \left( \sum h_i \rho D_{im} \frac{\partial Y_i}{\partial y} \right) + \frac{\partial}{\partial y} \left( \sum h_i \rho D_{im} \frac{\partial Y_i}{\partial y} \right) + \frac{\partial}{\partial y} \left( \sum h_i \rho D_{im} \frac{\partial Y_i}{\partial y} \right) + \frac{\partial}{\partial y} \left( \sum h_i \rho D_{im} \frac{\partial Y_i}{\partial y} \right) + \frac{\partial}{\partial y} \left( \sum h_i \rho D_{im} \frac{\partial Y_i}{\partial y} \right) + \frac{\partial}{\partial y} \left( \sum h_i \rho D_{im} \frac{\partial Y_i}{\partial y} \right) + \frac{\partial}{\partial y} \left( \sum h_i \rho D_{im} \frac{\partial Y_i}{\partial y} \right) + \frac{\partial}{\partial y} \left( \sum h_i \rho D_{im} \frac{\partial Y_i}{\partial y} \right) + \frac{\partial}{\partial y} \left( \sum h_i \rho D_{im} \frac{\partial Y_i}{\partial y} \right) + \frac{\partial}{\partial y} \left( \sum h_i \rho D_{im} \frac{\partial Y_i}{\partial y} \right) + \frac{\partial}{\partial y} \left( \sum h_i \rho D_{im} \frac{\partial Y_i}{\partial y} \right) + \frac{\partial}{\partial y} \left( \sum h_i \rho D_{im} \frac{\partial Y_i}{\partial y} \right) + \frac{\partial}{\partial y} \left( \sum h_i \rho D_{im} \frac{\partial Y_i}{\partial y} \right) + \frac{\partial}{\partial y} \left( \sum h_i \rho D_{im} \frac{\partial Y_i}{\partial y} \right) + \frac{\partial}{\partial y} \left( \sum h_i \rho D_{im} \frac{\partial Y_i}{\partial y} \right) + \frac{\partial}{\partial y} \left( \sum h_i \rho D_{im} \frac{\partial Y_i}{\partial y} \right) + \frac{\partial}{\partial y} \left( \sum h_i \rho D_{im} \frac{\partial Y_i}{\partial y} \right) + \frac{\partial}{\partial y} \left( \sum h_i \rho D_{im} \frac{\partial Y_i}{\partial y} \right) + \frac{\partial}{\partial y} \left( \sum h_i \rho D_{im} \frac{\partial Y_i}{\partial y} \right) + \frac{\partial}{\partial y} \left( \sum h_i \rho D_{im} \frac{\partial Y_i}{\partial y} \right) + \frac{\partial}{\partial y} \left( \sum h_i \rho D_{im} \frac{\partial Y_i}{\partial y} \right) + \frac{\partial}{\partial y} \left( \sum h_i \rho D_{im} \frac{\partial Y_i}{\partial y} \right) + \frac{\partial}{\partial y} \left( \sum h_i \rho D_{im} \frac{\partial Y_i}{\partial y}$$

Viscosity and heat conductivity of the gas mixture depend on component temperature and concentration; they are calculated by the following equations (Wilke 1950; Mason, Saxena 1958):

$$\mu = \sum_{i=1}^{n} \mu_{i} x_{i} / \sum_{k=1}^{n} G_{ik} x_{k}$$

$$\lambda = \sum_{i=1}^{n} \lambda_{i} x_{i} / \sum_{k=1}^{n} A_{ik} x_{k}$$
(6, 7)

$$G_{ik} = \frac{1}{2\sqrt{2}} \frac{(1 + (\mu_i/\mu_k)^{1/2} (M_k/M_i)^{1/4})^2}{(1 + M_i/M_k)^{1/2}} \quad A_{ik} = \frac{1}{2\sqrt{2}} \frac{(1 + (\lambda_i/\lambda_k)^{1/2} (M_i/M_k)^{1/4})^2}{(1 + M_i/M_k)^{1/2}}$$
(8, 9)

Values of viscosity and heat conductivity of every mixture component were set by polynomial functions of temperature of the 5th degree, plotted on the basis of references of (Vargaftik 1996), Diffusion coefficient and enthalpy of the mixture were determined as:

$$D_{i,j} = 0.1858 \cdot 10^{-6} \,\mathrm{T}^{3/2} [(M_i + M_j)/(M_i M_j)]^{1/2} / P \sigma_{i,j}^2 \Omega$$
 (10)

$$h_{i} = h_{i,0} + \int_{298}^{T} Cp_{i}dT \tag{11}$$

$$D_{1,m} = (1 - x_i) / \sum_{i=2}^{N} x_j / D_{1,j}$$

$$h = \sum_{i=2}^{N} Y_i h_i$$
(12, 13)

The differential scheme was approximated by the so-called cross scheme. To solve the system of algebraic equations, derived by substitution of derivatives by their difference approximations, we have used Seidel iteration method. A uniform rectangular mesh was used. At mach numbers below 0.005 the hydrodynamic pressure drop in the channel was not taken into account to reduce the time of calculations. The shock velocity profile was set at the channel inlet together with zero transverse velocity and constants over the channel cross-section: mixture temperature and mass concentrations of initial reaction components, such as methane and steam. Calculations were carried out in assumption of mirror symmetry of a stationary flow relative to the middle plane of the flow, where only a half of the channel was considered. The adhesion conditions were set on the channel walls for the velocity components. The following boundary conditions were used on the wall within the reaction zone:

$$-\rho D_i \frac{\partial Y_i}{\partial v} = s_{j,i} M_i \qquad -\lambda \frac{\partial T}{\partial v} = \sum_i r_{j,i} \Delta H_i + q_w \qquad (14, 15)$$

Numerical simulations were carried out with a channel gap H = 0.5 mm for the uniform mesh with 21 nodes across the channel under different conditions of heat supply to the reacting mixture. At the methane steam reforming modeling the initial ratio of steam and methane mass fractions equals  $X_{\rm H2O}/X_{\rm CH4} = 2$ . The pressure in a microchannel is 1 bar. At the water gas shift modeling the initial mole fractions of steam, carbkon monoxide and hydrogen were 0.329; 0.096 and 0.575 respectively. In front of the reaction zone in the channel there was a region of 20-mm length for stabilization of the mixture velocity profile.

To simulate the chemical reactions at the methane steam reforming kinetic scheme and the expressions for reaction rates (Hou, Hughes 2001) were used. The reaction rate parameters correspond with experimental data (Kuznetsov et al. 2009), obtained for nanosized rhodium catalyst.

Kinetic parameters of the water gas shift reaction were determined from the experimental data (Kuznetsov et al. 2010). It was assumed that the experimental conditions correspond to model of the isothermal plug flow reactor. The pressure drop along the length of the reactor was not considered. A mathematical model of such reactor is given in (Froment, Bischoff 1990):

$$\int_{x_{in}}^{x_{out}} \frac{dx_i}{r(x_1, ..., x_n, a_1, ..., a_j, T)} = -\frac{W_{cat}}{F}$$
(16)

The equation of the reaction rate in the frame of the Langmuir-Hinshelwood model was used as a model of the mechanism of water gas shift reaction (Germani, Schuurman 2006):

$$r = \frac{k_e e^{\frac{-E_{effi}}{RT}} K_{CO} K_{H_2O} P_{CO} P_{H_2O} \left( 1 - \frac{P_{CO_2} P_{H_2}}{K_{eq} P_{CO} P_{H_2O}} \right)}{(1 + K_{CO} P_{CO} + \sqrt{K_{H_2} P_{H_2}})^2 (1 + \sqrt{K_{H_2O} P_{H_2O}} + K_{CO_2} P_{CO_2})}$$
(17)

The equation (16) was solved numerically to find the mole fraction of CO. The regression analysis was performed by the Devidon-Fletcher-Powell technique

(Fletcher, Powell 1963) with the numerical calculation of derivatives (Amosov et al.2003). Kinetic parameters obtained by processing the experimental data (Kuznetsov et al. 2010) are presented in the Table 1:

Table 1

k <sub>e</sub> (mol/kg <sub>cat</sub> )	K <sub>CO</sub>	K <sub>H2O</sub>	K <sub>H2</sub>	K <sub>CO2</sub>	E <sub>кат</sub> (kJ/mol)
5.4 10 <sup>7</sup>	157.37	358.65	433.35	2.4	66.9

### 3. RESULTS

Fig. 1 (a) shows the distribution of the methane molar fraction at the methane steam reforming over the length and width of the microchannel with heat supply flux density 2.5 kW/m². External heat flux sets of a temperature loss under the cooling of the mixture due to the endothermic reactions. Fig. 1 (b) shows the distribution of the carbon monoxide molar fraction at the water gas shift reaction over the length and width of the microchannel with wall temperature linearly decreasing along the reactor wall. Temperature changes from 480 °C to 280 °C.

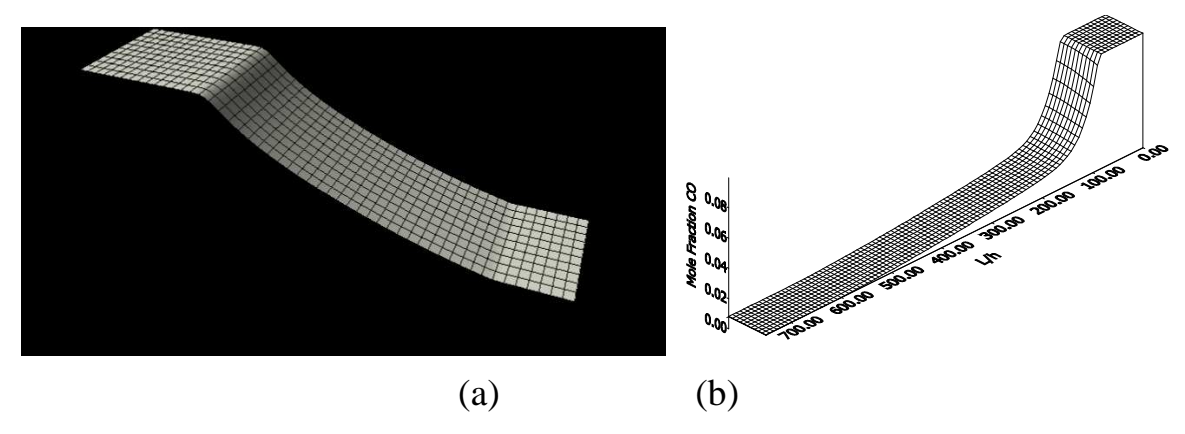


Fig. 1. The distribution of methane mole fraction at the methane steam reforming with uniform heat flux density  $2.5 \text{ kW/m}^2$  (a). The distribution of carbon monoxide mole fraction at water gas shift reaction with the temperature line-falling along the channel from  $480 \,^{\circ}\text{C}$  to  $280 \,^{\circ}\text{C}$  (b)

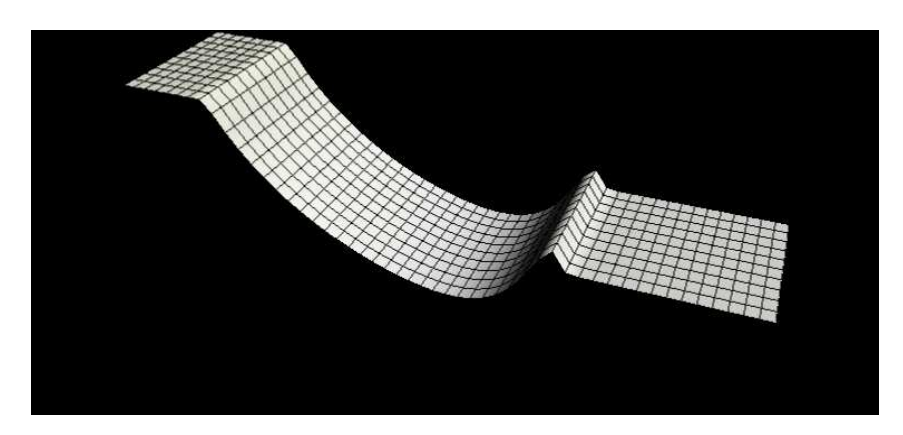


Fig. 2. The temperature of mixture over the channel width and length at heat flux 2.5  $kW/m^2$ 

The variation of the mixture components concentration at the channel cross section is negligible; it suggests the external diffusion resistance in the microchannel to be small. Diffusion processes equalize the mixture components concentration over the channel cross section and there is no need for additional mixing of the reacting mixture. The distribution of temperature along and across the microchannel is shown in Fig. 2 for the uniform external heat flux density 2.5 kW/m2. A conspicuous heating of the gas mixture occurs closer to the exit of the microchannel after the main reactions slowing down. This leads to the fact that the amount of supplied heat exceeds the amount of heat required for endothermic reactions, and heat surplus is spent for gas heating, what allows optimization of methane steam conversion not only by a change in the amount of heat supplied to the channel walls, but also by distribution of the heat flux density along the channel.

The variation of reacting mixture components mole fractions (a) along the channel are shown in Fig. 3 for the uniform and linear-falling heat fluxes with average density 3 kW/m2. It is obvious that for the heat flux, linearly falling along the channel, catalytic reactions are more intensive and the hydrogen yield is higher.

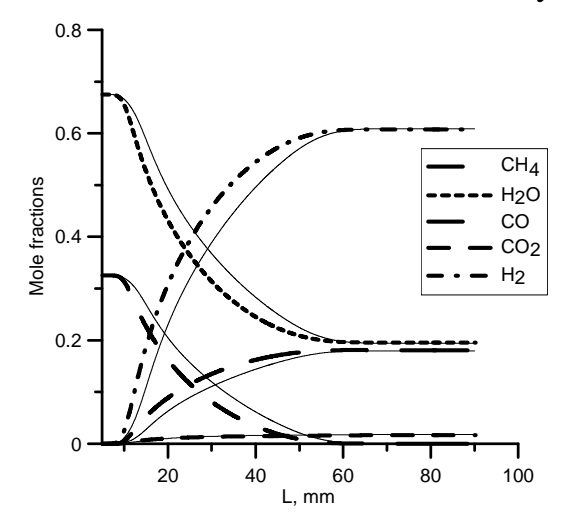


Fig. 3. The Variation of mole fraction of components at the axis of channel. The heat flux density 3 kW/m². Dashed lines – line-falling heat flux density; strong lines – uniform heat flux density

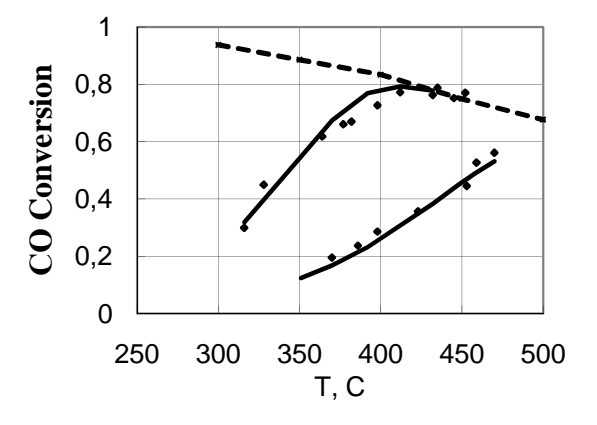


Fig. 4. A degree of CO conversion vs. the temperature of reactor: dots—experimental data, strong lines — results of numerical simulation, dashed line — the line of equilibrium conversion

The numerical simulations of water gas shift reaction in microchannel were performed to determine the conditions for increasing the yield of hydrogen in the conversion products. Fig. 4 shows a degree of CO conversion vs. temperature: dots - experimental data, solid line - numerical calculation. The peculiarity of the water gas shifts reaction is the equilibrium conversion increasing when the reaction temperature decreases - dashed line in Fig. 4. However, the rate of chemical reactions decreases significantly with the temperature decreasing. It does not allow obtaining the high conversion of carbon monoxide at low temperatures and short length of the reaction zone.

The numerical simulations of water gas shift reaction were performed in case the wall temperature linearly decreasing along the microchannel to find the optimum temperature regime. The temperature at the outlet of the reactor ranged from 350 C to 150 C on the stipulation that the inlet temperature of the mixture of the reactor 480 C,. The degree of carbon monoxide conversion depending on the output temperature of the mixture is shown in Figure 5. The monoxide concentration at the outlet is reduced to 0.8% when the output temperature is 280 C.

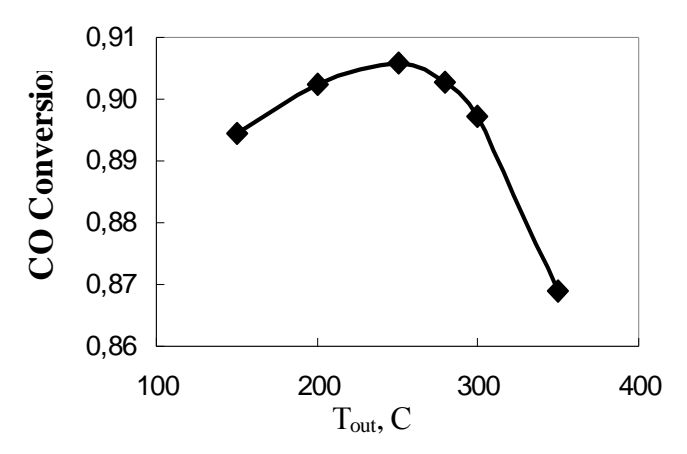


Fig. 5. A degree of CO conversion vs. outlet temperature at the constant inlet temperature 480 C

### 4. CONCLUSION

The methane steam reforming is a high endothermic process that requires the external heat supply. The results of numerical simulations provide the detailed information about the structure of the temperature and the mixture components concentration fields and the rates of chemical transformations in the microchannel. The high effective regimes of the reactor operating conditions were found. The using of microchannel technology allows improving the existing reactors and providing high conversions on the small scales. The results of numerical simulations show that diffusion processes equalize the concentrations across the microchannel. There are no diffusion limitations in microchannels with gap below 1.2 mm. Not only is important the amount of heat supplied to the reacting mixture but the distribution along the channel. The numerical simulations of the water gas shift reaction make it possible to find the reactor operating conditions with the highest carbon monoxide conversion levels.

The numerical simulations performed in case the wall temperature linearly decreasing along the microchannel has allowed enhancing the water gas shift reactor. The superior operating conditions are the following: the temperature at the outlet of the reactor is 280 C and the inlet temperature of the mixture is 480 C. The CO yield with uniform profile of temperature along the microchannel is about 2.7 % and with non-uniform temperature is about 0.8 %. So, non-uniform temperature distribution along the reactor makes it possible to combine the advantages of high-temperature and low-temperature conversions.

### **ACKNOWLEDGMENTS**

This work was supported by Rosnauka, the state contract N 02.740.11.0054 and Program of the Branch of Power Industry, Machine Building, Mechanics and Control Processes (PIMBMCP RAS), the project N 5. 4.

### **NOMENCLATURE**

Ср	[J/(kgK)]	Specific heat		
D	$[m^2/s]$	Diffusion coefficient		
h	[J/kg]	Specific enthalpy		
h0	[J/kg]	Standard enthalpy of formation		
Н	[m]	Channel height		
M	[kg/mol]	Molar weight		
P	[kPa]	Pressure		
q	$[W/m^2]$	Heat flux		
r	$[\text{mol/(m}^2\text{s})]$	Reaction rate		
R <sub>un</sub>	[J/molK]	Gas constant		
S	$[\text{mol/}(\text{m}^2\text{s})]$	Rate of component appearance (disappearance)		
T	[K]	Temperature		
U	[m/s]	Longitudinal velocity		
V	[m/s]	Transverse velocity		
X	[m]	Cartesian axis direction		
X	[-]	Mole fraction		
y	[m]	Cartesian axis direction		
Y	[-]	Mass fraction		
Gree	Greek characters			
λ	[W/mK]	Thermal conductivity		
μ	[kg/ms]	Dynamic viscosity		
ω	[s <sup>-1</sup> ]	Vorticity		
Ψ	[kg/ms]	Stream function		
ρ	[kg/m <sup>3</sup> ]	Density		
Subs	Subscripts			
0		Wall		
i		Index		
j		Index		

### **REFERENCES**

1. Amosov A.A., Dubinskyi U.A., Kopchenova N.V., 2003, Vichislitelnie metodi dlya injenerov. Moscow "MEI".

- 2. Fletcher R., Powell M.J.D., 1963, A rapidly convergent descent method for minimization, Computer J. Vol.6 N.2 pp 163–168.
- 3. Froment G.F., Bischoff K., 1990, Chemical Reactor Analysis and Design. 2nd ed. New York: Wiley.
- 4. Germani G., Schuurman Y., 2006, Water-Gas Shift Reaction Kinetics Over μ-Structured Pt/CeO2/Al2O3 Catalysts, AIChE, vol.52 No.5. pp 1806–1813.
- 5. Hou, K. H. and Hughes R., 2001, The kinetics of methane steam reforming over a Ni/ $\square$ -Al2O3 catalyst, Chem Eng Journal, Vol. 82(1–3) P. 311–328.
- 6. Kuznetsov V.V. Kozlov S.P., 2008 Modeling of methane steam reforming in a microchannel with a heat flow distributed in length, Journal of Engineering Thermophysics. Vol. 17 N. 1. pp. 53–59.
- 7. Kuznetsov V.V, Vitovsky O.V, and Gasenko O.A., 2009, Methane steam reforming in an annular microchannel with Rh/Al2O3 catalyst, Journal of Engineering Thermophysics, Vol 18, N3, PP 187–196.
- 8. Kuznetsov V.V, Vitovsky O.V, and Gasenko O.A., 2010 Upravlenie reakciyami polucheniya vodoroda pri parovoi konversii na micro i nano mashtabah., RNHTC5 2010 Moscow.
- 9. Mason E.A., Saxena S.C., 1958, Formula for the thermal conductivity of gas mictures, The Physics of Fluids, Vol. 1, 361–369.
- 10. Reid T.K. Sherwood R.C., 1966, The Properties of Gases and Liquids, New York: McGraw-Hill.
- 11. Spatenka S, Fila V, Bernauer B, Fulem J, Germani G, Schuurman Y., 2005, Modelling and simulation of microchannel catalytic WGS reactor for an automotive fuel processor, CICEQ. Vol. 11, iss. 3, pp. 143–151.
- 12. Tonkovich Anna Lee Y., Yang B, Perry S.T, Fitzgerald S.P. and Wang Y, 2007, From seconds to milliseconds to microseconds through tailored microchannel reactor design of a steam methane reformer, Catalysis Today, Vol. 120, Iss 1, P 21–29.
- 13. Vargaftik N.B.,1996, Handbook of Thermal Physical Properties of Liquids and Gases, Begell House, New York.
- 14. Wender I. 1996, Reactions of synthesis gas, Fuel Processing Technology Volume 48, Issue 3, Pages 189–297.
- 15. Wilke C.R.,1950, Viscosity equation for gas mixtures, J. Chem. Phys., Vol. 18, 517–521.

### **BIOGRAPHICAL NOTES**

- Mr. **Stanislav P. Kozlov** is PhD student at Institute of Thermophysics Siberian Branch of Russian Academy of Sciences. He is a graduate of Novosibirsk State University (2008). His research interests are concerned with the study of catalitic reactions, hydrogen production, fluid dynamics, heat and mass transfer in microchannels.
- Prof. Dr. Vladimir V. Kuznetsov is a head of Department of Engineering Thermophysics and Laboratory of Multiphase System at Institute of Thermophysics Siberian Branch of Russian Academy of Sciences. He also is Professor of Novosibirsk State University, Russia. He is a graduate of Novosibirsk State University (1972) and he was awarded PhD (1978) and DSc (1995) at Institute of

Thermophysics Siberian Branch of Russian Academy of Sciences. His current research interests are concerned with the study of capillarity, fluid dynamics, heat and mass transfer in multiphase and multi-component flows including the phase change phenomena and catalytic reactions in mini and microchannel systems. Prof. Kuznetsov has published more then 140 articles covering a variety of topics. He is Deputy Editor-in-Chief of Journal of Engineering Thermophysics.

### **CONTACTS**

Prof. Dr. Vladimir V. Kuznetsov

Kutateladze Institute of Thermophysics SB RAS 1, pr. Akademika Lavrentjeva Novosibirsk, 630090 Russian Federation Tel. +7 (383)3307121

Email: vladkuz@itp.nsc.ru

© S. Kozlov, V. Kuznetsov, 2010

# SYNTHESIS OF ZNO, ZRO2 AND WO3 NANOPARTICLES AT INTERACTION OF BULK METAL SAMPLES WITH SUB- AND SUPERCRITICAL WATER

# Anatoly A. VOSTRIKOV, Andrey V. SHISHKIN, Oxana N. FEDYAEVA and Mikhail Ya. SOKOL, Russian Federation

Key words: oxide nanoparticles, synthesis, supercritical water

### **SUMMARY**

Bulk samples of solid and liquid metals (Me: Zn, Zr, W) were oxidized by suband supercritical water with formation of nanodimensional crystals with various morphology: hexagonal ZnO nanoparticles, nanowhiskers; monoclinic ZrO<sub>2</sub> nanoparticles; monoclinic WO<sub>3</sub> nanowiskers. At synthesys the flow and batch reactors were used. In experiments we measured temperature T and pressure in the reactor, reagent composition and parameters of synthesized samples. The cluster mechanism of MeO<sub>x</sub> nanoparticles formation is offered. Using quantities measured in experiment, the change of H<sub>2</sub> amounts from T and time t:  $n_{H2}(T, t)$  is determined. At calculations we took into account the nonideality of mixing in H<sub>2</sub>O-H<sub>2</sub> system. On the basis of  $n_{\rm H2}(T, t)$  curves the kinetics parameters of Me oxidizing by water were calculated. Synthesized samples were studied by scanning and transmission electron microscopy with EDX spectrometer, BET method, electron and X-ray diffraction. The photoluminescence of ZnO samples was investigated. Carried out researches have shown an opportunity of making of new technologies of nanodimensional crystals synthesis with the given properties and the formation of nanostructured materials, in particular cermets, on the basis of an oxidizing of metals by sub- and supercritical water.

### **АННОТАЦИЯ**

Массивные образцы твердых и жидких металлов (Me: Zn, Zr, W) были окислены суб- и сверхкритической водой с образованием наноразмерных кристаллов различной морфологии: наночастицы и наноусы гексагонального ZnO; наночастицы моноклинного ZrO<sub>2</sub>; наноусы моноклинного WO<sub>3</sub>. При синтезе использованы реакторы проточного и периодического действия. В экспериментах измерялись температура T и давление в реакторе, состав реагентов и параметры полученных образцов. Предложен кластерный механизм образования наночастиц. Используя измеренные в экспериментах величины, было определено изменение количества  $H_2$  от T и времени t:  $n_{H2}(T, t)$ . При вычислениях учитывалась неидеальность взаимодействия в системе Н<sub>2</sub>О-Н<sub>2</sub>. На основе кривых  $n_{\rm H2}(T,\ t)$  были вычислены кинетические параметры окисления Ме водой. Синтезированные образцы были исследованы на сканирующем и просвечивающем электронных микроскопах, оборудованных спектрометром, методом БЭТ, электронным и рентгеновским дифрактометрами. Исследована фотолюминесценция образцов ZnO. Проведенные исследования

показывают возможность создания новых технологий синтеза наноразмерных кристаллов с заданными свойствами и образования наноструктурированных материалов, в частности керметов, на основе окисления металлов суб- и сверхкритической водой.

### 1. INTRODUCTION

The prospects of ZnO application is first of all related in optoelectronics due to the wide band gap ( $E_g \approx 3.37$  eV, at 25 °C) and high energy of excitons ~60 meV [Özgür 2005]. Photoelectric properties of nanodimensional ZnO samples serve a basis for various photoemission devices [Huang 2001], photosensors and phototransistors [Fan 2004], frontal layers of plasma display panels [Yoon 2007].

Using ZnO nanorods as a component of field-effect transistor the higher coefficient of switching up to 10<sup>6</sup> can be obtained [Kim 2006]. Perspectives of ZnO application as highly sensitive element in sound vibration generators and receivers are based on the higher value of effective piezoelectric module d<sub>33</sub> in nanodimensional template (2.7 times compare to bulk single-crystal) [Zhao 2004]. Varistors obtained by means of sintering of nanocrystal ZnO, show puncture potential 1.7 times higher compare to industrial disk ones [Pillai 2003]. Strong dependence of electric conductivity of ZnO from surface electronic states at molecular adsorption serves to the development of highly effective gas and vapor sensors: H<sub>2</sub>, dimethylamin [Roy 2002], ethanol [Chen 2006], NH<sub>3</sub>, CO [Wang 2006], H<sub>2</sub>S, CH<sub>2</sub>O, liquefied petroleum gas, gasoline [Xu 2006] on the basis of ZnO nanoparticles. Use of nanostructured ZnO for catalysts development (for example, Cu/ZnO, applied for methanol synthesis [Ertl 1997]) can improve their catalytic properties for example by active centers stabilization [Khassin 2006].

Nanocrystalline zirconia has attracted considerable attention because of its diverse practical applications in fuel-cell technology as electrolyte membranes [Xin 2007], its use as Ni/ZrO<sub>2</sub> catalyst for hydrogen production [Yan 2009], and its use as oxygen and ethanol sensor [Tan 2004].

Tungsten trioxide is an indirect-gap semiconductor. Nanodimensional WO<sub>3</sub> has the strong photoluminescence [Feng 2005], that is unusual for massive samples. Electrochemical properties of WO<sub>3</sub> allow using it as the positive electrode in recharged lithium batteries [Huang 2008]. Nanoparticles of WO<sub>3</sub> used as a sensitive element of gas and vapor sensors: ethanol, methanol, 1-buthanol, NO<sub>2</sub>, NO, NH<sub>3</sub>, CO, H<sub>2</sub>S, acetone, formaldehyde, benzene, moisture [Cao 2009, Chen 2010, Ho 2003, Li 1996, Li 2006, Shen 2009, Solis 2001, Xu 2008]. The gas- and electrochromic effect of WO<sub>3</sub> has important applications in energy savings, for example, in a smart window [Luo 2009] and flexible electrochromic devices [White 2009]. Nanocrystalline WO<sub>3</sub> shows enhanced photocatalytic activity for organic substances decomposition under visible light [Sadakane 2008].

To receive nanodimensional ZnO, ZrO<sub>2</sub> and WO<sub>3</sub> structures various methods are used. The easiest is gas-phase methods based on chemical vapor deposition (CVD) at oxidation of metal vapor or metal organic compound in current or atmosphere with oxygen-containing gas [Zhang 2006, Codato 1999, Cao 2009, Solis 2001]. To decrease the temperature of the generation process of nanostructured ZnO, ZrO<sub>2</sub>,

WO<sub>3</sub> various solution methods are widely used [Sun 2005, Caracoche 2009, Wang 2009].

Hydrothermal synthesis has become widespread since included various technologies of crystal generation in water solutions with high temperature at high pressure. Most often researchers use "soft" option of hydrothermal synthesis (T < 523 K). As a rule, water solutions of inorganic and organic salts of metal are used as a source of Zn, Zr, W. Choice of metal precursor, temperature regimen and time of growth, surfactants and reactionary agents determine morphology of growing nanocrystalline metal oxides and synthesis time [Wei 2007, Kumari 2008, Shen 2009, Xu 2008].

In the area of sub- and supercritical water parameters properties (density, dielectric penetrability, ionic product of water, and structure of hydrogen bonds) significantly change [Wagner 2002]. As a result sub- and supercritical water can be used as a solvent, reagent and catalyst. High density of water and high temperatures serve to decrease synthesis time to several minutes and even fractions of a second that makes possible the use of flow reactors for synthesis [Sue 2003, Hayashi 2009]. At the reaction of sub- and supercritical water with bulk samples of bulk zinc, aluminum free of extra additions and reagents we have found out fast forming nanoparticles of ZnO,  $Al_2O_3$  [Vostrikov 2009a, Vostrikov 2010]. This paper presents results of ZnO,  $ZrO_2$  and  $WO_3$  nanoparticles production at bulk metal samples oxidizing by sub- and supercritical  $H_2O$  and characterization of samples.

### 2. EXPERIMENTAL

The principal scheme of the experimental setup with flow or batch reactors and procedure of experiments are described in [Vostrikov 2009a]. In experiments we measured temperature T and pressure P in the reactor, reagent composition and parameters of synthesized samples. Pressure was measured by the membrane strain gauges and written digitally; the temperature was measured by the chromel-alumel thermocouples. The reactor and preheaters were heated by the outer ohmic heaters with temperature programming. Metal (Me) samples were prepared by zinc, zirconium, tungsten of a high-purity grade, and prior to be loaded into the reactor they were cleaned mechanically from oxide film, which impeded (MeO<sub>x</sub>)<sub>n</sub> synthesis at oxidizing [Vostrikov 2009a, b]. Zinc samples were plates of ~2-mm thickness, zirconium samples were plates of 0.1 mm thickness, and tungsten samples were plates of ~2-mm thickness or semicylinders of 5 mm diameter.

Experiments carried out in isothermal and nonisothermal technique. At nonisothermal technique cell with metal and cell with water were loaded into reactor at room temperature and inert atmosphere, and further reactor heated with rate 2 K/min up to 1020 K. Such technique allows determining the initial temperature of appreciable oxidizing at selected rate of heating. The pressure of water fluid of reactor reached up to 54 MPa.

At isothermal technique cell with metal were loaded into reactor at room temperature and inert atmosphere. Preheater filled by water completely. Further reactor and preheater divided by valve are heated up to given temperature (up to 1020)

K). At supporting of given pressure in preheater the surplus of water let out. After achievement of given temperature the valve was opened and water fluid (or vapour at  $T < T_c$ ) injected to reactor. The pressure in reactor and preheater was aligned the valve was closed. Experiments carried out at water pressure up to 35 MPa. To determine the amount of  $Me_xO_y$ , we used the results of weighting of a metal comprising cell before and after the experiment.

The structure and elementary composition of synthesized samples of  $(MeO_x)_n$  were analyzed by the transmission electron microscopes (TEM) of high resolution JEM-2010, equipped by the energy dispersive X-ray analyzer (EDX) with energy resolution not lower than 130 eV, and scanning electron microscopes (SEM) JSM-6700F (with EDX system), LEO 420. Also structural characterization was conducted using X-ray diffraction (ThermoARL X-ray diffractometer).

Photoluminescence (PL) measurements of ZnO were carried out on the basis of an open architecture unit [Sorokin 2001] in the scheme designed similar to [Rastorguev 2007]. A 250 W hydrogen lamp was used as the radiation source. The lamplight was filtered by a monochromator, and the excitation line with wavelength of 365 nm (3.4 eV) was extracted. Then the radiation was focused on the sample. The PL radiation was analyzed by another monochromator of the same type, and then proceeded to a multialkali photocathode low-noise photomultiplier (PhEU-100). Further the reinforced signal was transmitted to a computer. During PL-spectra scanning the breadth of slots was fixed and provided resolution less than 3 Å. The spectra were recorded at room temperature in air without any correction for spectral response of a registering section. The choice of a procedure was conditioned by separation of exciton band ( $\lambda \approx 393$  nm) specific for ZnO and reacting to crystalline perfection of a sample.

Samples of ZnO were studied by the BET method from isotherms of nitrogen absorption.

### 3. RESULTS AND DISCUSSION

Reaction between bulk metal and water fluid (or vapour) may be described by equation

$$Me + xnH_2O = Me \cdot (MeO_x)_n + xnH_2.$$
 (1)

The cluster mechanism of  $(MeO_x)_n$  nanoparticles formation on ZnO example is offered in [Vostrikov 2009a]. Using quantities measured in experiment, the change of  $H_2$  amounts from T and time t: amount of  $H_2$  mole  $n_{H2}(T, t)$  is determined. At calculations we took into account the nonideality of mixing in  $H_2O-H_2$  system. On the basis of  $n_{H2}(T, t)$  curves the kinetics parameters of Me oxidizing by water was calculated.

At assumption of first order of reaction (1) and Arrhenius dependence for reaction rate constant

$$k = k_0 \exp(-E / RT), \tag{2}$$

Where: E is activation energy, R is universal gas constant, we have kinetic equation

$$dn_{H2} / dt = n_w v_w (S / V_{R,f}) k_0 exp[-E / RT],$$
 (3)

Where:  $n_w$  is amount of  $H_2O$  mole in reactor,  $v_w$  is average thermal speed of water molecules, S is initial surface of metal sample,  $V_{R,f}$  is volume of reactor free for gas and water fluid. Calculation shows at T=973 K the effective rate constant k of oxidizing reaction grows in series W, Zr, Zn. Activation energy E for studied metals grows in series W, Zn, Zr.

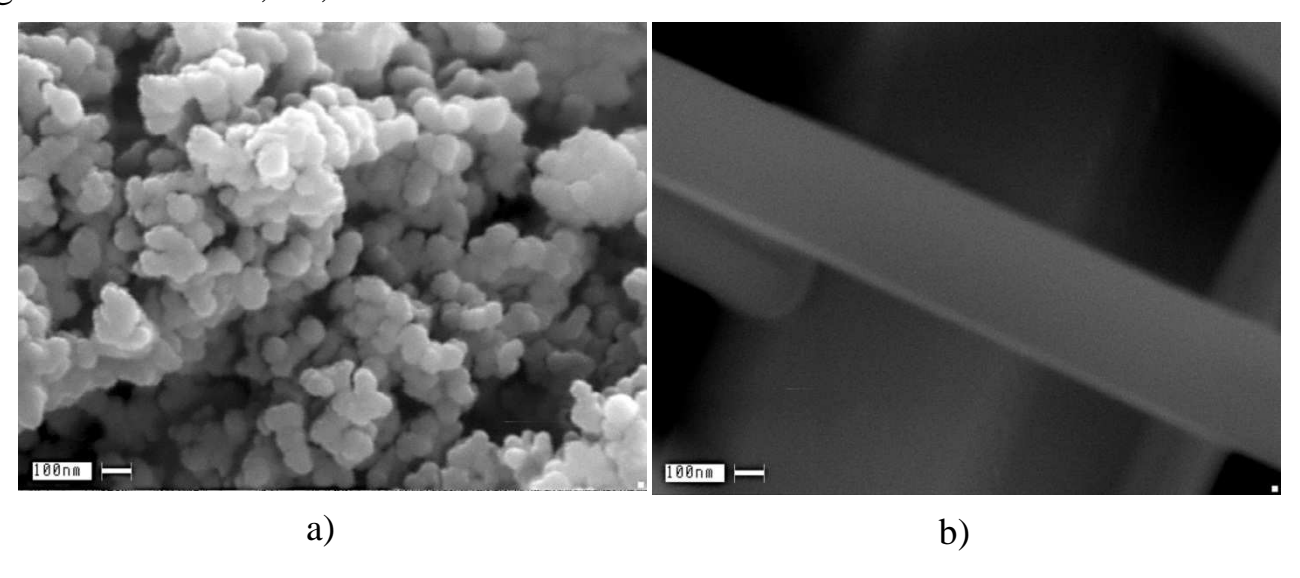


Fig. 1. SEM (LEO 420) images of ZnO nanocrystals: a) nanoparticles formed at 1020 K; b) nanorods formed at 520 K

Electron microscope study shows:

- Formation ZnO nanoparticles with the size of 2–100 nm, nanorods and nanowhiskers with the diameter of 10–100 nm and length up to 50  $\mu$ m, Fig. 1;
  - Formation ZrO<sub>2</sub> nanoparticles with the sizes of 4–100 nm, Fig. 2;
- $-\,$  Formation WO  $_{\!3}$  nanorods with the diameter of about 15 nm and length up to 1  $\mu m,$  Fig. 3.

Measurements of interfacial distance, carried out with application of 2D Fourier transformation [Vostrikov 2009b], showed formation of hexagonal ZnO (see JCPDS card 36-0101). X-ray diffraction study of product of oxidizing of Zr and W by supercritical water showed formation of monoclinic ZrO<sub>2</sub> (see JCPDS card 37-1484) and monoclinic WO<sub>3</sub> (see JCPDS card 43-1035) respectively.

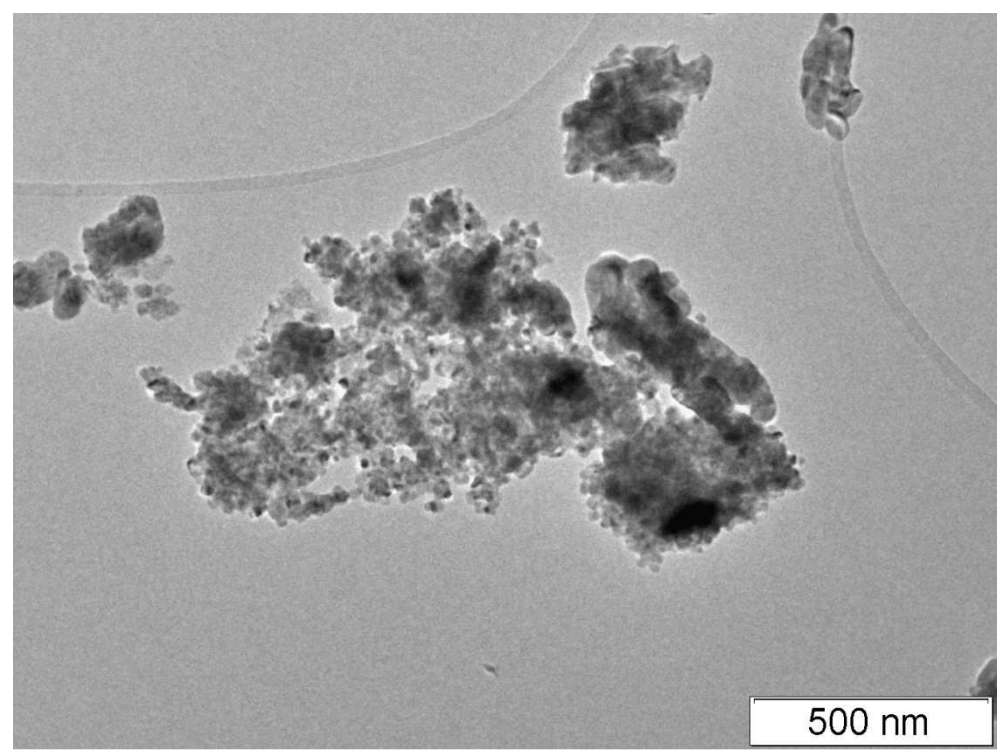


Fig. 2. TEM images of ZrO<sub>2</sub> nanoparticles formed at 870 K

Synthesized by us ZnO nanoparticles can have a higher catalytic activity: a specific area of  $(ZnO)_n$  samples, determined by the BET method from isotherms of nitrogen absorption at 77 K, was  $10.0\pm0.5$  m<sup>2</sup>/g, and for industrial ZnO with the average size of particles of  $300\pm50$  nm it did not exceed  $4.9\pm0.4$  m<sup>2</sup>/g.

PL study of different samples demonstrates that PL-spectra of ZnO nanostructures are sensible to the shape of particles, their size, temperature and method of formation [Vostrikov 2009b]. Comparing spectra and average size of nanoparticles in the samples we can conclude that in the range of 60 - 300 nm impact of the average particle onto PL spectrum is inessential. Impact of the crystal shape is more significant. Narrower radiation spectrum (only green band of the spectrum) belongs to ZnO sample with nanoparticles and flat nanowhiskers. Samples with ZnO nanoparticles only showed PL in widest interval of the visible diapason.

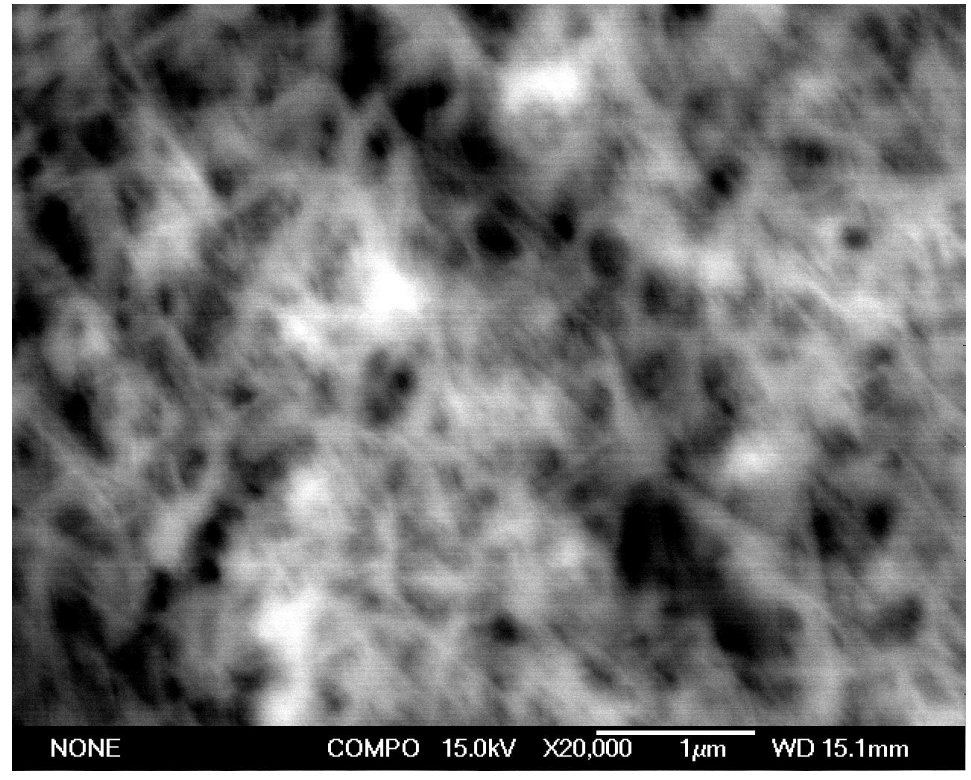


Fig. 3. SEM (JSM-6700F) images of WO<sub>3</sub> nanoparticles formed at 870 K

### 4. CONCLUSION

Carried out researches have shown nanodimensional crystals synthesis on the basis of an oxidizing of bulk metals by sub- and supercritical water. Characterization of oxide nanocrystals have directed that its properties depend on morphology and hence they depend on conditions of synthesis. The properties of water significantly change in sub- and subcritical field of temperature and pressure. So we can to create new nanostructural materials with given properties finely operating by parameters of synthesis.

#### **ACKNOWLEDGEMENTS**

The authors thank V.I. Zaikovskii, V.S. Danilovich for the electron-microscopic analysis of samples, S.V. Tsybulya for X-ray diffraction analysis, and A.A. Rastorguev for analysis of photoluminescence.

This work was supported by the Russian Foundation for Basic Research (Grant No. 09-08-00206) and Presidium of the Russian Academy of Sciences (Grant 13.8).

#### **REFERENCES**

Caracoche, M C, Martínez, J A, Rivas, P C, et al., 2009, Short range investigation of sub-micron zirconia particles, Journal of Physics: Conference Series., 167, 12041(1)–012041(5).

Cao, B B, Chen, J J, Tang, X J, Zhou, W L, 2009, Growth of monoclinic  $WO_3$  nanowire array for highly sensitive  $NO_2$  detection, J. Mater. Chem., 19, 2323–2327.

Chen, D L, Hou, X X, Wen, H J, et al., 2010, The enhanced alcohol-sensing response of ultrathin WO<sub>3</sub> nanoplates, Nanotechnol., 21, 035501(1)–035501(12).

- Chen, Y, Zhu, C L, Xiao, G, 2006, Reduced-temperature ethanol sensing characteristics of flower-like ZnO nanorods synthesized by a sonochemical method, Nanotechnology, 17, 4537–4541.
- Codato, S, Carta, G, Rossetto, G, 1999, Chem. MOCVD growth and characterization of ZrO<sub>2</sub> thin films obtained from unusual organo-zirconium precursors, Vapor Depos., 5, 159–164.
- Ertl, G, Knözinger, H, Weitkamp, J, (Eds.), 1997, Handbook of heterogeneous catalysis, Vol. 4, Weinheim, Wiley-VHC, 1856.
- Fan, Z, Chang, P, Lu, J G, et al., 2004, Photoluminescence and polarized photodetection of single ZnO nanowires, Appl. Phys. Lett., 85, 6128–6130.
- Feng, M, Pan, A L, Zhang, H R, et al., 2005, Strong photoluminescence of nanostructured crystalline tungsten oxide thin films, Appl. Phys. Lett., 86, 141901(1)–141901(3).
- Hayashi, H, Ueda, A, Suino, A, Hakuta, Y, 2009, Hydrothermal synthesis of yttria stabilized ZrO<sub>2</sub> nanoparticles in subcritical and supercritical water using a flow reaction system, J. Sol. State Chem., 182, 2985–2990.
- Ho, J-J, 2003, Novel nitrogen monoxides (NO) gas sensors integrated with tungsten trioxide (WO<sub>3</sub>)/pin structure for room temperature operation, Solid-State Electronics, 47, 827-830.
- Huang, M H, Mao, S, Feick, H, et al., 2001, Room-temperature ultraviolet nanowire nanolasers, *Science*, 292, 1897–1899.
- Huang, K, Pan, Q, Yang, F, et al., 2008, Controllable synthesis of hexagonal WO<sub>3</sub> nanostructures and their application in lithium batteries, J. Phys. D: Appl. Phys., 41, 155417(1)–155417(6).
- Khassin A A, Pelipenko V V, Minyukova T P, et el., 2006, Planar defect of the nano-structured zinc oxide as the site for stabilization of the copper active species in Cu/ZnO catalysts, Catalysis Today, 112, 143–147.
- Kim, H-J, Lee, C-H, Kim, D-W, Yi, G-C, 2006, Fabrication and electrical characteristics of dual-gate ZnO nanorod metal-oxide semiconductor field-effect transistors, Nanotechnology, 17, S327–S331.
- Kumari, L, Li, W, Wang, D, 2008, Monoclinic zirconium oxide nanostructures synthesized by a hydrothermal route, Nanotechnology, 19, 195602(1)–195602(7).
- Li, X, Zhang, G, Cheng, F, et al., 2006, Synthesis, characterization, and gassensor application of WO<sub>3</sub> nanocuboids, J. Electrochem. Soc., 153, H133–H137.
- Li, Y J, Tsai, P P, 1996, Lacunar pyrochlore-type tungsten oxides as humidity-sensing materials, Solid State Ionics, 86–88, 1001–1004.
- Luo, J Y, Deng, S Z, Tao, Y T, et al., 2009, Evidence of localized later molecules and their role in the gasochromic effect of  $WO_3$  nanowire films, J. Phys. Chem. C., 113, 15877–15881.
- Özgür, Ü, Alivov, Ya I, Liu, C, et al., 2005, A comprehensive review of ZnO materials and devices, J. Appl. Phys., 98, 041301(1)–041301(103).
- Pillai, S C, Kelly, J M, McCormack, D E, et al., 2003, The effect of processing conditions on varistors prepared from nanocrystalline ZnO, J. Mater. Chem., 13, 2586–2590.

- Rastorguev, A A, Belyi, V I, Smirnova, T P, et al., 2007, Luminescence of intrinsic and extrinsic defects in hafnium oxide films, Phys. Rev. B., 76, 235315(1)–235315(6).
- Roy, S, Basu, S, 2002, Improved zinc oxide film for gas sensor applications, Bull. Mater. Sci., 25, 513–515.
- Sadakane, M, Sasaki, K, Kunioku, H, et al., 2008, Preparation of nano-structured crystalline tungsten(VI) oxide and enhanced photocatalytic activity for decomposition of organic compounds under visible light irradiation, Chem. Commun., N 48, 6552–6554.
- Shen, X P, Wang, G X, Wexler, D, 2009, Large-scale synthesis and gas sensing application of vertically aligned and double-sided tungsten oxide nanorod arrays, Sensor. Actuator. B Chem., 143, 325–332.
- Solis, J L, Saukko, S, Kish, L, et al., 2001, Semiconductor gas sensors based on nanostructured tungsten oxide, Thin Solid Films, 391, 255–260.
- Sorokin, A M, Kaichev, V V, Timoshin, A I, et al., 2001, A Multipurpose UV-visible spectroscopic system, Instrum. Exp. Tech., 44, 375–380.
- Sue, K, Murata, K, Kimura, K, Arai, K, 2003, Continuous synthesis of zinc oxide nanoparticles in supercritical water, Green Chemistry, 5, 659–662.
- Sun, B, Sirringhaus, H, 2005, Solution-processed zinc oxide field-effect transistors based on self-assembly of colloidal nanorods, Nano Lett., 5, 2408–2413.
- Tan, O K, Cao W, Hu Y, Zhu W, 2004, Nanostructured oxides by high-energy ball milling technique: Application and gas sensing materials, Solid State Ionics, 172, 309–316.
- Vostrikov, A A, Fedyaeva, O N, Shishkin, A V, Sokol, M Ya, 2009a, ZnO nanoparticles formation by reactions of bulk Zn with H<sub>2</sub>O and CO<sub>2</sub> at sub- and supercritical conditions. I. Mechanism and kinetics of reactions, J. Supercrit. Fluids, 48, 154–160.
- Vostrikov, A A, Fedyaeva, O N, Shishkin, A V, Sokol, M Ya, 2009b, ZnO nanoparticles formation by reactions of bulk Zn with  $H_2O$  and  $CO_2$  at sub- and supercritical conditions. II. Morphology and properties of nanoparticles, J. Supercrit. Fluids, 48, 161–166.
- Vostrikov, A A, Fedyaeva, O N, Fadeeva, I I, Sokol, M Ya, 2010, Formation of Al<sub>2</sub>O<sub>3</sub> nanoparticles at oxidizing of aluminium by water at sub- and supercritical parameters, Supercrit. Fluids: Theory and Practice, 5(1), 48–61.
- Wagner, W, Prub, A, 2002, The IAPWS formulation 1995 for the thermodynamic properties of ordinary water substance for general and scientific use, J. Phys. Chem. Ref. Data, 31, 387–535.
- Wang, J M, Lee, P S, Ma, J, 2009, Synthesis, growth mechanism and room-temperature blue luminescence emission of uniform WO<sub>3</sub> nanosheets with W as starting material, J. Cryst. Growth. 311, 316–319.
- Wang, J X, Sun, X W, Yang, Y, et al, 2006, Hydrothermally grown oriented ZnO nanorod arrays for gas sensing applications, Nanotechnology, 17, 4995–4998.
- Wei, M, Qi, Z, Ichihara, M, et al., 2007, Single-crystal ZnO nanorods fabricated with different end morphologies, Nanotechnology, 18, 095608(1)–095608(7).

White, C M, Gillaspie, D T, Whitney E, et al., 2009, Flexible electrochromic devices based on crystalline WO<sub>3</sub> nanostructures produced with hot-wire chemical vapor deposition, Thin Solid Films., 517, 3596–3599.

Xin X, Lu Z, Zhu Q, et al., 2007, Fabrication of dense YSZ electrolyte membranes by a modified drypressing using nanocrystalline powders, J. Mater. Chem., V17, 1627–1630.

Xu, J, Chen, Y, Chen, D, Shen, J, 2006, Hydrothermal synthesis and gas sensing characters of ZnO nanorods, Sensors and Actuators B, 113, 526–531.

Xu, Y X, Tang, Z.L, Zhang, Z T, et al., 2008, Large-scale hydrothermal synthesis of tungsten trioxide nanowires and their gas sensing properties, Sens. Lett., 6, 938–941.

Yan, B, Wu, J, Xie, C, et al., 2009, Supercritical water gasification with Ni/ZrO<sub>2</sub> catalyst for hydrogen production from model wastewater of polyethylene glycol, J. Supercrit. Fluids, 50, 155–161.

Yoon, S-H, Yang, H, Kim, Y-S, 2007, Ordered growth of ZnO nanorods for fabrication of a hybrid plasma display panel, Nanotechnology, 18, 205608(1)–205608(5).

Zhang, X N, Li, C R, Zhang, Z, 2006, Controlling the growth direction of one-dimensional ZnO nanostructures by changing the oxygen content in the reaction atmosphere, Appl. Phys. A. Mat. Sci. Process., 82, 33–37.

Zhao, M-H, Wang, Z-L, Mao, S X, 2004, Piezoelectric characterization of individual zinc oxide nanobelt probed by piezoresponse force microscope, Nano Lett., 4, 587–590.

### **CONTACTS**

## Prof. Anatoly A. Vostrikov

Kutateladze Institute of Thermophysics SB RAS

1, Lavrentyev av.

Novosibirsk, 630090

**Russian Federation** 

Tel. +7 383 3308094

Fax +7 383 3308480

Email: vostrikov@itp.nsc.ru Web site: http://www.itp.nsc.ru

© A.A. Vostrikov, A.V. Shishkin, O.N. Fedyaeva, M.Ya. Sokol, 2010

# FLOW BOILING HEAT TRANSFER OF REFRIGERANT IN MINI AND MICRO CHANNELS

# Alisher SHAMIRZAEV, Vladimir KUZNETSOV, Stanislav KOZLOV, Russian Federation

### **Summary**

Liquid flow boiling in mini and microchannels is characterized by determining the influence of the effects of constraint on the flow regime and heat transfer. This paper considers heat transfer in boiling of refrigerant R21 in a rectangular minichannel with cross section 1.6x6.3 mm and in the assembly of microchannels - 0.64x205 mm in the range of mass velocities from 33 to 230 kg/m2s and heat flux up to 160 kW/m2, the reduced pressure from 0.03 to 0.07 and the vapor quality from 0 to 1. The experiments were conducted at initial underheating and given initial vapor quality at the entrance to the channel. The data on local heat transfer coefficients, including in crisis mode of heat transfer was obtained. A comparison of experimental data with known models of heat transfer during liquid flowboiling in mini and microchannels was done. The modification of models for calculation heat transfer at liquid flow boiling was offered.

### **Summary**

Кипение движущейся жидкости в мини и микроканалах характеризуется определяющим влиянием эффектов стесненности на режим течения и теплообмена. В данной работе рассмотрен теплообмен при кипении хладона R21 в прямоугольном миниканале с зазором 1.6х6.3 мм и в сборке микроканалов 0.6х2 мм в диапазоне массовых скоростей от 33 до 230 кг/м2с и тепловых потоков до 160 кВт/м2, приведенного давления от 0.03 до 0.07 и паросодержания от 0 до 1. Опыты проведены при начальном недогреве и заданном начальном паросодержании на входе в канал. Получены данные по структуре течения и локальным коэффициентам теплоотдачи, в том числе в режиме кризиса теплообмена. Проведено сравнение экспериментальных данных с известными моделями теплообмена при кипении движущейся жидкости в мини и микроканалах, предложена их модификация.

### 1. INTRODUCTION

Heat transfer at the flow boiling in microchannels is widely studied since it has the high efficiency for cooling of electronic components (**Bar-Cohen, Rahim**, 2007) and for application in energy industry potentially. The ratio of the heat transfer surface to the micro channel's volume increases in inverse proportion to the diameter of the channel which causes the high intensity of heat transfer in the mini and microchannels devises.

Despite the considerable number of works performed in the fluid flowboiling in channels of small size, the data of these experimental studies rather contradictory. In (**Steinke, Kandlikar**, 2004), (**Kuznetsov, Shamirzaev**, 2007a), the microchannels in

the heat transfer coefficients in boiling depend mainly on the heat flux and pressure. In (**Kuznetsov**, **Shamirzaev**, 2007b), (**Dong et al**, 2008) shows that for minichannels systems contribute to the nucleate boiling heat transfer is not determinative, the heat transfer coefficients increase with increasing velocity and steam content, and influence of the heat flux is small.

The aim of this work is to conduct systematic studies of heat transfer during boiling of a moving R21 refrigerant in a rectangular minichannel and in microchannel heat exchanger. The use of channels in two sizes possible to distinguish the influence of the channel's size on heat transfer, to investigate the mechanism of heat transfer in these circumstances, to verify existing models for calculating heat transfer during boiling of a moving fluid in confined space and propose their development.

### 2. EXPERIMENTAL APPARATUS AND METHODS

Scheme of the experimental setup used to study the heat transfer at the flow boiling in a rectangular minichannel is presented in (**Kuznetsov**, **Shamirzaev**, 2007b). The thin-walled rectangular minichannel heated with the alternating electric current was made by pressing a stainless tube with diameter of 5mm, wall thickness of 0.1 mm and length of 350 mm. The rectangular cross-section of minichannel is 1.6x6.3 mm. The length of the minichannel rectangular section is 250 mm. The rectangular section of the channel is installed in a vertical way. The wall roughness is about of 5 microns. T-type thermocouples are glued in 4 sections of the channel on the outer surface. It make possible to measure the heat transfer coefficient distribution on the perimeter of the channel.

Scheme of the experimental setups used to study the heat transfer at the flow boiling in a microchannel heat exchanger is shown in Fig. 1. The Freon from condenser is fed through a filter and the flow controller Bronkhorst HI-TECH via the pump. Then it goes through the thermostat and enters into the evaporator to make liquid-vapor mixture flow with defined vapor quality. The flow from the evaporator enters into an experimental test section and then into the condenser. Fluid flow rate was determined by the flow controller with an accuracy of 0.022 g/sec.

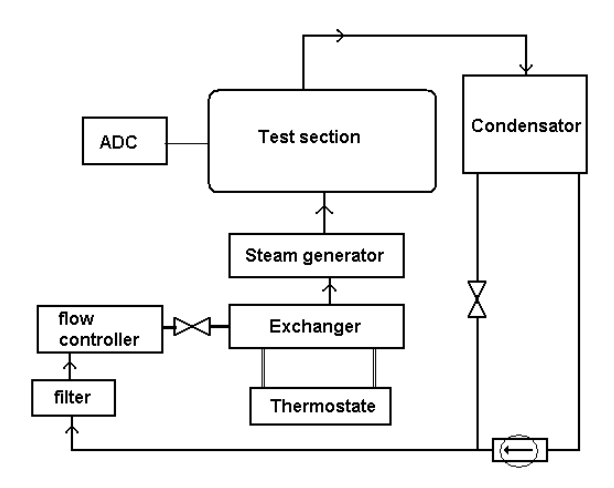


Fig. 1. Scheme of the experimental stand

Microchannel plate of the experimental test section is made by the stainless steel milling, Fig. 2 (a). It has 10 microchannels of width 640 mm, hydraulic diameter of 0.975 mm, 1.15 mm thickness of the ribs, the distance from the outer wall to the base of the ribs is 2.4 mm. 14 T-type thermocouples are embedded to a depth of 0.6 mm into the wall at the seven sections along the length of the heat exchanger to measure the temperature of the wall. Thermocouples are installed at the 5, 30, 55, 65, 90, 110 and 115 mm from the beginning of the channels.

Two insulated K-type thermocouples are installed at the inlet and outlet chamber to measure the input and output temperature of the flow. The evaporator at the entrance of the experimental site defines the initial vapor quality regardless of the value of the heat flux supplied to the heat exchanger. The heat supply to the heat-exchanger is realized on the one side of the exchanger via the copper block with mounted heat-cartridges, Fig.2 (b). Second copper block compensates the heat loss. The Size of blocks is 130x60x25 mm. The maximum power is 380W.

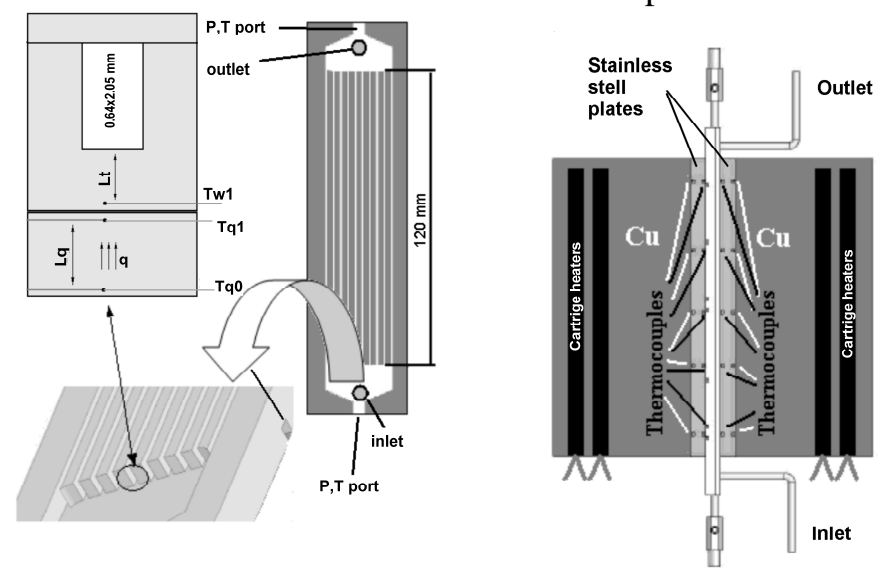


Fig. 2. Scheme of the experimental test section

During the experiment, there is a continuous survey of temperature and is determined by the standard deviation of each temperature on the five dimensions. Complete cycle of 5 measurements takes 50 seconds. The regime is established, when measured by the drift of the average wall temperature does not exceed 0,1 K within fifteen minutes. The field of temperatures in experimental set up has been registered during 15-20 minutes after stabilization of flow. Thermocouple K and T types calibrated together by a platinum resistance thermometer Pt-100 (ATA-2210) in the temperature range from 15 to 100 C, the error in measuring the temperature does not exceed 0.1 K.

The measured local overall heat transfer coefficient is defined as:

$$K_{j} = q_{w,j} / (T_{w,j} - T_{sat,j})$$
 (1)

Where: Tsat, j – saturation temperature corresponding to the given thermocouple, Tw, j – external wall temperature microchannel plate, determined from the measured temperature, taking into account the temperature gradient in the wall, qw, j – a local

heat flux. Pressure distribution along the length of the microchannel was determined by linear approximation of the measured input and output values. Local heat flux was determined by measuring the temperature gradient at the plate

$$q_{w,i} = \lambda_w (\Delta T_{w,i} / L_{q,i}) \tag{2}$$

# 3. REFRIGERANT FLOW BOILING HEAT TRANSFER IN MINICHANNEL

### 3.1 Structure of flow

The fluid flow boiling in confined space was characterized by a significant influence of capillary forces on the structure of the flow. Carried out flow visualization revealed a fundamentally different flow regime for the Weber number is smaller and much larger than one, which varies with the pressure and mass velocity.

At high mass velocities and pressures shown are typical plug flow with intensive boiling of liquid in the liquid plug and annular flow (**Kuznetsov**, **Shamirzaev**, 2007a). The fundamentally different character is the boiling of refrigerant at low speeds and low pressures shown in Fig. 3. Characteristic flow regimes here are for large bubbles, slug and annular flow regimes with a significant liquid flow in the corners of the channel.



Fig. 3. Flow boiling regime in a rectangular channel, Refrigerant 11

### 3.2 Flow boiling heat transfer in minichannel

Fig. 4 shows the experimental data on the dependence of the coefficient of heat transfer during boiling of refrigerant 21 in rectangular mini-channel 1.6x6.3 mm with a mass velocity of 220 kg/m2s. It was found that up to the heat flux is equal to 30 kW/m² the crisis of heat transfer at the exit of channel is not observed and the complete evaporation of liquid in the channel may occur. Heat transfer coefficients depend only weakly on the density of heat flux and the predominant mechanism of heat transfer is a two-phase forced convection. Lines in Fig. 4 are shows calculations by model from (**Liu, Winterton,** 1991) which was modified in (**Kuznetsov, Shamirzaev**, 2007a, 2007b) and by model from (**Balasubramanian, Kandlikar**, 2004). A modified model of Liu & Winterton best describes the experimental data with the mass velocity 220 kg/m²s.

 $q{\sim}\{27\text{-}33\}~kW/m^2$  , R21, G={208-230} kg/m^2s, upflow.

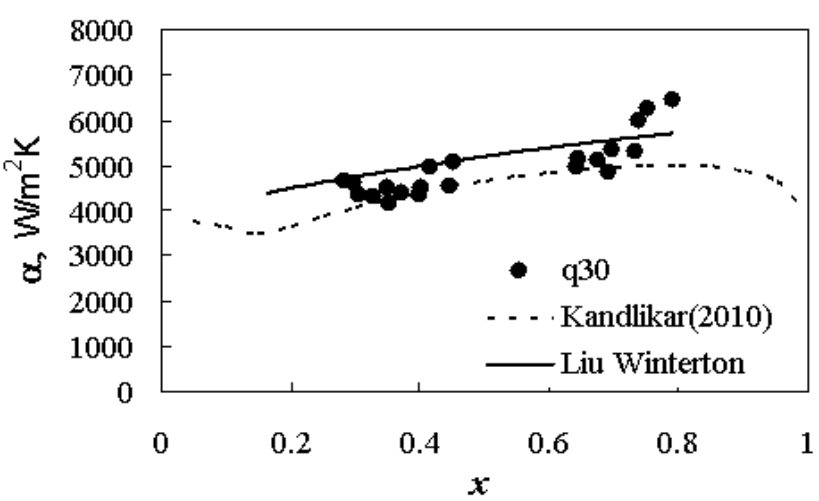


Fig. 4. Dependence of the local heat transfer coefficient averaged over perimeter of the channel vs. vapor quality. Upflow boiling of refrigerant R21 in the channel 1.6×6.3 mm

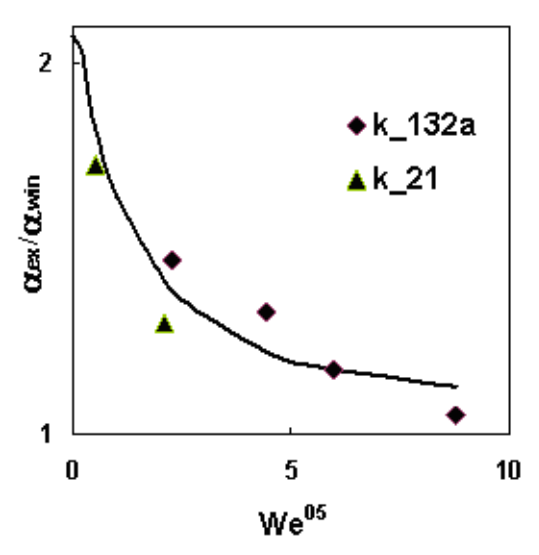


Fig. 5. The dimensionless heat transfer coefficient vs. Weber number Points - experiment

Experiments showed that for the mass speed of 50 kg/m²s there is a substantial, up to 2 times, the excess of the measured heat transfer coefficients compared with the calculation for all considered models. The reason for this may be changing the regime of heat transfer when changing the ratio of capillary pressure on the scale size of the channel and the dynamic pressure. Fig. 5 shows the dependence of the measured coefficient of heat transfer to the calculation by the modified model of Liu & Winterton for Refrigerant R21, and R132a, obtained by boiling in a tube diameter of 2.06 mm. Line in Fig. 5 shows the approximate relation for the constraint factor

$$\Psi_{con} = 1 + 1.2 / \exp(0.8 \cdot W e_{all\_liquid}^{0.35})$$
 (3)

Using constraint factor (3) in the modified model of Liu & Winterton (**Kuznetsov**, **Shamirzaev**, 2007a, 2007b) as a multiplier factor in the factor of suppression of boiling increases the accuracy of calculation of heat transfer in boiling in micro and mini channels, especially for small mass velocities and reduced pressure.

# 4. REFRIGERANT FLOW BOILING HEAT TRANSFER IN ASSEMBLAGE OF MICROCHANNELS

The studied the heat exchanger was made of stainless steel a material with low thermal conductivity. In the case where the dominant mechanism of heat transfer is boiling, local heat transfer coefficients depend on the heat flux. Since the fins of the heat exchanger have a low thermal conductivity the temperature along the fin varies considerably and consequently the local heat flux and the local value of the heat transfer coefficient changes during boiling. Therefore the use of fin efficiency methods for determining the values of local heat transfer coefficients in cross-section of the heat exchanger is incorrect, and here the definition of overall transfer coefficients was done.

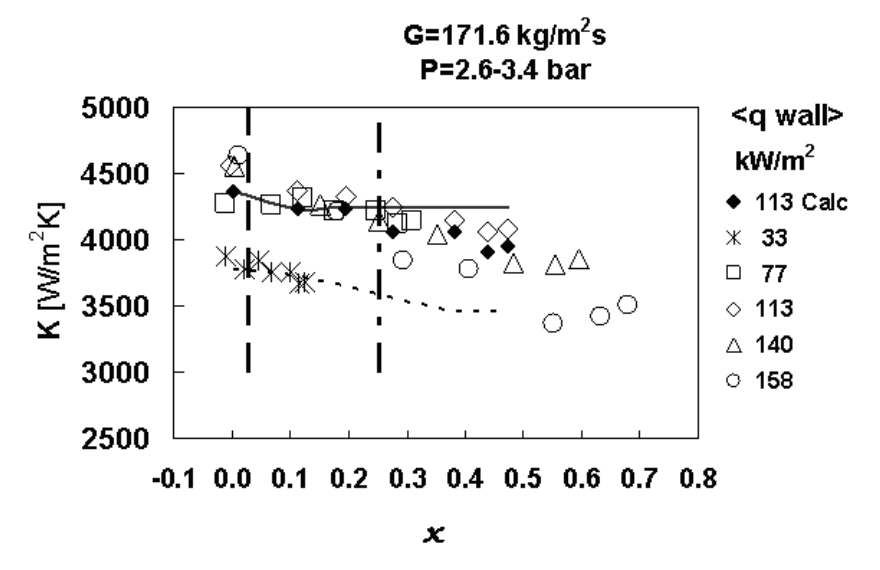


Fig. 6. Dependence of the local heat transfer coefficient microchannel heat exchanger of the heat flux at a mass flow rate of 171.6 kg/m<sup>2</sup>s

Fig. 6 shows the dependence of overall heat transfer coefficient in forced boiling of refrigerant R 21 in the microchannel heat exchanger at a mass flow rate of 171.6 kg/m<sup>2</sup>s. Vertical bold lines – flow regime transition: dashed line Bubble – plug and intermitted flow regime; dotted dashed – plug and intermitted – annular flow regime. Transition of flow regimes was determined by (**Taitel et al,** 1980).

We find that for bubble flow regime overall heat transfer coefficient increases with increasing heat flux density, therefore, the nucleating boiling mechanism is dominant. In plug and intermitted flow regime the overall heat transfer coefficient increases with increasing heat flux density up to qwall < 113 kW/m². In larger heat flux density the saturation reaches and the growth of heat transfer coefficient is terminated. For plug and intermitted flow regime heat transfer coefficients have low dependence from vapor quality. When vapor quality corresponding to annular flow

regime the heat transfer coefficients decrease with vapor quality increase. This indicates to suppression of boiling in liquid film for annular flow regimes.

In the (**Kuznetsov and Shamirzaev**, 2007c) the criteria for boiling suppression were proposed as ratio of the thermal sublayer thickness (yth) determined as:

$$\frac{y_{th}\sqrt{\Pr_f}\sqrt{\tau_w/\rho_f}}{v_f} = 5 \tag{4}$$

Where: wall shear stress determined by (Asali et al, 1985), to the cavity diameter based on the tangency criterion for incipience in the film (dtan) determined as

$$d_{tan} = \sqrt{\frac{8\sigma T_{sat}(\rho_f - \rho_g)k_f}{\rho_g \rho_f h_{fg} q_w}}$$
 (5)

Boiling suppression starts if the ratio of thermal sublayer thickness to the cavity diameter based on the tangency criterion for incipience falls less then 3.5 and becomes completely suppressed, when it becomes less than 2.

To compare the data with known models of heat transfer during boiling in small size channels the numerical calculations of heat transfer was done for heat flux trough external wall equal  $113~\rm kW/m^2$ . Simulation was performed for the real heat exchanger's geometry. On the surface of the channel were set boundary conditions of the third kind. Overall heat transfer coefficient was defined as the ratio of the heat flux on the outer wall to the difference between saturation temperature and the temperature of the outer surface. The results of calculations are shown in Fig. 6 as thin lines – dotted line by corrected Kandlikar's correlation (Kandlikar 2010); solid line by modified Liu & Winterton correlations with taking into account constraint factor (3), solid point – numerical calculations by modified Liu & Winterton correlations with taking into account constraint factor (3) and boiling suppressing for annular flow regimes as a multiplier factor **FK** depending from **y**th/dtan. When **y**th/dtan > 3.5 the **FK** is 1, for 2< **y**th/dtan < 3.5 the **FK** determined as linear function from 1 to zero and for **y**th/dtan < 3.5 **FK** is zero.

Calculation overall heat transfer coefficients by (Kandlikar 2010) have similar dependence from vapor quality but underestimate experimental data. Corrected Liu Winterton correlation is close to experimental data.

Different distribution of local heat transfer coefficient can give close value of overall heat transfer coefficient for microchannel heat exchanger. For checking the best correlation the calculation of temperature's field in real heat exchanger geometry for conditions corresponding to experimental data in annular flow regimes with different boundary conditions was done. Fig. 7 shows the field of temperature for different cases. We measure temperature on the cold side of heat exchanger in the middle. Experimental difference between cold side and saturation temperatures in considered case is 5.5 K. For constant heat transfer coefficient this difference is 1.9 K. For heat transfer coefficient determined by Liu Winterton correlation with eq. (3) this difference is 3.5 K. For heat transfer coefficient determined by Liu Winterton correlation with eq. (3) and with factor of boiling suppression this difference is 5.1 K. Last case has a best agreement with experiment.

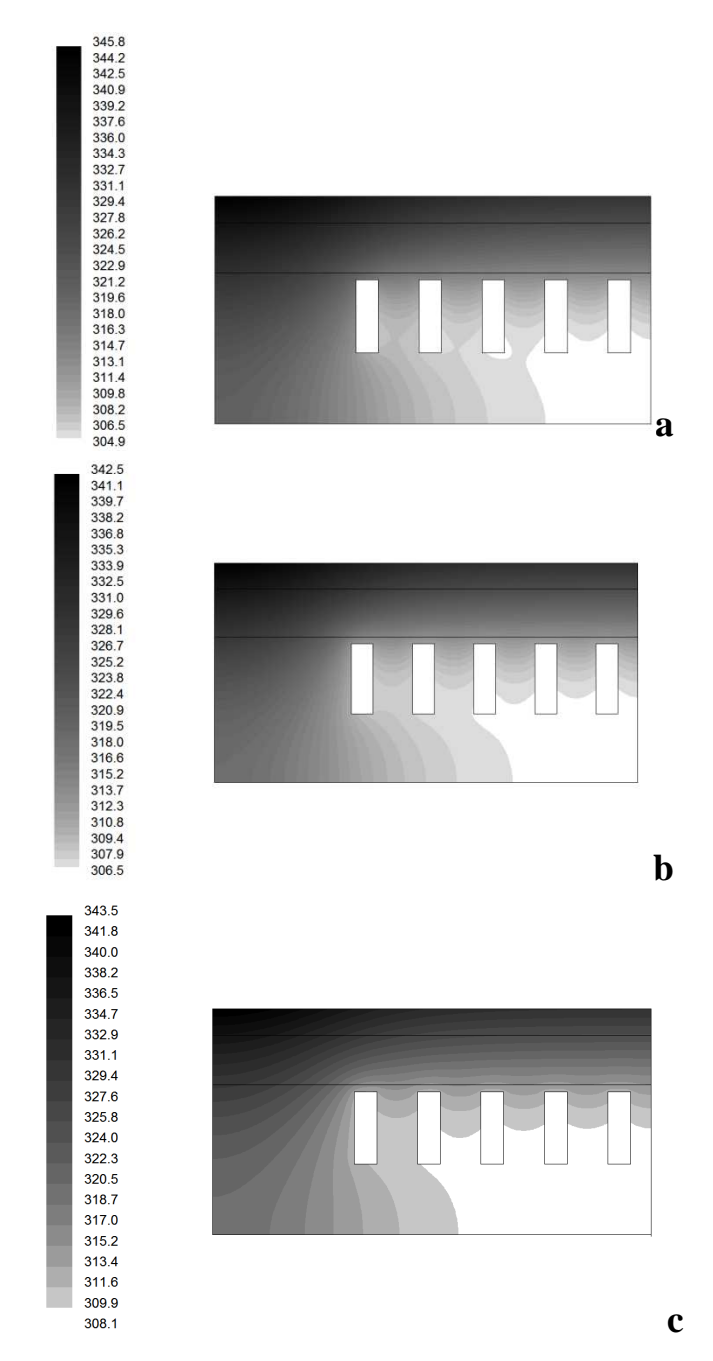


Fig. 7. Temperature fields for different boundary condition (element of symmetry). Heat transfer coefficient along the perimeter of channel calculated as: case (a) – constant; case (b) – by Liu Winterton with constraint factor (3); case (c) – by Liu Winterton with constraint factor (3) and suppressing boiling. T saturation is 303 K

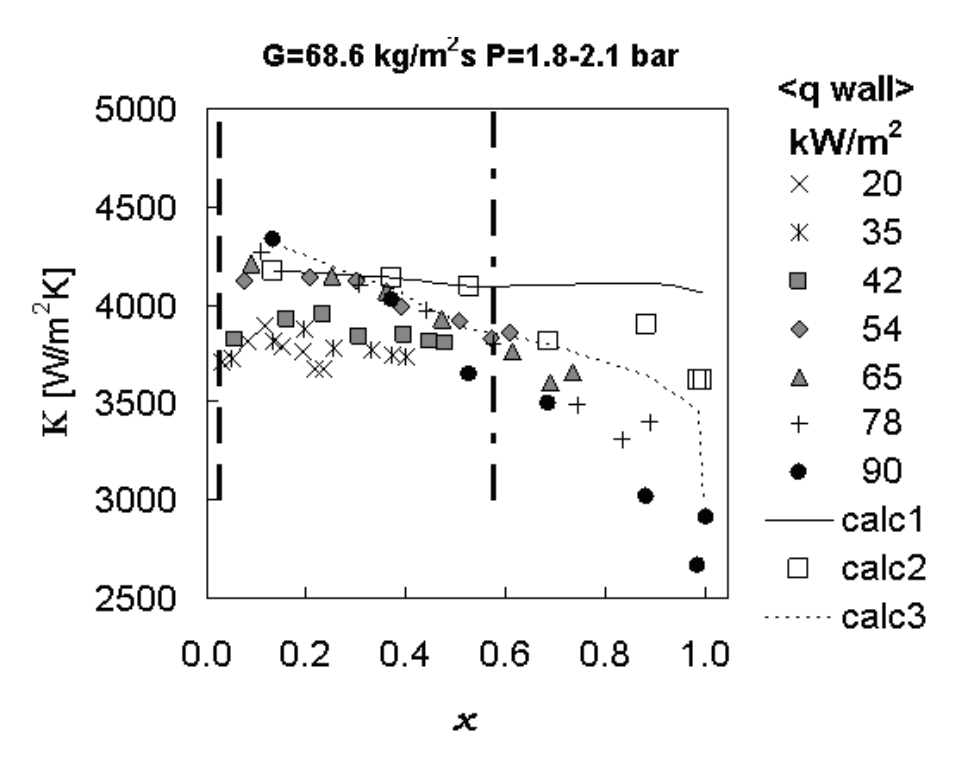


Fig. 8. Dependence of the local heat transfer coefficient microchannel heat exchanger of the heat flux at a mass flow rate of 68.6 kg/m<sup>2</sup>s

Fig. 8 shows the dependence of overall heat transfer coefficient in forced boiling of refrigerant R 21 in the microchannel heat exchanger at a mass flow rate of 68.6 kg. Calc1 is numerical calculation by modified Liu Winterton correlation with eq. (3), calc2 calculated like calc1 with taking into account the boiling suppression, calc 3 is numerical calculation by (Kandlikar 2010). Vertical lines depict to flow regimes transition like in Fig. 6. Calculation overall heat transfer coefficients by empirical Kandlikar's calculation (Kandlikar 2010) have best agreement to experimental data. All calculations are close to experimental data at non annular flow regime conditions and overestimate experimental data at annular flow regime conditions. The reason for this is probably surface dryness at high vapor quality and low mass velocities.

### 5. CONCLUSION

Experimental study of boiling heat transfer during flow boiling refrigerant R21 in minichannel showed that heat transfer coefficients increase with the decreasing ratio of capillary pressure on the scale size of the channel to the dynamic pressure. At Weber numbers much greater than one data correspond to the calculation of the modified model of Liu & Winterton and models Kandlikar, and with Weber numbers less than unity in the calculation must take into account the constraint that takes into account the intensification of nucleate boiling.

Experimental data on boiling of refrigerant R21 in the microchannel heat exchanger showed that with increasing heat flux density is more limiting, the growth coefficient of heat transfer is terminated, and it begins to decrease with increasing vapor quality. Comparison of experimental data with known models of heat transfer showed that the divergence of experimental data and calculation may reach 30 % or

more depending on the heat flux density and the local steam content. This shows that a universal model for calculating heat transfer during boiling of a moving fluid in the microchannel does not currently exist. The more factors influencing on two-phase heat transfer in confinement space are taking into account the best agreement calculation with experiment is obtained. A wide variety of factors that determine the mode of heat transfer in boiling causes the need to continue the work in this area.

This work was supported by RFBR, grant number 08-08-00953a.

### **REFERENCES**

Asali J.C., Hanratty T.J. and Paolo Andreussi, 1985, Interfacial Drag and Film for Vertical Annular Flow, AIChE J., vol.31, N6, pp 895–902.

Balasubramanian P., and Kandlikar S.G., 2004, An Extension of the Flow Boiling Correlation to Transition, Laminar and Deep Laminar Flows in Minichannels and Microchannels, Heat Transfer Engineering, V. 25, pp. 86–93.

Bar-Cohen A., Rahim E., 2007, Modeling and prediction of two-phase refrigerant flow regimes and heat transfer characteristics in microgap channels, in: Proceedings of the 5th International Conference on Nanochannels, Microchannels, and Minichannels ICNMM2007-30216.

Dong T., Yang Z., Bi Q., Zhang Y., 2008, Freon R141b flow boiling in silicon microchannel heat sinks: experimental investigation, Heat Mass Transfer, V.44, pp 315–324.

Liu Z. and Winterton R.H.S., 1991, A general correlation for saturated and subcooled flow boiling in tubes and annuli, based on a nucleate pool boiling equation, Int. J. Heat and Mass Transfer, vol.34 pp. 2759–2766.

Kandlikar S.G., 2010, Similarities and Differences Between Flow Boiling in Microchannels and Pool Boiling, Heat Transfer Engineering, V.31, pp. 159–167.

Kuznetsov V. V. and Shamirzaev A. S., 2007a, Flow patterns and flowboiling heat transfer of freon R318C in an annular minichannel, V.14, N1, PP53-61.

Kuznetsov V.V., Shamirzaev A.S., 2007b, Boiling heat transfer for freon R21 in rectangular minichannel, Heat Transfer Engineering, V. 28, pp 738–745.

Kuznetsov V.V, Shamirzaev A.S., 2007c, Flow boiling heat transfer mechanism in minichannels, in: Proceedings of the 5th International Conference on Nanochannels, Microchannels, and Minichannels ICNMM2007-30210.

Shiferaw D., Huo X., Karayiannis T.G., Kenning D.B.R., 2007, Examination of heat transfer correlations and a model for flow boiling of R134a in small diameter tubes, Int. Journal of Heat and Mass Transfer 50 5177–5193

Steinke M.E., Kandlikar S.G.,2004, An Experimental Investigation of Flow Boiling Characteristics of Water in Parallel Microchannels, Journal of Heat Transfer, V.126, pp 518-526.

Taitel Y., Barnea D., Dukler A.E., 1980, Modeling flow pattern transition for steady upward gas-liquid flow in vertical tubes, AIChE J. vol.26, pp. 345–354.

### **BIOGRAPHICAL NOTES**

Prof. Dr. Vladimir V. Kuznetsov is a head of Department of Engineering Thermophysics and Laboratory of Multiphase System at Institute of Thermophysics Siberian Branch of Russian Academy of Sciences. He also is Professor of Novosibirsk State University, Russia. He is a graduate of Novosibirsk State University (1972) and he was awarded PhD (1978) and DSc (1995) at Institute of Thermophysics Siberian Branch of Russian Academy of Sciences. His current research interests are concerned with the study of capillarity, fluid dynamics, heat and mass transfer in multiphase and multi-component flows including the phase change phenomena and catalytic reactions in mini and microchannel systems. Prof. Kuznetsov has published more then 140 articles covering a variety of topics. He is Deputy Editor-in-Chief of Journal of Engineering Thermophysics.

Mr. Alisher S. Shamirzaev is a researcher at Institute of Thermophysics Siberian Branch of Russian Academy of Sciences. He is a graduate of Novosibirsk State University (1993) and he was awarded PhD (2007). His research interests are concerned with the study of capillarity, fluid dynamics, heat and mass transfer in multiphase flows including the phase change phenomena in mini and microchannel systems.

Mr. **Stanislav P. Kozlov** is PhD studet at Institute of Thermophysics Siberian Branch of Russian Academy of Sciences. He is a graduate of Novosibirsk State University (2008). His research interests are concerned with the study of catalitic reactions, hydrogen production, fluid dynamics, heat and mass transfer in microchannels.

### **CONTACTS**

### Prof. Dr. Vladimir V. Kuznetsov

Kutateladze Institute of Thermophysics SB RAS 1, pr. Akademika Lavrentjeva Novosibirsk, 630090 Russian Federation

Tel: +7 (383)3307121 Email: vladkuz@itp.nsc.ru

© A. Shamirzaev, V. Kuznetsov, S. Kozlov, 2010

### STRUCTURE OF TWO-PHASE FLOW IN MINI- AND MICRO CHANNEL

### Igor A. KOZULIN, Vladimir V. KUZNETSOV, Russian Federation

**Key words**: micro channel, two-phase flow, flow regimes, slug flow, statistical analysis

### **Summary**

The use of mini-and micro channels in various types of equipment such as compact heat exchangers, the space satellite in small sizes, microelectronics has led to an understanding that the motion of two-phase gas-liquid flow in small channels has become the subject of intense research In this paper, the experimental research of the structure of adiabatic gas-liquid flow was made in rectangular mini-and microchannel with transverse dimensions 1.78×3.75mm and 0.67×2mm respectively. For mini channel experiments were performed for cocurrent flow of water/carbon dioxide under saturation conditions in the range of gas velocity 0.1÷10 m/s and liquid 0.07÷0.7 m/s. For the microchannel with transverse dimensions 0.67×2mm as a gasphase nitrogen is used, the range of gas velocities 0.04÷11 m/s, liquid 0.07÷0.41m/s. The experiments were conducted in predominance conditions of laminar flow liquid and gas. Using the method of laser scanning, high-speed photo and video received the main regimes of adiabatic upward gas-liquid flow in vertical mini channel. As a result of the experiments were constructed maps of flow regimes. a comparison of border regimes of flow calculated by the model of Mishima Ishii (1984), which gives the best fit to experimental data. Dual-beam laser scanning method allowed to measure slug velocity in two-phase flow. We obtained the statistical characteristics of liquid and gas phases. For the micro channel was determined pressure drop for single phase and two-phase flow regime. The pressure drop was compared with different models.

## **Summary**

Использование мини- и микроканалов в охлаждающих системах различного вида оборудования таких как компактные теплообменники, в космических спутниках малых размеров, микроэлектронике привело к тому, что понимание движения двухфазного газо-жидкостного потока в каналах малого размера стало предметом интенсивного исследования

В данной работе проведено экспериментальное исследование структуры адиабатного газожидкостного потока в прямоугольном мини- и микроканале с поперечными размерами  $1,78\times3,75$ мм и  $0.67\times2$ мм соответственно. Для миниканала опыты проведены для спутного потока вода/углекислый газ в условиях насыщения в диапазоне приведённых скоростей газа  $0.1\div10$  м/с и жидкости  $0.07\div0.7$  м/с. Для микроканала с поперечными размерами  $0.67\times2$ мм в качестве газовой фазы использовался азот, диапазон приведенных скоростей газа  $0.04\div11$ м/с, жидкости  $0.07\div0.41$ м/с. Опыты проведены в условиях преобладания ламинарного течения по жидкости и газу. С использованием метода лазерного сканирования, высокоскоростной фото и видеосъёмки

получены основные режимы восходящего адиабатного газожидкостного потока в вертикальных миниканалах. В результате проведенных экспериментов были построены карты режимов течения. Проведено сравнение границ режимов течения с расчётом по модели Mishima Ishii (1984), которая даёт наилучшее соответствие экспериментальным данным. Использование двулучевого метода лазерного сканирования потока позволило измерить скорость перемещения снарядов двухфазном потоке. В работе получены статистические характеристики движения жидкой и газовой фаз. Для микроканала был определен перепад давления для однофазного и двухфазного режима течения. Данные по перепаду давления были сравнены с различными моделями.

### 1. INTRODUCTION

Currently, there is substantial growth of interest in capillary hydrodynamics in microsystems, boosted by the development of microelectronics in computers, supercomputers, high-power lasers, medical equipment, compact heat exchangers in space systems. Two-phase flow in a channel with transverse size of order and less capillary constant characterized determining the influence of capillary forces and the effects of constraint on the regime of flow and heat transfer. For such small channels it were important the problems of describing boundaries of transitions between different flow regime and to identify areas of influence of capillary, gravitational, inertial and viscous forces, the statistical parameters of the flow of gas/liquid distribution slug velocity in slug-bubble flow regime and pressure drop.

Many works made on the study of two-phase regime for small diameter pipes. Characteristics of two-phase flow in channels of small cross section and a brief overview of works are presented in (Coleman J.W. & Garimella S., 1999). Review work performed by adiabatic gas-liquid flow in microchannels of different cross-section given in (Sarisorn S., Wongwises S., 2008).

Most of the works on the study of two-phase flows in small channels devoted to determining the flow regimes (Barnea D., Luninsky Y., 1983; Suo M., Griffith P. 1984).

Flow regime in two-phase flow depends on many parameters, such as given speed phases, the geometrical parameters of the microchannel, the viscosity, capillary effects, etc.

For the two-phase flow in a microchannel is of particular importance slug flow regime. In paper (Van Hout R., Barnear D., 2001) was obtained the statistical characteristics of slug flow, and their development along the channel in tubes with a diameter of about an centimeter.

At the same time, the statistical characteristics of gas-liquid flow are absent in channels of small transverse size in the literature. In this paper the structure of vertical upward gas - liquid flow and its statistical characteristics was obtained in rectangular mini- and microchannel with a transverse size of the order and less than the capillary constant.

### 2. EXPERIMENTAL SETUP

Experimental setup for determining parameters of the two-phase flow in rectangular mini- and microchannel is shown in Fig. 1. Transverse dimensions minichannel 1.78×3.75mm (hydraulic diameter 2.4 mm) length 0.7 m, the transverse dimensions of the microchannel 0.67×2 mm (hydraulic diameter 1 mm) length of the microchannel 0.5m.

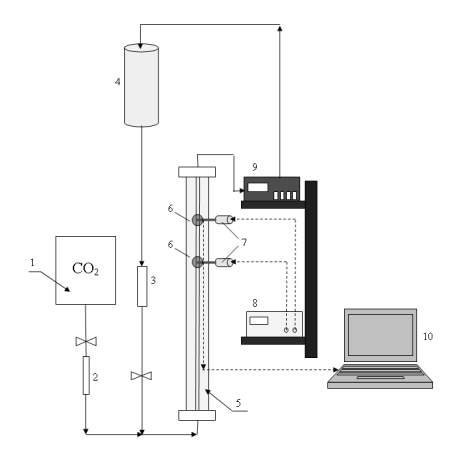


Fig. 1. Experimental setup

The working gas is carbon dioxide or nitrogen, which came from the container (1) through the adjusting valve and the flowmeter (2) in the experimental site (5). Water was supplied from the tank (4), then through the adjusting valve for liquid flow, the flowmeter (3) and then into the mixing chamber, located at the bottom to the experimental plot. The experimental section made of four parallel glass plates glued by epoxy adhesive with length L = 70 and L = 50 cm for mini- and microchannel, respectively. Hydraulic diameter of the mini- and microchannel is less than the capillary to Permanent Water  $b = \sqrt{\sigma/g(\rho_{liq} - \rho_{gas})} = 2.72$  mm.

At the outlet of experimental section the gas-liquid mixture was pumped by peristaltic pump (6) into open tank with water (4); at this carbon dioxide was escaped into the atmosphere, and saturated water was returned into the experimental section.

To study the patterns of the gas-liquid flow the method of double laser scanning was used. Two lasers (7) were located to illuminate the short side of the rectangular channel by a light spot with the diameter of about the channel size. The distance between the beams was 35 mm. The lasers were powered by TEC-42 source (8). Intensity of transmitted light was measured by photodiodes (9) on the opposite side of the channel. Signals from the photodiodes were registered by the high-speed card of ADC (Lcard L-264) with the maximal sampling frequency through all channels of 200 kHz, and then they were processed by PC 10. Signals were digitized with frequency v = 2 kHz during 60 - 120 s. The flow was registered from the face of the channel by the digital video (WebCam Pro Ex) and photo (OLIMPUS E330) cameras.

### 3. STRUCTURE OF FLOW

Using the method of dual-laser scanning and high-speed photo and video obtain the main modes of adiabatic upward gas-liquid flow in vertical mini-and microchannel. A result of the experiments highlighted the following flow regimes: slug-bubble, slug, emulsion and ring. Mode with discrete bubbles in the channels was not observed.

Bubble-slug regime in minichannel observed for the superficial velocity of gas and liquid in the range  $J_{liq} = 0.51 \div 0.64$  m/s,  $J_{gas} = 0.07 \div 0.84$  m/s. The structure of the flow was more like a slug mode, with numerous short liquid bridges. Figure.2 shows the time sweep of the signal optical sensors and photographs of the flow structure for the bubble-slug flow regime in minichannel. With increasing reduced velocity in the range  $J_{liq} = 0.07 \div 0.38$  m/s,  $J_{gas} = 0.52 \div 1.57$  m/s. observed slug flow regime, with the characteristic form of the signal is shown in Fig.3. This observed long shells, separated by a short liquid bridge.

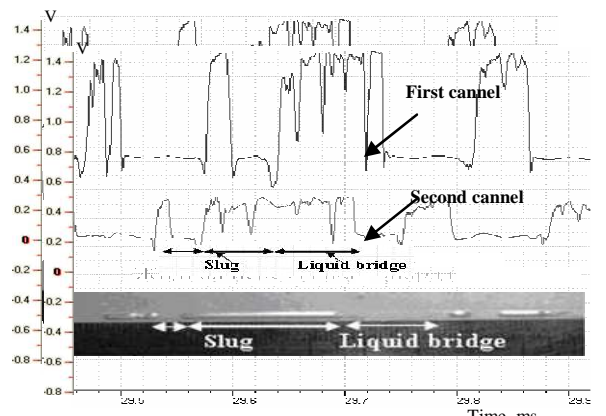


Fig. 2. The optical signal from the phoodiode to the slug-bubble regime in minichannel J<sub>liq</sub>=0.64m/s J<sub>gas</sub>=0.07m/s

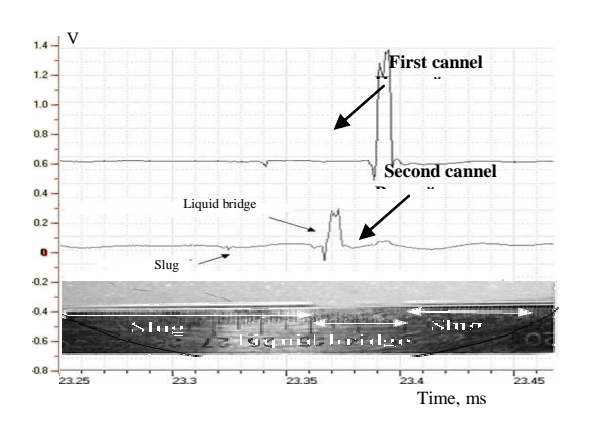
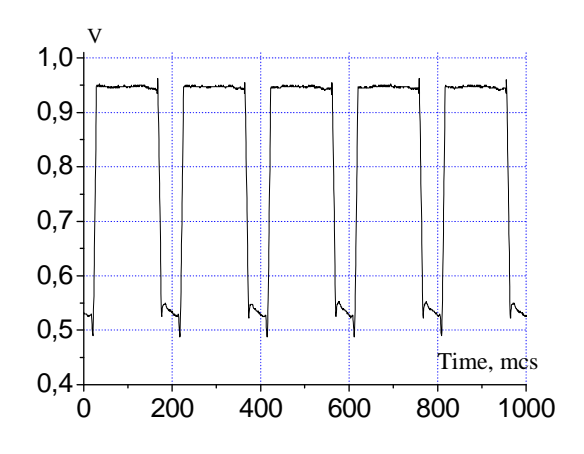


Fig. 3. The optical signal from the photodiode to the slug regime in minichannel  $J_{liq}$ =0.12m/s  $J_{gas}$ =1.18m/s

In microchannel bubble-slug flow regime is observed in the range superficial velocity of the liquid  $J_{liq}$ =0.11÷0.407 m/s and gas  $J_{gas}$ =0.04÷0.31 m/s. the optical signal is shown in Fig. 4.

In the range of superficial velocity  $J_{liq} = 0.066 \div 0.407$  m/s,  $J_{gas} = 0.51 \div 2.35$  m/s was observed slug flow regime shown in Fig. 5. Slug flow regime characterized by the fact that the observed long gas slugs, separated by a short liquid bridge, whose size is less than or equal gas bridges. In microchannel slug flow is characterized by frequency, and the lack of a significant number of small bubbles in a shell.



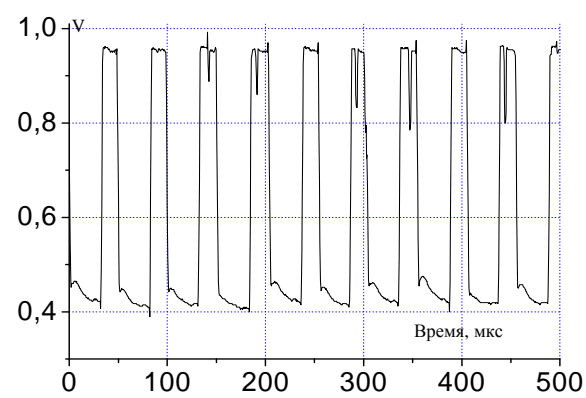
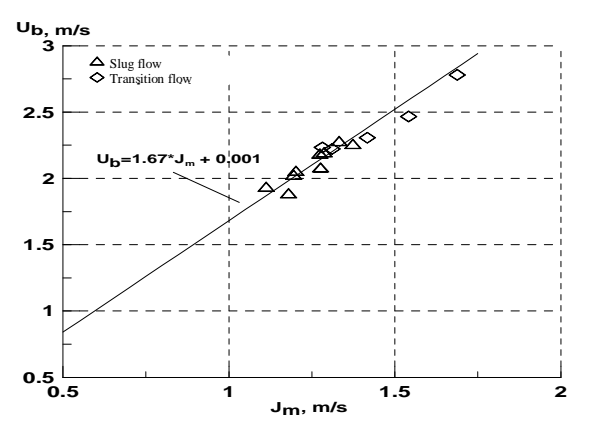


Fig. 4. The optical signal from the photodiode to the slug-bubble regime in microchannel with  $J_{liq}$ =0.17m/s,  $J_{gas}$ =0.16m/s

Fig. 5. The optical signal from the photodiode to the slug regime in microchannel with  $J_{liq}$ =0.27m/s,  $J_{gas}$  = 0.61m/s

### 4. STATICAL PARAMETERS OF THE FLOW

Fig. 6, 7 show the slug velocity  $U_b$  of the superficial velocity of the mixture  $J_m$  for mini-and microchannel, respectively.



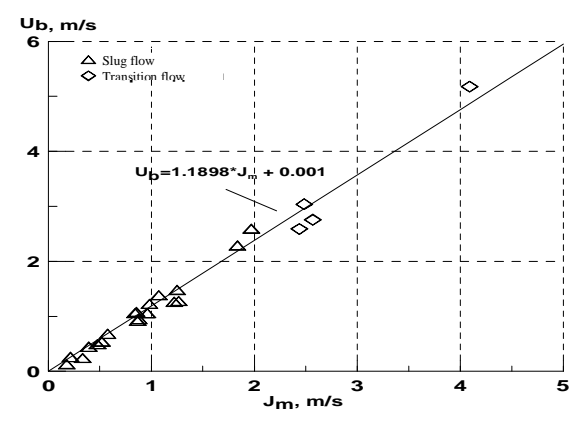
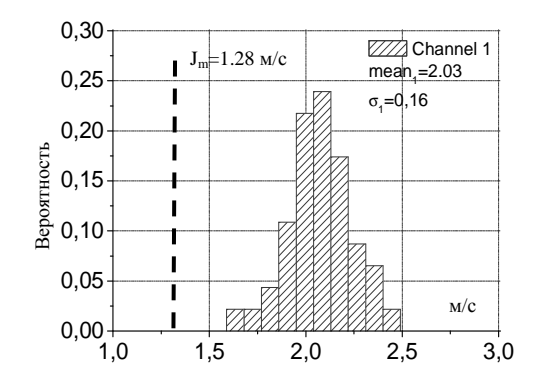


Fig. 5. Slug velocity depends on the superficial velocity of the mixture in a rectangular minichannel  $1.75\times3.8$  mm  $(H_2O/CO_2)$ 

Fig. 6. Slug velocity depends on the superficial velocity of the mixture in a rectangular microchannel 0.67×2.0 mm

Experimental data obtained using dual laser scanning stream, shown by points. The optical method allowed us to fix the speed of the gas slug and liquid plugs. Data processing for surfacing velocity projectiles in the form  $U_b=C_0\cdot J_m+U_{bfree}$  for slug regime showed that the coefficient  $C_0=1.67$  for minichannel, higher than in the work (Nicklin D.J., Davidson J.F., 1962). For the microchannel distribution parameter  $C_0=1.2$ , which well agrees with data (Sowinski J., Dziubinski M., 2009).

Was carried out statistical processing of data on speed ascent of slugs and their length measurements were performed for the statistical parameters of slug-bubbly and slug flow regimes. The statistical characteristics of motion of the liquid and gas phases obtained in the microchannel at two distances from the entrance to the mixing chamber  $\frac{x_1}{D} = 199$  and  $\frac{x_2}{D} = 256$ . Figure 8, 9 shows histograms velocity distribution for a given flow regime in the mini- and microchannel.



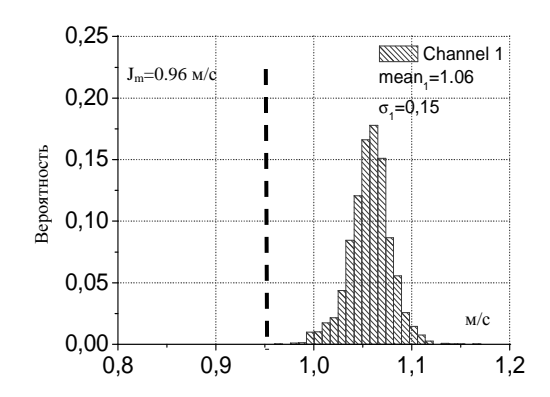


Fig. 8. Histogram of the slug velocity in minichannel for slug flow regime at a flow rate  $J_{liq} = 0.091 \text{m/s}$  and  $J_{gas} = 1.19 \text{ m/s}$ 

Fig. 9. Histogram distribution of the slug velocity in microchannel for slug flow regime at a flow rate  $J_{liq}=0.17~\text{m/s}$  and  $J_{gas}=0.79~\text{m/s}$ 

#### 5. MAP OF FLOW REGIMES

Fig. 10, 11 shows maps of flow regimes for mini-and microchannel obtained using the method of laser scanning beam. Solid lines correspond to calculations on the model Mishima & Ishii (Mishima K., Ishii M., 1984). We present the following flow regimes: BS - slug-bubble, S - slug, C - churn, A - annular, AW - dispersion-annular. The boundaries of regimes, in general, consistent with the calculation of the model Mishima & Ishii.

Annular

Transition

Churn

Slug

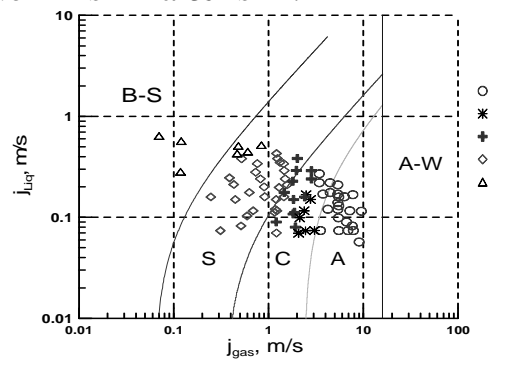


Fig. 10. Map of flow regimes for the minichannel

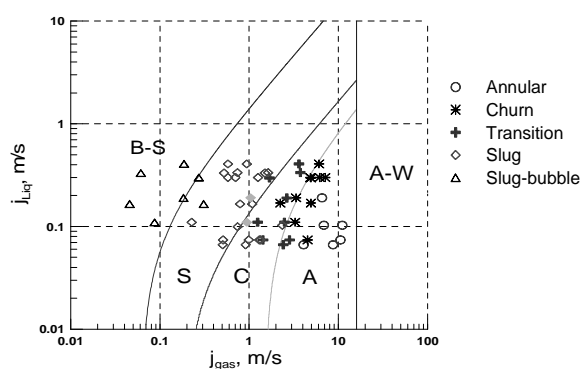


Fig. 11. Map of flow regimes for the microchannel

#### 6. PRESSURE DROP

Fig. 12 shows the dependence of the pressure drop from the Reynolds number for single phase flow of liquid, gas and gas-liquid flow in a microchannel. It is seen that the experimental data for single phase flow is consistent with the calculations for the laminar (Shah R.K., London A.L., 1978) and turbulent flow regimes. Experimental data for gas-liquid flow are processed in the homogeneous model

(Ungar E.K. and Cornwell J. D. 2002; Triplett K. A., Ghiasian S. M., 1999). We find that in the turbulent flow of the experimental data lie significantly above the calculation of the homogeneous model, the experimental data exceed the calculations up to 2 times. For turbulent flow model of Garcia et al (Garcia F., Garcia R., Padrino J.C, 2003) best matches the data.

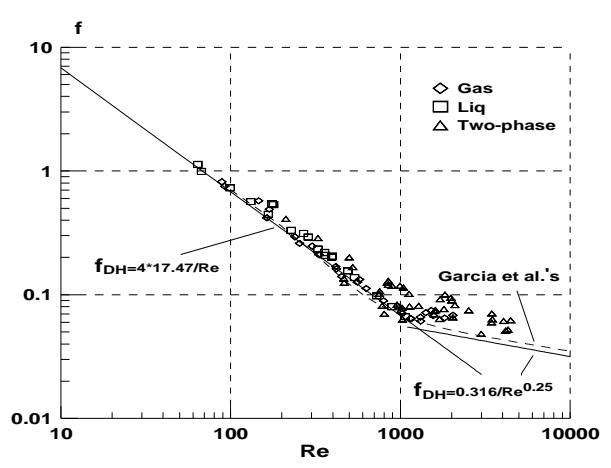


Fig. 12. Pressure drop for microchannel 0,67×2 mm

#### **CONCLUSION**

In this paper we study the structure of adiabatic upward gas-liquid flow in vertical mini- and microchannel. The use of dual-beam laser scanning has allowed determining the main modes of gas-liquid flow, slug, transition, churn, annular flow regimes, defined by their boundaries. Maps of flow regimes for minimicrochannel, we find that the border regime, in general, consistent with the calculation of the model Mishima & Ishii. It was found that slug flow in a microchannel is characterized by periodic, and the lack of a significant number of small bubbles in shell. Experimentally was explored the dependence slug velocity on superficial velocity of the mixture for mini-and microchannel. For the slug-bubbly and slug flow regimes was obtained the statistical parameters of the flow, including the distribution of velocity, length of liquid bridges and gas shells. For the microchannel measured pressure drop for single phase and two-phase flow, the data for single phase flow in good agreement with calculations based on known models. For gas-liquid turbulent flow experimental data lie above the calculation for the homogeneous model and the model of Garcia et al best matches the data of experiment.

This work was supported in part by: RFBR, grant number 08-08-00953a.

#### LIST OF SYMBOLS

J<sub>liq</sub> – superficial velocity of liquid phase

J<sub>gas</sub> – superficial velocity of gas phase

σ – surface tension

 $C_0$  – distribution parameter

J<sub>m</sub> – superficial velocity of mixture

 $x_1$ ,  $x_2$  – nates of the photodiodes

 $U_b$  – slug velocity

D<sub>h</sub> – hydraulic diameter

U<sub>bfree</sub> – ascent slug velocity in a stationary liquid

#### **REFERENCES**

Barnea D., Luninsky Y., Taitel Y. 1983, Flow pattern in horizontal and vertical two phase flow in small diameter pipes // Can. J. Chem. Eng., Vol. 61, P. 617-620.

Coleman J.W. and Garimella S. 1999, Characterization of two-phase flow patterns in small diameter round and rectangular tubes // Int. J. Heat Mass Transfer, Vol.42, P. 2869–2881.

Garcia F., Garcia R., Padrino J.C, Mata C., Trallero J.L and Joseph D.D., 2003, Power Law and Composite Power Law friction factor correlations for Laminar and Turbulent Gas-Liquid Flow in Horizontal Pipelines // Int. J. Multiphase Flow, vol. 29, pp. 1605–1624.

Mishima K., Ishii M. 1984, Flow regime transition criteria for upward two-phase flow in vertical tubes // Int. J. Heat and Mass Transfer, vol. 27, № 5, pp 723–738.

Nicklin D.J., Davidson J.F. Paper №4, 1962. Two-phase Flow Symp., Inst. Mech. Engrs, London.

Sarisorn S. Wongwises S. 2008, A review of two-phase gas-liquid adiabatic flow characteristics in micro-channels // Renewable and Sustainable Energy Reviews, 12, P. 824–838.

Shah R.K., London A.L. 1978, Laminar Flow Forced Convention in Ducts // Supplement 1 to Advances in Heat Transfer, Academic, New York.

Sowinski J., Dziubinski M., Fidos H. 2009, Velocity and gas void fraction in two-phase liquid-gas flow in narrow mini-channels // Arch. Mech., 61.1.pp. 29-40.

Suo M., Griffith P. 1984, Two-phase flow in capillary tubes // J. Basic Engineering., P. 576–582.

Triplett K. A., Ghiaasiaan S. M., Abdel-Khalik S. I., LeMouel A. and McCord B. N. 1999, Gas-Liquid Two-Phase Flow in Microchannels". Part II: Void Fraction and Pressure Drop // Int. J. Multiphase Flow, vol. 25, pp. 395–410.

Ungar E.K. and Cornwell J. D. 2002, Two-Phase Pressure Drop of Ammonia in Small Diameter Horizontal Tubes // Proc. AIAA 17th Aerospace Ground Testing Conf., Nashville, TN, July 6–8.

Van Hout R., Barnear D., 2001, Shemer L. Evolution of statistical parameters of gas-liquid slug flow along vertical pipes// Int. J. of Multiphase Flow, Vol. 27, No. 9, P. 1579–1602.

#### **BIOGRAPHICAL NOTES**



Prof. Dr. Vladimir V. KUZNETSOV is a head of Department of Engineering Thermophysics and Laboratory of Multiphase System at Institute of Thermophysics Siberian Branch of Russian Academy of Sciences. He also is Professor of Novosibirsk State University, Russia. He is a graduate of Novosibirsk State University (1972) and he was awarded PhD

(1978) and DSc (1995) at Institute of Thermophysics Siberian Branch of Russian Academy of Sciences. His current research interests are concerned with the study of capillarity, fluid dynamics, heat and mass transfer in multiphase and multi-component flows including the phase change phenomena and catalytic reactions in mini and microchannel systems. Prof. Kuznetsov has published more then 140 articles covering a variety of topics. He is Deputy Editor-in-Chief of Journal of Engineering Thermophysics.

Mr. **Igor A. Kozulin** is PhD student at Novosibirsk State University Siberian Branch of Russian Academy of Sciences. He is a graduate of Novosibirsk State University (2008). His research interests are concerned with the study of adiabatic two-phase gas-liquid flow in vertical rectangular mini- and microchannel, statistics characteristics of slug flow, explosive boiling of the water layer of varying thickness, metastable liquid. Research conducted at Institute of Thermophysics Siberian Branch of Russian Academy of Sciences.

#### **CONTACTS**

#### Prof. Dr. Vladimir V. Kuznetsov

Head of Department of Engineering Thermophysics and Laboratory of Multiphase System at Kutateladze Institute of Thermophysics SB RAS

1, pr. Lavrenteva

Novosibirsk, 630090

Tel: +7 (383) 330-71-21

1, Pravdu, Room 20

Novosibirsk, 630090

Russian Federation

Tel: +7(383) 330-57-94,

E-mail: vladkuz@itp.nsc.ru

#### Igor A. Kozulin

PhD student, Novosibirsk State University,

1, pr. Lavrenteva

Novosibirsk, 630090

Tel: +7 (383) 316-57-31

18, Pirogova Str., Room 221

Novosibirsk, 630090

Russian Federation

Tel: +7 9231820897

E-mail: igornt@yandex.ru

# MANUFACTURING OF A SPUTTER MASK FOR SELECTIVE COATING OF LARGE-AREA RESIST STRUCTURES BY MICRODRILLING

## Thomas GIETZELT, Lutz EICHHORN, Markus GUTTMANN<sup>1)</sup>

Karlsruhe Institute of Technology, Institute for Micro Process Engineering (IMVT), P.O. Box 3640, 76021 Karlsruhe, Germany

Karlsruhe Institute of Technology, Institute of Microstructure Technology, P.O. Box 3640, 76021 Karlsruhe, Germany

**Keywords:** micro drilling, micro machining, electropolishing, electroplating

### **Summary**

When electroplating large areas of non-conducting photoresists, e. g. for manufacturing replication tools using the LIGA process, problems can arise. In case of a non-conducting resist surface, bumps may form when growing fronts join. If the resist surface is flushed with a conductive metal layer, deep and narrow cavities can be closed by overgrowing without being filled with electroplated metal. Poor adhesion of flushed metal films due to intrinsic tensions may also be a problem on resist structures. Both the formation of bumps as well as incomplete filling of microstructures can be avoided by partly metallizing the resist surfaces using microstructured sputter masks [1]. A sputter mask was manufactured for seeding small sputtered gold dots all over the large photoresist areas as supports for flat and defect-free electroplating. The parameters of the microdrilling process were optimized and a total number of about 114.500 holes were drilled. The sputter mask was finished by electropolishing to remove burrs from microdrilling.

#### 1. INTRODUCTION

During electroplating of microstructured photoresists, e. g. for manufacturing metallic microparts or for the production of replication tools, problems may arise from overgrowing of large areas. Without any additional metallization, the growth fronts of the electroplated metal tend to form bumps, as shown in Fig. 1, since the advancing angle increases significantly with increasing distance on a non-conductive surface. Moreover, the speed and uniformity of electroplating depend on the width of the features, since the metallization rate is diffusion-controlled. Under extreme conditions, narrow trenches may be encapsulated before the growth front inside the structures reaches the surface of the resist [2]. The same happens, if the whole surface of the resist is flushed with a metal film. In most cases, the perpendicular side walls of the microstructures are also coated, as a result of which the whole resist surface becomes conductive and voids are formed within narrow trenches. Additionally, the adhesion of a large-area metal film to photoresists is poor due to intrinsic tensions.

Filling of narrow trenches with high aspect ratios may also cause problems due to gas bubbles or overgrowing by a second growth front. Fig. 2 shows an UV-LIGA mold insert with both effects due to an additional metallization of large areas of the photoresist.

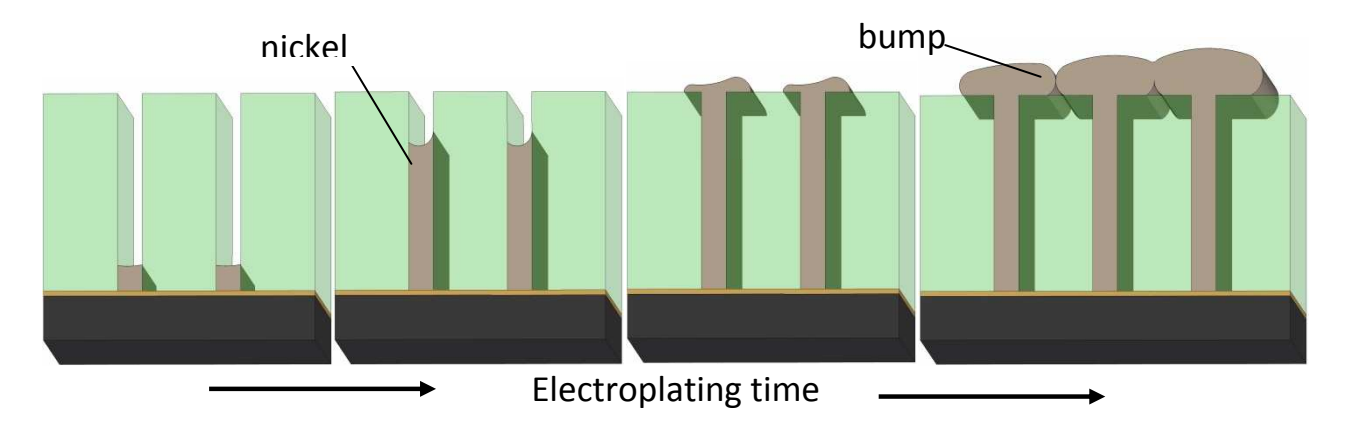


Fig. 1. Overgrowing by electroplating large areas of a photoresist by contacting the conductive substrate

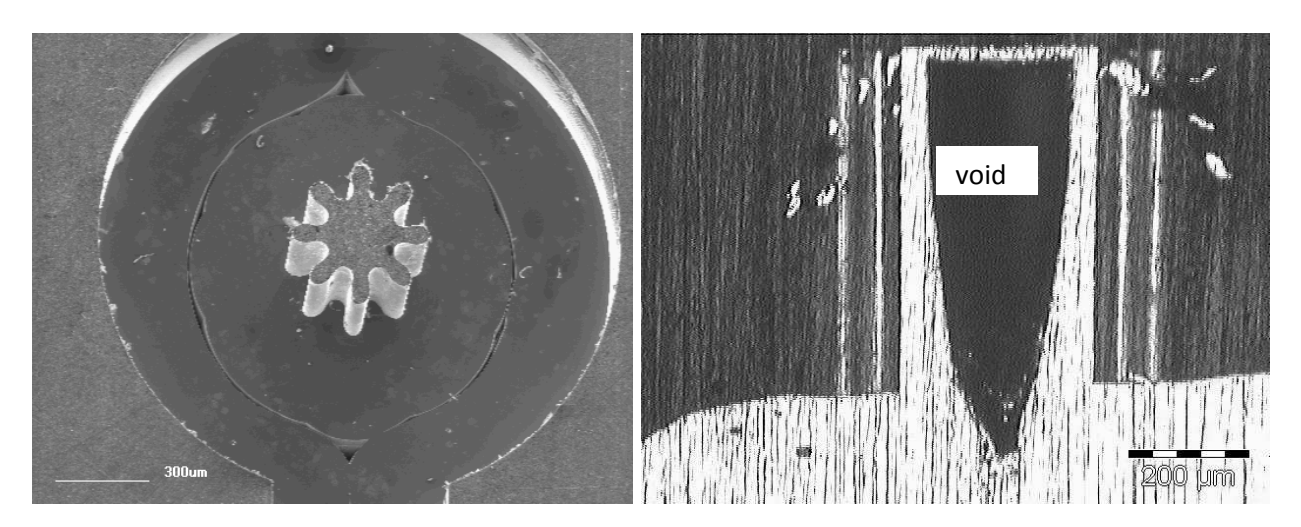


Fig. 2. Typical defects of electroplated microstructures. Left: UV-LIGA mold insert with bump formation. Right: cross section of a micro gearwheel pin with void

Often, such faults are not visible, but become obvious when external forces or elevated temperatures are applied as is the case in injection molding (Fig. 3).

Hence, selective metallization of the resist surface level is much better. The spotted metallization of large resist areas may prevent incorrect electroplating by influencing the advancing angle of the electroplated metal. For this, an additional mask is needed to deposit electrically conductive seed points to be contacted by the advancing electroplating front (Fig. 4). These seed points, however, must be located at a certain distance from the edge of the microstructures in order to prevent coating of the side walls of the microstructures with metal.

Generally, such sputter masks can be made by:

- Mechanical micromilling
- Lithographic processes or
- Etching

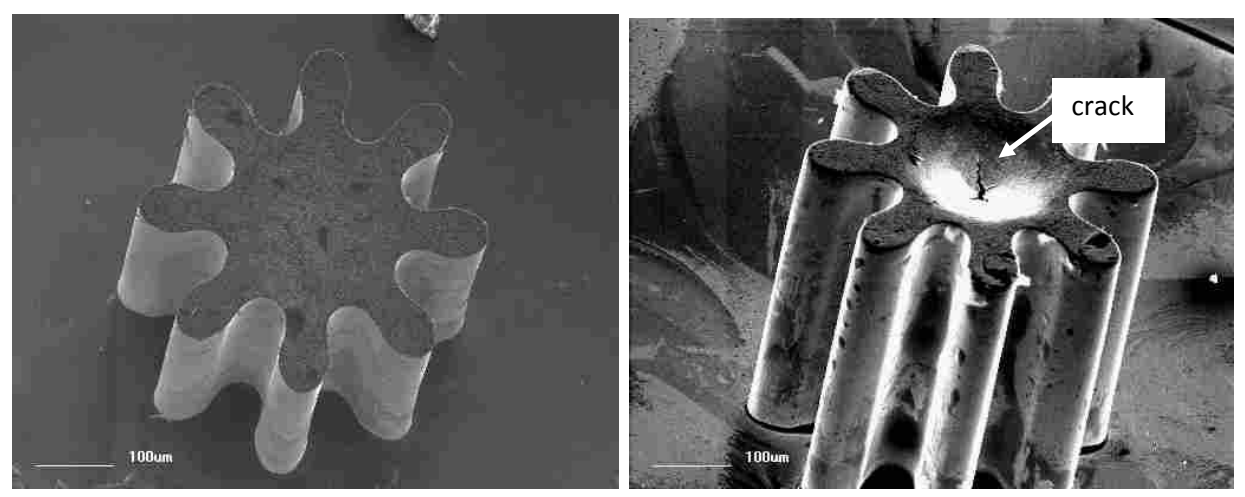


Fig. 3. Micro gearwheel pin before (left) and damaged surface with crack of a hollow micro gearwheel pin after injection molding (right)

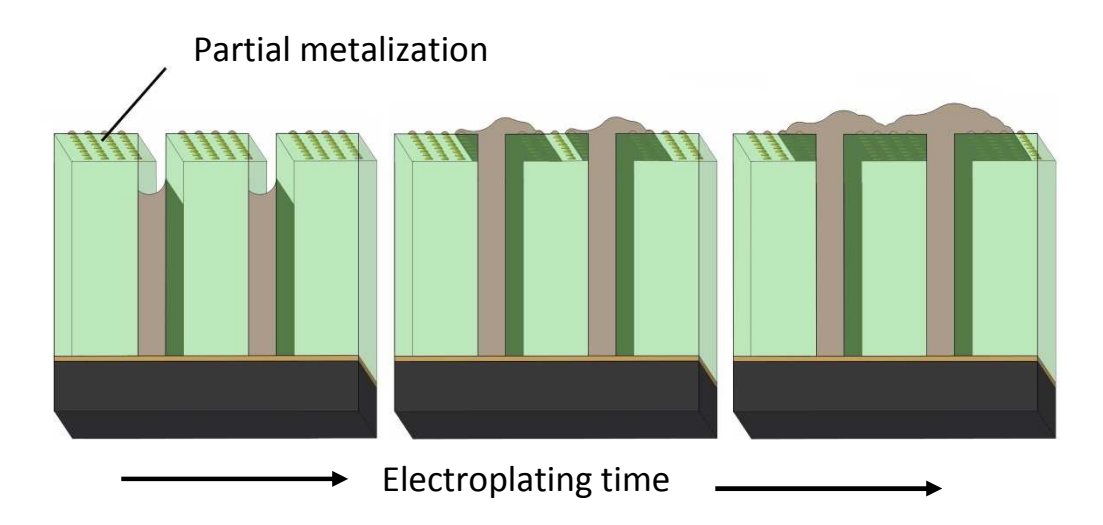


Fig. 4. Partly metalized large photoresist areas to prevent inclusions during electroplating

#### 2. SPUTTER MASK FABRICATION BY MICRODRILLING

A sputter mask of 100  $\mu m$  in thickness was made of brass MS63 by micromilling. A brass substrate was prepared by precision milling using an ultramiller SP2600 by Leica Microsystems GmbH. A 100  $\mu m$  thick sheet of brass, approximately 100 by 70 mm, was glued onto this surface using Wafermount 562 by Kager Industrieprodukte GmbH. The glue forms a sheet of approximately 0.1 mm thickness and can be cut to appropriate shapes. Substrate, glue layer, workpiece and a weight of about 2 kg on top of the workpiece were put into a vacuum drying chamber. After reaching 100 °C and waiting for one hour, vacuum was applied. After another two hours, the drying chamber was cooled down and vented when the temperature was below 50 °C. When using a tailored glue of constant thickness, it is not necessary to displace part of the glue to obtain a constant thickness of the glue layer and, hence, a flat surface level. Measurements showed that the surface level of the workpiece was within 5  $\mu m$ .

The sputter mask was of irregular design. In total, approximately 114,500 holes with a diameter of 50  $\mu$ m were drilled on an area of 63 by 23 mm. The wall between the holes was 50  $\mu$ m in each direction. Fig. 5 shows the design of the sputter mask in back light. In the dark areas, the photoresist was removed in the developing step. A more detailed view is shown in Fig. 6.

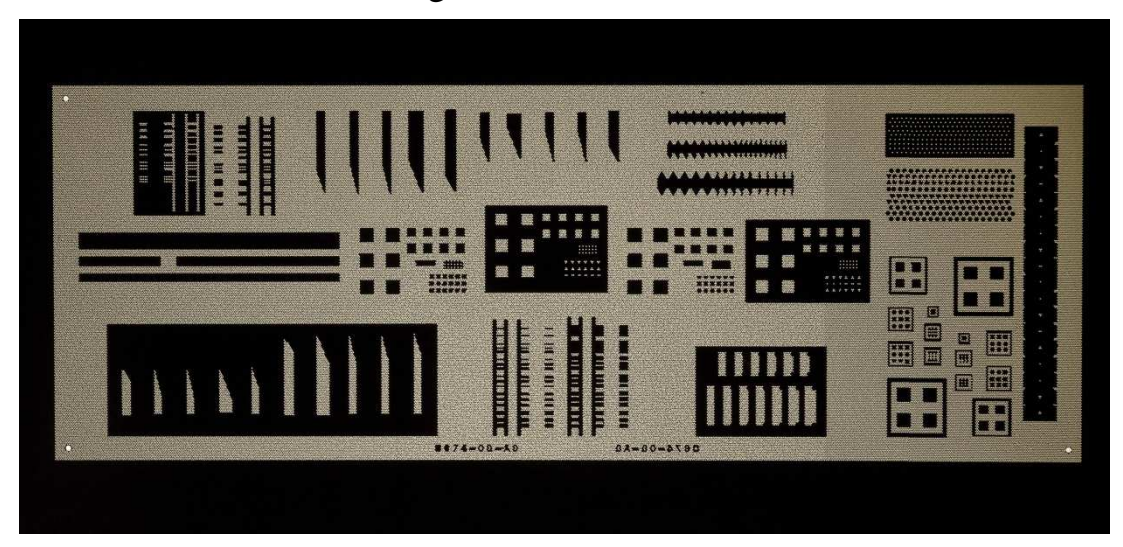


Fig. 5. Sputter mask with 50 µm holes, microstructured area 63 by 23 mm

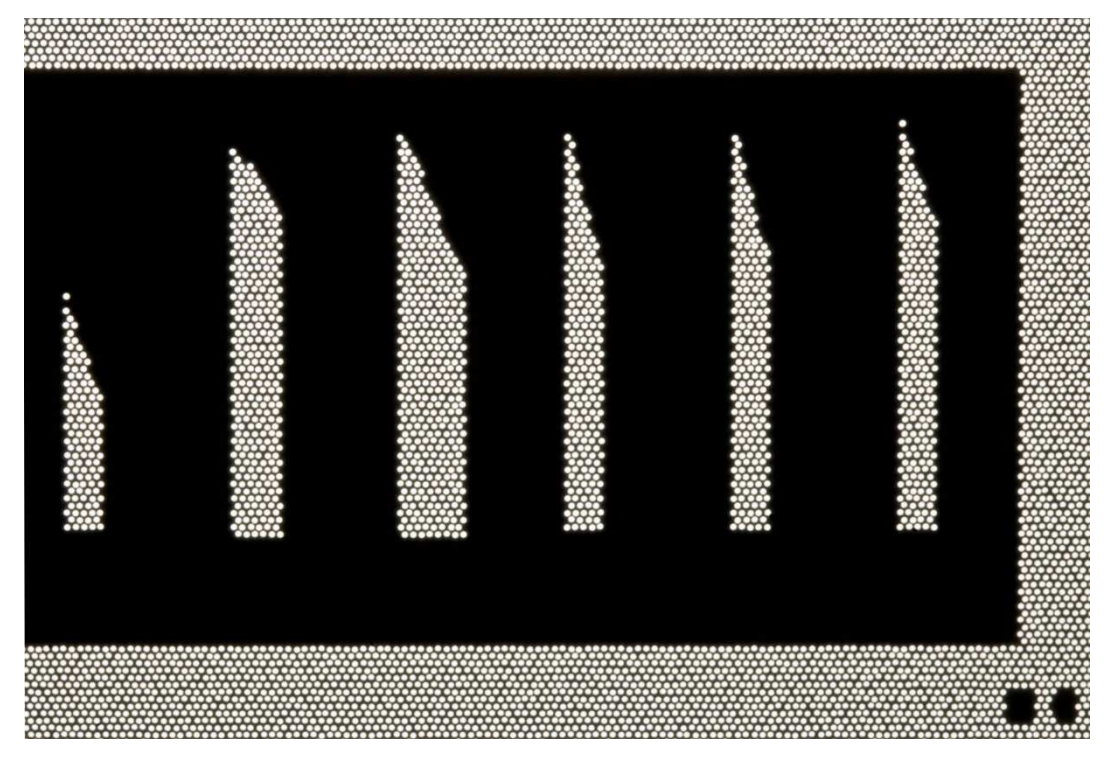


Fig. 6. Detailed view of the sputter mask

Normally, MS58 would be the best choice, because it is easy to machine due to its lead content. The lead forms precipitations at the grain boundaries, which cause short breaking chips. However, lead prevents good results when electropolishing is needed for burr removal. For this reason, MS63, a lead-free brass, was chosen. It can

be electropolished very well. On the other hand, machining is not as good as for MS58.

The absolute depth of drilling was 200  $\mu$ m, starting from a safety distance above the workpiece surface of 50  $\mu$ m and taking into account the thermal drift of the machine spindle and the conical tip of the microdrill.

Fig. 7 shows some pictures of a new uncoated 50 µm drill bit made of hard metal by HAM GmbH. The overall length is approximately 1 mm. From the detailed view, it can be seen that the cutting edge is jagged. Since hard metal is a composite material consisting of hard tungsten carbide particles in a soft cobalt binder matrix, the grinding process does not form an ideally sharp cutting edge. As a consequence, burr formation in ductile materials must be taken into account.

A 1/8" chuck was used for clamping the tool. The true running accuracy was measured to be within 2  $\mu m$ .

Compared to milling, where torsion and deflection forces occur, drilling is associated with torsion only. Milling results in the intermittent formation of chips causing vibrations and chatter marks on the workpiece. Hence, fatigue of the tool material, crack propagation, and breaking of the micro end mills is a much more serious problem than for micro drill bits. Depending on the tool length and feed rate, however, bending may also be a problem.

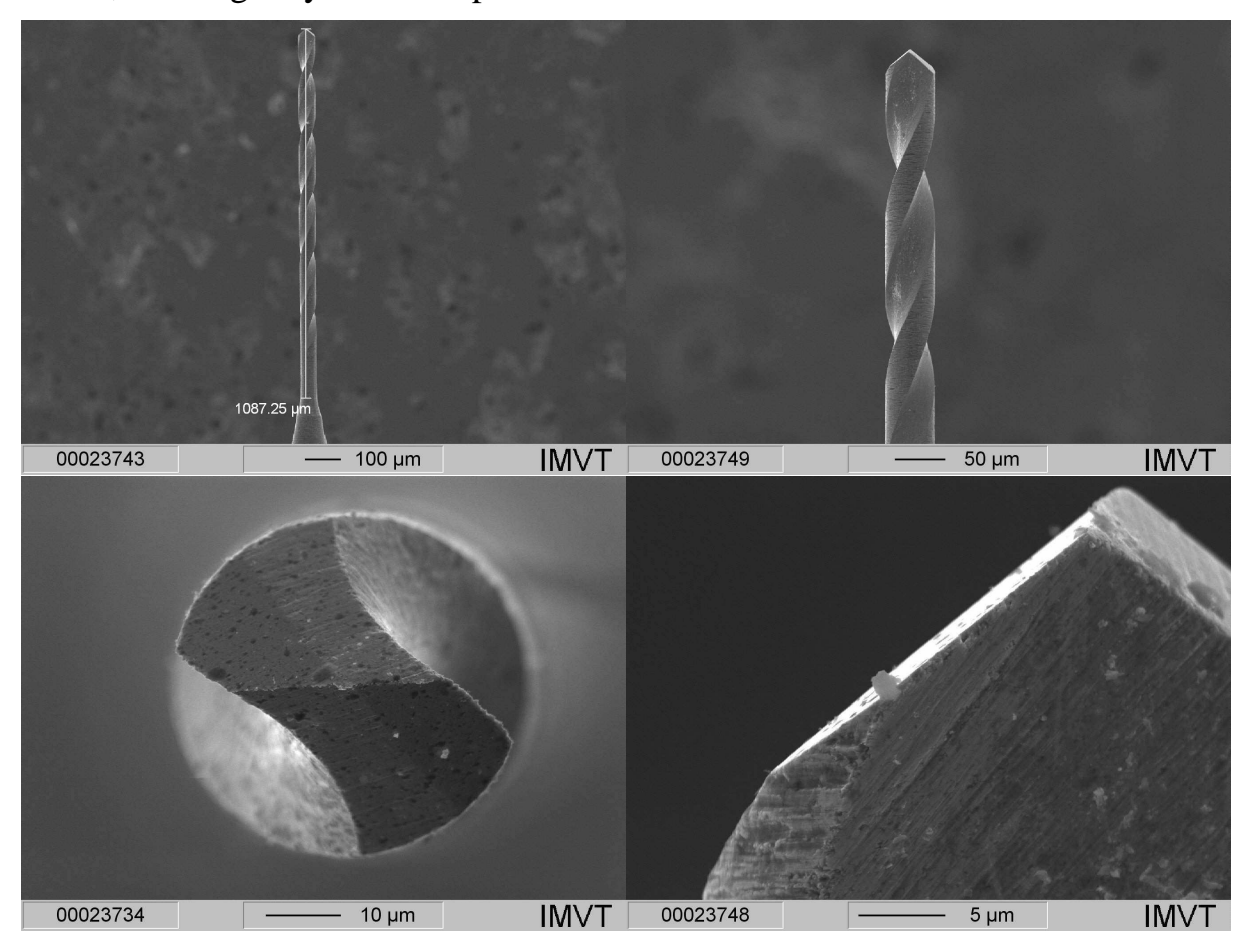


Fig. 7. New 50 µm drill bit by HAM GmbH

Several speeds and feeds and drilling of a hole in three steps were investigated. Finally, a speed of 15,000 rpm and a feed of 90 mm/min (3 µm per tooth) were used. The holes were drilled in one pass. One thousand holes were drilled within approximately 15 min. In total, the machining time was a little longer than three days of eight hours each. The parameter test showed that it was not possible to increase speed and feed at a fixed ratio, e. g. to 40,000 rpm with a corresponding feed.

For lubrication, the tool was flushed with Wicos VA ST80.6 by WILKE Kühlschmiertechnik GmbH.

After drilling approximately one third of the sputter mask, corresponding to 30,000 - 40,000 holes, the drill bit was exchanged by a new one. A worn 50  $\mu$ m drill bit can be seen in Fig. 8.

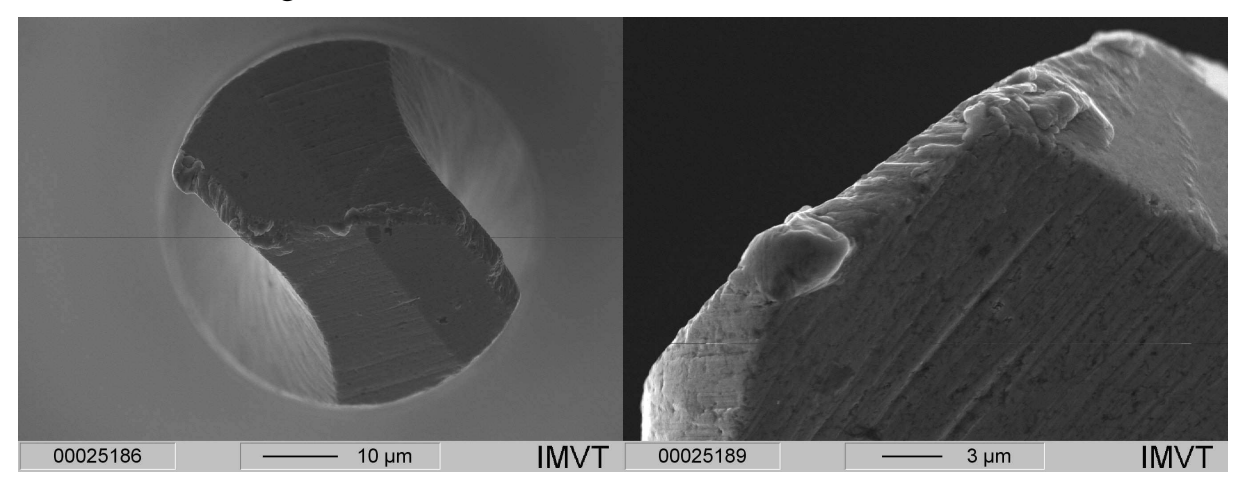


Fig. 8. Used 50 µm micro drill bit with wear marks

# 3. MACHINING RESULTS AND FINISHING BY ELECTROPOLISHING

After removing the sputter mask from the glue, the edges of the holes were found to be burred (Fig. 9 and Fig. 10). Due to the plasticity of the material and reduced chip breaking compared to MS58, burr formation was very pronounced, especially at the bottom of the brass sheet (Fig. 10). It is not possible to use a mask of such a poor quality for sputtering, since the burrs would prevent tight fitting to the photoresist or could damage it when adjusting the position.

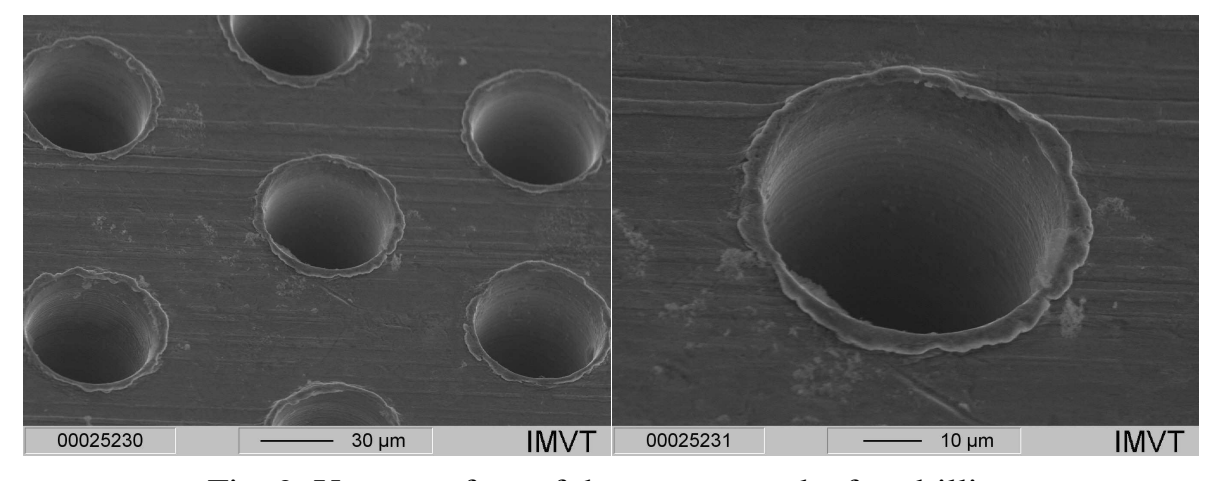


Fig. 9. Upper surface of the sputter mask after drilling

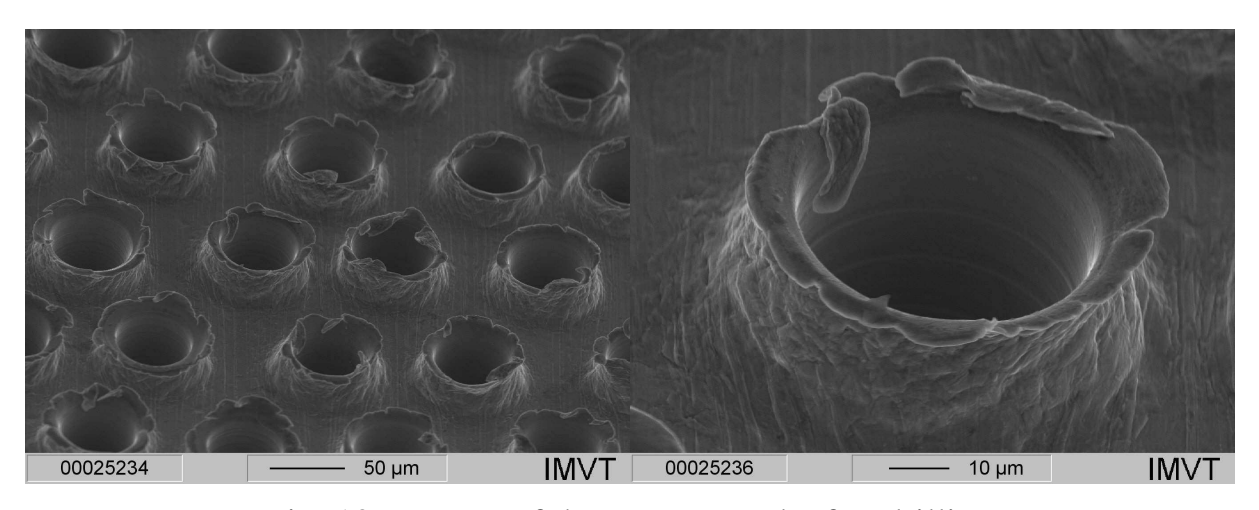


Fig. 10. Bottom of the sputter mask after drilling

Contrary to the lead-containing brass MS58, however, it is possible to electropolish MS63 very well. Due to the inert oxide layer on lead, alloys containing this metal behave like a two-phase material during electrochemical local element formation. Lead could not be removed electrochemically. Since ignoble material is removed, lead particles are exposed and subsequently protrude from the surface.

The sputter mask was electropolished using Polstar B1 by Enthone GmbH. Polstar B1 contains phosphoric acid and is applied at a temperature between 20-23°C [3]. The voltage is in the range between 6-10 V and current density should not exceed 5-6 A/dm². The material removal rate is between 1-3  $\mu$ m/min. The process was interrupted every 2 min and the result observed using a stereo microscope. After finishing, SEMs were made to monitor the result.Fig. 11 and Fig. 12 show that all burrs could be removed and a smooth surface was generated even at the bottom that had been subject to heavy burr formation.

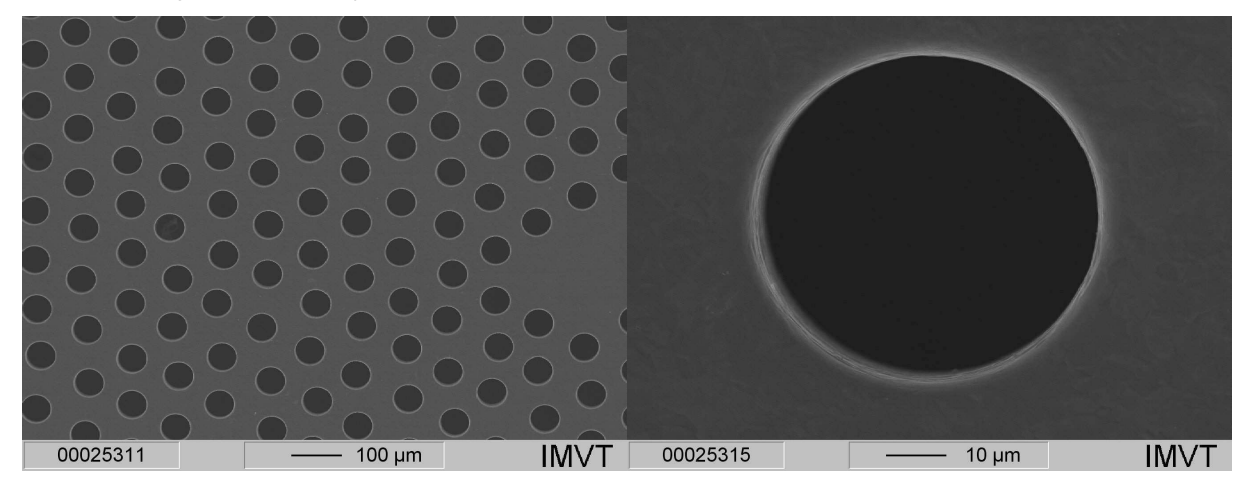


Fig. 11. Surface of the sputter mask after electropolishing

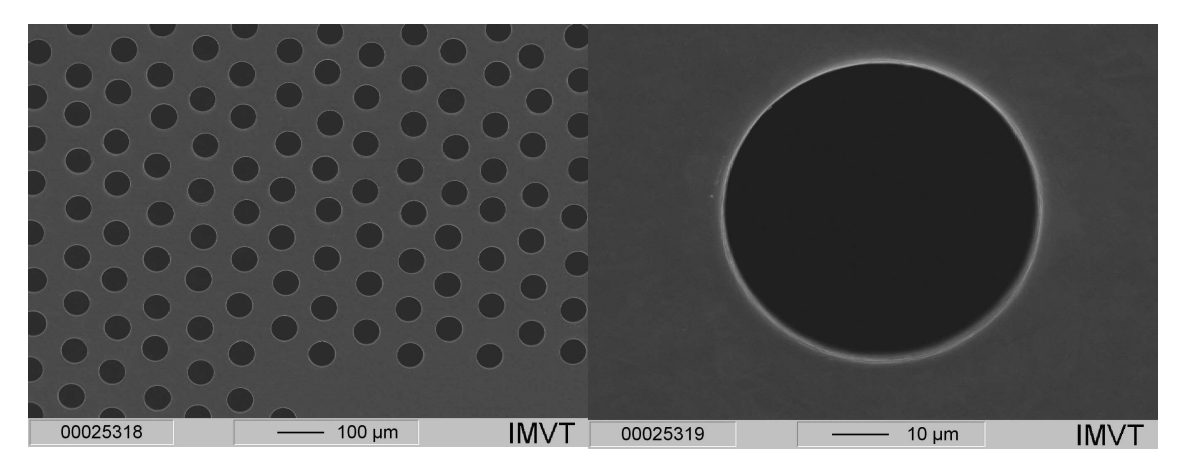


Fig. 12. Bottom of the sputter mask after electropolishing

#### 4. CONCLUSIONS

Manufacturing of a sputter mask with more than 100,000 holes showed that microdrilling is a stable process over a long period, if the machining parameters are optimized. Tool failure was not observed despite several hours of machining time per tool and considerable wear marks on the microdrills used.

In addition, microdrilling is a very flexible process compared to etching or lithographic processes, where a new photo mask is required for each design variation.

However, the formation of burrs must be taken into account. For this reason, appropriate workpiece materials have to be selected for successful finishing operations like electropolishing.

It was demonstrated that even heavy burrs could be removed by electropolishing, thus generating a very smooth surface. It has to be mentioned that electroplating removes material according to the field line density. For this reason, it is important to have a uniform burr formation all over the microstructure. It is essential to stop the process at the right time when the burrs have gone, but the edges are still sharp. Irregular burr formation will lead to partly rounded edges.

#### 5. ACKNOWLEDGEMENT

The authors wish to thank Dennis Scherhaufer for his substantial work in optimizing the machining parameters and testing several joining procedures for fixing the workpiece and achieving a flat surface.

#### 6. REFERENCES

- 1. Winter S., Wilson S., Guttmann, M., 2009: "Partielle Resistmetallisierung für hohe Aspektverhältnisse", Mikroproduktion, No.3, pp. 46–50.
- 2. Guttmann M., Walch E., Schanz G., Konys J., 2000: "Mikrostrukturen herstellen. Galvanische und außenstromlose Abformung von verlorenen Kunststoffformen", Metalloberfläche, vol. 54, No.11, pp. 16–28.
- 3. Gietzelt T., 2008: "Einsatz des Elektropolierens in der Mikrosystemtechnik", Galvanotechnik, vol. 99, No. 2, pp. 456–461.

#### IR LIDAR SOUNDING OF ATMOSPHERIC GASES

### Valerik S. Ayrapetyan, Oleg K. Ushakov, Russian Federation

**Keywords**: IR(Infrared), OPO(Optical parametric oscilator), Lidar, FPE(Fabry-Perot etalon).

### **Summary**

Automated differential lidar set for measurement of atmospheric gases small concentration is developed, created and tested on the bases of Optical Parametric Oscillator (OPO), tunable in middle infrared (IR) range.

Measurable sensitivity accuracy obtained for atmospheric methane is not less than 1 ppm. Being smoothly tunable in the wavelength range of 1.4 ÷ 4.2um with the spectral bandwidth of 3cm<sup>-1</sup> (for 1.4÷1.8um and 2.9÷4.2um) and pulse energy up to 40mJ, the OPO irradiation allows measurement of gas concentrations in an open atmosphere up to 5km. If required computer controlled Fabry-Perot etalon (FPE) insertion into the resonator is provided to narrow the bandwidth up to 0.6cm<sup>-1</sup>. Construction of the OPO allows also radiation wavelength stepwise change (pulse to pulse) with a smooth regulation from 0 to 12cm<sup>-1</sup> that is necessary to carry out gas concentration measurement by the method of differential absorption with one laser. Lidar set is equipped with a self-regulated system, tuned at the absorption line of the gas under investigation that is initially installed into the system.

#### Introduction

Activity expansion of the industrial companies is accompanied with the increase of hazardous industrial and anthropogenic emissions. Remote laser systems, Lidar set in particular allows highly accurate identification of the molecular constituents of the atmospheric gases. These type of sets can operate both on stationary platforms, as well as on vehicles and aircrafts. Among all types of lidars those operating by the principle of differential absorption and scattering (DAS) and combining high sensitivity and spatial resolution, prove to be the most universal ones. This method is based on the comparison of two back scattered laser pulses, one from the maximum of absorption line and the other from the wing of the line [1].

It is also known [2, 3], that the fundamental rotationally-oscillatory absorption bands, combined frequencies and intensive isolated lines of practically all molecules of atmospheric gases are at the near and middle IR range. In this connection the IR Lidar investigations of spectroscopic parameters of the atmospheric gases by DAS method is of certain interest.

In the recent years there is an information on the increased sensitivity of IR Lidar sets operating by DAS method [4, 5, etc.], however these sets are used either two OPO sources, or one OPO with wide irradiation spectral line and with modest output energy. For the last decades SSGA Novosibirsk, Russia has concentrated its efforts on the investigation of solid-state laser sources of IR radiation, that are capable of smooth and/or discrete tuning of the wavelength, simultaneously

maintaining high monochromaticity and energy pick-up [7]. Such laser sources are a basis for IR Lidar sets that are capable of investigating spectral parameters of the atmospheric gases.

### Operation principle of IR Lidar

Requirement compliance to international health standards on use of eye-safe laser radiation, remote and local monitoring and control of the environment [8,9], on one hand, and high-energy, monochromaticity and high sensitivity of the sensors, on the other hand, determine the main requirements to Lidars operating in the range of optical transparency of the atmosphere.

Fig. 1 shows the Lidar set, and Fig. 2 gives its optical scheme.



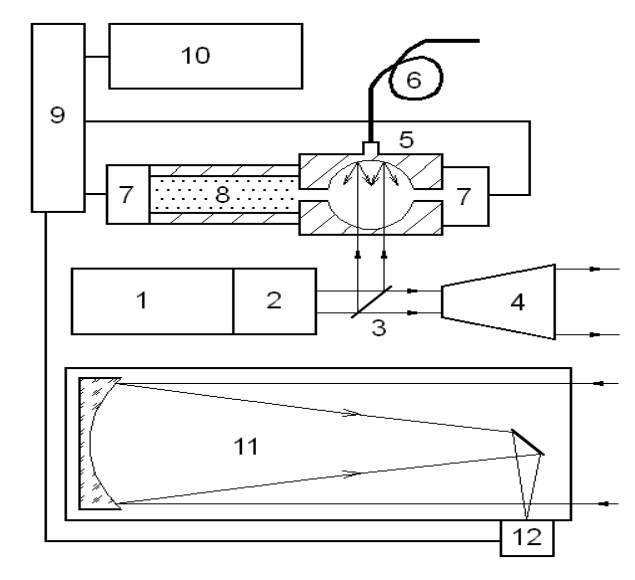


Fig. 1. IR Lidar in action

Fig. 2. Optical scheme of IR Lidar

The OPO (2) based on the ring-type resonator with a LiNbO<sub>3</sub> crystal provides effective conversion of the pulsed Nd:YAG laser ( $\lambda$ = 1.06um) (1) radiation into a spectral range of  $\lambda = 1.41 \div 4.2$ um wavelength. Computer controlled highly accurate rotating table, in horizontal plane, carries out smooth tuning of the wavelength by a LiNbO<sub>3</sub> crystal. It is also possible to change the OPO radiation discretely, applying DC voltage of 0 to 5kV to the side surfaces of the LiNbO<sub>3</sub> crystal, with the regulated width of the step varied from 0 to 12cm<sup>-1</sup>. Discrete pulse-to-pulse shifting of the OPO radiation wavelength is realized using one laser to measure gas absorption intensity at the line maximum and its wing. OPO radiation wavelength change due to heating of the LiNbO<sub>3</sub> crystal is PC controlled and compensated with up to 0,1°C accuracy. For radiation bandwidth narrowing, by necessity, the FPE insertion into the OPO resonator is also provided. Total output OPO energy at pulse duration 10ns varies within 1÷40mJ range, depending on the wavelength. Definition of the absolute value of the OPO wavelength ( $\lambda_{mes}$ ) is carried out by the method of  $\lambda_{mes}$  correction with the known gas absorption line. For this purpose the part of the OPO radiation (~3 %), enters to the diffusion-scattered sphere (5), after reflection from the flat parallel CaF<sub>2</sub> plate (3). The scattered radiation of the first channel enters to the receiver (7), by

passing through the cell (8) with known gas (in this case with 90% pure methane at 1atm pressure). Simultaneously, the scattered radiation of the second channel enters directly to the next identical photo-receiver (7). The electrical signals from the photo-receivers arrive to the two inputs of the analog-digital converter (ADC) (9), which is connected to the PC (10). The rotationally-oscillatory absorption spectrum of  $\upsilon_3$  band of methane, the central Q- branch of which is considered to be the initial point, is displayed on the PC monitor. Special software processes the received data, corrects it with the Q-branch and displays the real values of OPO ( $\lambda_{mes}$ ) wavelengths on the monitor. For OPO wavelength calibration on the scattering sphere, the possibility of IR light guide (6) installment is also foreseen, through which the laser radiation enters to the monochromator's slot.

After expanding and collimation (4) the main part of the OPO radiation is directed to the topographic target along the atmospheric trace, the gas constituents of which is being investigated. Constructively laser emitter with the receiving telescope (11) is installed on the computer controlled two-axes platform. A micrometric screw carries out highly accurate coincidence of laser radiation with the field of vision of the receiving telescope controlled by the CCD camera. Image of the topographic target is also displayed on the monitor. The back-scattered radiation from the topographic target is receiving by the 30cm Newton telescope (11), in the focal surface of which the cryogen InSb photo-receiver (12) is located. The signals received on the photo-receiver are processed and the real spectrum of the atmospheric gas absorption is displayed on the PC monitor.

The present Lidar set allows scanning of atmosphere transparency in the range of  $1.41 \div 4.2$ um and simultaneously measures gas concentration in the atmosphere.

Table 1 presents the main technical parameters of Lidar set.

Table 1. Main technical parameters of Lidar set

Laser type	YAG:Nd <sup>+3</sup> with OPO
Tuning wavelength	1.41÷1.85; 2.9÷4.1um
Pulse energy	1÷40mJ depending on wavelength
Radiation spectral width	3÷3.5cm <sup>-1</sup>
Repetition rate	20Hz
Wavelengths shifting	0÷12cm <sup>-1</sup>
Pulse duration	10ns
Distance to the object	2÷5km (methane)
Registration sensitivity	1ppm along the integral trace (methane)
Platform rotation angle across	$\pm 30^{0}$
Platform rotation angle in vertical	$-10^{\circ} \div +25^{\circ}$
Platform setting accuracy towards the object	0.8mrad

# Results of the experimental measurements and comparison with the calculations

From the basic Lidar equation for laser pulse back scattering [1, 10] applied to the boundary conditions of our Lidar system is:

$$P(\lambda_0, R) = P_0 \xi(\lambda_0) (\rho^s \tau_d / \tau_L \pi) A_0 R^{-2} \xi(R) \exp\left[-2 \int_0^R \alpha(r) dr\right]$$
 (1)

From the above equation we can obtain the minimal laser energy equation:

$$P_{0 \min} \approx 2 R^2 (S/N)_{\min} / \{ \xi(R) \rho^s / \pi U (\lambda_0) \exp \left[ -2 \int_0^R \alpha(r) dr \right] \}$$
 (2)

Where: U ( $\lambda_0$ ) is the modified parameter of the receiving system.

In (1) P ( $\lambda_0$ , R) is the instant value of the applied laser pulse power, P<sub>0</sub> - is the sent laser radiation power,  $\xi(\lambda_0)$  – is the spectral transmission coefficient of the receiving optical; system,  $\rho^s$  - coefficient of the back scattering for the topographic target,  $\tau_d$  – is integration period of detector,  $\tau_L$ - is the pulse duration, A<sub>0</sub>- is the receivers effective area, R- is the distance to the topographic target,  $\xi(R)$  – is the geometric factor of the lidar system,  $\alpha(r)$ -is the relaxation volume coefficient.

It is possible to obtain minimal output energy, necessary to register the gas concentration at the ppm unit level in reality.

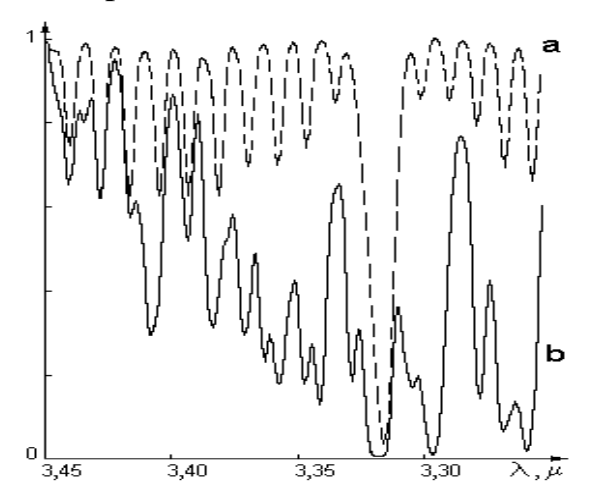
The corresponding calculations according to (1) and (2) show that the minimum output energy of laser for atmosphere sounding of up to 5km should be more than 10mJ, which is obtained in the given work.

As an experimental sample and available pollutant the methane molecule was chosen (CH<sub>4</sub>) the background existence of which in the atmosphere of Yerevan city corresponds to 1.7ppm. It is well known [11], that among the four fundamental rotationally-oscillatory absorption bands of the methane molecule, the  $\upsilon_3$  band with the central Q-branch (3020cm<sup>-1</sup>) is considered to be the most intensive one, which is located within the tunable range of the parametric laser (1.4 ÷4.2um).

In order to measure methane concentration with a high accuracy and sensitivity, it was necessary to carry out preliminary calculation and experimental works on measurement of atmospheric transmission spectrum in the wavelength range of  $3.25 \div 3.45$ um with a better resolution than the width of separate lines of P, Q and R of  $\upsilon_3$  branch band of the methane absorption. Fig 3 gives the calculated absorption spectrum of  $\upsilon_3$  methane band at 1.7ppm concentration at a distance of 2km and sum absorption spectrum of  $CH_4$  and  $H_2O$  correspondingly, at probing laser radiation line width of  $3.0\text{cm}^{-1}$ , with scan step of  $0.1\text{cm}^{-1}$ . Fig 4 gives the experimentally measured spectrum of  $\upsilon_3$  methane band and experimentally obtained atmosphere absorption spectrum in the range of  $3.25 \div 3.45$ um (scanning accuracy is  $0.1 \text{ cm}^{-1}$ ), where main radiation absorbers are considered to be  $CH_4$  and  $H_2O$ .

While comparing the calculated (Fig.3a) and experimental (Fig.4a) spectra it is possible to note good frequency coincidence of certain lines of P, Q and R branches of  $v_3$  methane band, with experimental error accuracy (~2 %). Relative intensities of certain lines of P and R branches also do correlate well enough. From the spectrum it is seen that the R branch (< 3.30 um) is completely closed, Q branch (3.312um) and part of P branch (3.35÷3.45 um) appear weakly. Lines P7 and P9 are more or less observed and the atmosphere is transparent only in the region of line P10. That is why for the methane concentration measurement the radiation wavelength of the first OPO pulse is set at maximum absorption of the P10 ( $v_{max}$ ) line, whereas the following

shifted pulse is discretely tuned at the null level of that line ( $\nu_{min}$ ). The back-scattered signals of these frequencies are directed to the photoreceiver, in the ADC transform into numerical form and the relative signals are displayed on the PC monitor. According to [12], with the help of these signal intensities it is possible to calculate the atmospheric methane concentration.



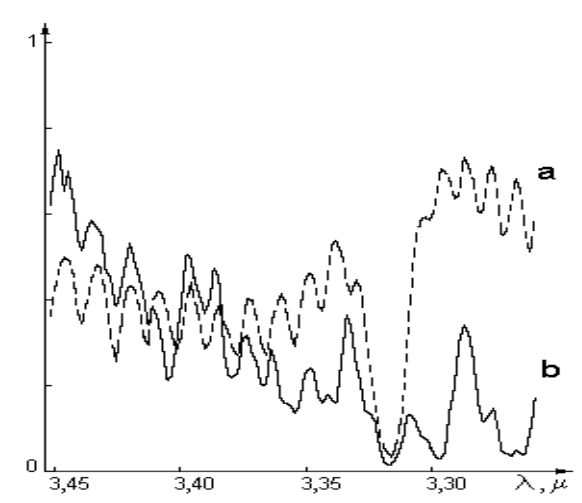


Fig. 3. Calculated transmission spectra CH4 (a) and CH<sub>4</sub>+H<sub>2</sub>O (b) for OPO radiation line width of 3cm<sup>-1</sup>

Fig. 4. Measured spectra CH<sub>4</sub> (a) and atmosphere transmission spectrum at the distance of 2200m (b)

Fig. 5 gives relative back-scattered signals of the methane flow that are registered close to Lidar set (a) and scattered from the topographic target (b) at the distance of 2.2 km at an average height of 50m from the ground

The moment, when the methane is extracted from the balloon, Lidar set sensor registers drastic signal increase, the level of which is maintained at some value, different than that of the background, while there is a leakage of methane. After the gas leakage stops the signal starts relaxation, with some fluctuations, back to the background level. The fluctuation character is probably due to non-homogenous gas flow and the weather conditions (wind, humidity, etc.). Measurements were carried out by averaging of 10 pulses at each point, at laser repetition rate of 20 Hz.

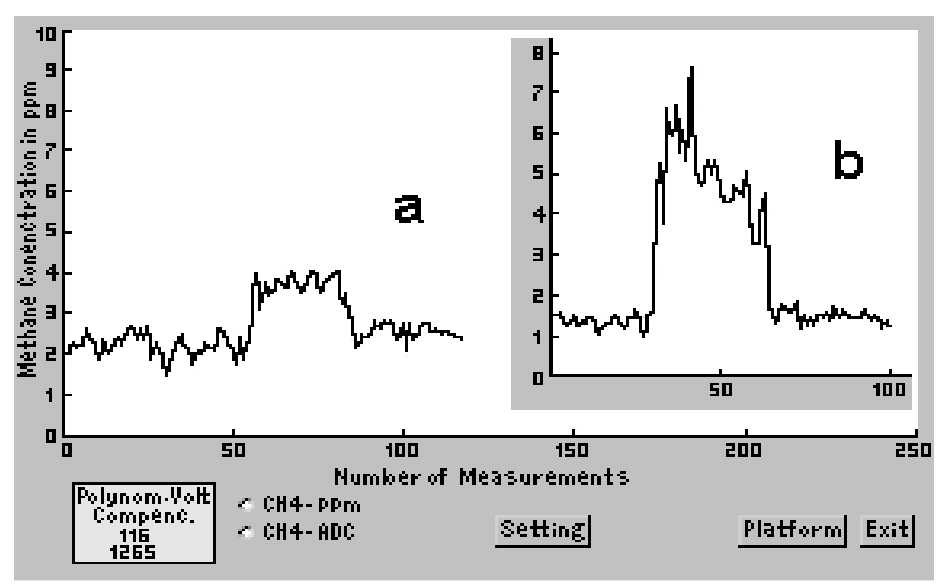


Fig.5. Methane concentration measurement close to Lidar (a) and at the distance of 2.2km (b)

The results of data processing of the calculated and experimental spectra are given in Table 2.

Table 2. Calculated and experimental spectra of atmosphere absorption in a range of lengths of waves 3.25 - 3.45 mkm at the distance of up to 2.2 km

Branch	$\frac{\Delta v_p}{cm^{-1}}$	$\Delta v_{\rm 3KC.}$ $cm^{-1}$	$\Delta v_{cm,}$ $cm^{-1}$	v <sub>0</sub> (расч.) см <sup>-1</sup>	v <sub>0</sub> (экс.) см <sup>-1</sup>	I <sub>расч., отн.</sub> ед.	${ m I}_{ m 9KC},$ отн. ед.
Q	5.2	7.79	2.59	3015.9	3014.6	0.91	0.63
P1	3.2	-	-	2999.76	3008.14	0.13	-
P2	4.46	-	i	2987.62	2995.3	0.24	0.075
P3	3.79	5.08	1.29	2976.19	2981.25	0.27	0.094
P4	3.78	3.785	0.05	2969.86	2970.49	0.27	0.074
P5	4.37	5.01	0.64	2957.35	2959.8	0.34	0.188
P6	3.11	6.21	3.10	2947.37	2948.61	0.34	0.014
P7	3.085	4.93	1.85	2937.47	2936.24	0.34	0.28
P8	3.67	-	1	2926.16	2931.31	0.34	0.19
P9	3.64	4.85	1.21	2914.82	2910.61	0.36	0.14
P10	3.62	4.83	1.21	2906.94	2905.77	0.19	0.19

Let's note high compliance of corresponding central frequencies of the calculated ( $n_0$  (calculated)) and experimental ( $n_0$  (ex.)) spectra, separate lines of the P, Q and R branches of the  $v_3$  fringe (band) of methane. The accuracy of compliance is not worse than  $\pm 0.13$  %.

There is no spectral displacement of the  $v_3$  fringe of methane that is basically due to the average speed of relative movement of molecules of gas in the atmosphere, as during the measurements there was a windless weather. At the same time, from the experimental spectrum (Fig.2) it is seen that the Q-branch and separate lines of the P-branch are widened. It could be explained both by the Doppler broadening (temperature influence), and by the influence of water vapour and aerosol particles

(collisional broadening). The latter factors have an impact on the spread of the corresponding values of the relative intensities when comparing calculated  $(I_P/I_Q)_{pacq.}$  and experimental spectra  $(I_P/I_Q)_{_{3KC}}$ .

Minimal allowable concentration of methane in the open atmosphere has been calculated on the basis of these signals' intensities, according to [13]:

$$[N(R)]_{\min} = \frac{1}{2\Delta\sigma(\nu)\Delta R} \ln[1 + \frac{1}{(C/III)_{\min}}]$$

Where:  $C\backslash III$  (R) – the ratio a "signal/noise" at the distance R from the lidar,  $\Delta\sigma(\nu) = \sigma(\nu_{max}) - \sigma(\nu_{min})$  – differential section on a maximum and on a minimum of absorption of the given molecule,  $\Delta R$  – extent of area of sounding.

Thus, the calculated value of the minimal concentration of methane in the open atmosphere does not exceed 1ppm that is confirmed by the experimental measurements.

#### **Conclusion**

The analysis results of obtained data showed the following:

- 1. For the remote trace measurements of gas concentrations the high-energy (>10mJ) lasers with smooth and/or discrete wavelength are most suitable tuning.
- 2. To provide sensitivity and accuracy for gas concentration measurement with DAS method it is expedient to use an OPO, tunable along the wavelengths, with the laser spectral width  $\leq$  to the width of lines of the gas absorption band under investigation.
- 3. Spectral areas P7, P9 and P10 of  $v_3$  absorption band the methane are the most optimal ones for methane concentration measurement in the atmosphere at the level of background values.
- 4. The present Lidar set on the basis of DAS method, allows remote registration of gas absorption spectra, rotationally-oscillatory bands of which are within the range of tunable laser radiation (1.4÷4.2um). The concentration and line width of the investigated gas should be no less than 2ppm and 3cm<sup>-1</sup>, correspondingly.

#### References

- 1. Mezheris R. Remote Laser Sensing. M.; Mir, 1987, 550 c.
- 2. L.S. Rothman, R.R. Gamache, R.N. Tipping e.a. The HITRAN Molecular Database: edition of 1991 and 1992, JQSRT, 1992, V 48, P. 469–507.
  - 3. Yelyashevich M.A. Atomic and Molecular Spectroscopy M. 1962, 892 c.
- 4. Kabanov M.V., Andreev Yu.M., Geiko P.P. Emission Monitoring of Anthropogenic and Natural Methane. Present. II International conference on Methane Emission Reductions, Novosibirsk, 2000. 800 c.
- 5. Takuya Nayuki, Tetsuo Fukuchi, Nianwen Cao, Hideto mori, Takashi Fujii, Koshichi Nemoto, and Nobuo Tekeuchi. Sum-frequency-generation System for Differential Absorption Lidar Measurement of Atmospheric Nitrogen Dioxide, Appl. Opt., 41, No.18, pp.3659-3664 (2002).
- 6. G.M. Apresyan, V.S. Ayrapetyan, K.A. Sargsyan, T.K. Sargsyan. "Tunable OPO for Differention Absorption LIDARs". LAT 2002, Moscow (2002) 89.

- 7. Lasers and Optical Radiation Environmental Health Criteria. Geneva (1982).
- 8. Koechner W. Solid statelaser engineering (Berlin:Springer-Verlag, 1999).
- 9. Laser Control of the Atmosphere. Edit. E.D.Hinkly, M. 1979, 416 c.
- 10. W.L. Barnes, F.J. Susskind, R.H. Hunt, and E.K. Plyler.Measurement and Analysis of the  $\nu_3$  Band of Methane, The Journal of Chemical Physics, v. 56, No.10, pp. 5160–5172 (1972). Scotland R.M., J. Appl. Meteo.

#### **CONTACTS**

### Prof. Oleg K. Ushakov, PhD

Director of the Institute of Optics and Optical Technologies

Siberian State Academy of Geodesy

10, Plakhotnogo St..

Novosibirsk, 630108

**Russian Federation** 

Tel/Fax: +7(383) 344-40-58 E-mail: inst.oot@ssga.ru

www.ssga.ru

### Valerik S. Ayrapetyan, PhD

Siberian State Academy of Geodesy

Department of Physics

10, Plakhotnogo St.

Novosibirsk, 630108

**Russian Federation** 

Mobile: +7 913 462 10 75

E-mail: v.hayr100011@mail.ru

© V.S. Ayrapetyan, O.K. Ushakov, 2010

# TERMOMECHANICAL PROCESS IN MULTI-LAYER NANOSTRUCTURES INITIATED BY LASER IRRADIATION

## Vladimir V. CHESNOKOV, Dmitry V. CHESNOKOV, Valery A. RAYHERT

SSGA, Novosibirsk, Russian Federation, e-mail: phys003@ngs.ru

#### **Abstract**

Theoretical models and methods to calculate the thermal fields and thermomechanical process in the multilayer structures on substrates exposed to laser step shaped pulse are present. The spatial-temporal distribution of temperatures in a four layer thin-film nanostructure is studied, and values for displacements of outer boundary of the structure which are induced by laser irradiation are obtained.

The purpose of this work was to investigate the dynamics of changes in the thermal field induced in the layered nanostructures on the substrate surface by the laser pulse with sharp wavefront edge i.e. with the pulse rise time less than time of thermal wave passage through the structure layer and induced by irradiation of the physical processes in the structure layers. Values of the medium physical parameters in the laser irradiation region was estimated as well as the intensity of the processes occurred in the structure both as thermoelastic processes and with phase transition of the film material. The thermal expansion of layers leads to the outer edge movement. As an example the processes in the structure with layer thickness of 10–100 nm was analyzed.

The number of studies of the non-steady thermal fields in the monolayer coverage on substrates is known. So, the analysis of the propagation of the thermal wave induced by the continuous laser irradiation through a thin plate with multiple reflections from the plate surfaces taken into account is analyzed in the work [1]. The thermal wave propagation though metal film on the metal substrate considered as well. The thermal energy distribution between the film and the substrate under pulse laser irradiation is considered in the paper [2]. The formulas for the calculations of the thermal field in the structure of "film on the substrate"-type are presented in the paper [3] for different laser pulse shapes. In the work [4], the expression for maximum temperature of the surface of film on substrate during the pulse duration is obtained, and the intensity of the mechanical pulses caused by the thermal expansion of the surface layers on the substrate which spreads to the substrate. In the work [5], the pulse theory of thermal conductivity of solids including solids with layered structure is presented. The references of studies on light-induced thermoelastic stresses in the semi-infinite target are presented in the paper [1].

In this work, in order to determine changes of thermal field and spatial distribution taking place when the thin-layer structure is exposed to the laser irradiation, the Fourier expansion of thermal pulse [5] is used as well as the method of electric analogies. Mechanical stresses and deformations concomitant to the heating are also determined.

At the beginning let us consider thermokinetic processes in the multilayer structure (Fig.1) occurring during the laser pulse absorption in the outer surface of the structure.

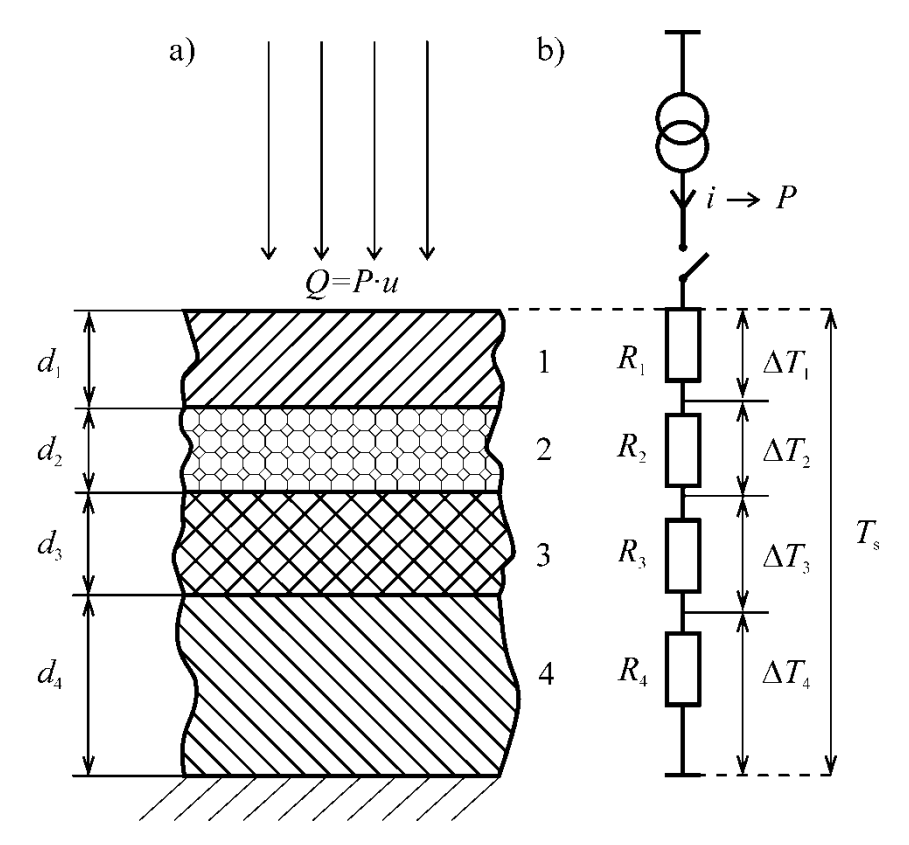


Fig. 1. Multilayer structure (a) and corresponding analog electric scheme (b) for steady-state irradiation rate

Assume that time dependance of exposure is step shaped: P(u) = 0 when  $u \le 0$ ;  $P(u) = P_0$  when u > 0; where u is a exposure time,  $P_0$  – power density of irradiation incident on the surface on the first layer.

Surface density of the energy absorbed by the first layer is:

$$Q_s = P_0 u (1 - R_{refl}) = P_S u, (1)$$

Where:  $R_{omp}$  – reflection index;  $P_S = P_0 (1 - R_{refl})$ .

At further consideration the thermal changes of material thermophysical characteristics is neglected. Output surface temperature of the last layer is assumed to be time-independent and to be equal to the value before irradiation started. Volumetric heat capacity  $\gamma$ , thermometric conductivity h, thermal conductivity k and thickness d of the layers has indexes corresponded to the layer number.

In the case of infinite continuation of the irradiation, the process of thermal transmission through the multilayer structure will be steady, and the heat flow in the all layers is equal to the flow of absorbed part of the incident radiation. Calculations can be done taking recourse to the electric analogy, where heat flow  $P_s$  is corresponded to the electric current i. Equivalent electric scheme of the current generator, simulating the heat flow in the structure of layers is shown in the Fig.1b.

In the scheme (Fig.1b)  $R_1, R_2, R_3, R_4$  are electric resistances equivalent to the thermal resistances of the layers;  $\Delta T_1, \Delta T_2, \Delta T_3, \Delta T_4$  - temperature differences of the layers surface equivalent to electric difference of electric potentials.

As the heat flow has the same value in the all layers of structure, the following expression is correct:

$$T_{\infty S} = \Delta T_1 + \Delta T_2 + \Delta T_3 + \Delta T_4 = P_s \left( \frac{d_1}{k_1} + \frac{d_2}{k_2} + \frac{d_3}{k_3} + \frac{d_4}{k_4} \right). \tag{2}$$

Where fractions within brackets are the resistances of the layers,  $T_{\infty s}$  -temperature increment of outer surface of the structure for the steady regime.

Physical pattern of the thermal phenomena in the thin-film structure during the transient process of the establishing of steady thermal field is characterized as described further:

Temperature at the any point of the structure embraced by a wave is increasing with time. Heat flow, appeared in the first layer, travels deep through the layered structure in the form of thermal wave. Differences in the thermal conductivity and thermal capacitance of the layers material lead to the changes of the heat propagation velocity in the layers and to the dependance of the temperature spatial-time distribution in the layer on the thermal processes in the next layers. Appearance of the heat absorbing phase transition when the heat absorption continues can be represented as appearance of the negative thermal pulse in this layer. The thermal pattern of the influence of such a pulse on the surrounding layers overlaps with the thermal pattern due to the heating of the structure by external radiation. The possibility of existence of a layer with phase transition leads to the possibility of negative pulse to appear not only during transient process but also at the stage of reaching the steady thermal state.

It is quite complicated to obtain an analytic expression for the thermal field in the multilayer structure and for the temporal evolution of this field, in the transient state. Therefore the number of approximations is taken for the further analysis. Let us assume the film structure as the system of elements with lumped parameters for simplicity. Then, on the analogy with the electric circuits let us use the concept of time constant

$$\tau = RC = \frac{d}{k} \cdot \gamma d = \frac{d^2}{h}.$$
 (3)

Where:  $\tau$  – layer heating time constant, h – thermometric conductivity.  $\tau$  approximately characterizes the time of the thermal wave wavefront passage through a layer.

Fourier's low of heat transfer is presented in the work [5] in the form of onedimensional heat transfer equation:

$$\frac{\partial T}{\partial t} = h \frac{\partial^2 T}{\partial x^2}.$$
 (4)

In this work it was obtained that at the heat release conditions mentioned above, the temperature distribution in the uniform layer of medium has a form of spatial pulse, which can be represented with a series using Fourier method:

$$T(t,x) = \frac{2P_S}{\gamma d} \int_{u_1}^{t} \sum_{m=0}^{\infty} \cos \frac{(2m+1)\pi}{2} \frac{x}{d} \cos \frac{(2m+1)\pi}{2} \frac{l}{d} \times \exp \left[ -\frac{(2m+1)^2 \pi^2}{4d^2} h(t-u) \right] du$$
(5)

Where: u – duration of time when the heat releases in the layer with coordinate l of uniform side;  $u_1$  – moment when the heat release starts; t – time of the observation of the temperature changes (independent of the heat release duration); m – number of series term. When  $u_1$  = 0, heat release occurs on the input surface of the side (l = 0), reference time of observation is equal to the heat release start time (t = u), and one can obtain:

$$T(t,x) = \frac{2P_S}{\gamma d} \sum_{m=0}^{\infty} \cos \frac{(2m+1)\pi}{2} \frac{x}{d} \int_{0}^{t} \exp \left[ -\frac{(2m+1)^2 \pi^2}{4d^2} h(t-u) \right] du.$$
 (6)

After integration (6) we have:

$$T(t,x)=$$

$$= \frac{8P_{S}d}{\gamma h} \sum_{m=0}^{\infty} \frac{\cos\left[\frac{(2m+1)\pi}{2} \frac{x}{d}\right]}{(2m+1)^{2} \pi^{2}} \left\{1 - \exp\left[-\frac{(2m+1)^{2} \pi^{2}}{4d^{2}} ht\right]\right\}.$$
(7)

Exponential term decreases rapidly when increasing m. If  $\frac{ht}{d^2} \ge 0,005$  than within curly brackets one can neglect almost all terms with the exception of terms with c m = 0, m = 1, m = 2 u m = 3 (within the error of temperature calculations of about 5%), which allows us to represent the sum of series as:

$$\sum_{m=0}^{\infty} = \sum_{m=0}^{\infty} \frac{\cos\left[\frac{(2m+1)\pi}{2} \frac{x}{d}\right]}{(2m+1)^{2} \pi^{2}} - \sum_{m=0}^{3} \frac{\cos\left[\frac{(2m+1)\pi}{2} \frac{x}{d}\right]}{(2m+1)^{2} \pi^{2}} \exp\left[-\frac{(2m+1)^{2} \pi^{2}}{4d^{2}} ht\right]. \quad (8)$$

Taking into account that  $0 \le \frac{x}{d} \le 2$ , the first sum at the right side of Eq. (8) is equal to [5]:

$$\sum_{m=0}^{\infty} \frac{\cos\left[\frac{(2m+1)\pi}{2} \frac{x}{d}\right]}{(2m+1)^2 \pi^2} = \left(1 - \frac{x}{d}\right) / 8.$$
 (9)

Finally, taking into consideration Eq.(3), the spatial-time distribution of temperature increment in the layer, when the temperature of layer output surface kept constant:

$$T(t,x) = \frac{P_{s}\tau}{\gamma d} \times \left\{ \left(1 - \frac{x}{d}\right) - \frac{8}{\pi^{2}} \sum_{m=0}^{3} \frac{\cos\left[\frac{(2m+1)\pi}{2} \frac{x}{d}\right]}{(2m+1)^{2}} \exp\left[-\frac{(2m+1)^{2}\pi^{2}t}{4\tau_{0}}\right] \right\}$$
(10)

Providing that  $t/\tau_0 \ge 0.005$ , only four first term in series (10) are taken into account, and providing that  $t/\tau_0 \ge 0.2$  it is sufficient to consider only two terms. Equate  $t = \infty$ , x = 0, we obtain:

$$T_{\infty S} = \frac{P_S \tau}{\gamma d} \qquad (11)$$

It follows from the last expression that the factor before curled brackets (10) means the increment of temperature  $T_{\infty S}$  of the input layer surface for infinite time of heating. Considering (2), one can obtain:

$$T_{\infty S} = \sum_{1}^{N} \Delta T_i , (12)$$

Where N is a number of the layer in the multilayer structure next to the substrate.

Let us replace real multilayer structure with multilayer side with coordinate axis y, which has the same temperature of input surface and same constant thermal current through input surface as multilayer structure, but unlike the multilayer structure determine the value of thermometric conductivity  $h_1$  of the first structure layer for all layers. In this case sections thicknesses  $D_i$  have to be such as the time constants of sections remains as for corresponding structure layers, i.e. in order to fulfill the condition:  $D_i = d\sqrt{h_1/h_i}$ . Thermal conductivity indexes  $K_i$  should be such that their thermal resistance also remains equal to the thermal resistance of corresponding layers:  $d_i/k_i = D_i/K_i$ , where  $K_i = k_i\sqrt{h_1/h_i}$ . In a steady regime, temperatures both of layers and sections is determined by Eq. (2). Sections coordinates  $y_i$  of an analog side is measured from input surface of analog side, which coincides with input surface of the first structure layer. For this surface  $y_i = 0$ .

In order to obtain equation for spatial-time distribution of temperature in the analog side, let us do the following replacements in Eq. (10):

$$x / d \to y_i / D$$
,  $\tau_0 = \frac{d^2}{h} \to \tau_D = \left(\sum_{i=1}^N \sqrt{\tau_i}\right)^2$ . (13)

Where:  $D = \sum_{i=1}^{N} D_i$  – analog side thickness,  $\tau_D$  – it's time constant. After replacements we have:

$$T(t,x_{i}) = T_{\infty S} \left\{ \left(1 - \frac{y_{i}}{D}\right) - \frac{8}{\pi^{2}} \sum_{m=0}^{2} \frac{\cos\left[\frac{(2m+1)\pi}{2} \frac{y_{i}}{D}\right]}{(2m+1)^{2}} \exp\left[-\frac{(2m+1)^{2} \pi^{2}}{4} \frac{t}{\tau_{D}}\right] \right\}, (14)$$

Where:  $T_{\infty S}$  – temperature increment of the input surface of analog side for the steady heating regime, equal to the temperature increment of the input surface of the multilayer structure for the same regime

$$T_{\infty S} = \sum_{i=1}^{N} \Delta T_{\infty i} . (15)$$

For the steady regime  $(t = \infty)$ , the equation (14) comes to the following:

$$\frac{T\left(\infty, y_i\right)}{T_{\infty}} = 1 - \frac{y_i}{D}. \quad (16)$$

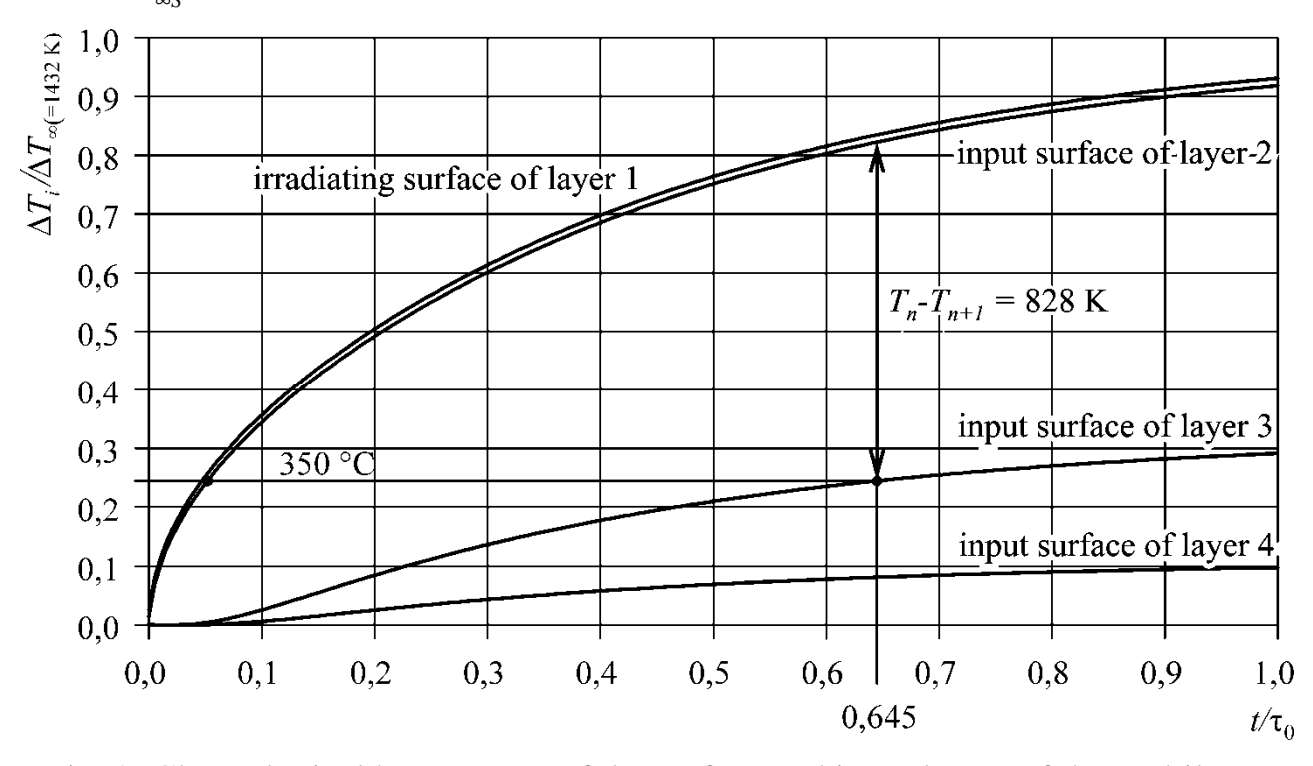


Fig. 2. Chronological heat pattern of the surface and inner layers of the multilayer structure

Based on Eq. (2) the temperature increments of the layers for the steady regime can be represented as:

$$\frac{T(\infty, y_i)}{T_{\infty S}} = \frac{\sum_{i=1}^{N} \Delta T_i}{T_{\infty S}}. (17)$$

It can be obtained from Eqs. (2), (16) and (17) that:

$$\frac{y_i}{D} = 1 - \frac{\sum_{i=1}^{N} \Delta T_i}{\Delta T_{\infty S}} = 1 - \frac{\sum_{i=1}^{N} \frac{d_i}{k_i}}{\sum_{i=1}^{N} \frac{d_i}{k_i}}.$$
 (18)

Results obtained above may be represented in the form of topological an chronological heat patterns. The heat patterns are shown in Fig.2 and 3 in the form of dependencies  $\frac{T_s}{P_s}(t)$  and  $\frac{T_s}{P_s}(x)$ , where x – is a coordinate measured from the surface depthward the structure. Calculations are carried out for the case of constant physical characteristics of used materials in the whole range of temperatures in correspondence with the Eqs. (14), (17), (18).

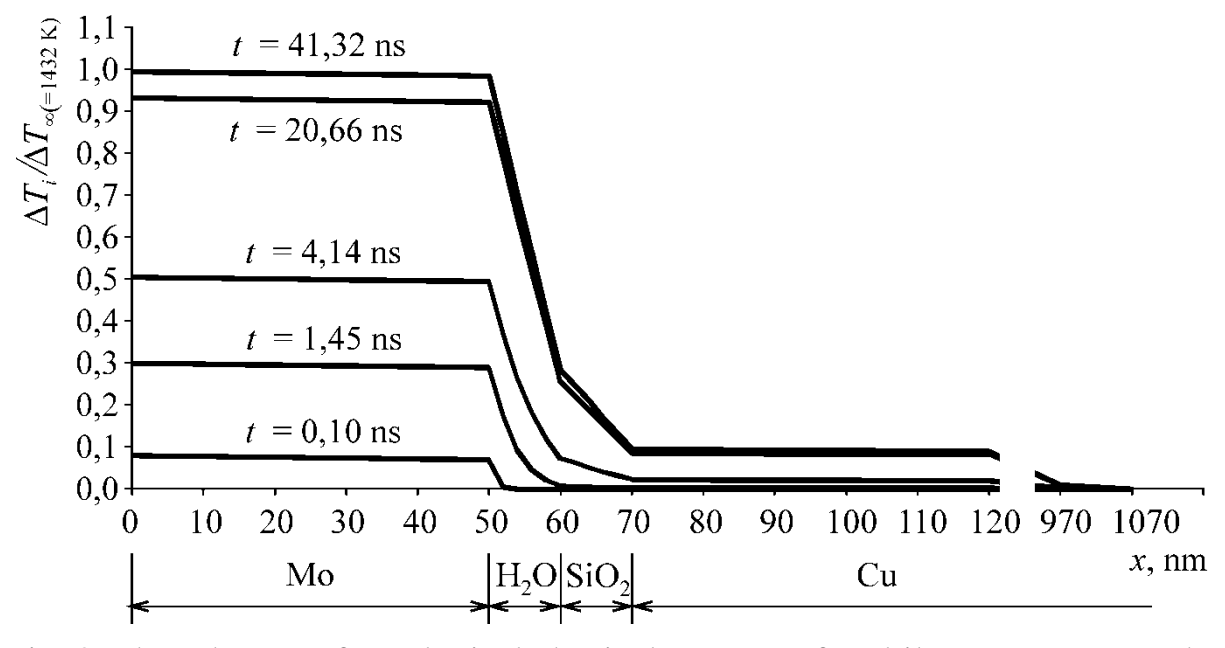


Fig. 3. The schemes of topological physical patterns of multilayer structure at the moments of time t = 0.103 ns; t = 1.447 ns; t = 4.137 ns; t = 20.66 ns; t = 41.32 ns (structure parameters are the same as in the Fig.2, the edges of structure layers are marked with dashes)

The calculations are presented for the (molybdenum – water – silicon oxide – copper) structure. The layers thicknesses and their materials thermophysical characteristics used in calculations are presented in Table 1. The absorbed power density  $P_s = 0.6 \cdot 10^{11} \text{ W/m}^2$ .

Table 1. The multilayer structure parameters

Layer	у	$d_{i}$	h	$ ho$ / $ ho_{cr}$	k	С	τ	$d_i/k_i$
	nm	nm	$10^6 \frac{\mathrm{m}}{\mathrm{s}^2}$	$10^{-3} \frac{\mathrm{kg}}{\mathrm{m}^3}$	$\frac{W}{m\cdot K}$	$10^{-3} \frac{J}{\text{kg} \cdot \text{K}}$	ns	$10^9 \cdot \frac{K \cdot m^2}{W}$
Mo	50	50	45,6	10,65	158	0,264	0,055	0,316
H <sub>2</sub> O at 250 °C	171,2	10	0,16	0,78/0,2	0,5	4,87	0,625	20,000
SiO <sub>2</sub>	187,5	10	0,78	2,2	1,84	1,07	0,128	5,435
Cu	700	1000	100	8,8	365	0,4	10	2,741
analog side							$\tau_0 = 20,66$	D = 28,49

In conclusion it may be said that obtained analytic expressions allow us to study physical processes in the multilayer structure on the substrate exposed by the flow modulated with the step shaped form of time dependence, though this expressions are approximate due to accepted simplications.

Results obtained in this work may be in-demand for the nondestructive analysis of the multilayer structures and for development of the optical mechanical converters of information.

© V.V. Chesnokov, D.V. Chesnokov, V.A. Rayhert, 2010

# INVESTIGATION OF PHOTOELECTRIC PROPERTIES OF ANOMALOUS PHOTOVOLTAIC CDTE FILMS AND DEVELOPMENT OF OPTOELECTRONIC DEVICES ON THEIR BASIS

# Bakhtiyor N. RAKHIMOV, Oleg K. USHAKOV, Nematzhon R. RAKHIMOV, Russian Federation

**Keywords:** anomalous photovoltaic films, self-contained optical radiation receivers, photoelectrical properties.

#### **Abstract**

The photoelectrical properties of anomalous photovoltaic (APV) CdTe, CdTe: Ag films have been investigated. It was for the first time to establishe that if the back side of the film is put on a silver-plated substrate, the APV effect in such film increases to 30%. On the basis of these films the self-contained optical radiation receivers and photoelectronic transformers for sensitive control of coordinates of moving objects have been developed.

#### 1. Introduction

Optical detectors based on anomalous photo voltage (APV) films [1,2] are functional generators that transform a luminous flux of intensity  $\Phi_0$  into photo voltage  $V_{AVP}$ . According to the accepted model [3], this transformation consists of three phases: (1) inducing photoelectric current  $I_{\Phi_0}$  by photogeneration and spatial separation of nonequilibrium carriers at each micro p-n junction; (2) generating elementary voltages across micro p-n junctions through the accumulation of bulk charges produced by the photocurrent; and (3) forming an anomalously high photovoltage by summing elementary photovoltages across the p-n junctions.

The technology of APV film deposition is based on the thermal evaporation of semiconductor materials in vacuum of  $10^{-3}$ – $10^{-5}$  Torr. Using the vacuum evaporation method, it is possible to obtain AVP films of different semiconductor materials with broad and narrow forbidden bands (CdTe, Si, Ge, GaAs, GaP, Se, PbS, and chalcogenide alloys) [1, 3]. However, the voltage generated by these films is low.

The technological conditions for obtaining APV films depend on a great number of parameters: the substrate and evaporation temperatures, the sputtering angle, the wall's thickness, the composition and pressure of the residual gases in the vacuum chamber, the conditions of heat treatment of films after their deposition, etc.

The investigation of photoelectrical properties of semiconductor films attracts more attention of specialists [1–7]. The films which have an anomalous photovoltaic (APV) effects are of great theoretical and applied importance for the designing of primary converters – receivers of optical radiation (ROR).

Existing ROR and the devices on their basis require obligatory application of power supplies, which results in distortion of a photo-electric signal (handicap). In them the outgoing voltage created by p-n-transition is obviously limited to the width of the band gap of the semiconductor. One of perspective optical methods is an

optoelectron control, on a basis light source and APV-receiver, which allows excluding the external power supply for ROR, to lower of weight and dimensions, provides a complete electrical outcome between circuits the ROR light-emitting diode.

The applied importance of this investigation is that the developed methods of manufacturing APV receivers make it possible to make a new step in the development of optical electronic instrument-making [8].

The aim of the present work is to investigate the photoelectrical properties of APV films on the basis of CdTe, CdTe: Ag, to develop the self-contained optical radiation receivers and photoelectronic transformers for control of quality parameters of fluids.

### 2. Experimental technique

Most efficient is the manufacture of APV films based on cadmium telluride compound. The source material (cadmium telluride) is deposited by thermal evaporation in vacuum on one side of the substrate. A silver layer is applied to the other side of the substrate (substrate temperature, 250–300°C; pressure,  $5 \cdot 10^{-4} - 5 \cdot 10^{-3}$  Torr) to impart reflecting properties to it. The substrate is located at an angle of  $45^{\circ}$  to the molecular beam to create an angular surface anisotropy that gives rise to an anomalous photovoltage. A portion of the light beam that passes through the source materials and the glass substrate is incident on the silver layer, is reflected from it, and returns to the other side of the substrate (i.e., to the cadmium telluride layer). As a result, this layer absorbs more light, and, hence, is photovoltage generated in grows in value [2].

The CdSe, CdTe and CdTe: Ag APV-films have been obtained in vacuum by thermal evaporation method. The vacuum installation provided the pressure about 10<sup>-4</sup> Pa. As evaporator the aluminium or beryllium oxides were used.

Three ways of activization of APV-films have been used:

- 1. At first a thin layer of silver with thickness 1–2 monolayers is deposited on a substrate, and then a CdTe film is evaporated on this surface. After evaporation of CdTe the thermal processing in vacuum will be carried out.
- 2. During condensation of a CdTe layer the simultaneous evaporation of silver on a substrate was made by separate evaporator.
- 3. The manufacturing of a mechanical mix of cadmium telluride and silver by a way hashing of their powders with subsequent evaporation during one hour in vacuum of  $10^{-4}$  Pa has been made. In this case the temperature of the evaporator and substrate were supported at 200 °C on the heated up substrate.

Carried out on the large number of samples of research have shown, that most effective ways are the first and second methods. At that the films have most stable photovoltaic properties. At their illumination by light source with intensity of  $\sim 8\times10^{-2}$  Wt/cm<sup>2</sup> the APV was generated up to 800 V on 1 cm<sup>2</sup> sample at room temperature.

The voltampere characteristics of all investigated APV-films at room temperature, at lightness  $I = 3.5 \times 10^4$  Lucks and at electrical field  $E = 10^3 \text{V/cm}^2$  submit to Ohm law.

Lucks-volt characteristics are essential non-linear and the photovoltage practically achieves saturation at lightness about 10 Lucks. The fast reaching the lucks-volt dependencies on saturation provides the stability of optoelectron of systems to changes of light exposure.

#### 3. Results and discussion

At illumination of the backside of APV-films by a light source with intensity  $\sim 8\times10^{-2}$  Wt/cm<sup>2</sup> the APV were generated up to 300 V on cm<sup>2</sup>. It testifies that the APV is generated at reflection of light too. If the backside of a glass or quartz substrate is covered by a reflecting Ag coverage the APV should increase.

In Fig. 1 the APV-films with the reflecting silver layers are presented where 1 – the photosensitive layer of cadmium telluride crystal; 2 – a glass substrate; 3 – reflecting silver layer; 4 - metal contacts.

The incident flow of light  $\Phi_0$  the APV, the part of a flow of light  $\Phi_1$  passing through a substrate, gets on a layer of silver and being reflected gets on the backside of cadmium telluride film, as a result of that the additional absorption of light is observed and in this connection the generated anomalous photovoltage is increased. The results showed the APV effect in such film increases to 30 %.

On the basis of GaP, GaAs, CdSe, CdTe, CdTe: Ag the APV-receivers were made. As a photosensitive element of the independent receiver of an optical element the film with size of 4x2 mm has been used. The curves  $V_{APV}(\lambda)$  show the good spectral coordination of optoelectron pairs of CdTe:Ag and AJI-108A (Fig. 2).

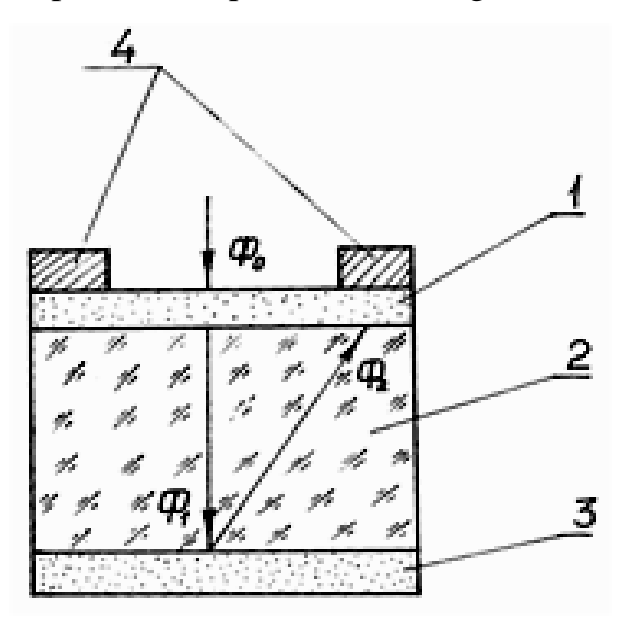


Fig. 1. The APV-film with the reflecting silver layers: 1 – the photosensitive layer of cadmium telluride crystal; 2 – a glass substrate; 3 – reflecting silver layer; 4 – metal contacts.

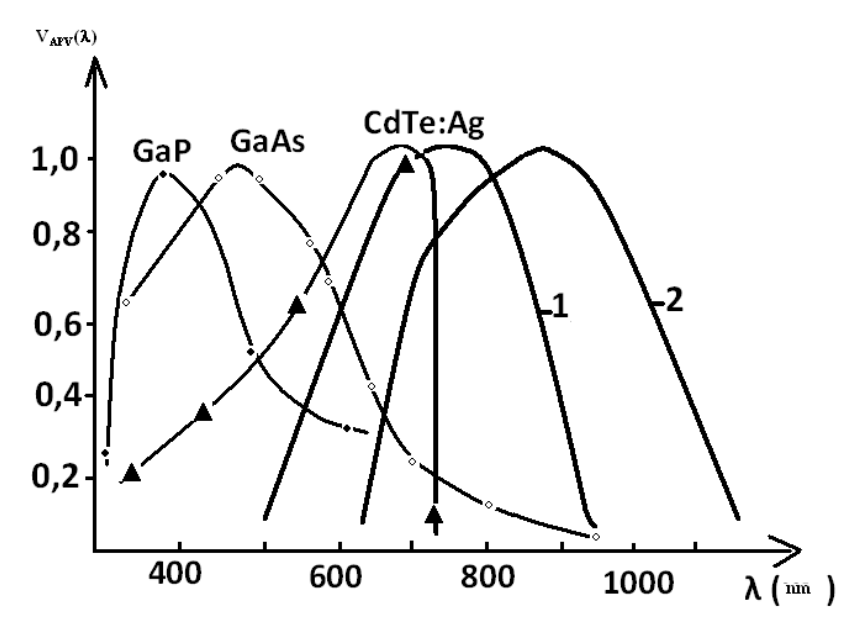


Fig. 2. Spectra  $V_{APV}(\lambda)$  of some APV-films and light radiation diodes AL-108A (1), AL 307M (2)

In [7], we proposed a design for a position-sensitive optical detector and a technique for its manufacture. In this paper, we describe an experimental technique and present the results from investigating an optical detector composed of a semiconductor APV film with a stepwise configuration, the steps of which gradually increase in thickness, starting with a value of ~1µm.

Films of different thicknesses were obtained using a VUP-2k vacuum system. The vacuum in the work chamber was on the order of  $10^{-4}$ – $10^{-5}$  Torr. A substrate, heated to temperatures of 310-480 $^{0}$ C, was placed at an angle of 45 $^{0}$  with the molecular beam.

Pieces of glass 2 mm thick were used as substrates. When prepared, each substrate was inserted into a holder, and a mask made of insulating material (a paper-based laminate) was attached to its surface. A micro motor (2 rpm) placed inside the work chamber was used to cover or uncover the substrate's surface. As the motor rotated, it pulled a light heat-resistant cord attached to the mask, and the substrate's surface was gradually uncovered. The films deposited thereby on the substrate of dimensions 2x20 mm were of a stepwise configuration. The thickness of each step was measured with MI-4 interference microscope.

A diagram of a film with an anomalous photovoltage is shown in the figure. The photovoltage is generated by incident luminous flux  $\Phi_0$ . As the position of incidence of monochromatic radiation changes step-wise from 1 to 2.0  $\mu$ m, photovoltage  $V_{APV}$  generated in the film declines proportionally.

For producing the coordinate-sensitive elements we made the film with various thicknesses. The effective thickness of a sensitive layer is 1  $\mu$ m for cadmium telluride films. With increase of thickness in the region more than 1  $\mu$ m the APV decreases (Fig. 3).

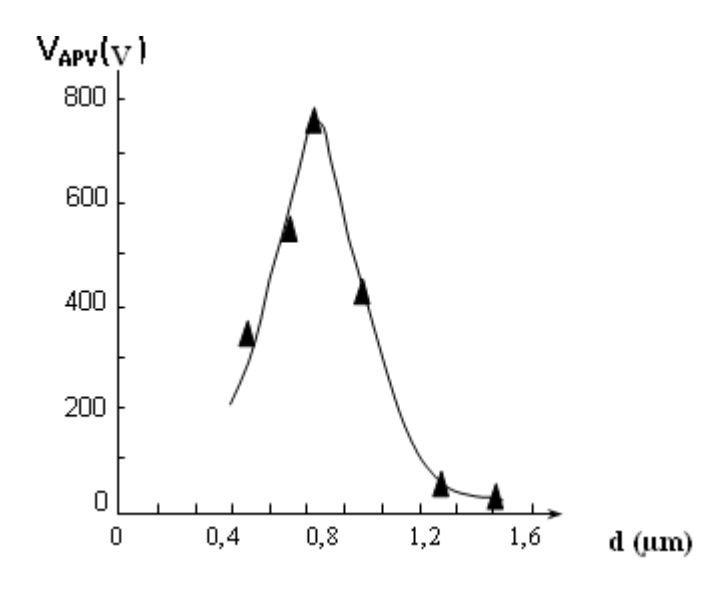


Fig. 3. The dependence of V<sub>APV</sub> versus the thickness of CdTe film

As substrate the glass with thickness of 2 mm was used. The prepared substrates were located in the special holder and on a surface of a substrate the mask from a isolation material was fixed. In the working chamber the microelectric motor 2 rev/min was fixed for opening or closing of a surface of substrate. Thus, there was obtained the step film on a substrate with the size  $2x20 \text{ mm}^2$ .

In Fig. 4 the APV-step film was shown, where 1-a photosensitive step layer of cadmium telluride crystal; 2-a glass substrate, 3- the metal contacts,  $\Phi_0-$  an incident flow of directed monochromic radiation.

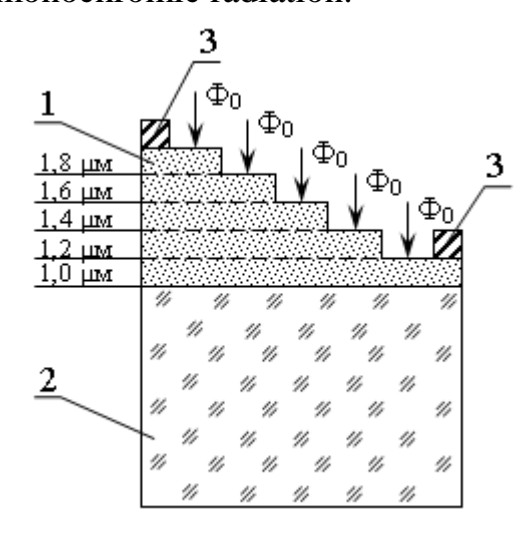


Fig. 4. The coordinate-sensitive APV-step film: 1-a photosensitive step layer of cadmium telluride crystal; 2-a glass substrate, 3- the metal contacts,  $\Phi_0-$  an incident flow of directed monochromic radiation

The incident flow of light  $\Phi_0$  generates the APV. Changing coordinates of monochromic radiation on step with thickness of 0.2  $\mu$ m from 1 to 2.0  $\mu$ m the generated APV proportionally decreases.

In coordinate-sensitive photogenerators on a basis cadmium telluride films it is possible to develop the coordinate-sensitive independent receiver of optical radiation. The entrance signal contains the information on a direction and size of displacement of radiating object. On the basis of such films the coordinate-sensitive independent receiver of optical radiation "KCHP-1M" was made.

#### 4. Conclusion

The obtained results for APV-films such as CdTe is characteristic by that the magnitude of photovoltage depends on thickness of film. Optimum thickness of a film is ~1  $\mu$ m, at which the APV reaches the maximum. With increase of thickness in the region more than 1  $\mu$ m the APV decreases. On the basis of such dependence the coordinate-sensitive independent receiver of optical radiation was made.

The technique of increase of the anomalous photovoltage in semi-conductor film structures is developed. It was established that if the back side of the film is put on silver-plated substrate, the APV in such film increases to 30%.

An optical sensor based on cadmium telluride films can be used in a self-contained position-sensitive optical detector.

The main parameters of the position-sensitive optical detector based on a CdTe APV film are as follows: sensitivity, 2–5 V/mm (at an illumination intensity of 10 1x): internal resistance,  $10^{12}$ – $10^{14}$   $\Omega$ ; response time, 0.8–1.0 s; emission spectrum, 0.5–0.83  $\mu$ m; and sensitive area, 2×15 mm. the detector measures 2×2×20 mm overall, and its mass is no more then 3.0 g.

#### REFERENCES

- 1. Starkiewich J., Sosnovski L., Simpson O., Nature, 158 (1946) 28.
- 2. Rakhimov N.R. and Mamadaliyeva L.K., Izv. Vyssh. Ucheb. Zaved., Priborostroenie, 2004, vol. 47, no. 8, p. 53.
  - 3. Chonussot G., Class A.M., Phys. Lett., A59 (1976) 405.
  - 4. Von der Linde D., Class A.M., Appl. Phys., 8 (1975) 85.
- 5. Rakhimov, N.R. in Sovremennye metody i sredstva nerazrushayushchego kontrolya I tekhnicheskoi diagnostiki (State-of-the-Art Methods and Means of Non-Destructive Inspection and Engineering Diagnostics), Kiev: UITs "Nauka, Tekhnika, Tekhnologiya", 2000, p. 59.
- 6. Fotoelektricheskie yavleniya v poluprovodnikakh i optoelektronike (Photoelectric Phenomena in Semiconductors and Optoelectronics), Adirovich, E.I., Eg., Tashkent: Physical Inst., 1972, p. 177.
- 7. Rakhimov, N.R. and Ser'eznov, A. N. RF Patent 2 246 779, Byull. Izobret., 2005, no. 5, p. 121.

# PRINCIPLE AND ARRANGEMENT OF ABSORPTION SPECTRUM MEASUREMENT OF THE LAYERS ADSORBED ON TRANSPARENT SUBSTRATES

# Daria S. MIKHAYLOVA, Vladimir V. CHESNOKOV, DmitryV. CHESNOKOV, Russian Federation

**Keywords**: spectrum absorptances nanolayers, principle, frustrated total internal reflection (FTIR), optical fiber

#### **Abstract**

The principle of measurement of spectrum absorptances nanolayers of the elementorganic compounds, based on use of the optical fibre measuring converter is described in article.

The purpose of this work is developing of absorptances of monomolecular layers adsorbed on substrates method of measurement. For realization of this problem we develop a fibre-optical attachment to spectrophotometer.

The developed method is based on using frustrated total internal reflection (FTIR) phenomenon. If monochromatic radiation directed along optical fibre on which surface the adsorbed condition of molecule elementorganic compounds are located, the last fall into in the field of radiation, optically tunneling from an optical fiber in surrounding space. The adsorbed monolayer absorbs falling radiation. Advantage of a method of measurements is possibility of passage of a light bunch not across, but along the deposited layer of molecules elementorganic compounds, that should increase essentially relative "thickness" of a layer of a material through which there passes radiation. Though absorptance does not vary, the absorption factor grows to the value, allowing it to measure.

The method is realized in the attachment represented on Fig. 1.

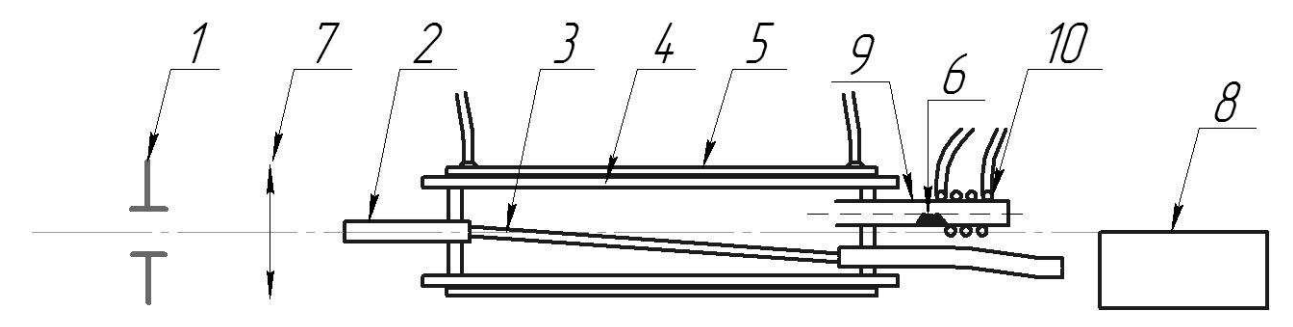


Fig. 1. The scheme of the developed attachment

The radiation, leaving through the monochromators slit 1 are focused by a lens 7 on butt-end single-core optical fibre cable 2 on a section 3 which all external covers are removed and the core is exposed. This section is placed into the chamber 4 with heater 5.

The reagent 6 is in the tubular evaporator 9 having a heating element 10. The radiation which has left an optical fiber, gets on an detector window of the photomultiplier tube 8 [1, 2].

During development of the method of research the transmission spectrum the adsorbed iodine in a range of lengths of waves from 290 up to 600 nanometers has been received. In the further work on expansion of a spectral range of researches will be lead.

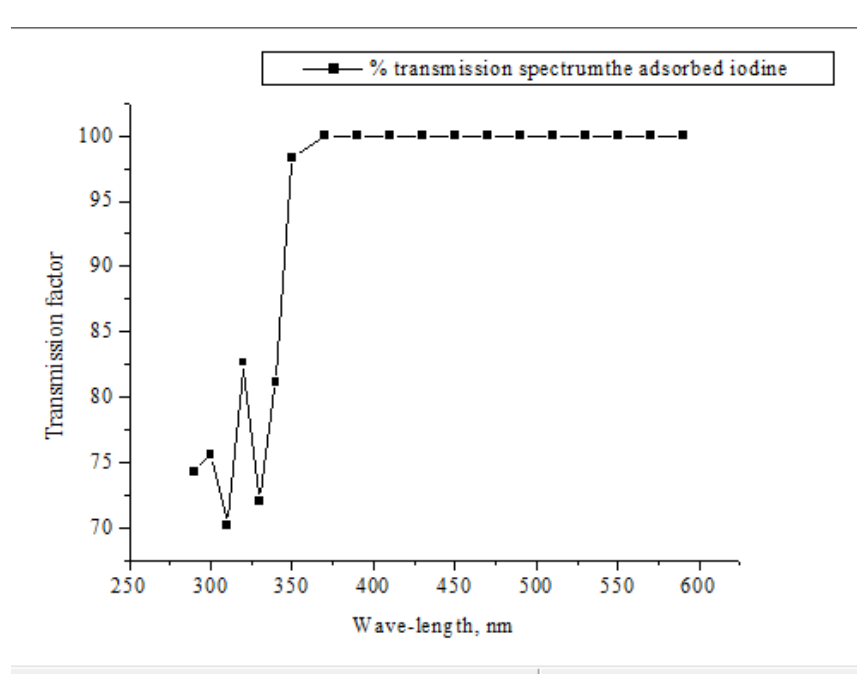


Fig. 2. The transmission spectrum the adsorbed iodine

#### References

- 1. V.V. Chesnokov, E.F. Reznikova, D.V. Chesnokov, under general editorial staff D.V. Chesnokov. Laser nanosecond microtechnologies, Novosibirsk: SSGA, 2003.
- 2. D.S. Mihailova D.V. Chesnokov. Research of spectra of absorption of the metalloorganic compounds applied at photoinduced sedimentation of thin films. Novosibirsk: GeoSiberia-2007.

© D.S. Mikhailova, V.V. Chesnokov, D.V. Chesnokov, 2010

# Dmitry M. NIKULIN, Vladimir V. CHESNOKOV, Dmitry V. CHESNOKOV, Russian Federation

**Keywords**: multiplex-optical filter, an interference, micro-and nanotechnologies

#### **Abstract**

The present paper deals with the questions of development and expected parameters of tunable multiplex-optical filters which use the combination of two interference optical filters - with one of high and with the first interference orders.

Now interference optical filters are widely used in physical research, measuring and military equipment, industry [1,2]. Their advantages are simplicity and convenience in work, high degree of monochromaticity of an optical filter's spectrum band. It is possible for these devices to obtain some additional benefits if they are capable to tune an allocated spectrum band that can be reached when using micro-and nanotechnologies [3, 4, 5].

In interference optical filters presented in the paper it is used an electro-driven regulation of an air clearance between mirrors of the Fabry-Perot resonator at the size of the clearance corresponding to the first order of an interference; metal films on glass substrates are used as mirrors. This paper considers the questions of development and expected parameters of tunable multiplex-optical filters which use the combination of two interference optical filters - with one of high and with the first interference orders.

In a tunable multiplex-optical filter under development the clearance regulation between mirrors of the resonator with the first interference order is provided with the use of direct piezoelectric effect, the clearance between mirrors of the second resonator does not change. With the use of two consecutive on the course of a beam adjusted optical filters – low and high orders – it is possible to increase monochromaticity of radiation allocated from the spectrum of the source and keep the width of a tunable diapason [5]. The simplified scheme of such an optical filter is shown in Figure 1. The optical filter of the first order is formed by mirrors I and I and an air clearance between them. The optical filter of a high order is formed by mirrors I and I and a transparent plate I between them. A holder I is attached to a piezoceramic bead I and a transparent plate I is fixed in a holder. A transparent plate is covered by mirror I and I the most important design feature of the device is the usage of a submicron equidistant I air clearance between mirrors I and I this clearance is adjusted within I the most importance between mirrors I and I this clearance is adjusted within I the most importance between mirrors I and I this clearance is adjusted within I the most importance between mirrors I and I this clearance is adjusted within I the mirror I the clear aperture of I the mirror I the mirror I the most importance between mirrors I and I this clearance is adjusted within I the mirror I the clear aperture of I the mirror I

The control of the air clearance amount is piezoelectric: control voltage  $U_0$  is applied between plates of piezoceramic beads 8. When the voltage  $U_0$  is applied, a piezoceramic bead 8 (Figure 1) changes its thickness depending on the amount of the applied voltage; the change of thickness can be calculated by the formula:

$$\Delta \ell = \ell d_{33} E = d_{33} U_0, \qquad (4)$$

Where  $d_{33}$  – piezoelectric modulus of the material of a piezoelectric element,  $\Delta \ell$  – deformation on the thickness of a piezoelectric element E – electric field intensity in a piezoelectric element,  $U_0$  – voltage.

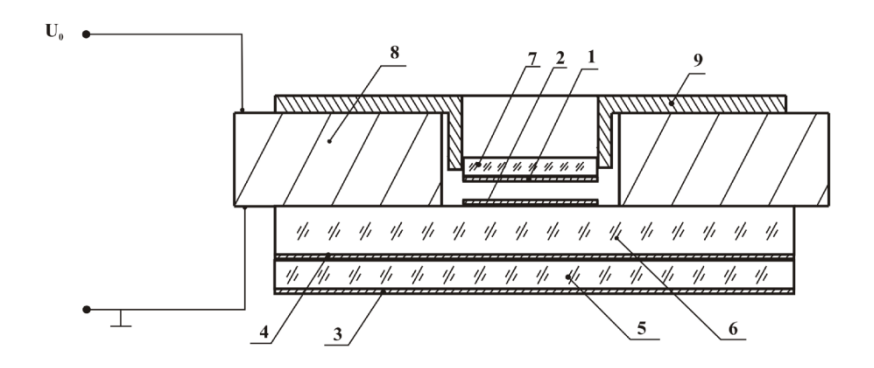


Fig. 1. The simplified scheme of a tunable multiplex-optical filter

If for a piezoelectric element we use piezoceramics PKB-590 (TsTS<sub>t</sub> BS-2), which has  $d_{33} = 500 \cdot 10^{-12}$  C/N for a multiplex-optical filter tuning within the whole visible diapason of the spectrum on  $\Delta \ell = 0.2$  µm, the required voltage is up to  $U_0 = 400$  V.

Let's consider optical characteristics of an optical filter. In a multiplexinterferometer under the proportion of optical thickness of interferometers, divisible by an integer, dispersion area is defined by the area of dispersion of a thin interferometer, and dispensation is defined by a thick interferometer.

The multiplex-optical filter transparency is similar to a transparency of a four-mirror interferometer and is calculated by the formula [1]:

$$T_{M} = \frac{T^{4}}{\left(1+R\right)^{2} \left[\left(1-R\right)^{2} + 4R\sin^{2}\frac{\delta_{2}}{2}\right]}, (5)$$

Where:  $\frac{\delta_2}{2} = \frac{2\pi}{\lambda} n L_2$  (without jumps of phases on reflecting surfaces), T and R -power transparency and reflection index of each mirror. The spectrum order is calculated by the formula:

$$q = \frac{2Ln}{\lambda_{cp}}, \qquad (6)$$

Where: Ln – an optical width of the distance between mirrors;  $\lambda_{cp}$  – an average length of a wave of the interferometer dispersion area.

The dispersion area of a multiplex-optical filter is approximately equal to the dispersion area of a thin optical filter [2]:

$$\Delta \lambda_{M} = \frac{\lambda_{cp}}{q_{1}}, \qquad (7)$$

Where:  $q_1$  – a spectrum order of a thin optical filter.

The acceptable difference of wave lengths in a multiplex-optical filter is calculated by the formula [2]:

$$\delta_{\lambda} = \frac{\lambda}{q_2} \cdot \frac{1 - R}{\pi \sqrt{R}}. (8)$$

Let's perform a quantitative estimation of the achievable parameters of the considered device in which interferometer with a smaller clearance has an order  $q_1 = 1$ ; an adjustable diapason of the spectrum  $\Delta \lambda = 0, 4 \div 0, 8$  µm; according to (3) the amount of the clearance  $L_1$  in extreme points of the tuning diapason:  $L_1 = 0, 2 \div 0, 4$  µm.

Instrument function of a multiplex-optical filter is equal to the product of instrument functions of its components; the optical filter passes radiation with the lengths of waves which are simultaneously present at pass-bands of both its constituent optical filters.

When tuning (by changing the clearance between mirrors) an optical filter with the first order of an interference, its pass-band is displaced on a spectrum, the allocation of one dispersion band occurs, then - the allocation of the other band of the second optical filter, i.e., "switching" of the diapasons  $\Delta \lambda_2$  passing through an optical filter with the big interference order. We can calculate the optimum combination of spectral characteristics of optical filters by equaling the width of a pass-band of an optical filter with a smaller clearance  $\delta_{\lambda 1}$  to the dispersion band  $\Delta \lambda_2$  of the second one:  $\delta_{\lambda 1} \approx \Delta \lambda_2$ .

Number *M* of "switched" dispersion bands equals:

$$M = \frac{\Delta \lambda_1}{\Delta \lambda_2}.$$
 (9)

Let's find the dispersion band of the second interferometer:

$$\Delta \lambda_2 = \frac{\lambda}{q_2}.\tag{10}$$

Distance  $L_2$  corresponding to this band between the mirrors of the second interferometer is calculated by the formula:

$$nL_2 = \frac{\lambda}{2\pi} \cdot q_2. \quad (11)$$

Here n - an index of environment refraction. The results of the calculations are provided in Table 1.

Table 1. Calculation optical parameters of a micromechanical multiplex-optical filter  $(R = 0.9, T = 0.07, n_2L_2 = 5.8 \mu m)$ 

$L_1$ , $\mu \mathrm{m}$	λ, μm	$δλ_1,$ μm	$\Delta \lambda_M$ , $\mu m$	$δλ_M,$ $μm$	q	$M = q_{\min} - q_{\max}$	$T_{M}$
0,2	0,4	0,013	0,013	0,00046	29	14,5	0,24
0,3	0,6	0,02	0,031	0,001	19,3	14,5	0,0009
0,4	0,8	0,027	0,055	0,0019	14,5	14,5	0,0007

Fig. 2 presents the design dependence chart of the transmission of a multiplexoptical filter on the wave length at the size of an adjustable clearance.

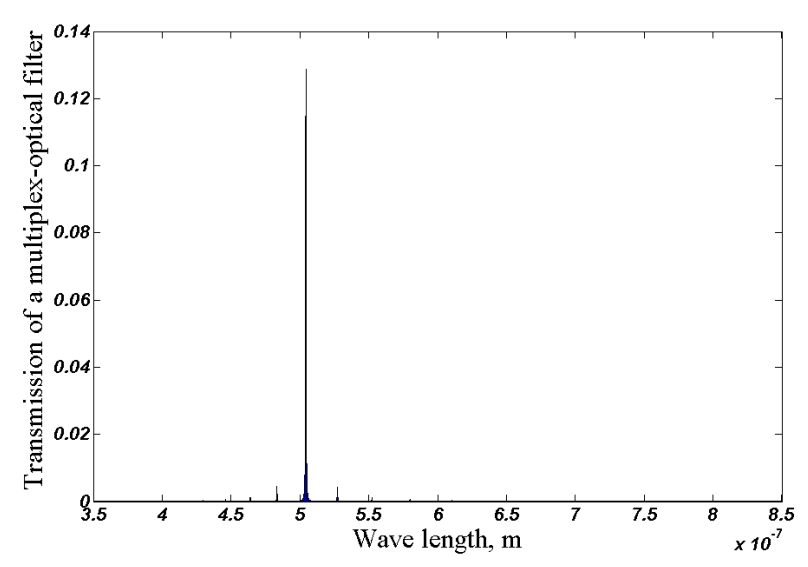


Fig. 2. The calculation design chart of the transmission of a multiplex-optical filter.

The performed calculations show that a micromechanical multiplex-optical filter can work overlapping all visible diapason of a spectrum with the dispensation about 10~Å, what is clear from the Figure 2 which presents the design dependence chart of the transmission of a multiplex-optical filter on the wave length at the size adjustable clearances:  $1.7~\mu m$  of an optical filter with high interference order, 250~nm of an optical filter with low interference order. The reflexion index of the mirrors is equal 0.85, transmission index of the mirrors 0.05, transmission index of an optical filter 0.01.

Preliminary research of experimental samples has been carried out. An air clearance between the resonator mirrors with the first interference order having deviations from the equidistance of the order 0.09  $\mu m$  (it was defined on the basis of interference colours) on clear aperture of 8 mm; at the clearance change of 0,125  $\mu m$  the resonator was tuned from blue colour transmission to red colour transmission.

The similar optical filter, in our opinion, can be applied in systems of the express analysis of chemical substances and various industrial liquids and gases, in research of harmful substances content in environment. The optical filter can have modifications working in IR-diapasons of a spectrum.

#### REFERENCES

- 1. Skokov, I.V.Multibeam interferometers in measuring equipment I.V.Skokov. M: Mechanical engineering, 1989. p. 256.
- 2. Lebedev, V.V. Experimental optics. 3 ed. / V.V. Lebedev. M: MSU, 1994. p. 265.
- 3. Research of physical problems nano and microdimensional functional devices of information optoelectronic systems: the report about NIR / SGGA; sup. V.V. Chesnokov; exec. Chesnokov D.V. Novosibirsk, 2003. p. 71. № GR 0199.0010326. Inv. № 02200 1.03177.

- 4. Chesnokov, A.E. Research of optical characteristics of multilayered structures of the adjusted Fabry-Perot resonator/ A.E.Chesnokov // GEO-Sibir 2007. T. 4. Specialised instrument making, metrology, thermophysics, microtechnics. P. 1: source book III Internat. Scient. Congr. «GEO-Sibir-2007», 25–27 apr. 2007 Novosibirsk. Novosibirsk: SGGA, 2007. p. 167–170.
- 5. Chesnokov, V.V. Interference optical filters with a tunable pass-band / V.V. Chesnokov, D.V.Chesnokov, D.M.Nikulin // source book IV Internat. Scient. Congr. «GEO-Sibir-2008», Novosibirsk, 2008. T.4., p. 1. pp. 11–16.
- 6. Chesnokov V.V., Chesnokov D.V., Nikulin D.M., Chesnokov A.E. Manufacturing process of a tunable optical filter with Fabry-Perot interferometer / Application №2008130196, Russia. a priority of 21.07.2008.

© D.M. Nikulin, V.V. Chesnokov, D.V. Chesnokov, 2010